

University of Southampton

Faculty of Engineering and Physical Sciences
School of Physics and Astronomy

**Shining Lights, Even in Death: Modelling the
Optical and Ultraviolet Emission from Tidal
Disruption Events**

by

Edward John Parkinson

ORCID: [0000-0003-3902-052X](https://orcid.org/0000-0003-3902-052X)

*A thesis for the degree of
Doctor of Philosophy*

May 2022

Any great warrior is also a scholar, and a poet, and an artist.
- Steven Seagal

University of Southampton

Abstract

Faculty of Engineering and Physical Sciences
School of Physics and Astronomy

Doctor of Philosophy

**Shining Lights, Even in Death: Modelling the Optical and Ultraviolet Emission from
Tidal Disruption Events**

by Edward John Parkinson

When an unlucky star wanders too close to a supermassive black hole, the self-gravity keeping that star together is completely overwhelmed by the tidal forces of the interaction and is torn asunder in something known as a tidal disruption event (TDE). The fallback of the stellar debris, and subsequent accretion, onto the black hole drives a powerful, but transient, luminous flare visible across the electromagnetic spectrum: a shining light, even in death.

Within the past decade, the census of TDEs has rapidly grown to a dizzying 56 events. Theoretical progress, on the other hand, has somewhat lagged behind and our understanding of these events is held back by our ignorance of the emission mechanisms fuelling the luminous flare. Given their extreme luminosities, TDEs are expected to generate significant mass loss in the form of radiation driven winds, but their properties remain poorly understood even though their importance is widely acknowledged.

In this thesis, I use state-of-the-art Monte Carlo radiative transfer and ionization software to model the profound impact such powerful outflows could have on the optical and ultraviolet (UV) spectra of these events. Focusing exclusively on the sub-Eddington accretion phase, I first show how the diverse family of UV spectra, showcasing broad absorption and emission lines, can be unified as an orientation effect associated with line formation in an accretion disc wind. And if true, I suggest that the relative number of broad absorption to emission line TDEs could be used to estimate the outflow covering fraction.

I also demonstrate how such outflows can efficiently reprocess thermal emission from an accretion disc, producing the broad Balmer and helium optical recombination features characteristic of TDEs, as well as a spectral energy distribution (SED) with a much lower characteristic colour temperature. I next apply the exact same numerical techniques to post-process a snapshot of a realistic hydrodynamic model of the super-Eddington accretion phase, illustrating how different reprocessing regimes can modify the SED and influence the observable signatures of TDEs.

In summary, then, this thesis demonstrates how optically thick outflows impact and shape the observational properties of TDEs, and why, in the future, detailed radiative transfer calculations are required to understand the full complexities of TDE emission.

Contents

Abstract	v
Contents	vii
List of Figures	xi
List of Tables	xxi
Definitions and Abbreviations	xxiii
Physical Constants	xxv
Acknowledgements	xxvii
Declaration of Authorship	xxix
1 Introduction	1
1.1 Accretion	4
1.1.1 Basics of accretion	4
1.1.2 The Eddington limit	5
1.2 Accretion discs	7
1.2.1 The steady state accretion disc	8
1.2.2 A slim accretion disc	9
1.2.3 The spectra of accretion discs	10
1.3 Accretion disc winds	14
1.3.1 Driving mechanisms	14
1.3.1.1 Thermal	14
1.3.1.2 Radiation	15
1.3.1.3 Magnetic	15
1.3.2 Observational evidence	17
1.4 Tidal disruption events	19
1.4.1 Rate of tidal encounters	21
1.4.2 Disruption	21
1.4.3 Fallback of material	23
1.4.4 Accretion discs	24
1.4.4.1 Formation	25
1.4.4.1.1 Dissipation due to the nozzle shock	27
1.4.4.1.2 Dissipation due to self-intersection	27
1.4.4.2 Evolution	28

1.4.4.3	Eccentric accretion discs	29
1.4.5	Spectroscopic observations	29
1.4.5.1	Spectral line profiles	29
1.4.5.2	Optical spectra	31
1.4.5.3	Ultraviolet	34
1.4.6	Photometric properties	36
1.4.7	Outflows in tidal disruption events	39
1.4.8	Reprocessing	41
1.4.8.1	Atomic/absorption	41
1.4.8.2	Bulk scatter reprocessing	42
1.4.8.3	Comptonization	45
1.4.9	Unifying X-ray and optically bright TDEs	45
1.5	The aims of this thesis	47
2	Monte Carlo Radiative Transfer and Ionization	49
2.1	Fundamentals of radiative transfer	49
2.1.1	The radiation field	50
2.1.2	Absorption and emission processes	51
2.1.2.1	Emission	51
2.1.2.2	Absorption	51
2.1.3	Random walk of photons	52
2.1.4	The optical depth	53
2.1.5	The equation of radiative transfer	54
2.1.6	Scattering	56
2.1.7	Radiative equilibrium	57
2.1.8	Local thermodynamic equilibrium	57
2.1.9	The dilute blackbody approximation	58
2.2	The Monte Carlo method	59
2.3	Monte Carlo radiative transfer and ionization	60
2.3.1	Basics	61
2.3.2	Wind models	62
2.3.2.1	The Shlosmann & Vitello wind model	62
2.3.3	Micro-clumping	64
2.3.4	Atomic data	66
2.3.5	Radiation sources	66
2.3.5.1	Accretion disc	66
2.3.5.2	Central source	67
2.3.5.3	The outflow	67
2.3.6	Photon packets	67
2.3.7	Radiative transfer	68
2.3.7.1	Sobolev approximation	69
2.3.7.2	Doppler shifts	70
2.3.7.3	Special relativity	71
2.3.8	Calculating the ionization state	71
2.3.8.1	Heating and cooling balance	72
2.3.8.2	Modelling the radiation field	73
2.3.8.3	Ionization fractions and level populations	74

2.3.8.3.1	Simple two-level atoms	74
2.3.8.3.2	Macro atoms	76
2.3.8.3.3	A hybrid scheme	79
2.3.9	Synthetic spectrum generation	80
3	Ultraviolet Spectral Lines as Orientation Indicators	81
3.1	Introduction	81
3.2	Model setup	83
3.3	Results	86
3.3.1	A fiducial wide-angle disc wind	87
3.3.1.1	The physical properties	87
3.3.1.2	The emergent spectrum	90
3.3.2	Wide-angle vs equatorial winds	90
3.3.3	Clumping	92
3.3.4	Abundances	92
3.4	Discussion	95
3.4.1	UV lines as geometry and orientation indicators	95
3.4.2	The optical depth of disc winds in TDEs	97
3.4.3	Limitations and future work	98
3.5	Summary	100
3.6	Data availability	101
4	Optical Line Spectra from Reprocessing in Optically Thick Outflows	103
4.1	Introduction	103
4.2	Model setup	105
4.3	Results	107
4.3.1	A fiducial model	108
4.3.1.1	Physical properties	109
4.3.1.2	Optical spectra	111
4.3.2	Synthetic spectra across the simulation grid	113
4.3.2.1	Disc mass-accretion rate	116
4.3.2.2	Wind mass-loss rate	116
4.3.2.3	Terminal velocity	117
4.3.2.4	Black hole mass	117
4.4	Discussion	118
4.4.1	The origin of optical emission	118
4.4.2	Formation of optical lines	120
4.4.3	The effect of electron scattering on the line profiles	121
4.4.4	Comparison to observations	122
4.4.5	UV spectral lines as geometry and orientation indicators	124
4.4.6	Limitations	126
4.5	Summary	127
5	Reprocessing in Super-Eddington Tidal Disruption Events	131
5.1	Introduction	131
5.2	Model setup	133
5.2.1	θ -averaged models	134

5.2.2	ϕ - and t -averaged model	137
5.2.3	Atomic data	138
5.3	Reprocessing mechanisms	139
5.4	Results	139
5.4.1	A benchmark test case	140
5.4.2	Results in two dimensions	142
5.4.2.1	Physical properties	142
5.4.2.2	The optical depth	145
5.4.2.3	The synthetic spectra	147
5.5	Discussion	149
5.5.1	Bulk scatter vs. atomic reprocessing in the outflow	149
5.5.2	The optical-to-X-ray ratio as a function of inclination	152
5.5.3	How important is treating radiative transfer in 2D?	154
5.6	Limitations	157
5.7	Future work	158
5.8	Summary	159
6	Conclusions and Future Work	161
6.1	Conclusions	161
6.2	Future work	164
6.2.1	Accelerating photon transport in optically thick regions	164
6.2.2	Emission from different disc geometries	165
6.2.3	Radiation hydrodynamic simulations of TDEs	165
6.2.4	Extending modelling into three dimensions	166
Appendix A	Optically Thick Monte Carlo Radiative Transfer	169
Appendix A.1	Modified random walk	170
Appendix A.1.1	Diffusion along a random path	170
Appendix A.1.2	The modified random walk algorithm	172
Appendix A.1.3	Partially grey random walk	173
Appendix A.2	Packet splitting and Russian Roulette	174
Appendix A.2.1	Packet splitting	174
Appendix A.2.2	Russian Roulette	176
Appendix A.2.3	Coupled packet splitting and Russian Roulette	177
Appendix A.3	Path stretching	178
References		181

List of Figures

1.1	The influence of spin on the event horizon radius and ISCO (top panel), as well as the accretion efficiency (bottom panel) for a SMBH of mass $M_{\text{BH}} = 10^9 M_{\odot}$. A spin value of $a = 0$ corresponds to a non-rotating Schwarzschild black hole, whilst a value of $a = 1$ and $a = -1$ correspond to either a prograde and retrograde Kerr black hole, respectively.	6
1.2	The effective temperature profiles for an α -disc (Equation 1.15) and slim disc (Equation 1.16) for the Eddington accretion fractions labelled in the figure. For small Eddington fractions, both temperature profiles are essentially the same. However, as the Eddington fraction increases, the effective temperature for the slim disc drops because of increased radiative trapping which results in a lower radiative efficiency for the slim accretion disc atmosphere. To calculate these profiles, the following parameters were used to model the accretion disc for a Schwarzschild SMBH: $M_{\text{BH}} = 10^7 M_{\odot}$, $R_{\text{in}} = R_{\text{ISCO}}$, $R_{\text{out}} = 4.5 R_{\text{ISCO}}$ and an Eddington accretion fraction as labelled assuming an accretion efficiency of $\eta = 0.1$	10
1.3	The accretion disc spectrum for three distinct systems assuming an α -disc with an accretion efficiency of $\eta = 0.1$, as follows: 1) a QSO with $M_{\text{co}} = 10^9 M_{\odot}$, $\dot{M}_{\text{acc}} = 10 M_{\odot} \text{ yr}^{-1}$, $R_{\text{in}} = 8.85 \times 10^{14} \text{ cm}$, $R_{\text{out}} = 1 \times 10^{17} \text{ cm}$, 2) an XRB with $M_{\text{co}} = 10 M_{\odot}$, $\dot{M}_{\text{acc}} = 10^{-7} M_{\odot} \text{ yr}^{-1}$, $R_{\text{in}} = 10^7 \text{ cm}$, $R_{\text{out}} = 10^{12} \text{ cm}$, and, 3) a CV with $M_{\text{co}} = 0.8 M_{\odot}$, $\dot{M}_{\text{acc}} = 10^{-8} M_{\odot} \text{ yr}^{-1}$, $R_{\text{in}} = 7 \times 10^8 \text{ cm}$, $R_{\text{out}} = 2.4 \times 10^{10} \text{ cm}$	11
1.4	The accretion disc spectrum for two Eddington accretion regimes using a standard α -disc temperature profile (solid lines) and a slim disc temperature profile (dashed lines) for two Eddington fractions, using the same disc parameters as in Figure 1.2. For low Eddington fractions, the spectra are identical. However, the high frequency turnover in the near critical regime is attenuated and features a steeper exponential cutoff.	12
1.5	The accretion disc spectrum for four model. The “base” model is based on a α -disc used later in Chapter 4, but with a larger outer radius. It has the following parameters: $M_{\text{BH}} = 3 \times 10^6 M_{\odot}$, $R_{\text{in}} = R_{\text{ISCO}}$, $R_{\text{out}} = 376 R_{\text{ISCO}}$ and $\dot{M}_{\text{acc}} = 0.15 \dot{M}_{\text{Edd}}$ using an accretion efficiency of $\eta = 0.1$. The other models correspond to the same disc parameters, with either the outer or inner radius truncated, or a smaller accretion rate. Each change in disc parameters changes the spectrum of the accretion disc.	12
1.6	The accretion disc spectra for the XRB model in Figure 1.3 using a colour-corrected blackbody with $f = 1.3$ and $f = 1.7$ and using a simple blackbody profile ($f = 1$). When using the colour-corrected blackbody, the spectrum is shifted to higher frequencies.	13

- 1.7 A schematic showing the formation of P-Cygni lines in an expanding spherical outflow. The black arrows show the direction of the outflow and the blue arrows show the typical scattering direction of photons. Figure from Matthews (2016). 16
- 1.8 A synthetic spectrum generated by Long & Knigge (2002) comparing the HUT spectrum of Z Cam (black line) to the synthetic spectrum (gray line), using a simple biconical prescription. The model shows very good agreement with the observations. Figure taken from Long & Knigge (2002). 17
- 1.9 Normalized, geometric composite spectra of multiple QSOs from the SDSS early data release (Stoughton et al., 2002), differing by their type of BALs within their spectra. The top blue spectrum is a non-BAL QSOs. Figure from Reichard et al. (2003). 18
- 1.10 A simple schematic diagram of the disruption process. The star is *disrupted* when it comes within the disruption radius of the SMBH and is ripped apart. Half of the material becomes bound to the SMBH, whilst the rest is ejected from the system at speeds $v \sim 10^4$ km s $^{-1}$. Figure adapted from Rees (1988). 20
- 1.11 Sketches representing the self-intersection caused by an intersection of the stream with itself for two scenarios: apsidal precession and expansion due to a nozzle shock. The sketch also shows the evolution of the streams in both cases. *Left:* the collision is caused by relativistic apsidal precession, which makes the tip of the debris stream precess by an angle $\Delta\phi$ during pericenter passage. This interaction causes the the dissipation of kinetic energy associated with the radial motion of the stream, and causes an outflow driven by radiation pressure (orange sphere). *Right:* The nozzle shock produces very different widths for the two components of the debris stream (the stream before and after pericenter passage). As a result, the debris stream intersections at a broad range of radii, even if relativistic apsidal precession is basically non-existent. It is possible that a bow shock may cause further expansion of the debris, as shown by the orange half-sphere bounded by dashed lines. In both circumstances, the material which remains bound after the intersection eventually returns to pericenter, where it can undergo additionally interactions. Figure from Bonnerot & Stone (2021). 26
- 1.12 *Left:* a demonstration of line broadening by electron scattering in a homologous outflow for fixed electron temperature (top panel) and for fixed scattering optical depth (bottom panel). All fluxes have been scaled to their value at line centre. *Right:* a comparison between the H α profile in ASASSN-14ea (blue curve; Holoiien et al., 2014) to a radiative transfer model by SEDONA (Kasen et al., 2006) of an optically thick homologous outflow. The model reproduces the same line profile, including the blueshifted emission and asymmetric red wing due to bulk scatter reprocessing of line photons. Figures from Roth & Kasen (2018). 30
- 1.13 Spectroscopic classification of 17 TDEs, following the three spectral classes proposed by van Velzen et al. (2020a). *Left:* TDEs with Balmer line features only (TDE-H, in red). *Right:* TDEs with Balmer and He II, and N III and O III Bowen fluorescence features (TDE-H+He, in green) and TDEs with only He II (TDE-He, in blue). The spectra have not been host galaxy subtracted and have been normalized to arbitrary units. Figure from van Velzen et al. (2020a). 32

- 1.14 The optical spectrum of the TDE iPTF15af (Blagorodnova et al., 2019). Bowen fluorescence lines are marked in red and green, depending on the atomic species. Figure from Blagorodnova et al. (2019). 32
- 1.15 Optical host-subtracted spectra of AT2018zr for multiple epochs. The spectra have been smoothed. The original unsmoothed spectra are plotted underneath in grey for each observations. The corresponding post-flare phase for each observation is labelled on the right of the figure. At early times, the spectra are dominated by broad H α , H β and He II emission lines, which become significantly narrower and weaker in the late time spectra. Figure from Hung et al. (2019). 33
- 1.16 UV spectroscopic observations for four TDEs and a composite spectrum for a LoBALQSO (taken from Brotherton et al., 2001). The grey dashed lines mark the approximate continuum for each object, given by a blackbody of the appropriate temperature. The spectra, and the continua fits have been normalized to arbitrary units. Figure from Hung et al. (2019). 35
- 1.17 Three epochs of UV spectra for three high ionization UV absorption lines, labelled in the bottom right of each sub-panel, for AT2019qiz (Nicholl et al., 2020; Hung et al., 2020). The spectrum for the first epoch, $\Delta T = 13$ days, is shaded in blue, whilst the other spectra are represented by solid orange and green lines. The absorption troughs are shifted to lower velocities at later epochs. Figure from Hung et al. (2020). 36
- 1.18 A compilation of bolometric luminosity curves of TDEs. The light curves are constructed by scaling the r -band light curve by the peak bolometric luminosity determined from a blackbody fit to the optical and UV photometry reported by van Velzen et al. (2020a) assuming no evolution in temperature. Also shown for each TDE is a $t^{-5/3}$ power law decline, fitting the curves after peak. Figure from Gezari (2021). 37
- 1.19 The rest-frame blackbody temperature for the sample of 17 TDEs presented by van Velzen et al. (2020a). Most of the TDEs show a relatively small, but significant, increase in temperature after peak brightness. Figure adapted from van Velzen et al. (2020a). 38
- 1.20 The blackbody luminosity below 228 Å (the helium ionizing SED) plotted against the inferred radius of the optical/UV photosphere for a sample of 28 TDEs. The points are colour-coded by their optical spectra class as labelled in the figure. It seems that TDE-H+He (TDE-H+He) events appear to occur with bright UV flares and compact photospheres, whereas TDE-H events preferentially exhibit smaller photospheres. TDE-He objects, on the other hand, appear to exist over a large range of this parameter space. Figure from Gezari (2021). 38
- 1.21 A rest-frame UV spectrum of iPTF15af at $\Delta t = 52$ days after discovery. Marked by the dashed black line is a best-fit blackbody spectrum for the FUV. The spectrum has been corrected for extinction and important absorption and emission lines have been labelled. This spectrum looks strikingly similar to that of a BALQSO and features broad and blueshifted absorption lines, the smoking gun signatures of outflowing material. Figure from Blagorodnova et al. (2019). 40

1.22 The ratios of various absorptive opacities (labelled in the legend) as a function of wavelength, as calculated from non-LTE radiation transport calculations for a physically motivated spherical outflow using SEDONA (Kasen et al., 2006; Roth, 2016). <i>Left:</i> soft X-ray and EUV. <i>Right:</i> optical. Figures from Roth et al. (2016)	42
1.23 A diagram showing a schematic for a expanding spherical wind geometry originating from an inner radius. A photon emitted from the inner boundary is scattered by an electron with velocity \mathbf{v}_1 and is received by an electron moving with velocity \mathbf{v}_2 . The change in frequency between events is $\nu_2 = \nu_1[1 + (\mathbf{v}_1 - \mathbf{v}_2) \cdot \mathbf{n}/c]$. In a expanding (diverging) flow, $(\mathbf{v}_1 - \mathbf{v}_2) \cdot \mathbf{n}/c < 0$ and photons are redshifted. The colour of the dashed lines show the relative frequency shift in the frame of the observer. Figure adapted from Titarchuk & Shrader (2005); Laurent & Titarchuk (2007)	43
1.24 Synthetic spectra generated from a homologous outflow, showing how reprocessing affects the spectral energy distribution. The dashed green spectrum shows the thermal emission from a $T_{bb} = 2.95 \times 10^5$ K blackbody, whilst the dashed red line shows SED reprocessed by bulk scatter reprocessing. The solid black spectrum shows the SED when it has been reprocessed by absorption processes and bulk scatter reprocessing. Figure from Roth & Kasen (2018)	44
1.25 A schematic picture showing the viewing-angle dependence for the observed emission from a super-Eddington TDE accretion disc. The emission from the inner disc is reprocessed by the optically thick outflows and outer disc. Only when an observer is looking into the optically thin funnel is the inner disc exposed, which can reveal strong, beamed X-ray and EUV radiation. Otherwise, the disc X-ray emission is reprocessed into optical/NUV emission via photo-ionization or bulk scatter reprocessing. Figure from Dai et al. (2018)	46
2.1 A cartoon of a beam of light passing through a medium of area dA , at an angle θ into a cone of solid angle $d\Omega$. The angle θ is measured from the direction of the normal of the surface.	50
2.2 A flowchart showing the basic steps carried out in a PYTHON simulation.	62
2.3 A cartoon showing the basic geometry of the Shlosman & Vitello (1993) biconical disc wind model. Adapted from Long & Knigge (2002)	63
2.4 An example of a modelled cell spectrum, compared to both the “true” MC spectrum and to a dilute blackbody approximation. The modelled spectrum accurately reproduces the MC spectrum, whilst the dilute blackbody does not.	73
2.5 A schematic representation of the interaction process of an energy packet with energy ϵ_0 interacting with a macro atom. The macro atom is activated by absorbing the energy packet, makes two internal transitions, and deactivates by emitting an energy packet of equal energy ϵ_0 . Figure from Lucy (2002)	78

- 3.7 Synthetic UV spectra generated for clumped winds for both of the wind geometries using Solar and CNO-processed abundances at a low, medium and high inclination angle. The accretion disc SED is also shown with a dashed line and important line transitions are marked at the top. As in Figure 3.6, the most significant change is the N V absorption line which is stronger with CNO-processed abundances. 96
- 3.8 The continuum optical depth of the fiducial model shown in Figure 3.4. Marked by the solid blue is the angle averaged accretion disc SED for the model and shown by the solid orange line is the angle averaged emergent luminosity for the model. Included in the legend are the hydrogen column densities of each sight line. Important absorption edges are marked at the top of the figure. High frequency flux from the accretion disc is absorbed and re-radiated at longer wavelengths. 98
- 4.1 The Eddington luminosity fraction against inferred black hole masses for a sample of 20 TDEs taken from Ryu et al. (2020) and the spectra included in Figure 4.8, labelled in the legend. Each point from the Ryu et al. (2020) sample has been coloured depending on the mass return time p since disruption, measured in days. The Eddington luminosity is estimated using the inferred black hole masses. The bounded region represents the black hole mass parameter space covered by the grid. 106
- 4.2 Colour plots showing a selection of physical properties for the fiducial model on logarithmic axes. The $r - z$ plane, where r is the cylindrical radius, is shown and the wind is rotationally symmetric about the z -axis. The lines drawn over the wind show sight lines for an observer for inclination angles indicated in the legend. The spatial scales and colour maps are both logarithmic. *Top left*: the electron temperature. *Top right*: the Hydrogen number density. *Middle left*: the ionization parameter. *Middle right*: H I ionization fraction. The contour lines show the origin of H α photons contributing to the spectra from a cylindrical radius $r < 10^{16}$ cm. From darkest to lightest colour, the contours are regions where the photon count is 0 N_{tot} , 0.25 N_{tot} , 0.5 N_{tot} , 0.75 N_{tot} and 1.0 N_{tot} and where N_{tot} is the total number of H α photons. *Bottom left*: the poloidal velocity. *Bottom right*: the rotational velocity. 110
- 4.3 Synthetic optical spectra of the fiducial model. The spectra for five inclination angles are shown, each coloured as labelled by the legend. For each inclination angle, the model produces broad Balmer and helium recombination features. At low inclinations, the emission lines are single peaked but transition into double peaked lines as the inclination angle increases. Notably, the intermediate and high inclination spectra are almost identical as the base of the wind, which these sight lines cut through, dominates spectrum generation. The spectra are plotted on a log-linear axes and have not been smoothed. Labelled at the top of each panel are important line transitions. 111

- 4.4 Synthetic optical spectra for the four parameter grids on log-linear axes. The first three panels show spectra for the mass accretion rate (\dot{M}_{disc}), the wind mass-loss rate (\dot{M}_{wind}) and the terminal velocity of wind streamlines (v_∞) grids, using a black hole mass of $M_{\text{BH}} = 3 \times 10^6 M_\odot$. The bottom right panel shows spectra of the fiducial model for three black hole masses (M_{BH}). In each panel, the orange spectrum corresponds to the fiducial model in Section 4.3.1. All of the spectra exhibit broad Balmer and helium recombination features, strongly reminiscent of TDE-H+He objects. The emission lines are double peaked and feature an extended red wing. Each spectrum is for an intermediate, in-wind, inclination angle of 60° . The spectra have not been smoothed. Labelled at the top of each panel are important line transitions. 114
- 4.5 The continuum optical depth as a function of frequency for various sight lines (right axis) and both the emergent and disc SEDs for the same models as in Figure 4.4. The middle column corresponds to the fiducial model from Section 4.3.1. The spectra have been plotted on logarithmic axes and important photo-ionization edges have been labelled at the top. Each model is producing a redder (reprocessed) SED relative to the input disc SED. In general, denser winds are more efficiently reprocessing the disc SED and result in optically bright spectra. The main reprocessing mechanism is photo-ionization of He I and He II, but in some winds H I also contributes significantly. The electron scattering optical depth (corresponding to the “flat” region of the optical depth spectra) is roughly the same between models. 115
- 4.6 The continuum optical depth as a function of frequency for various sight lines (right axis) and both the emergent and disc SEDs (left axis) for the fiducial model in Chapter 3 and in this work (Section 4.3.1). Both axes are logarithmically spaced and important photo-ionization edges have been labelled at the top. Relative to the (Chapter 3) fiducial model, reprocessing is more efficient in the fiducial model presented in this work. Crucially whilst the both models have similar optical depth for the same photo-ionization edges, the disc continuum peaks at a higher frequency in the “new” fiducial model. In the Chapter 3 model, the disc SED does not include enough *ionizing* photons resulting in reprocessing via photo-ionization becoming inefficient. 120
- 4.7 Synthetic spectra for two inclinations (labelled in the top right of each panel) of photons contributing toward the emergent spectrum (labelled as full as in the figure) of the H α line profile for the fiducial model. Included are “pure” continuum photons (free-free, bound-free and electron scattered), as well as H α photons and H α photons which have electron scattered at least once between emission and escape (H α w/ ES). The spectra have been smoothed by a six pixel boxcar filter. Importantly, electron scattering is responsible for the broad wings of the emission lines. It also smooths out the double peaked line profile at low inclinations. *Left:* a low inclination spectrum (10°). *Right:* an intermediate inclination spectrum (60°). 121

- 4.8 Rest frame synthetic optical spectra for two models (labelled in the legend) plotted on linear axes and against the optical spectra of ASASSN14-li bat $\Delta t = 54$ days (Holoien et al., 2016) and AT2019qiz at $\Delta t = 49$ days (Nicholl et al., 2020). The spectra for the objects have been corrected for foreground extinction assuming a Cardelli et al. (1989) extinction curve with $R_v = 3.1$ for both TDEs and $E(B - V) = 0.0225$ and $E(B - V) = 0.0939$ for ASASSN14-li and AT2019qiz respectively. Photometry for ASASSN-14li, taken from Holoien et al. (2016), has also been included with the filters labelled in the legend. The distance of the object and inclination of the model are labelled in the top right of each panel. The spectra have not been smoothed. Important line transitions are marked at the top of each panel. The synthetic spectra are in rather excellent agreement with the observations, especially considering neither model has been tailored to fit the specific observation, producing the same recombination features with similar continua. 123
- 4.9 Synthetic spectra of the fiducial model (blue) and a modified fiducial model with a truncated inner disc radius (orange, $R_{\text{co}} = 3.8 R_{\text{ISCO}}$). The fiducial model in this work (blue) is too highly ionized to produce the UV BAL features reported by Chapter 3. By truncating the inner disc radius of the fiducial model, the disc SED is softened and the ionization state of the wind is lowered. The result is that the BEL vs. BAL behaviour reappears for the truncated disc model (orange). Absorption features, such as in C IV, form for sight lines which look into the wind cone (top panel) and emission features form for sight lines with do not look into the wind cone (bottom panel). *Top panel:* an intermediate sight line looking into the wind cone (60°). *Bottom panel:* a sight line looking below the wind cone (75°). 125
- 5.1 A colour plot showing the mass density of the model from D18 for the region covering $0^\circ < \theta < 90^\circ$. The regions labelled and bounded by the dashed lines are the four 1D θ -averaged models described by D18 in their section 2.2. As in previous PYTHON models, the disc plane is located at 90° 135
- 5.2 Density and velocity profiles, as a function of r , for the 1D model in this work (solid) and the 1D models (dashed) by D18. The profiles shown for the remapped model are excellent agreement with the original models. The small discrepancies in some of the profiles are due to differences from remapping. 136
- 5.3 Density and velocity profiles, as a function of r , for a selection of sight lines for the 2D model in this work (solid) and the 3D-GRRMHD model (dashed) from D18. The profiles shown for the 2D remapped model are generally in good agreement with the original. 138
- 5.4 Synthetic rest-frame spectra generated by PYTHON using a reduced atomic data set for the four 1D θ -averaged models, and the same spectra by D18 using SEDONA. Additionally, shown, as a black dashed line, is the input SED. The name of each model has been labelled in the top left. The spectra have been smoothed slightly and normalized to the peak. All of the PYTHON spectra have been reprocessed more, relative to SEDONA. . . 140

- 5.5 The continuum optical depth as a function of frequency for the θ -averaged models. Solid coloured lines show the total continuum optical depth, whereas the dashed lines show the optical depth without electron scattering. For bin 3 and 4, electron scattering dominates the opacity throughout. But in bin 1 and 2, opacity due to photo-ionization of oxygen is important at soft X-ray and EUV frequencies. 141
- 5.6 Various colour plots for a selection of physical parameters for the 2D model using the full atomic species, constrained to $5^\circ < \theta < 88^\circ$. *Top left*: electron temperature. *Top right*: hydrogen density. *Middle left*: radiation temperature. *Middle right*: ionization parameter. *Bottom left*: H I ion fraction. *Bottom right*: He II ion fraction. 143
- 5.7 The continuum optical depth, for the 2D model, as a function of frequency for various sight lines with electron scattering included (solid lines) and without electron scattering (dashed lines). Along the base of the wind, there is significant opacity due to the photo-ionization of He II. 145
- 5.8 A colour plot showing the mass density of the outflow and solid lines showing the outline for multiple electron scattering photospheres for values of τ_{es} labelled in the legend. The outflow is optically thick to electron scattering ($\tau_{\text{es}} > 1$) out to a radius of $1000 r_g$, with the highest electron scattering in the disc atmosphere which is traced almost neatly by the $\tau_{\text{es}} = 10$ photosphere. 146
- 5.9 Rest-frame synthetic spectra for the 2D geometry using both the reduced and full atomic data sets, as labelled in the legend. Each panel shows a different inclination spectrum, which has been labelled in the top left, as well as the input SED shown by a dashed black line. The spectra have been smoothed and normalized to peak. Each spectrum has been reprocessed, forming a distinctive stretched blackbody SED with an enhanced optical continuum. 148
- 5.10 Rest-frame synthetic spectra generated for various grid cells at different gravitational radii along two sight lines, labelled in the top right of each panel. Each SED represents the local SED of a grid cell at the given radius and inclination. Various photo-absorption edges have been labelled at the top of each panel. Along the low sight line, there is very little absorption of the radiation and the SED has been modified due to bulk scatter reprocessing, reducing the photon energy of the population. But along high inclinations, there is significant absorption of high frequency radiation which is re-emitted at longer wavelengths. 151
- 5.11 Rest frame synthetic spectra for four sight lines (labelled in the legend) for the ϕ - and t -averaged 2D model. The input SED is shown in black. Shown by the shaded purple and coral areas are the X-ray and optical wavebands. The optical-to-X-ray ratio increases with inclination angle. At high inclinations, observers see a bright optical spectrum with little to no accompanying X-ray emission. This result is consistent with the unified model proposed by D18. 153
- 5.12 The integrated optical-to-X-ray luminosity ratios as a function of inclination angle. The X-ray band has been defined to include photons with energies 0.2 keV and above, and the optical waveband is defined between 1500 - 7000 Å. The optical luminosity of the spectra increases with inclination, whilst the X-ray luminosity decreases. Observers who look at high inclinations will see an optically bright TDE. 154

-
- 5.13 Peak normalized rest-frame synthetic spectra for the 1D and 2D models, including hydrogen, helium and oxygen. The 2D models shown are the respective mid-point inclination angles for the opening angles of each 1D bin. Shown by the black dashed line is the input SED used for the models. The emergent spectra in both geometries are reprocessed blackbodies, which have been stretched and redshifted to longer wavelength. But in 1D, the amount of shifting is far greater (due to more efficient photon trapping) and a number of absorption and line features differ between the two geometries. At the core of it, most of these differences are due to multi-d photon transport effects. 155
- 5.14 Angle integrated synthetic spectra generated for the 2D model using the reduced atomic species data. In blue is the spectra produced where the input SED is a single colour blackbody emitted from the origin of the model. In orange is the same outflow, but using a multi-colour disc SED following from a simple slim-disc prescription (e.g. Strubbe & Quataert, 2009). The faded curves of the same colour are the input SEDs for the respective simulation. 158
- Appendix A.1 A schematic of three photons which can be considered for MRW transport. Photon (A) is not transported via MRW as it travels straight through the cell without interacting. Photon (B) interacts within the cell, but as the distance to the next interaction is larger than R_0 , it is not transported via MRW. Photon (C) will be transported via MRW as it interacts in the cell and the next interaction event is within the MRW sphere with radius R_0 . The hatched regions at the edge indicate regions where MRW will not be invoked due to being close to the edge of the cell. 172
- Appendix A.2 Packet splitting with $N_{\text{high}} = 1$ and $N_{\text{low}} = 5$. A high luminosity photon enters an optically thick region and interacts until it reaches the boundary between an optically thick and thin region. At the boundary, the high luminosity photon is split into N_{low} photons which interact with the optically thin region until they exit. 175

List of Tables

1.1	Approximate values for the compactness and accretion efficiency for four compact objects. For both SMBH examples, the radius has been set to the innermost stable orbit (R_{ISCO}) where this is taken for a prograde orbit with a spin parameter $a = 0.9$ for the Kerr SMBH.	5
3.1	Parameters and their respective values adopted for the two wind geometries shown in figure 3.2.	87
4.1	Key parameters for the models presented. The top sub-table shows the values for the parameter grid as described in section 4.2, whilst the middle sub-table defines the parameters which control the geometry for each black hole mass. The bottom table shows conversion values of the Eddington accretion rate into solar masses per year for each black hole mass.	108
4.2	The hydrogen column density and the integrated optical depth for three frequencies corresponding to three photo-ionization edges and the electron scattering optical depth for the fiducial model in Section 4.3.1. In cases where the optical depth are constant across multiple frequencies, the electron scattering opacity is dominating the opacity from photo-absorption.	112
5.1	The opening θ_1 and closing θ_2 angles for the wedges shown in Figure 5.1, as well as the radius of the central source and the luminosity of the radiation source in units of $L_{\text{Edd}} = 6.28 \times 10^{44}$ ergs s ⁻¹	136

Definitions and Abbreviations

PYTHON	Monte Carlo radiative transfer software
Python	interpreted high-level general-purpose programming language
MC	Monte Carlo
MCRT	Monte Carlo radiative transfer
GRRMHD	general relativistic radiation magnetohydrodynamics
RTE	radiative transfer equation
LTE	local thermodynamic equilibrium
SED	spectral energy distribution
UV	ultraviolet
BEL	broad emission line
BAL	broad absorption line
FWHM	full width at half maximum
TDE	tidal disruption event
SMBH	supermassive black hole
AGN	active galactic nuclei
WD	white dwarf
CV	catclysmic variable
QSO	quasar
BALQSO	broad absorption line quasar
LoBALQSO	low ionization broad absorption line quasar

Physical Constants

Speed of light	c	2.9979×10^{10} cm s $^{-1}$
Gravitational constant	G	6.6743×10^{-8} cm $^{-3}$ g $^{-1}$ s $^{-2}$
Planck constant	h	6.6261×10^{-27} cm 2 g s $^{-1}$
Boltzmann constant	k_B	1.3807×10^{-16} cm $^{-2}$ g s $^{-2}$ K $^{-1}$
Sefan-Boltzmann constant	σ_{SB}	5.6704×10^{-5} g s $^{-3}$ K $^{-4}$
Thompson cross section	σ_T	6.6625×10^{-25} cm 2
Proton mass	m_p	1.6725×10^{-24} g
Electron mass	m_e	9.1094×10^{-28} g
Electron charge	q_e	4.8032×10^{-10} cm $^{-3/2}$ g $^{1/2}$ s $^{-1}$ (esu)
Electron volt	eV	1.6021×10^{-12} erg
Solar mass	M_\odot	1.9891×10^{33} g
Solar radius	R_\odot	6.9550×10^{10} cm
Year	yr	3.1560×10^7 s
Angstrom	Å	1.0000×10^{-8} cm
Parsec	pc	3.0856×10^{18} cm 2.3999×10^{14} football fields

Acknowledgements

First of all, I would like to thank my supervisor, Christian Knigge, for being a particular excellent and fashionably late person and supervisor. I always, after a few hours, left our meetings feeling a little smarter, more motivated and better about my research. *Good enough for government work*, as he would say. I would also like to extend thanks to the rest of the PYTHON gang, Knox Long, James Matthews, Nick Higginbottom, Mandy Hewitt, Stuart Sim and Sam Mangham, whose experience and support has been invaluable. Standing on the shoulders of giants, or something, I guess? I am particularly in gratitude for their support during the final stages, especially when everything was going wrong at the very last minute, due to a seemingly never ending stream of scary bugs and disasters.

I am also grateful for the fabulous bunch of people I have had the pleasure of being around in the astronomy, space environment and NGCM groups at Southampton, which made my PhD far more enjoyable. In particular, I want to mention my ever present office mates, Bella and Maria, who always had something inane and interesting to talk about. I am also fortunate to have known such great people to go to the pub with on Friday nights (before the plague happened, of course), David, Miika, Michael, Ella, Triana, Dale, Klaudia, Arianna, Matt and Phil, and all the other people who I also quite like; but won't mention to not inflate their egos (and to not completely fill up this page with names). Also, this needs to be in writing: Pip, Jamie and Michael are the worst.

I also should thank, or at least acknowledge the existence of, a bunch of (poggers) people outside of academia, who have helped keep me *semi-sane* and distracted. Most of all, the people who I regularly deal with every day: Marley (especially for cycling 91 miles to deliver me some excellent whisky), Razvan, Jack, Meghun, Gareth, Jordan, Adam, Sam, Kilo, Adriaan and penecks. The endless stream of insanity and streaming content was a near constant source of distraction, keeping me from doing what I needed to do.

I would like to thank my family: my mum, dad, sister, Michael, Donna and Kris. Without them and their support, I wouldn't have been able to get to this point. Finally, thank you to Hanna (and Mayo) for being in my life, and providing so much support, joy and happiness throughout it all.

Now for the boring stuff. Figures were prepared using `matplotlib` (Hunter, 2007), unless they were taken from another piece of work, then who knows how those were prepared. I acknowledge the use of the `GNU Science Library` (Galassi, 2006) and of the IRIDIS High Performance Computing Facility, and associated support services at the University of Southampton. I acknowledge financial support from the EPSRC Centre for Doctoral Training in Next Generation Computational Modelling grant EP/L015382/1.

The acronym "TDE" appears 372 times throughout this thesis.

Declaration of Authorship

I declare that this thesis and the work presented in it is my own and has been generated by me as the result of my own original research.

I confirm that:

1. This work was done wholly or mainly while in candidature for a research degree at this University;
2. Where any part of this thesis has previously been submitted for a degree or any other qualification at this University or any other institution, this has been clearly stated;
3. Where I have consulted the published work of others, this is always clearly attributed;
4. Where I have quoted from the work of others, the source is always given. With the exception of such quotations, this thesis is entirely my own work;
5. I have acknowledged all main sources of help;
6. Where the thesis is based on work done by myself jointly with others, I have made clear exactly what was done by others and what I have contributed myself;
7. Parts of this work have been published as: Parkinson et al. (2020), Parkinson et al. (2022)

Signed:.....

Date:.....

Chapter 1

Introduction

Why do smart people exist, if not to figure out convoluted problems?

Mikhail Bulgakov

When an unlucky star wanders too close to a supermassive black hole (SMBH), its self-gravity is completely overwhelmed by the tidal stresses from the close encounter. The star, unable to hold itself together, is ripped asunder in something known as a tidal disruption event (TDE) (Hills, 1975; Rees, 1988). In some circumstances, however, a star can actually survive the encounter and have only the outer layers of its atmosphere stripped away (see, e.g. Mainetti et al., 2017; Stone et al., 2019).

In either case, roughly half of this *disrupted* stellar debris becomes bound to the SMBH, eventually forming a quasi-circular accretion disc which feeds the SMBH, until the reservoir of stellar material is emptied (Cannizzo et al., 1990; Shiokawa et al., 2015; Hayasaki et al., 2016; Bonnerot et al., 2016, 2021). The initial fallback of material – and accretion rate if circularization is efficient – is typically super-Eddington and, eventually, transitions into a sub-Eddington accretion flow as the fallback of material declines and the reservoir empties (Strubbe & Quataert, 2009; Wu et al., 2018). The accretion of the material converts gravitational potential energy into heat which is radiated away, fuelling a powerful and transient flare visible across the electromagnetic spectrum (Saxton et al., 2020; van Velzen et al., 2020b; Jiang et al., 2021; Alexander et al., 2020; Gezari, 2021). A shining light, even in death.

The transient flares of TDEs are some of the best probes available for the undetectable quiescent SMBH thought to be lurking at the centre of many galaxies, where direct dynamical measurements are difficult or impossible (Stone & Metzger, 2016). TDEs can be used to determine the properties of the host galaxy, such as the black hole mass (Mockler et al., 2019) and spin (Stone et al., 2019). Furthermore, given that the

circularization of the debris stream and formation of an accretion disc can happen on a timescale as short as a few months, TDEs are one way for us to study the real-time formation of an accretion disc and the launching of an accompanying outflow. And once the accretion process starts proper, TDEs become a laboratory to study variable accretion (e.g. LaMassa et al., 2015).

Whilst much of our basic understanding and theory of TDEs was formulated decades ago in the 70's and 80's (Hills, 1975; Young et al., 1977; Hills, 1978; Frank, 1978; Rees, 1988), recent technological breakthroughs in transient astronomy and numerical simulations has meant the established theory has been challenged. For example, characteristic temperatures inferred from the spectral energy distributions (SED) of a few recently discovered TDEs are lower than expected (i.e. PS1-10jh; Gezari et al., 2012). Similarly, numerical studies have additionally suggested that the fallback rate of material could in fact be steeper than the accepted fiducial power law (see, e.g., Guillochon & Ramirez-Ruiz, 2013), depending on the type of encounter.

Even as the numerical simulations of TDEs have become more sophisticated, within the past decade the number of *physically grounded* and motivated models has lagged behind and not kept pace with the growing census of 56 TDEs (see Table 1 by Gezari, 2021). We still lack a number of good models which broadly describe and explain key TDE properties. Of course, this task is made more difficult due to the, still, small population of well studied TDEs and the range of variability within. One of these key properties which we still are fairly ignorant about is the emission mechanism(s) powering the luminous flares we observe. Furthermore, our understanding of how an accretion disc forms and their exact dynamics and geometries is still in its infancy and an area of ongoing intense research (e.g. see Bonnerot et al., 2021).

One still existing area of contention, which I hope to shed some light on with this thesis, is the growing population of TDEs with bright optical and ultraviolet (UV) components, but weak X-ray emission. With our current understanding, the SEDs of TDEs should be dominated by thermal X-ray emission from the hot inner edge of a quasi-circular accretion disc. Therefore the fact that a sub-set of TDEs with weak X-ray but bright optical components exists is, at the very least, inconsistent with our (admittedly) incomplete understanding of TDE emission. However, this could be rectified and consistent if the X-ray emission is reprocessed and re-radiated at longer wavelengths by an optically thick envelope, such as an outflow (Strubbe & Quataert, 2009; Metzger & Stone, 2016; Roth et al., 2016; Roth & Kasen, 2018; Lu & Bonnerot, 2019; Piro & Lu, 2020; Bonnerot et al., 2021). Equally possible, however, is that the optical emission could instead be due to the dissipation of heat caused by powerful shocks between infalling stellar debris streams (Dai et al., 2015; Piran et al., 2015; Shiokawa et al., 2015).

Regardless of the uncertainty of the emission mechanism, given the extreme luminosities which these events generate, significant mass-loss in the form of powerful radiation

driven outflows are expected to form. The recent discovery of broad, blueshifted absorption lines – the smoking gun signatures of outflowing material – in the UV spectra of several TDEs (Blagorodnova et al., 2019; Hung et al., 2019, 2020) provides unambiguous evidence for the existence of sub-relativistic outflows. Additionally, further evidence for sub-relativistic flows also comes from blueshifted BELs (Arcavi et al., 2014; Roth & Kasen, 2018; Hung et al., 2019; Nicholl et al., 2020) in the UV spectra, and, evidence for relativistic jetted outflows is found in radio data (Alexander et al., 2016, 2020; Matsumoto & Piran, 2021a; Horesh et al., 2021). Outflows are, in-fact, ubiquitous across the entire mass range of accreting objects. But even so, the physical properties of outflows in TDEs, their formation, geometry, kinematics, mass-loss rates, and energetics remain poorly understood, even though their importance is widely acknowledged (e.g. Strubbe & Quataert, 2009; Miller et al., 2015; Metzger & Stone, 2016; Roth et al., 2016; Roth & Kasen, 2018; Dai et al., 2018).

Moreover, outflows could be the solution to a few questions we have. The UV spectra of TDEs are diverse, and contain a dichotomy where some TDEs display broad absorption lines (BALs) whilst others show broad emission lines (BELs) at a similar post-disruption evolution. A similar phenomenology (of BALs vs. BELs) is observed in cataclysmic variables (CVs) and quasars (QSOs), where $\simeq 20\%$ of QSOs display BALs. In these objects, this dichotomy can be interpreted as an orientation effect of line formation in an accretion disc wind (Murray et al., 1995; Murray & Chiang, 1996, 1997; Elvis, 2000; Long & Knigge, 2002; Higginbottom et al., 2013; Matthews et al., 2016). Since the physics of accretion and the launching of outflows is universal across the mass scales over which it occurs, it is only reasonable, then, to assume the same framework could also explain the diversity of UV TDE spectra. Furthermore, given the extreme accretion rates and luminosities of these events, the associated outflows will only naturally transfer a considerable amount of mass and momentum to produce an optically thick envelope, capable of reprocessing even the most ionizing and X-ray bright SEDs. Outflows therefore could provide a natural solution to the supposed excess of optical events.

The scientific aim of this thesis is to decipher the impact accretion disc winds could have on the optical and UV emission observed in TDEs. By using powerful and state-of-the-art Monte Carlo radiative transfer and ionization software, the confusingly named PYTHON, I simulate the frequency dependent radiative transfer, tracking photons from emission to escape along their random walk, to construct synthetic spectra and predict the light emerging from these events. Using PYTHON, I test how line formation in an accretion disc wind could provide a unification scenario for the BAL vs. BEL dichotomy in the UV spectra. In addition to this, I also test and explore a realistic TDE parameter space, to see if and how an optically thick outflow can reprocess the emission from an accretion disc, giving rise to the distinctive optical emission of TDEs.

In the remainder of this chapter, I introduce the background theory on accretion discs and their outflows. I also more formally introduce TDEs, discussing the key theoretical

background and observational characteristics. And then, to finish, I reiterate the aims of this thesis and outline the remainder of its structure.

1.1 Accretion

Accretion is a universal processes throughout astrophysics, and occurs over a massive mass range. Accretion happens all the way from the smallest young stellar objects (YSOs) up to the massive active galactic nuclei (AGN), and, of course, it also plays an indispensable role in powering the observable flares of TDEs. More concretely, accretion is the accumulation of matter by an object caused by gravitational attraction and is the most efficient energetic process in the universe; even more efficient than nuclear fusion. As matter falls, or accretes, onto a central object, it often forms a disc of material known as an accretion disc, which efficiently radiates the gravitational potential energy released during accretion, often outshining the host object.

1.1.1 Basics of accretion

When matter falls onto an object, the gravitational potential energy is converted into kinetic energy. For a small piece of matter of mass m falling from infinity onto an *accreting* object, of mass M and radius r , the kinetic and gravitational energy of that small piece of matter is equal to,

$$\Delta E = \frac{1}{2}mv_{\text{ff}}^2 = \frac{GMm}{r}, \quad (1.1)$$

where G is the gravitational constant, v_{ff} is the free fall velocity and ΔE is the change in energy. When the matter strikes the surface of the object, its kinetic energy is converted into heat which is eventually radiated away. For matter accreting at a given rate $\dot{M} = dm/dt$, the luminosity, or the rate at which the kinetic energy is transformed into heat, is defined as,

$$L_{\text{acc}} = \frac{GM\dot{M}}{r}. \quad (1.2)$$

The maximum amount of energy which can be extracted from any piece of material is equal to its rest mass, given by the famous $E = mc^2$. This is the theoretical maximum, and any process is extremely unlikely to ever be able to reach it. The efficiency of any energetic process can be quantified, by relating the energy created to this theoretical maximum,

Object	M (M_\odot)	R (R_\odot)	M/R (M_\odot / R_\odot)	η
White dwarf	0.8	0.01	79.4	1.6×10^{-4}
Neutron star	1.4	1.4×10^{-5}	10^5	0.2
Schwarzschild SMBH	10^9	1.3×10^4	7.62×10^4	0.17
Kerr SMBH	10^9	3×10^3	3.4×10^5	0.7

TABLE 1.1: Approximate values for the compactness and accretion efficiency for four compact objects. For both SMBH examples, the radius has been set to the innermost stable orbit (R_{ISCO}) where this is taken for a prograde orbit with a spin parameter $a = 0.9$ for the Kerr SMBH.

$$\Delta E = \eta \Delta mc^2, \quad (1.3)$$

where η is the efficiency. The efficiency of the accretion process is therefore,

$$\eta = \frac{\Delta E}{\Delta mc^2} = \frac{G M}{c^2 r}. \quad (1.4)$$

Equation 1.4 shows us that the efficiency of accretion is related to how compact the object is; the ratio of M/r . The efficiency of accretion can be as small as $\eta \sim 10^{-4}$, and as large as $\eta \sim 0.7$ and higher. In the case of a SMBH, its spin, a , also plays an important role in setting the accretion efficiency. The spin changes the location of the innermost stable orbit (ISCO), essentially making the SMBH more or less compact. The influence of spin on the location of a SMBH's event horizon, ISCO and the corresponding accretion efficiency are shown in Figure 1.1. Furthermore, a summary of the accretion efficiency for four compact objects is shown in Table 1.1.

We can define the accretion luminosity (Equation 1.2) in terms of efficiency,

$$L_{\text{acc}} = \eta \dot{M} c^2. \quad (1.5)$$

This shows that for two objects with the same accretion rate, the more compact object – which is more efficient at extracting energy from accretion – will generate more luminosity and be brighter than something less compact.

1.1.2 The Eddington limit

At a first glance it looks like there is no limit to how much material can be accreted. This is not the case at all. For matter to be accreted onto an object, the gravitational force pulling that material in must be greater than any force pushing that material away. In the case of accretion, we really only need to consider the radiation force, defined as,

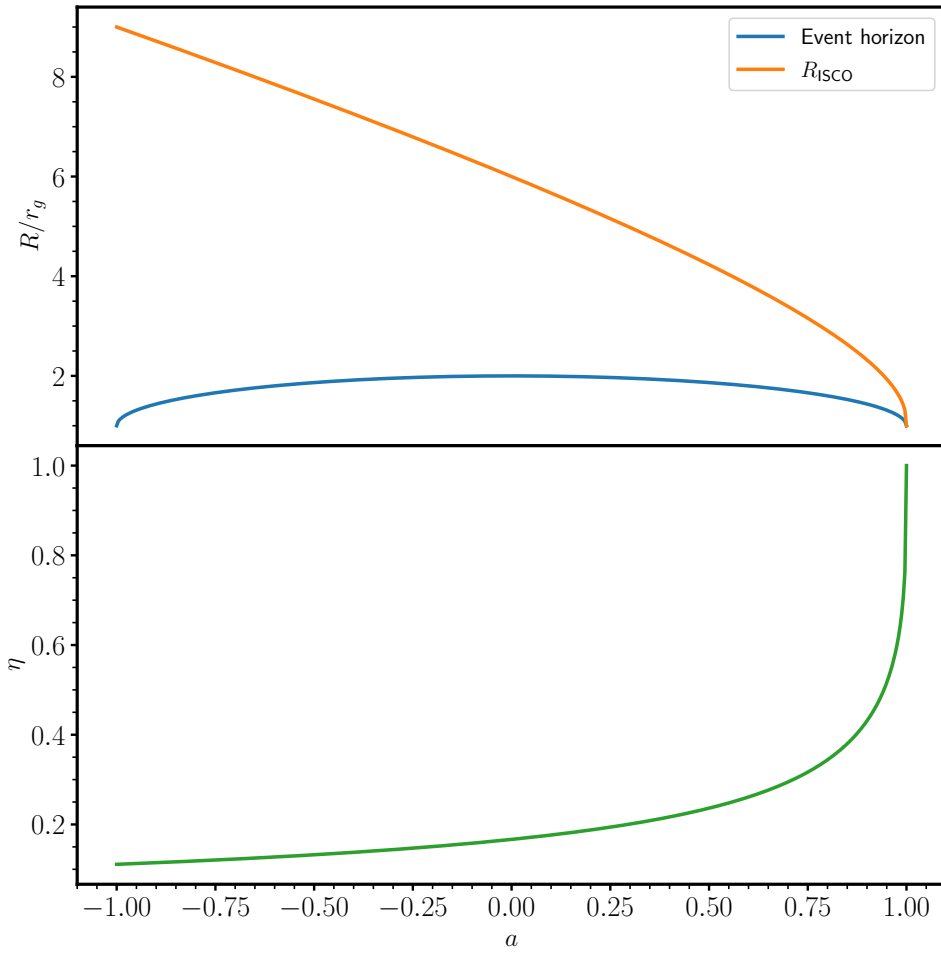


FIGURE 1.1: The influence of spin on the event horizon radius and ISCO (top panel), as well as the accretion efficiency (bottom panel) for a SMBH of mass $M_{\text{BH}} = 10^9 M_{\odot}$. A spin value of $a = 0$ corresponds to a non-rotating Schwarzschild black hole, whilst a value of $a = 1$ and $a = -1$ correspond to either a prograde and retrograde Kerr black hole, respectively.

$$F_r = \frac{\sigma_T L_{\text{acc}}}{4\pi c r^2}, \quad (1.6)$$

where σ_T is the Thomson scattering cross-section. Material can only accrete when the gravitational force, $F_g = GMm/r^2$, acting upon the material, m , is greater than the radiation force. If the radiation force dominates over the gravitational force, then the material will no longer be accreted and instead is blown away by radiation pressure. The point at where this happens is known as the *Eddington limit*. The luminosity required to reach this limit is derived by equating the radiation and gravitational force acting upon a piece of matter,

$$L_{\text{Edd}} = \frac{4\pi G M m_p c}{\sigma_T}, \quad (1.7)$$

or in terms of an accretion rate,

$$\dot{M}_{\text{Edd}} = \frac{4\pi GMm_p}{\eta c\sigma_T}, \quad (1.8)$$

where m_p is the proton mass. A number of assumptions have been made to calculate this. Firstly, the accretion flow has been assumed to be in a steady-state and spherical. It is also assumed that the accreting material is a plasma solely comprised of ionized hydrogen. Therefore the opacity of the plasma is dominated by electron scattering, and only the gravitational force acting upon the protons is important. But given the simplicity of these assumptions, there are actually many objects where one or more of these assumptions does not hold up. In these cases, it is entirely possible for the luminosity of the accreting object to exceed the Eddington luminosity, in something referred to as *super-Eddington* accretion.

1.2 Accretion discs

Accretion discs are flattened objects, comprised of rapidly rotating gas which slowly spirals onto a central gravitating object. Whenever an astrophysical object is accreting, if the material possess *enough* angular momentum, then it cannot simply fall straight onto the object. The accreting matter will eventually relax into its minimum energy state: a disc. As the material spirals inward, it is heated due to the motion (accretion) of the material, i.e. the conversion of gravitational potential to (rotational) kinetic energy and heat which is radiated away, powering the electromagnetic emission we observe. As a piece of material spirals inward, its kinetic energy is given by,

$$T = \frac{1}{2}mv^2 = \frac{1}{2}m\frac{GM}{r}, \quad (1.9)$$

where M is the mass of the black hole, r is the radial distance, m the mass of the material and v the velocity. The gravitational potential for the same piece of material is,

$$U_g = -\frac{GMm}{r}. \quad (1.10)$$

Upon inspection of Equation 1.9 and Equation 1.10, as well as following from the Virial theorem ($2T + U = 0$), we can see that,

$$T = -\frac{1}{2}U. \quad (1.11)$$

Therefore, the total energy of the system is,

$$E = T + U = \frac{1}{2}U. \quad (1.12)$$

Both Equation 1.11 and Equation 1.12 show that half of the released gravitational energy is converted to kinetic energy. This means that the other half of that energy is therefore available to heating the material in the disc. The luminosity of an accretion disc can then only be,

$$L_{\text{disc}} = \frac{1}{2}L_{\text{acc}} = \frac{1}{2}\frac{GMM}{r}, \quad (1.13)$$

as only half the energy is available to heat the material in the disc, which is the emission power source.

Since the net angular momentum of the matter is a conserved quantity, for anything to spiral inward and reach the surface of the accreting object, the angular momentum at the inner edge of the disc has to be transported outward. The precise mechanism for angular momentum transport is currently unknown, but there are several theories. Regular molecular viscosity does help to transport energy and momentum outward whenever two particles collide in the disc. But in itself, it is no where near enough to account for all of the outward momentum transport (e.g. Pringle, 1981). Other mechanisms have been proposed and include invoking a magnetorotational instability (Balbus & Hawley, 1991) or that momentum is lost via a hydromagnetic outflow (Blandford & Payne, 1982).

In the following (and previous) section, I have restricted the description to a purely Newtonian picture, for the sake of pedagogical purposes. Therefore, I have not taken into account the general relativistic properties of the matter in orbit. Detailed descriptions of relativistic disc models can be found in, e.g., Novikov & Thorne (1973); Cunningham (1975); Blandford (1999); Gierliński et al. (2001); Zhuravlev (2015).

1.2.1 The steady state accretion disc

Given that the precise momentum transport mechanism(s) is still unknown, it is often most pragmatic to parameterize the unknown physics into a single, convenient, parameter. One such model which does this is the α -disc model first developed by Shakura & Sunyaev (1973). Here, the accretion disc is assumed to be both geometrically thin and optically thick. The (kinematic) viscosity in the disc is assumed to arise due to turbulence caused by changes in pressure and velocity between the orbiting rings of matter in the disc. By assuming that the size of the largest turbulent eddies are of order the scale height of the disc, and that the eddies *do not* move faster than the local sound speed, then the viscosity can be parameterized as,

$$\nu = \alpha c_s H, \quad (1.14)$$

where c_s is the local sound speed, H is the scale height of the disc and $0 < \alpha \lesssim 1$ is the scaling parameter. If we assume that the mass accretion rate is constant throughout the disc, i.e. it is in a steady state, and that the viscosity is the dominant heating source within the disc, then the effective temperature profile, as a function of disc radius r , can be calculated using (e.g. Frank et al., 2002),

$$T_{\text{eff}}^4 = \frac{3GM_{\text{co}}\dot{M}_{\text{acc}}}{8\pi\sigma_{\text{SB}}r^3} \left[1 - \left(\frac{r_{\text{co}}}{r} \right)^{1/2} \right], \quad (1.15)$$

where r_{co} is the radius of the inner edge of the accretion disc and σ_{SB} is the Stefan-Boltzmann constant. For a SMBH, the effective temperature profile is also affected by its spin. In the case of a prograde spin, and assuming $r_{\text{co}} = R_{\text{ISCO}}$, the ISCO is closer in than for a non-rotating black hole (see Figure 1.1) resulting in a hotter peak temperature at the inner disc edge. For a retrograde spin, the ISCO is moved further out which results in a cooler temperature profile.

1.2.2 A slim accretion disc

In most cases, the α -disc prescription is a perfectly fine first-order approximation to model an accretion disc in many systems. However, the inner disc region in systems which are accreting close to, or above, the Eddington limit are likely radiation dominated, vertically extended and almost certainly not in a steady-state. The structure, evolution and even stability of such disc are still an area of intense research and highly uncertain (e.g. Hirose et al., 2009; Jiang et al., 2013; Shen & Matzner, 2014). In the near-Eddington critical accretion regime, where $\dot{M}/\dot{M}_{\text{Edd}} \approx 1$, so-called “slim” disc models often reign supreme (see, e.g. Strubbe & Quataert, 2009). Slim discs are different, as, for example, at large Eddington fractions the colour temperature of the inner disc region is lower because of increased radiation trapping which lowers the radiative efficiency.

The effective temperature profile for a slim disc model is given by (e.g. Strubbe & Quataert, 2009),

$$T_{\text{eff}}^4 = \frac{3GM_{\text{co}}\dot{M}_{\text{acc}}f_{\text{nt}}}{8\pi\sigma r^3} \left[\frac{1}{2} + \left\{ \frac{1}{4} + 6f_{\text{nt}} \left(\frac{\dot{M}_{\text{acc}}c^2 r_g}{L_{\text{Edd}}} \frac{r_g}{r} \right)^2 \right\}^{1/2} \right]^{-1}, \quad (1.16)$$

where $f_{\text{nt}} \equiv 1 - \sqrt{r_{\text{ISCO}}/r}$, r_g is the gravitational radius, c is the speed of light. For small Eddington fractions, i.e. $f_{\text{Edd}} = \dot{M}_{\text{disc}}/\dot{M}_{\text{Edd}} \ll 1$, Equation 1.16 resembles a

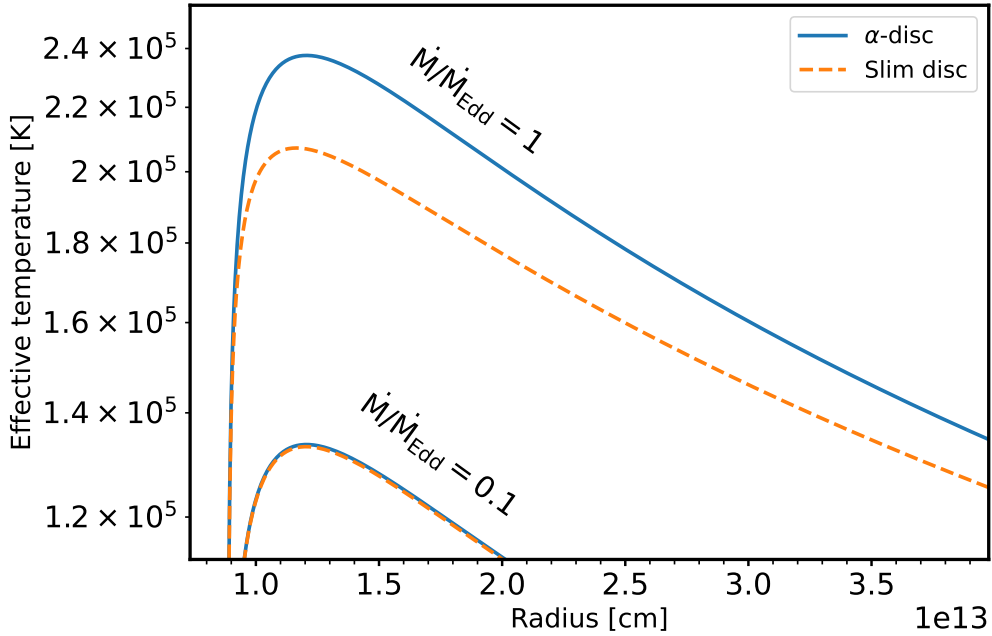


FIGURE 1.2: The effective temperature profiles for an α -disc (Equation 1.15) and slim disc (Equation 1.16) for the Eddington accretion fractions labelled in the figure. For small Eddington fractions, both temperature profiles are essentially the same. However, as the Eddington fraction increases, the effective temperature for the slim disc drops because of increased radiative trapping which results in a lower radiative efficiency for the slim accretion disc atmosphere. To calculate these profiles, the following parameters were used to model the accretion disc for a Schwarzschild SMBH: $M_{\text{BH}} = 10^7 M_{\odot}$, $R_{\text{in}} = R_{\text{ISCO}}$, $R_{\text{out}} = 4.5 R_{\text{ISCO}}$ and an Eddington accretion fraction as labelled assuming an accretion efficiency of $\eta = 0.1$.

standard α -disc temperature profile. A comparison of the temperature profiles between the slim-disc and α -disc prescriptions is shown in Figure 1.2 for two Eddington fractions.

1.2.3 The spectra of accretion discs

The previous two models give us a way to calculate the temperature profile for an accretion disc, given some disc parameters. By assuming that the accretion disc can be discretized into a series of annuli, each radiating as a blackbody of temperature $T_{\text{eff}}(r)$, then by integrating over the disc radius the SED of an accretion disc can be calculated. The specific intensity for each annulus is,

$$B_{\nu} = \frac{2h\nu^3}{c^2} \left[\exp\left(\frac{h\nu}{k_B T_{\text{eff}}}\right) - 1 \right]^{-1}. \quad (1.17)$$

For intermediate frequencies, given the above distribution, the spectrum of an accretion disc is expected to appear as a *stretched* blackbody and follows $L_{\nu} \propto \nu^{1/3}$, as shown in

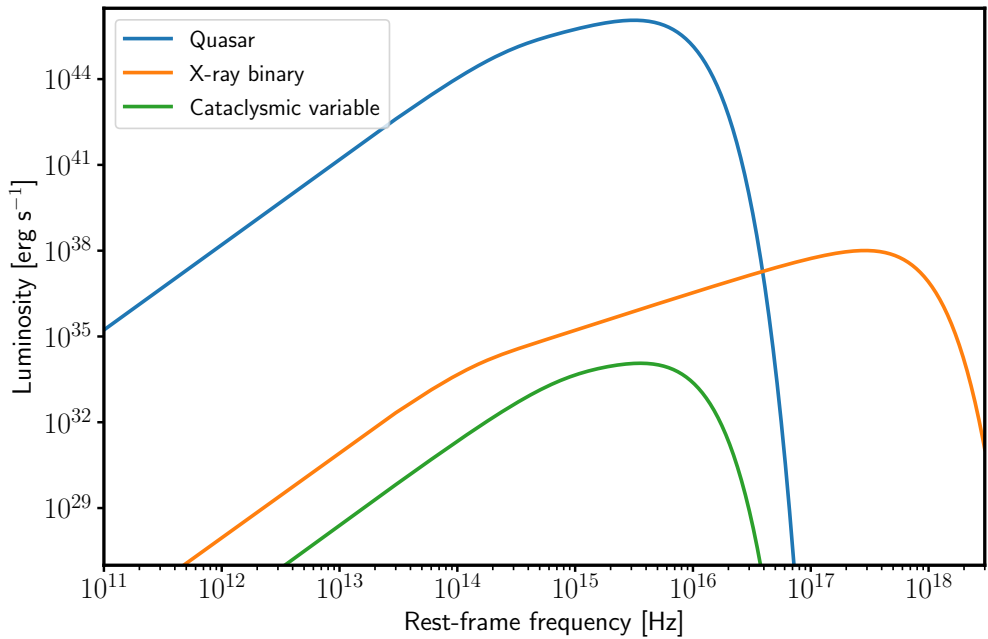


FIGURE 1.3: The accretion disc spectrum for three distinct systems assuming an α -disc with an accretion efficiency of $\eta = 0.1$, as follows: 1) a QSO with $M_{\text{co}} = 10^9 M_{\odot}$, $\dot{M}_{\text{acc}} = 10 M_{\odot} \text{ yr}^{-1}$, $R_{\text{in}} = 8.85 \times 10^{14} \text{ cm}$, $R_{\text{out}} = 1 \times 10^{17} \text{ cm}$, 2) an XRB with $M_{\text{co}} = 10 M_{\odot}$, $\dot{M}_{\text{acc}} = 10^{-7} M_{\odot} \text{ yr}^{-1}$, $R_{\text{in}} = 10^7 \text{ cm}$, $R_{\text{out}} = 10^{12} \text{ cm}$, and, 3) a CV with $M_{\text{co}} = 0.8 M_{\odot}$, $\dot{M}_{\text{acc}} = 10^{-8} M_{\odot} \text{ yr}^{-1}$, $R_{\text{in}} = 7 \times 10^8 \text{ cm}$, $R_{\text{out}} = 2.4 \times 10^{10} \text{ cm}$.

Figure 1.3. At the high frequency end, the spectrum will drop off exponentially (the Wien tail of the blackbodies) and the low frequency region is made up of Rayleigh-Jeans tails. Figure 1.4 shows how changes in the temperature profile affect the SED, given the temperature profiles derived from using an α - and slim-disc prescription. In Figure 1.5, I show an example of an accretion disc SED for disc parameters representative of a TDE (labelled as base) and how changes to several disc parameter change the appearance of the spectrum.

Naturally, when disc parameters are changed, the spectrum also changes. For example, by truncating the outer radius, the spectrum becomes dimmer at lower frequencies, as the proportion of *cool* blackbodies contributing to the Rayleigh-Jeans portion of the spectrum has decreased. Conversely, if the inner radius is truncated instead, the Wien tail of the spectrum changes as the peak temperature of the accretion disc is lower. Lowering the accretion rate affects the SED at all wavelengths, as each annulus is cooler and less luminous.

In reality, the spectra of accretion discs are far more complicated than a “simple” ensemble of blackbodies. There are many processes which a photon can undergo within the disc atmosphere, causing the local SED to deviate from a blackbody. One such case would be electron scattering. For example, if electrons inelastically scatter (e.g.

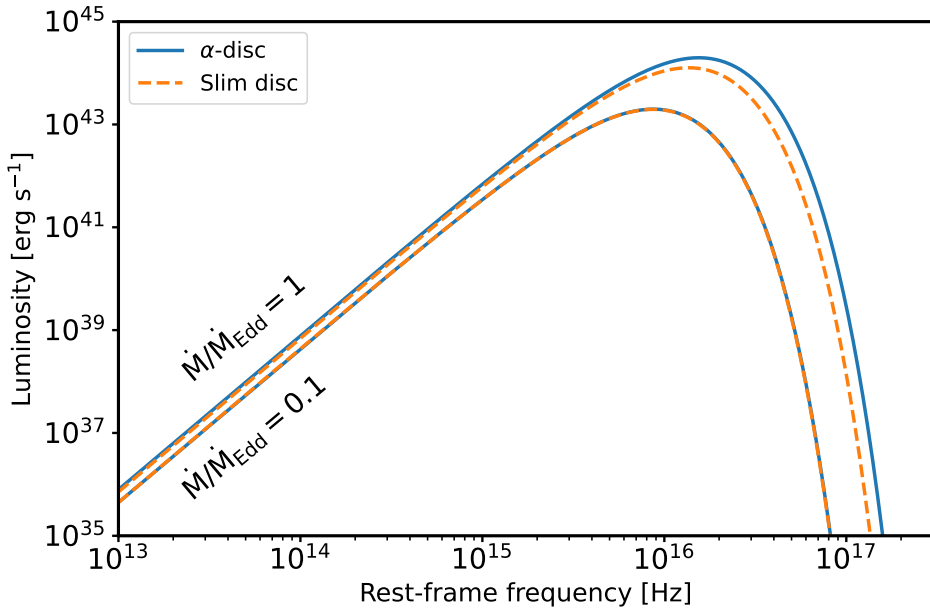


FIGURE 1.4: The accretion disc spectrum for two Eddington accretion regimes using a standard α -disc temperature profile (solid lines) and a slim disc temperature profile (dashed lines) for two Eddington fractions, using the same disc parameters as in Figure 1.2. For low Eddington fractions, the spectra are identical. However, the high frequency turnover in the near critical regime is attenuated and features a steeper exponential cutoff.

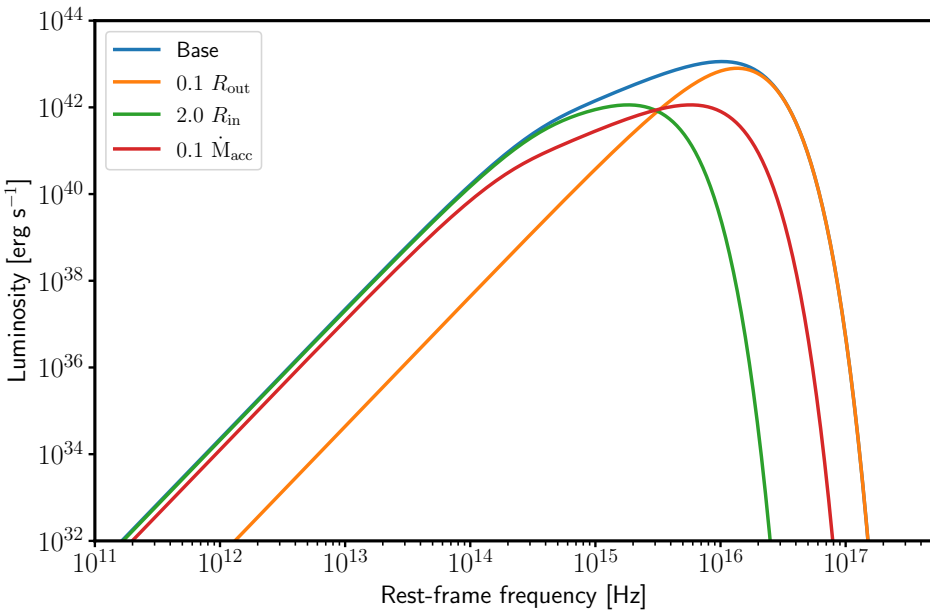


FIGURE 1.5: The accretion disc spectrum for four model. The “base” model is based on a α -disc used later in Chapter 4, but with a larger outer radius. It has the following parameters: $M_{\text{BH}} = 3 \times 10^6 M_{\odot}$, $R_{\text{in}} = R_{\text{ISCO}}$, $R_{\text{out}} = 376 R_{\text{ISCO}}$ and $\dot{M}_{\text{acc}} = 0.15 \dot{M}_{\text{Edd}}$ using an accretion efficiency of $\eta = 0.1$. The other models correspond to the same disc parameters, with either the outer or inner radius truncated, or a smaller accretion rate.

Each change in disc parameters changes the spectrum of the accretion disc.

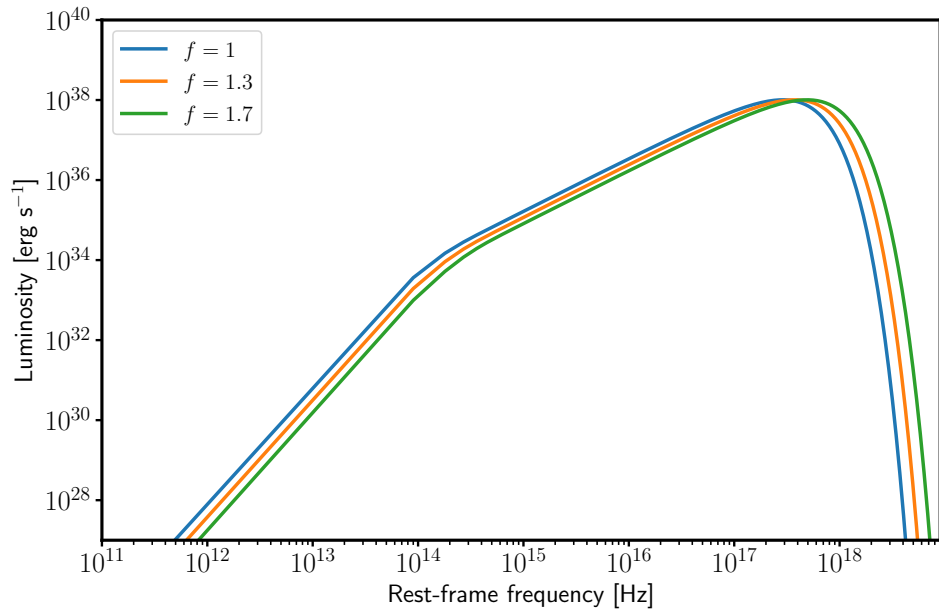


FIGURE 1.6: The accretion disc spectra for the XRB model in Figure 1.3 using a colour-corrected blackbody with $f = 1.3$ and $f = 1.7$ and using a simple blackbody profile ($f = 1$). When using the colour-corrected blackbody, the spectrum is shifted to higher frequencies.

Compton scatter), then we would expect the distribution of photon energies to be modified (e.g. Madej, 1974; Shimura & Takahara, 1995). In this case, Shimura & Takahara (1995) show that the resulting spectrum can be modelled instead by a *colour-corrected blackbody*,

$$I_\nu = \frac{2h\nu^3}{c^2f^4} \left[\exp\left(\frac{h\nu}{fk_B T_{\text{eff}}}\right) - 1 \right]^{-1}, \quad (1.18)$$

where f is the colour correction, or spectral hardening, factor. It is a multiplicative factor by which spectral features are shifted to higher energies. This approach relies on knowing what f should be for the object modelled. Efforts have been made to empirically measure f (Czerny et al., 2003; Pszota & Cui, 2007), and also through theoretical approaches (Shimura & Takahara, 1995; Davis & El-Abd, 2019). In the case of an XRB, a value of $f \sim 1.7$ is typically adopted (Davis & El-Abd, 2019). A comparison between using a colour-corrected and simple blackbody spectra is shown in Figure 1.6 for an XRB-esque accretion disc.

1.3 Accretion disc winds

The accretion of material onto an object is, in almost every case, accompanied by outflows in the form of powerful, oftentimes relativistic, polar jets of material and/or winds which rise from the surface of the accretion disc. The effect of these outflows on how we see an object is actually quite profound, and no analysis or discussion of accretion is really complete without worrying about the associated mass-loaded outflows. For example, the mass lost from an outflow can modify the accretion rate and therefore the effective temperature profile (e.g. Knigge, 1999; Laor & Davis, 2014; Miller et al., 2015). However, this is quite a small effect in cases where the mass loss of the wind is much smaller than the mass accretion rate, or when the mass loss is well outside the region where most of the energy is released (Knigge, 1999).

1.3.1 Driving mechanisms

For an outflow to actually happen, some kind of driving mechanism has to launch and accelerate the material making up the outflow. For an accretion disc wind, there are three likely driving mechanisms: thermal, radiation and magnetic pressure.

1.3.1.1 Thermal

An accretion disc wind can be thermally driven when the thermal speed of the material in the accretion disc exceeds the escape velocity. For an accretion disc to be in hydrostatic equilibrium, the gravitational force is balanced by the thermal pressure of the stuff in the disc atmosphere. If the thermal pressure in the disc increases and exceeds the gravitational force holding it down, then an outflow will form with the thermal pressure driving the outflow. Typically this requires temperatures in excess of $\gtrsim 10^7$ K, which are not really achievable for an α -disc (c.f. Figure 1.2), and typically happens in the outer annuli of irradiated accretion discs, where the escape velocities are low relative to the inner edge (Begelman et al., 1983). As such, AGNs are usually not viable candidates for hosting thermally driven winds, due to the massive escape velocities associated with their SMBHs and the challenge of heating the outer edge of the disc. But, a thermally driven wind could be the possible source for the so-called “warm absorbers” in AGN (Krolik & Kriss, 2001; Mizumoto et al., 2019). XRBs, however, are excellent candidates for hosting thermally driven winds, as the outer edges of their accretion discs are Compton heated to high temperatures, causing the thermal velocity to far exceed the escape velocity at this radius (e.g. Ponti et al., 2012; Higginbottom et al., 2017, 2019).

1.3.1.2 Radiation

For an outflow to be driven by radiation pressure, the source must be close to or exceed the Eddington limit (Equation 1.7) in order to power that outflow purely from the radiation pressure exerted on free electrons alone. A handful of objects are thought to be undergoing super-Eddington accretion, such as AGN with ultrafast outflows (Gofford et al., 2015; King & Pounds, 2015) and are prime candidates for radiation driven winds.

However, systems which are significantly below the Eddington limit can also drive outflows by radiation pressure. In this case, they are not driven by pressure on free electrons, but by pressure acting upon the bound electrons. These so-called line driven winds are very similar to radiation driven winds. The key difference is that the driving mechanism instead comes from *bound-bound* transitions (in a mildly ionized plasma), so the outflow is driven by photons line/resonance scattering and transferring momentum from themselves onto the bound electrons. The seminal work on this type of driving mechanism was by Castor et al. (1975), who quantify the contribution of bound electrons on the net radiation force via a multiplicative *force multiplier*, $\mathcal{M}(t)$. The additional acceleration due to radiation is therefore,

$$g_r = \frac{\sigma_T F}{\mu m_p c} \mathcal{M}(t), \quad (1.19)$$

where F is the continuum flux and μ is the mean atomic weight. The force multiplier is actually a function of a dimensionless parameter, t , which represents the scattering optical depth independent of the strength of the line. In a static atmosphere, t is essentially the electron scattering optical depth, but in expanding outflows t can be many factors lower than this. The force multiplier has a maximum value of around 2000 - 4000 (Castor, 1972; Owocki et al., 1988; Gayley, 1995), which shows that radiation driven winds, by lines, are possible when the accretion rate is much lower than the Eddington limit.

Line-driven winds are most commonly found in O- and Wolf-Rayet stars (Castor et al., 1975; Friend & Abbott, 1986). However, line-driving has also been suggested as a mechanism to launch accretion disc winds (Shlosman & Vitello, 1993; Proga et al., 2000), in both high-state CVs (Pereyra et al., 1998; Proga et al., 1998; Feldmeier & Shlosman, 1999; Froning, 2005) and AGNs/QSOs (Proga et al., 2000; Proga & Kallman, 2004; Laor & Davis, 2014; Higginbottom et al., 2014).

1.3.1.3 Magnetic

Accretion discs are thought to contain strong magnetic fields, due to the large electrical current carried by the motion of electrons in the plasma making up the disc. Such

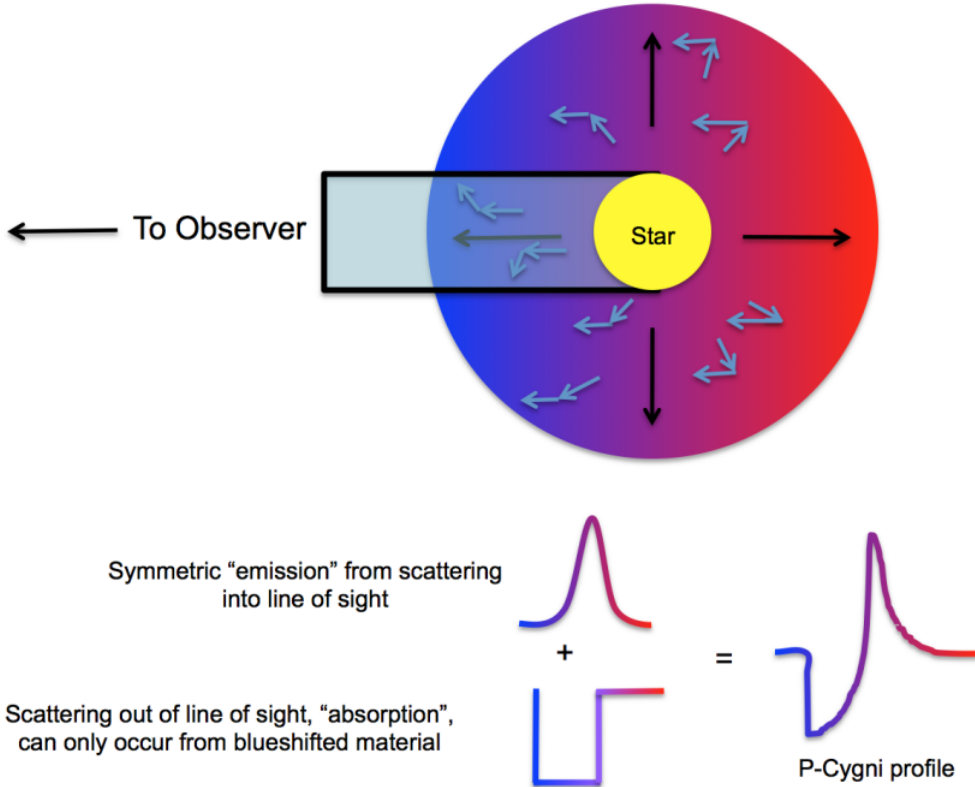


FIGURE 1.7: A schematic showing the formation of P-Cygni lines in an expanding spherical outflow. The black arrows show the direction of the outflow and the blue arrows show the typical scattering direction of photons. Figure from Matthews (2016).

strong magnetic fields are another way to drive an outflow, which can extract significant amounts of angular momentum from the disc. A simple and insightful model of such an outflow is the “bead on a wire” picture, first proposed by Blandford & Payne (1982). In this model, an outflow is initially launched by thermal expansion (or some other mechanism), but the material becomes channelled by the poloidal magnetic field lines of the accretion disc, causing the material to rotate. If the poloidal component of the magnetic field makes an angle $30^\circ < \theta < 60^\circ$, then the centrifugal forces push the material along the magnetic field lines, driving an outflow.

These outflows are known as magnetocentrifugal winds and do not require any further driving mechanisms once the outflow has been initially launched. Therefore, magnetically driven winds are excellent candidates for explaining how low luminosity and otherwise unassuming objects are able to sustain an outflow, such as YSOs (Pelletier & Pudritz, 1992; Kudoh & Shibata, 1997), AGN (Pelletier & Pudritz, 1992; Konigl & Kartje, 1994) or over-ionized outflows (Proga, 2007).

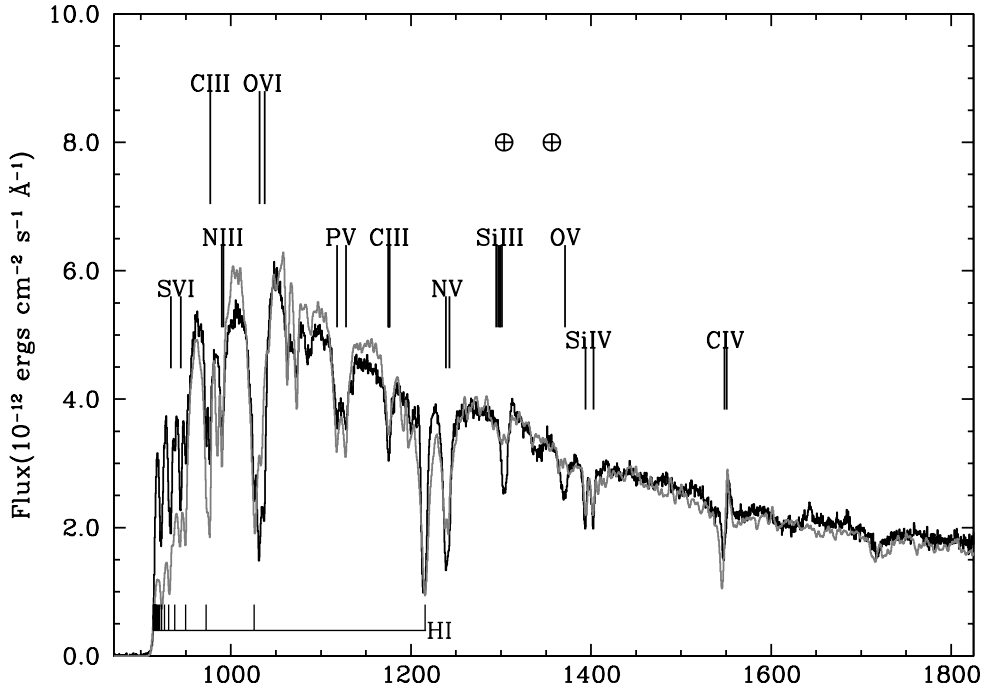


FIGURE 1.8: A synthetic spectrum generated by Long & Knigge (2002) comparing the HUT spectrum of Z Cam (black line) to the synthetic spectrum (gray line), using a simple biconical prescription. The model shows very good agreement with the observations. Figure taken from Long & Knigge (2002).

1.3.2 Observational evidence

Outflows are ubiquitous amongst accreting astrophysical systems on all scales, and a plethora of observational evidence exists for the presence of powerful, mass-loaded outflows. One of the clearest outflow signatures in systems containing moderately ionized winds are blueshifted BALs and P-Cygni lines associated with strong UV resonance transitions, such as Ly α λ 1216, N v λ 1240, Si iv λ 1400 and C iv λ 1550. These features are seen, for example, in hot stars, CVs, QSOs and TDEs.

P-Cygni lines/profiles are characterised as having both a strong emission component and a blueshifted absorption component. Figure 1.7 shows a schematic of how a P-Cygni line forms in an expanding outflow with significant line opacity. Photons which are moving toward an observer are blueshifted and scattered *out* of the line of sight, creating an absorption component of the line. In contrast, photons which are scattered *into* the line of sight of an observer increase the amount of flux seen, resulting in the red emission component of P-Cygni profiles. The contribution of both of these processes is what gives rise to the unique P-Cygni profile.

It is a fairly well established fact in CVs that outflows rising from an accretion disc are rather common, and that they impact the UV spectra (Greenstein & Oke, 1982; Cordova

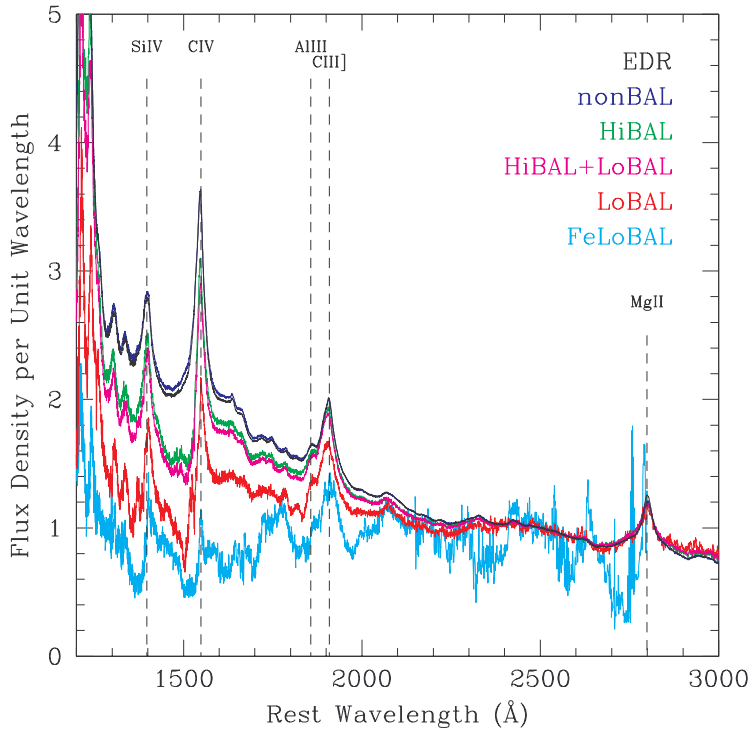


FIGURE 1.9: Normalized, geometric composite spectra of multiple QSOs from the SDSS early data release (Stoughton et al., 2002), differing by their type of BALs within their spectra. The top blue spectrum is a non-BAL QSOs. Figure from Reichard et al. (2003).

& Mason, 1982; Drew & Verbunt, 1985; Hartley et al., 2002). The most compelling evidence for outflowing material in these objects are the P-Cygni lines, commonly seen in the UV spectra, associated with strong UV resonance lines. Substantial effort has been put into modelling these outflows, and how P-Cygni lines can form in them (e.g. Drew & Verbunt, 1985; Shlosman & Vitello, 1993; Knigge et al., 1995; Long & Knigge, 2002; Hartley et al., 2002, to name a few from times gone by). The general consensus from this modelling effort is that a fairly wide outflow can carry away anywhere between $\simeq 1 - 10\%$ of the material accreting onto the WD. Modelling has also shown that line formation in these outflows could be responsible for the P-Cygni lines. Figure 1.8 shows a model by Long & Knigge (2002) who, using a simple biconical outflow prescription, produce a model in excellent agreement with the UV spectrum of Z Cam. Much less is known, however, regarding the effect outflows have on the optical spectra of CVs. In a few cases, P-Cygni-like profiles have been observed for H α and He I $\lambda 5876$ (Patterson et al., 2001), and some modelling has taken place to explore this regime and the formation of these features in greater detail (e.g. Matthews et al., 2016).

A swathe of observational evidence also exists which suggests that AGN harbour powerful outflows, as well. Some of the clearest and most compelling, is again, found by looking at the UV spectra of AGN. In approximately 20% of the QSO population, blueshifted broad absorption lines (BALs) are found (the so-called BALQSOs; e.g. Weymann et al.,

1991; Knigge et al., 2008; Dai et al., 2008; Allen et al., 2011), while “pure” BELs are observed in the remaining systems. These BALs and BELs occurs in species such as C IV, Si IV and N V, with the most prominent often being associated with C IV. Additionally, $\simeq 10\%$ of BALQSOs also exhibit absorption in lower ionization species, such as Mg II and Al III (low ionization broad absorption line quasars (LoBALQSOs) Gibson et al., 2009). In Figure 1.9, I show a sample of composite QSO spectra constructed from the Sloan Digital Sky Survey (SDSS) Early Data Release (Stoughton et al., 2002), which includes a non-BAL QSO and the different sub-classes of BALQSOs.

One simple explanation for the incidence of BALs in BALQSOs is in terms of line formation in an accretion disc wind, where the BEL vs. BAL dichotomy is explained as an orientation effect. This provides a concise geometric unification scenario for BALQSOs and non-BAL QSOs (e.g. Murray et al., 1995; Elvis, 2000; Matthews et al., 2016). In such a unified model, BALs are preferentially observed when looking *into* the wind cone, which obstructs the continuum source. By contrast, observers who do not look into the wind will preferentially see BELs. The fraction of BALQSOs is therefore related the covering factor, $f_\Omega = \int_{\theta_{\min}}^{\theta_{\max}} \sin(\theta) d\theta$, of the outflow.

1.4 Tidal disruption events

Hitherto, I have discussed the very basic physics of the accretion process and of accretion disc winds, as well as evidence of their existence. But I have not yet said anything much in detail about the events this thesis is all about. To very quickly remind ourselves what a TDE is: a TDE transpires when an unlucky star wanders too close to a SMBH, and is ripped apart (full disruption) by extreme tidal forces. However, it is not always the case that a star will be completely destroyed, as in some cases only some of the star’s atmosphere may be stolen away by the SMBH (partial disruption). Roughly half of the *disrupted* stellar material, as shown in Figure 1.10, is ejected out, whilst the rest becomes bound to the SMBH and eventually forms a quasi-circular accretion disc (Cannizzo et al., 1990; Shiokawa et al., 2015; Hayasaki et al., 2016; Bonnerot et al., 2016, 2021). The fallback of the debris to the orbital pericenter powers a transient and luminous flare detectable across the electromagnetic spectrum (Saxton et al., 2020; van Velzen et al., 2020b; Jiang et al., 2021; Alexander et al., 2020; Gezari, 2021). The initial fallback – and accretion, if circularization is efficient – of the material is, given the right conditions, usually super-Eddington initially and gradually transitions into a sub-Eddington accretion flow, as the fallback of material declines, and the reservoir of stellar material empties.

Even though much of our basic theoretical understanding of TDEs was laid out in the late 1970’s (Hills, 1975; Young et al., 1977; Hills, 1978; Frank, 1978; Rees, 1988), our current census of TDEs is, still, quite small, standing at a population of a dizzyingly high

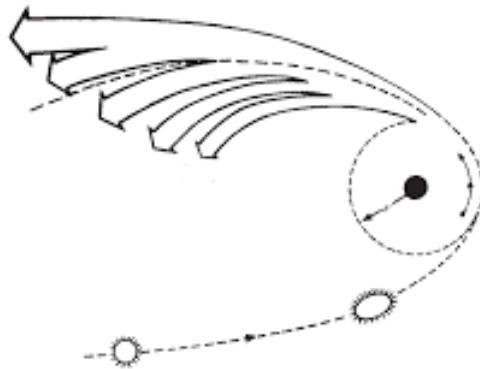


FIGURE 1.10: A simple schematic diagram of the disruption process. The star is *disrupted* when it comes within the disruption radius of the SMBH and is ripped apart. Half of the material becomes bound to the SMBH, whilst the rest is ejected from the system at speeds $v \sim 10^4 \text{ km s}^{-1}$. Figure adapted from Rees (1988).

56 well-studied events. The population is so small, in-fact, that Gezari (2021) is able to list them entirely within a single table. It was not until the mid-1990’s that the first TDE candidates actually emerged, and from archival searches of the *ROSAT All Sky Survey* (RASS; Voges, 1993) at that. In RASS, four galaxies were found with luminous (10^{41-44} ergs s^{-1}), but soft X-ray outbursts, yet showed no previous evidence of AGN activity. The fact that four were discovered within the time-frame of RASS implied an outburst rate of $\sim 10^{-5} \text{ yr}^{-1} \text{ galaxy}^{-1}$, which is consistent with the theoretical expected rate for TDEs (Donley et al., 2002). Since then, similar X-ray events have been discovered through either dedicated searches or serendipitously with *Chandra* and *XMM-Newton*. In addition, *Swift* has been invaluable in providing rapid follow-up observations for many candidate TDEs.

Within the last decade or so, a number of TDEs (approximately 30 events as of writing) with weak X-ray, but bright optical/UV emission, have been discovered. They were found mainly in time-domain optical surveys such as the *Palomar Transient Factory* (PTF; Law et al., 2009; Hung et al., 2018), the *Zwicky Transient Facility* (ZTF; Bellm et al., 2018) and the *All Sky Automated Survey for supernovae* (ASAS-SN Shappee et al., 2014). These events are somewhat at odds with the early theoretical models of TDE emission, which predicted that the light emerging from TDEs to be dominated by thermal X-ray emission from a hot accretion disc/flow. Lots of thought has been put into how to explain this discrepancy, and, so far, two mechanisms/processes have been proposed to account for the so-called “optical excess”. The first posits that the X-ray emission is reprocessed to longer, optical, wavelengths (Strubbe & Quataert, 2009; Metzger & Stone, 2016; Roth et al., 2016; Roth & Kasen, 2018; Lu & Bonnerot, 2019; Piro & Lu, 2020; Bonnerot et al., 2021). The second instead does away with the idea of

the optical emission having a disc origin, and instead proposes that the optical emission is a consequence of hydrodynamic shocks between infalling debris streams (Dai et al., 2015; Piran et al., 2015; Shiokawa et al., 2015). Having said that, very recent modelling has also shown that emission from an elliptical accretion disc is also a promising mechanism (Piran et al., 2015; Liu et al., 2018, 2021). But, as of the time of writing, this scenario has not been explored as extensively as the other two mechanisms.

Following from this, admittedly rather brief, introduction to these events, I will now move on to discuss in greater depth the physics behind the disruption and fall back of material, as well as the formation and dynamics of TDE accretion discs. Following this, I next discuss the observational properties of these events and the evidence for outflows associated with TDEs, as well as the role such outflows may have in shaping the observational properties (including the possibility that they may provide the requisite medium for reprocessing the accretion disc emission to longer wavelengths).

Given the presence and interactions with a SMBH, TDEs are, somewhat obviously, general relativistic events. I have chosen again (for the most part, at least) to restrict the background I present here within Newtonian gravity, for purely pedagogical purposes. A more thorough description taking into account the effects of general relativity can be found in, for example, Stone et al. (2019).

1.4.1 Rate of tidal encounters

If we consider a single galaxy with a SMBH at the centre, how often will we see a TDE in that galaxy? The rate at which they occur will depend, firstly, on the mass and spin of the SMBH at the centre of that galaxy (e.g. Kesden, 2012) and also the nuclear stellar density of the galaxy, as well as the orbital distribution of its stars (Frank & Rees, 1976; Frank, 1978). Taking all of these factors into account, the rate at which we should observe a TDE ranges anywhere between $10^{-4} - 10^{-5}$ $\text{yr}^{-1} \text{galaxy}^{-1}$ (Magorrian & Tremaine, 1999; Stone & Metzger, 2016). Rates can, however, be enhanced up to 10^{-3} $\text{yr}^{-1} \text{galaxy}^{-1}$ in post-starburst (E+A) galaxies (French et al., 2016; Stone & Velzen, 2016; Cen, 2019), galaxies with overdense nuclear regions, or in galaxies with eccentric nuclear discs (Foote et al., 2019)¹. Additionally, the disruption rate can be either enhanced or suppressed after a galaxy merger, due to an increase/decrease in the nuclear stellar density (Lezhnin & Vasiliev, 2019; Coughlin et al., 2019).

1.4.2 Disruption

A star will undergo a tidal disruption if its orbital pericenter, R_p , is within the tidal disruption radius of the SMBH. The disruption radius can be derived by equating the

¹In this scenario, only the disruption rate of high-mass stars is enhanced.

Newtonian surface tidal acceleration, $GM_{\text{BH}}R_{\star}/r_t^3$, with the star's self-gravitational acceleration, GM_{\star}/R_{\star}^2 , giving (Hills, 1975),

$$r_t = R_{\star} \left(\frac{M_{\text{BH}}}{M_{\star}} \right)^{1/3}, \quad (1.20)$$

where M_{\star} and radius R_{\star} are the mass and radius of the star, respectively, and M_{BH} is the mass of the SMBH. The strength of the event is quantified by using a dimensionless penetration factor,

$$\beta = r_t/R_p. \quad (1.21)$$

If the disruption radius is *within* the event horizon of the SMBH, then the star will be disrupted but no luminous flare will be observable, as the light cannot escape from within the event horizon. Since the size of the event horizon grows linearly with black hole mass, whilst the disruption radius scales $r_t \propto M_{\text{BH}}^{1/3}$, there is, in actual fact, an upper mass limit for observable TDEs commonly known as the Hills mass. The critical mass is easily derivable by equating the event horizon and the tidal disruption radius. For example, consider a non-rotating black hole whose event horizon is given by the Schwarzschild radius,

$$R_s = 2r_g = \frac{2GM_{\text{BH}}}{c^2}. \quad (1.22)$$

Then by equating this with Equation 1.20, we derive the Hills mass as (Hills, 1975),

$$M_H = M_{\star}^{-1/2} \left(\frac{R_{\star}c^2}{2G} \right)^{3/2} \simeq 10^8 M_{\odot} \left(\frac{R_{\star}}{R_{\odot}} \right)^{3/2} \left(\frac{M_{\star}}{M_{\odot}} \right)^{-1/2}. \quad (1.23)$$

It is at this critical mass where a SMBH will directly capture the star, swallowing it whole and leaving no evidence behind of its crime. This value is also sensitive to the spin of the SMBH, due to the event horizon moving depending on the spin; see Figure 1.1. Kerr SMBHs therefore are able to produce observable disruptions at higher masses, where Schwarzschild SMBHs would not. At the opposite end of the mass scale, the lowest inferred SMBH masses are $M_{\text{BH}} \simeq 5 \times 10^6 M_{\odot}$ (Wevers et al., 2017; Mockler et al., 2019; Ryu et al., 2020; Zhou et al., 2020) and partial disruptions have also been theorized for stellar mass black hole encounters as well (Wang et al., 2021).

As mentioned previously, the disruption of a star comes in two distinct flavours. Full disruption, where the star is completely destroyed, and, partial disruption, where only the outer layers of the star's atmosphere are stolen away by the SMBH (Guillochon & Ramirez-Ruiz, 2013). Equation 1.20 ignores completely the structure of the star and the

complex hydrodynamic details of the disruption process. In reality, a full disruption will only happen for penetration parameters above some critical value, $\beta > \beta_f$, while partial disruptions may happen for lower values, $\beta_p < \beta < \beta_f$. Passing stars with penetration parameters $\beta < \beta_p$ will survive and remain relatively unperturbed.

Since the hydrodynamics are complex, the values of these two critical parameters have only been derived in the simple case of polytropic stars, assuming a Lane-Emden density profile. In these simulations, for a $\gamma = 5/3$ polytropic star, $\beta_f \approx 0.92$, whilst for $\gamma = 4/3$ polytropes $\beta_f \approx 2.01$ (Guillochon & Ramirez-Ruiz, 2013; Mainetti et al., 2017). The critical value β_f is still currently unknown for more realistic stellar models, but recent research is beginning to include the stellar structure in more detail (e.g. Law-Smith et al., 2020; Spaulding & Chang, 2021; Nixon et al., 2021).

1.4.3 Fallback of material

When the star has been disrupted, roughly half of it becomes bound to the system, whilst the other half is launched away. The spread in energy across this debris stream is given by (Rees, 1988; Lodato et al., 2009; Bonnerot & Stone, 2021),

$$\Delta\epsilon = \frac{GM_{\text{BH}}R_{\star}}{r_t^2} = \frac{GM_{\star}}{R_{\star}} \left(\frac{M_{\text{BH}}}{M_{\star}} \right)^{1/3}. \quad (1.24)$$

The most bound material, i.e. at the very outer edge of the debris stream, has a semi-major axis given by,

$$a_{\min} = \frac{R_{\star}}{2} \left(\frac{M_{\text{BH}}}{M_{\star}} \right)^{2/3}. \quad (1.25)$$

As a not so bad, but still first-order approximation, it is convenient to ignore the self-gravity of the debris stream and assume that the disrupted material falls back onto the SMBH on a ballistic trajectory. This means the gas evolves into an elongated stream of stuff, eventually returning to the orbital pericenter. It is material at the very bound edge of the debris stream which first falls back to orbital pericenter. Following from Kepler's third law (Kepler, 1619) and Equation 1.25, the time it takes for the material to fallback is (see, e.g. Lodato & Rossi, 2011),

$$t_{\text{fb}} = \frac{\pi}{\sqrt{2}} \left(\frac{GM_{\star}}{R_{\star}^3} \right)^{-1/2} \left(\frac{M_{\text{BH}}}{M_{\star}} \right)^{1/2}. \quad (1.26)$$

The fallback timescale, t_{fb} , for the bound material is often referred to as the *characteristic minimum timescale*. One interesting quirk of Equation 1.26 is that it states the fallback

time scales with the square root of the black hole mass, thus the time from first disruption to the appearance of the TDE flare should, in principle, give some insight on the mass of the SMBH.

The mass fallback rate of the material depends on how the original energy is distributed. If we boldly assume that this distribution is uniform, i.e. $dM/dE = 0$, then the rate at which material returns to orbital pericenter is given by,

$$\dot{M}_{\text{fb}} = \dot{M}_{\text{peak}} \left(\frac{t}{t_{\text{fb}}} \right)^{-5/3}, \quad (1.27)$$

where \dot{M}_{peak} is the peak fallback rate, given by,

$$\dot{M}_{\text{peak}} = M_{\star} / 3t_{\text{fb}}. \quad (1.28)$$

Equation 1.27 shows that the rate of material returning to orbital pericenter declines with time, following a fiducial $\dot{M}_{\text{fb}} \propto t^{-5/3}$ power law. Following from the peak fallback rate (Equation 1.28), it is easy to see that the disruption of material can result in a range of potential accretion rates, and can be super-Eddington. In general, the fallback of the debris stream in TDEs with $M_{\text{BH}} \lesssim 3 \times 10^7 M_{\odot}$ is initially super-Eddington, whereas TDEs above this mass limit are within the sub-Eddington regime (Strubbe & Quataert, 2009; Metzger & Stone, 2016).

The previous equations have made the assumption of a full disruption. In the case of a partial disruption, the fallback rate of material instead follows a steeper power law $\dot{M}_{\text{fb}} \propto t^{-7/4}$ (Coughlin & Nixon, 2019). Having said this, factors such as the internal structure of the disrupted star, the penetration parameter of the disruption and the spin of the black hole all affect the energy distribution of the debris and hence the fallback rate, causing it to deviate from the fiducial $t^{-5/3}$ power law (Kesden, 2012; Guillouchon & Ramirez-Ruiz, 2013; Golightly et al., 2019; Gaftron & Rosswog, 2019).

1.4.4 Accretion discs

In the earliest, and simplest, models of TDEs, it is assumed that the emission is thermal radiation from a hot, and compact, accretion disc (e.g. Strubbe & Quataert, 2009) which forms almost immediately after disruption (e.g. Rees, 1988). In early work, a standard α -disc prescription was used to model the accretion disc. But this is not really good enough when dealing with super-Eddington accretion, as the disc is unlikely to be in a nice steady-state. Therefore, semi-analytic super-Eddington disc models have often been used instead (see Section 1.2.2 and Strubbe & Quataert, 2009), but the disk *emission* is modelled in conceptually the same way. Specifically, the accretion disc is assumed

to emit as a multi-colour ensemble of blackbodies, in which each discrete annulus has an effective temperature, for example, given by Equation 1.16. Within these painfully simple models, it is predicted that TDEs should shine brightly in the X-ray/EUV, which conveniently explains the emission for TDEs observed with strong X-ray emission (cf. Figure 1.4). However, these simple models cannot explain why a large sub-set of TDEs have been observed with bright optical/FUV emission and weak X-ray (and this will be discussed later in Section 1.4.5.2 and 1.4.8, as well as in Chapter 4 and Chapter 5.).

The formation and evolution of accretion discs in TDEs is an area of on-going and intense research (e.g. Shiokawa et al. 2015; Piran et al. 2015; Bonnerot et al. 2016; Bonnerot & Lu 2020; Bonnerot et al. 2021). From a purely Newtonian perspective, it is actually quite difficult to answer how the infalling debris stream (on Keplerian orbits) circularizes into an quasi-circular accretion disc, given a realistic set of astrophysical parameters and initial conditions (Stone et al., 2019). Current theoretical work suggests that general relativistic phenomena are *critical* to the circularization process of the debris stream. Following the disruption of a star, the bound debris evolves into an elongated stream, before making its way back to orbital pericenter on highly eccentric trajectories (e.g. Kochanek, 1994; Coughlin et al., 2016). As the debris falls back, it is affected by a number of additional different physical processes that may affect its evolution (and fallback), such as fragmentation into clumps and cooling via recombination. The returning material may also interact with the ambient medium in some way. These, however, are very much secondary effects and do not affect the basic picture presented in Section 1.4.3 or the disc formation process (Bonnerot & Stone, 2021).

1.4.4.1 Formation

Once the bound material has reached pericenter, completing an orbit, the formation of an accretion disc begins. The simplest scenario of disc formation assumes immediate circularization of the debris stream and formation of a circular accretion disc near the circularization radius ($R_c = 2R_p$), corresponding to the lowest energy state of the gas (Rees, 1984; Bonnerot & Stone, 2021). In practice, it is not as simple as this, and the full circularization of the debris requires that the specific energy,

$$\Delta\epsilon_{\text{circ}} \approx \frac{GM_{\text{BH}}}{4R_p}, \quad (1.29)$$

is lost entirely by the debris² (Bonnerot & Stone, 2021). To circularize into a disc, the material *has to* somehow lose the truly massive amount of orbital energy and momentum which belongs to it. The most likely sources of energy and momentum dissipation is through two types of hydrodynamic shock: 1) a nozzle shock when the debris stream

²Note that the mass of the debris stream has been neglected from this calculation as its mass is completely negligible in comparison to the mass of the SMBH.

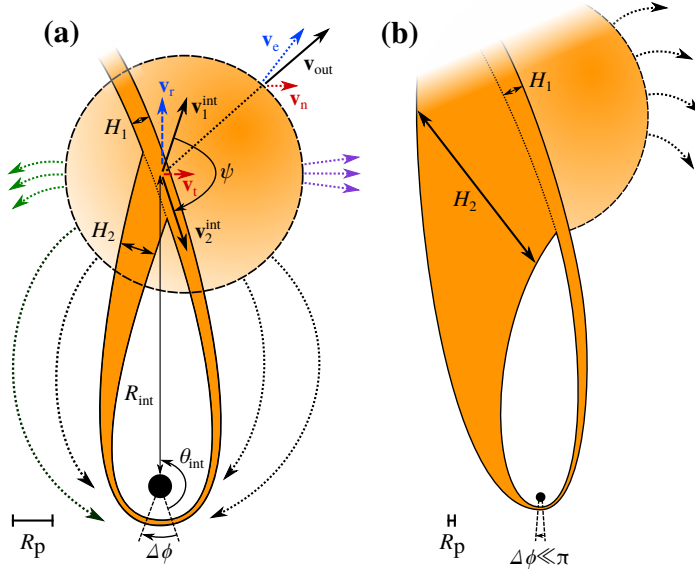


FIGURE 1.11: Sketches representing the self-intersection caused by an intersection of the stream with itself for two scenarios: apsidal precession and expansion due to a nozzle shock. The sketch also shows the evolution of the streams in both cases. *Left:* the collision is caused by relativistic apsidal precession, which makes the tip of the debris stream precess by an angle $\Delta\phi$ during pericenter passage. This interaction causes the the dissipation of kinetic energy associated with the radial motion of the stream, and causes an outflow driven by radiation pressure (orange sphere). *Right:* The nozzle shock produces very different widths for the two components of the debris stream (the stream before and after pericenter passage). As a result, the debris stream intersections at a broad range of radii, even if relativistic apsidal precession is basically non-existent. It is possible that a bow shock may cause further expansion of the debris, as shown by the orange half-sphere bounded by dashed lines. In both circumstances, the material which remains bound after the intersection eventually returns to pericenter, where it can undergo additionally interactions. Figure from Bonnerot & Stone (2021).

is compressed at orbital pericenter, and, 2) self-intersection shocks within or between debris streams. At the time of writing, it is thought that apsidal precession³, a general relativistic effect, is the main driving mechanism which forces the highly eccentric debris streams to self-intersect, creating shocks that dissipate the orbital energy (Stone et al., 2019; Lu & Bonnerot, 2019; Bonnerot et al., 2021; Bonnerot & Stone, 2021).

The first work on disc formation was conducted by Rees (1988) and Ulmer (1999). They assumed instant circularization and proposed that disc formation should occur on the order of the fallback time (Equation 1.26), with the resulting disc being vertically extended due to radiation pressure. A plethora of recent numerical studies (see Table 1 in Bonnerot & Stone, 2021), however, have shown that the dissipation mechanisms mentioned usually dissipate less than $\Delta\epsilon_{circ}$. This suggests that the formation of an accretion disc *could* require multiple returns to pericenter. If so, more than *one* fallback time would be required for the debris to completely circularize.

³The precession (gradual rotation) of the line connecting the apsides of the orbit.

1.4.4.1.1 Dissipation due to the nozzle shock

The nozzle shock is possibly the earliest source of dissipation. It occurs during the passage of the debris stream at orbital pericenter. As material with different orbital inclinations return, the debris stream(s) is compressed vertically, causing a nozzle shock which dissipates the kinetic energy associated with the motion of the gas. The resulting compression, and nozzle shock, heats up the gas, causing it to expand (Guillochon et al., 2014; Shiokawa et al., 2015). However, Guillochon et al. (2014) has shown that the dissipation provided by the nozzle shock is often negligible compared to that required to completely circularize the debris stream, other than for very low black hole masses, i.e. $M_{\text{BH}} \lesssim 10^4 M_{\odot}$. The nozzle shock still remains understudied, however, and our understanding of it is quite limited. It is, for example, unclear whether the resulting gas expansion significantly modifies the stream properties compared to the properties before pericenter passage (Bonnerot & Stone, 2021).

1.4.4.1.2 Dissipation due to self-intersection

This dissipation mechanism is due to the *self*-interaction between parts of a debris stream which have passed past pericenter and the other parts which are still approaching pericenter. There are a few mechanisms which make this happen. The first is relativistic apsidal precession, which changes the trajectory of the stream near pericenter putting it on a collision course with the still approaching debris. Another mechanism is the nozzle shock, again, as the expansion of the debris stream due to the nozzle shock increases the *width* of the stream. As the spread-out stream occupies a wider range of eccentric orbits, it can intersect with material on the original orbit. A final mechanism is nodal precession induced by the spin of the SMBH, which can modify the orbital plane of the debris. A diagram from Bonnerot & Stone (2021) showing how the first and second mechanisms mentioned result in intersections, and dissipation of orbital kinetic energy, is shown in Figure 1.11.

The self-intersection due to apsidal precession is highly sensitive to the penetration factor, where the centre of mass of the event precesses by an angle given by (e.g. Bonnerot & Stone, 2021),

$$\Delta\phi \approx 3\pi \frac{r_g}{R_t} \approx 11.5^\circ \beta \left(\frac{M_{\text{BH}}}{10^6 M_{\odot}} \right). \quad (1.30)$$

This implies a self-intersection radius, assuming the width of the stream before and after pericenter are the same (e.g. Bonnerot & Stone, 2021),

$$r_{\text{si}} = \frac{r_t}{\beta} \frac{1 + e_{\min}}{1 - e_{\min} \cos(\Delta\phi/2)}, \quad (1.31)$$

where e_{\min} is the eccentricity of the material at the most bound extremity. Equation 1.31 is sensitive to the penetration factor. For high β disruptions around small SMBHs, or disruptions around large SMBHs, the self-intersection radius will be at small radii, where the orbital energy within the debris can be efficiently dissipated by shocks. In TDEs where $\beta \sim 1$, the self-intersection radius is much further out and is roughly $r_{\text{si}} \simeq a_{\min}$. Circularization by apsidal precession in these events will be much less efficient, which may account for the delayed X-ray brightening seen in some TDEs (Gezari et al., 2017).

1.4.4.2 Evolution

In order to make life a little bit easier, accretion discs in TDEs have often been approximated via the simple α -disc prescription when modelling their properties and evolution (see Section 1.2.1 and Shakura & Sunyaev, 1973). Due to the short viscous timescale of the accretion disc at early times, the accretion rate is equal to the fallback rate (Ulmer, 1999). Therefore, referring back to Equation 1.27, the accretion rate is super-Eddington for the first few weeks to months of the event (Ulmer, 1999). The disc is hence within the super-Eddington regime, and it is both optically and geometrically thick. Recent numerical simulations by Bonnerot et al. (2021) suggest that, once formed, the accretion disc is expected to extend to a distance $R \approx 10 R_t$ with an *almost* Keplerian velocity profile. However, the authors also find that the accretion disc remains “thin” with an approximate $H \approx 2 R_t$. This is the result of efficient radiative cooling, which prevents the internal energy of the disc from building up and reduces pressure gradients in the disc atmosphere.

As the TDE evolves, the viscous and inflow timescales will increase. If the viscous timescale of the disc exceeds the fallback timescale of the debris, then the rate at which mass is lost through accretion onto the SMBH will be lower than the mass supply rate. Hence, the disc will grow in mass. Furthermore, at mid- to late-times, the originally super-Eddington accretion rate transforms into a sub-Eddington rate and the disc flattens, becoming geometrically thin while still remaining optically thick. van Velzen et al. (2019) and Mummery & Balbus (2020) have both shown that the late-time optical/UV and X-ray light curves are well explained by a geometrically thin and viscously spreading accretion disc with a declining accretion rate. One long-standing problems which still remains without a solid solution, however, is whether run-away thermal instabilities happen in radiation-dominated and geometrically thin accretion discs. Shen & Matzner (2014) suggest that if there are thermal instabilities, then this could lead to cycles of accretion bursts. But so far, no TDE has been observed that shows such cyclical behaviour.

1.4.4.3 Eccentric accretion discs

If the dissipation of energy is not *fast* enough – e.g. due to weak apsidal precession – the debris streams may fail to circularize and remain on highly eccentric orbits (Shiokawa et al., 2015; Bonnerot et al., 2016). Several models have been developed for the formation and emission of elliptical accretion discs, such as (Piran et al., 2015; Krolik et al., 2016; Liu et al., 2018, 2021). Certain observational signatures have been explained by invoking an elliptical accretion disc, such as the double-peaked and flat-topped broad H α emission lines (e.g. Holoién et al., 2019), and the apparent optical excess seen in a sub-set of TDEs (e.g. Liu et al., 2021). However, this type of TDE accretion flow has so far not been studied as extensively as the others mentioned above.

1.4.5 Spectroscopic observations

The physical processes involved in generating the luminous flare, and hence the observable radiation, are still uncertain. In the simplest, “canonical”, scenario, the flare is a consequence of bound stellar material forming a quasi-circular accretion disc through which material is transported at typically super-Eddington rates (see, e.g. Shiokawa et al., 2015; Hayasaki et al., 2016). The light observed is then thermal emission from this hot accretion disc. The emission from TDEs is therefore expected to be dominated by X-ray emission, with a weak optical and UV component (Rees, 1988; Strubbe & Quataert, 2009).

The spectra of TDE are vital for distinguishing TDEs from other nuclear/accretion activity or other transient objects, such as supernovae. In addition to this, spectroscopic observations also provide valuable insights into the source of emission and the dynamics of the emission source. Over the past decade, the number of TDEs with high quality spectroscopic observations has increased rapidly. These observations have revealed that most TDEs share similar line profiles and, in some cases, similar spectral evolution. It has also been found that, rather broadly, TDEs can be split into a set of three spectroscopic classes, based on their optical spectrum.

1.4.5.1 Spectral line profiles

Typically, the emission and absorption line profiles in TDEs are very broad, with FWHM $\sim 10^4$ km s $^{-1}$ at early times. If the dominant line broadening mechanism is Doppler broadening, the width of the early emission/absorption lines can provide us with some useful information, such as the size of the disruption radius (Arcavi et al., 2014; Brown et al., 2017a). Multiple TDEs have also been observed with blueshifted emission or absorption features (e.g. iPTF15af; Blagorodnova et al., 2019), and the lines also often exhibit an asymmetric red wing in their emission (e.g. Holoién et al., 2016; Roth & Kasen,

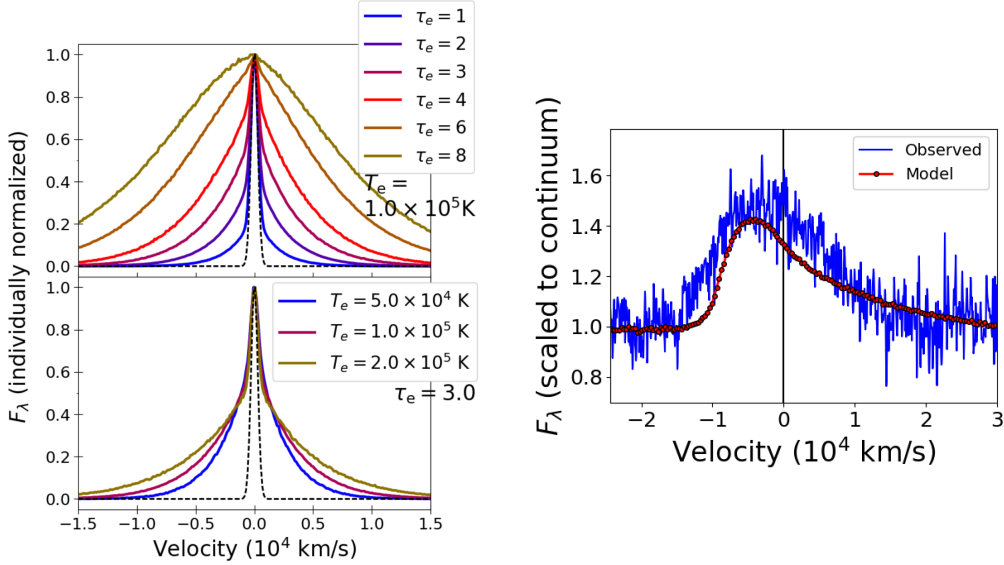


FIGURE 1.12: *Left:* a demonstration of line broadening by electron scattering in a homologous outflow for fixed electron temperature (top panel) and for fixed scattering optical depth (bottom panel). All fluxes have been scaled to their value at line centre. *Right:* a comparison between the H α profile in ASASSN-14ea (blue curve; [Holoi et al., 2014](#)) to a radiative transfer model by [SEDONA](#) ([Kasen et al., 2006](#)) of an optically thick homologous outflow. The model reproduces the same line profile, including the blueshifted emission and asymmetric red wing due to bulk scatter reprocessing of line photons. Figures from [Roth & Kasen \(2018\)](#).

2018; Hung et al., 2019). A few rare TDEs have exhibited double peaked emission lines (Arcavi et al., 2014; Holoi et al., 2019; Short et al., 2020).

If the spectral lines are formed in an optically thick outflow, Roth & Kasen (2018) show that the width of the emission lines could be broadened by non-coherent electron scattering rather than by Doppler broadening associated with the kinematics of the line forming region. The left panel of Figure 1.12 shows the results of a radiative transfer model by Roth & Kasen (2018), simulating line formation in an homogenously expanding outflow with either fixed electron scattering optical depth (top panel) or fixed electron temperature (bottom panel). Roth & Kasen (2018) show that, as the optical depth of the outflow decreases, then so should the width of the emission line. This is consistent with the observed behaviour of the emission lines in TDEs, which tend to become narrower with time (e.g., ASASSN-14li, iPTF16fnl, AT2018zr, AT2019qiz; [Holoi et al., 2016](#); Blagorodnova et al., 2017; Hung et al., 2019, 2020, respectively). Such a trend was originally unexpected, because – broadly speaking – the line-forming region was thought to be associated with “virialized” gas, $v \propto R^{-1/2}$. In this case, higher velocity material (and broader lines) should be revealed as the photosphere of the TDE shrinks and the continuum fades. Yet the opposite behaviour is actually observed.

In the same work, Roth & Kasen (2018) also show that the asymmetric red wing seen in the emission lines of some TDEs (such as ASASSN-14li or ASASSN-14ae) could also be

due to line formation in an optically thick outflow. Line photons which scatter in the expanding outflow lose energy. The cumulative effect of multiple scattering events is to *tire* the photon, redshifting their frequency. This is a processes – bulk scatter reprocessing, or what [Roth & Kasen \(2018\)](#) refers to as *adiabatic reprocessing* – results in the extended red wing in emission lines; see the right panel of Figure 1.12. Bulk scatter reprocessing does not only affect line photons and can also reprocess the continuum photons in the exact same way. Thus the entire spectrum is redshifted by this mechanism. Bulk scatter reprocessing will be discussed in greater detail later in Section 1.4.8.

1.4.5.2 Optical spectra

Contrary to the earliest TDE theory, an increasing number of TDEs are being detected which have bright optical and UV components, but a weak soft X-ray component. The existence of optically bright TDEs was initially surprising, since early theory predicts that the emerging light will be dominated by thermal X-ray emission from a hot accretion disc. The origin of this optical emission is still uncertain, but – as already noted above – two competing mechanisms have been proposed to explain its existence.

A relatively unique optical signature of TDEs is a broad emission line associated with He II $\lambda 4686$. In other transients, the same line is nowhere near as broad, bright or long-lived. The optical spectra of TDE are also often characterized by strong and broad H α and H β emission lines, and some TDEs also exhibit a complex series of nitrogen and oxygen emission lines associated with the Bowen fluorescence mechanism (see [Bowen, 1934, 1935](#)). Figure 1.13 shows optical spectra for 17 TDEs, presented originally by [van Velzen et al. \(2020a\)](#). At a first, quick, glance, it really looks like each TDE has a unique optical spectrum. However, a closer look allowed [van Velzen et al. \(2020a\)](#) to propose that three distinct types of optical TDE can be identified. In their taxonomy, TDEs are divided into three *distinct* classes:

1. TDE-H: broad H α and H β emission lines;
2. TDE-H+He: broad H α and H β emission lines with a complex of emission lines around He II $\lambda 4686$ with most due to Bowen fluorescence; and,
3. TDE-He: no broad Balmer features but a broad emission feature near He II $\lambda 4686$.

The optical spectrum of iPTF15af, a TDE belonging to the TDE-H+He class, is shown in Figure 1.14, and exhibits broad Balmer and He II lines, and the Bowen fluorescence lines discuss earlier. The most common class of optical TDE (to date) is TDE-H, followed by TDE-H+He and TDE-He.

The lack of hydrogen lines in TDE-He spectra was first attributed to the disruption of a helium star ([Gezari et al., 2012](#)). However, recent numerical simulations show that it

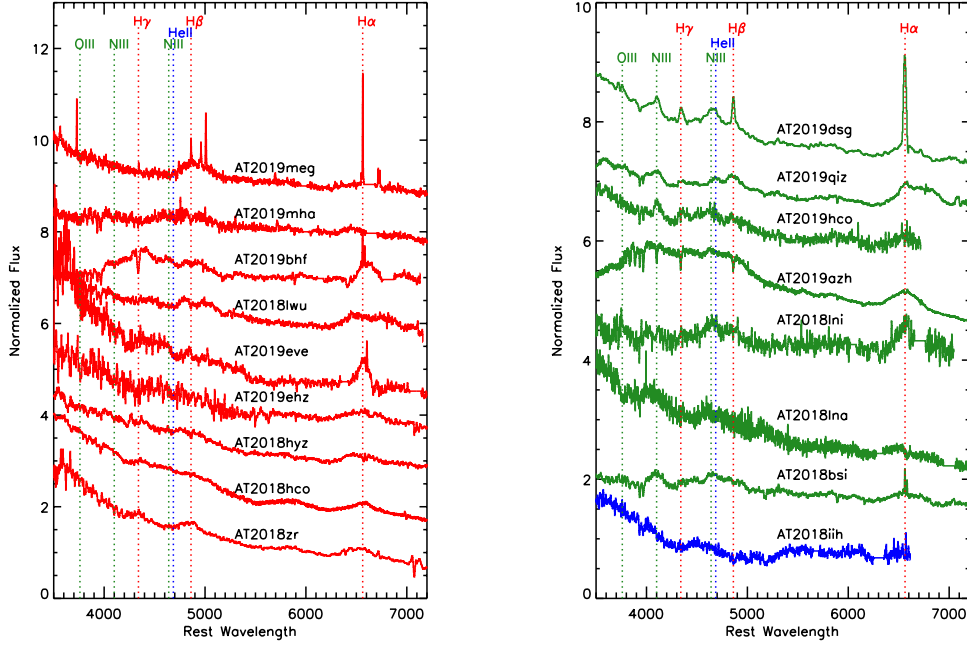


FIGURE 1.13: Spectroscopic classification of 17 TDEs, following the three spectral classes proposed by van Velzen et al. (2020a). *Left:* TDEs with Balmer line features only (TDE-H, in red). *Right:* TDEs with Balmer and He II, and N III and O III Bowen fluorescence features (TDE-H+He, in green) and TDEs with only He II (TDE-He, in blue). The spectra have not been host galaxy subtracted and have been normalized to arbitrary units. Figure from van Velzen et al. (2020a).

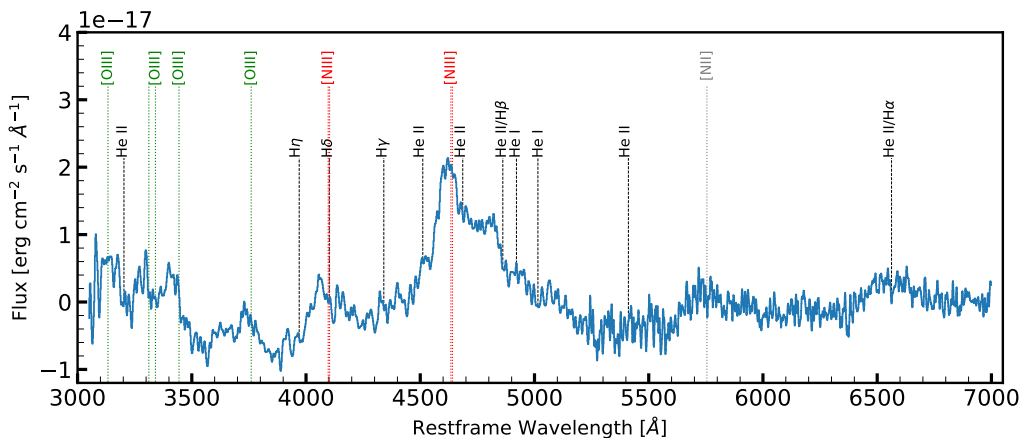


FIGURE 1.14: The optical spectrum of the TDE iPTF15af (Blagorodnova et al., 2019). Bowen fluorescence lines are marked in red and green, depending on the atomic species.

Figure from Blagorodnova et al. (2019).

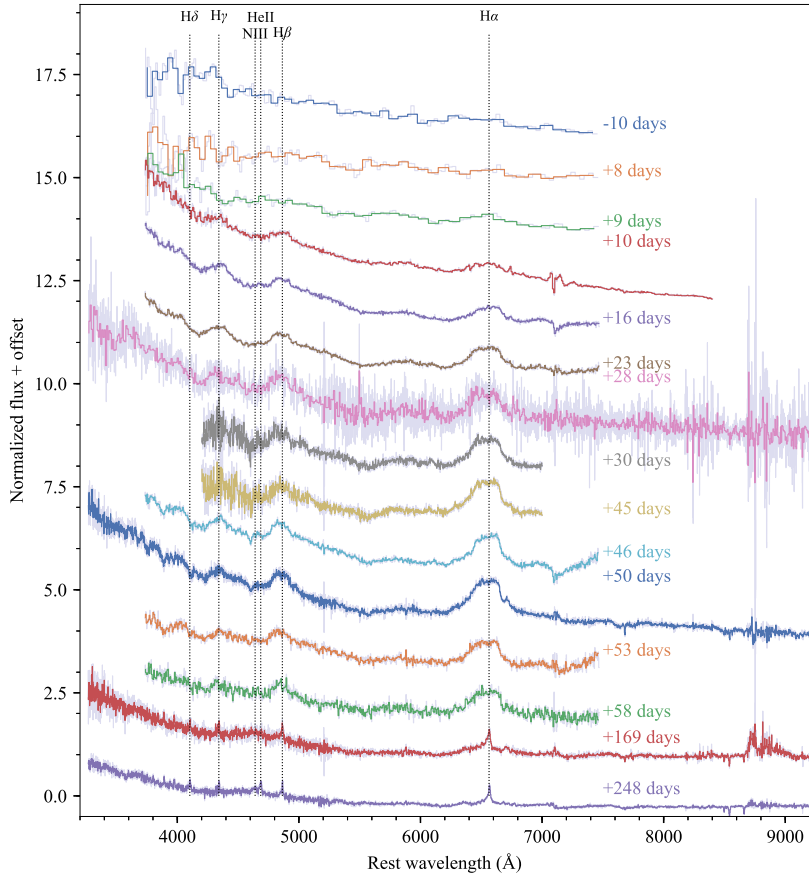


FIGURE 1.15: Optical host-subtracted spectra of AT2018zr for multiple epochs. The spectra have been smoothed. The original unsmoothed spectra are plotted underneath in grey for each observations. The corresponding post-flare phase for each observation is labelled on the right of the figure. At early times, the spectra are dominated by broad H α , H β and He II emission lines, which become significantly narrower and weaker in the late time spectra. Figure from Hung et al. (2019).

is possible to form hydrogen-free spectra from the disruption of a main-sequence star (Guillochon et al., 2014; Roth et al., 2016). In these models, line formation takes place within an optically thick envelope and the strength (or weakness) of hydrogen features in the spectra are determined by the physical conditions, and radiative reprocessing properties, of the line-forming outflow.

It is commonly observed that the emission lines in optical TDEs evolve with time, beginning their transient life as broad and bright features (with FWHM $\sim 10^4$ km s $^{-1}$), before becoming significantly narrower and dimmer on a time scale of several months (e.g. Brown et al., 2017a; Hung et al., 2019). As an example, the evolution of H α , H β and He II is shown for AT2018zr (Hung et al., 2019) in Figure 1.15. In this TDE, the

emission lines are very broad in the early spectra, at $\Delta t \sim 25$ days, before becoming significantly narrower somewhere between 2 - 5 months post-flare. As mentioned in the previous section, this evolution was not exactly expected, and the evolving width of the lines could be due to line formation in an optically thick outflow, where line widths are set by the electron scattering optical depth, rather than by the kinematics of the outflowing material (Roth & Kasen, 2018).

1.4.5.3 Ultraviolet

Even though an increasing number of optically and UV-bright TDEs are being detected, the sample of TDEs with UV spectroscopic observations is much smaller than the sample of TDEs with optical data. At the time of writing, only *eight* objects belong to the rather exclusive group of TDEs for which UV spectroscopic data is available. In Figure 1.16, I show the NUV spectra for four of these TDEs, alongside a composite spectrum of a low ionization broad absorption line quasar (LoBALQSOs), for comparison.

In all of the spectra in Figure 1.16, the NUV continuum can be modelled rather well by a single temperature blackbody. However, the same blackbody, whilst fitting the general *shape* of the SED, often underpredicts the luminosity in the FUV region. The defining spectral features are absorption lines in atomic species such as Ly α , C IV, N V and Si IV; labelled at the top in Figure 1.16. The absorption is typically rather broad (FWHM $\sim 10^3 - 10^4$ km s $^{-1}$) and is usually significantly blueshifted by $v \sim 10^3 - 10^4$ km s $^{-1}$. But, as is obviously the case looking at Figure 1.16, not all TDEs display BALs at similar stages of their outburst evolution. In particular, Figure 1.16 shows that some TDEs, such as ASSASSN-14li, instead exhibit the same atomic species predominately in emission.

This dichotomy of BELs vs. BALs is reminiscent of Type I QSOs. Most QSOs exhibit BELs in the UV, but, as mentioned previously, a small subset ($\simeq 20\%$) exhibit BALs instead (Weymann et al., 1991; Knigge et al., 2008; Dai et al., 2008; Allen et al., 2011). The similarity between QSO and TDEs does not end there, either, as the spectra of TDEs bear a striking similarity to QSO spectra (c.f. the LoBALQSO spectrum in Figure 1.16). There are differences between the two objects, though. First of all, the continua in TDEs are significantly bluer than those in QSO. Also, TDEs tend to lack the low ionization lines, such as Mg II $\lambda 2796, 2803$, which are common in QSOs. As Cenko et al. (2016) suggests, this could be caused due to photo-ionization by a hard continuum source, and the lack of low ionization lines could be a transient feature since the hard continuum will one day fade away. Lastly, TDEs also tend to display strong N III] $\lambda 1750$ emission, a feature which is rarely observed in QSOs (Batra & Baldwin, 2014). This could be an abundance effect associated with the disruption of a CNO processed star (Kochanek, 2016); this is discussed in Chapter 3.

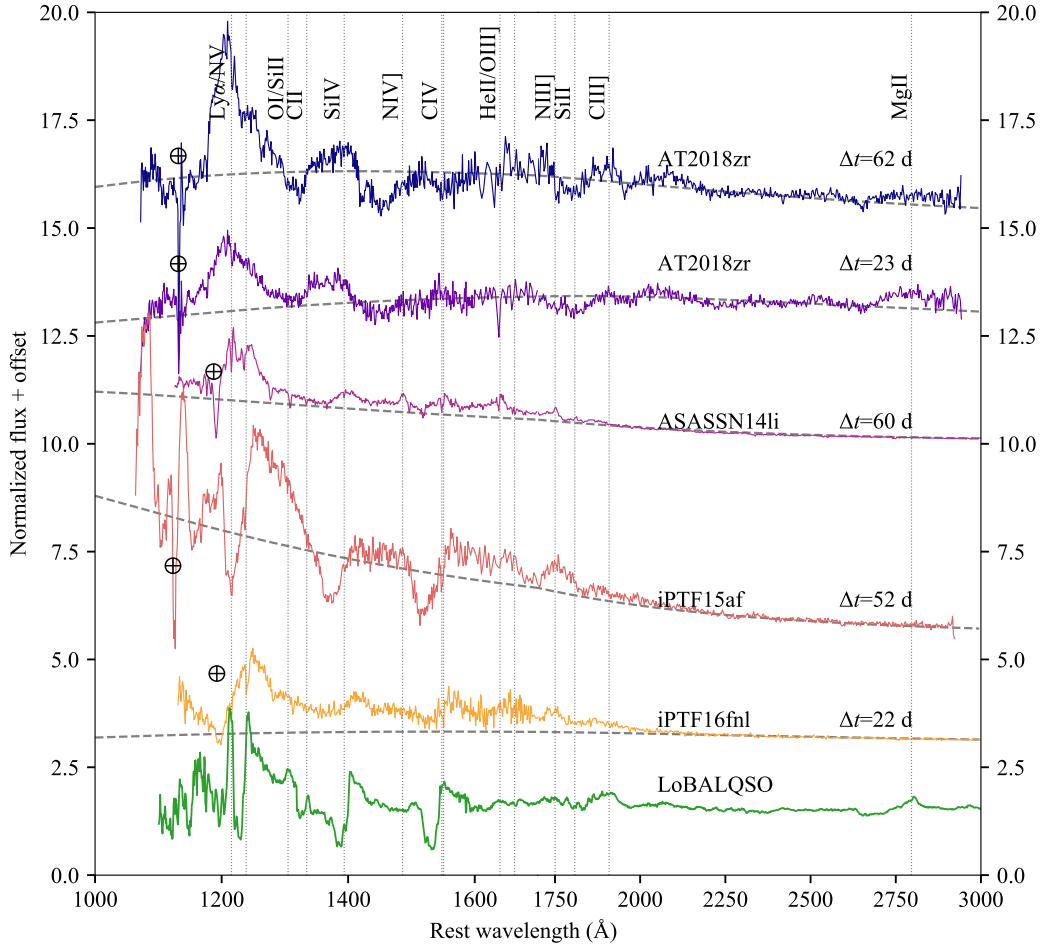


FIGURE 1.16: UV spectroscopic observations for four TDEs and a composite spectrum for a LoBALQSO (taken from Brotherton et al., 2001). The grey dashed lines mark the approximate continuum for each object, given by a blackbody of the appropriate temperature. The spectra, and the continua fits have been normalized to arbitrary units. Figure from Hung et al. (2019).

In QSOs, at least, one way to explain the the dichotomy of BELs vs. BALs is by invoking line formation in an accretion disc wind (Murray et al., 1995; Higginbottom et al., 2013; Matthews et al., 2016, 2017). In this scenario, BALs are observed when the observers line of sight of the continuum source falls within the wind cone, and consequently looks through the disc wind. Photons are scattered out of the line of sight of the observer, by the wind, and absorption lines are produced. BELs, on the other hand, are preferentially observed for inclinations which are not obstructed by the disc wind, hence the observer is able to see the emission from the dense base of the wind, where BELs are produced via collisional excitation. I explore this exact same scenario in the context of TDEs later in Chapter 3.

The sample of TDEs with UV spectra is already small, but the sample of TDEs with UV spectra for *multiple* epochs is even smaller. At the time of writing this thesis, only a meagre sample of *three* TDEs have a sequence of UV spectra. One of these TDEs

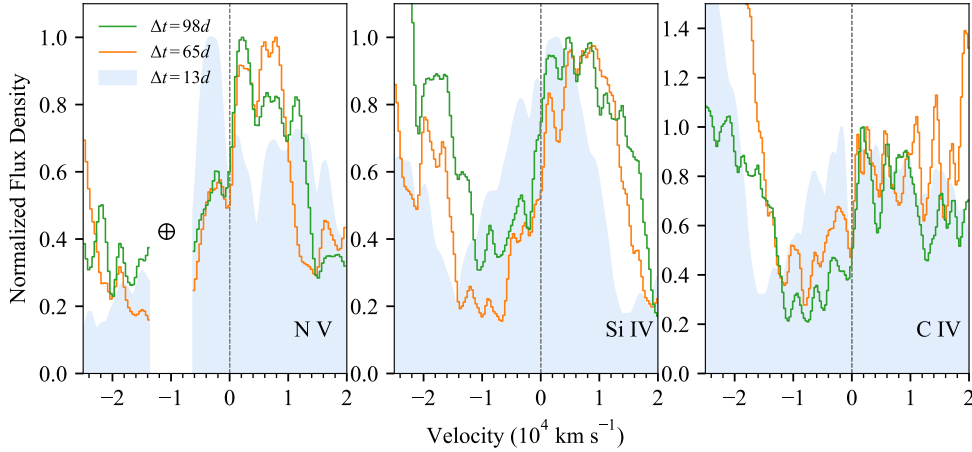


FIGURE 1.17: Three epochs of UV spectra for three high ionization UV absorption lines, labelled in the bottom right of each sub-panel, for AT2019qiz (Nicholl et al., 2020; Hung et al., 2020). The spectrum for the first epoch, $\Delta T = 13$ days, is shaded in blue, whilst the other spectra are represented by solid orange and green lines. The absorption troughs are shifted to lower velocities at later epochs. Figure from Hung et al. (2020).

is AT2019qiz (Nicholl et al., 2020; Hung et al., 2020), and the evolution of three UV absorption lines is shown in Figure 1.17. Comparing the evolution of the three TDEs with a sequence of spectra is quite difficult, as so far, it seems that each TDE has followed its own UV evolutionary path. For example, AT2018zr (Hung et al., 2019) began its UV life displaying prominent BALs before evolving into a BEL system (and so the BAL vs. BEL dichotomy may also be an “evolutionary” effect), whereas AT2019qiz has, so far at least, kept its BALs. This is one of the main reasons why a larger sample of TDEs with multiple epochs of UV spectra is required, as the UV evolution of these objects is still largely shrouded in mystery. Focusing our interest on AT2019qiz, however, Figure 1.17 shows how its high ionization UV absorption lines evolve with time. The most obvious evolutionary change is that the velocity shift of the absorption troughs decrease as time progresses. If these lines are formed in an expanding outflow, then this change in velocity shift could be explained by a decrease in outflow velocity.

1.4.6 Photometric properties

The light curves of TDEs, i.e. the brightness as a function of time, typically reach a peak luminosity (usually $L \sim 10^{43} - 10^{45}$ erg s $^{-1}$) on a timescale of a few weeks to a few months. Rather naturally, the brightness of the TDE will fade following the waning fallback rate of the debris stream. Observations of TDEs actually show that the late decline of TDE brightness broadly follows the general shape of the theoretical $t^{-5/3}$ fallback rate (Equation 1.27), as shown for a selection of TDEs in Figure 1.18. However, at early times, the decline in the brightness of TDEs is often shallower than this fiducial fallback rate. This is because much of the light in the early stages of a TDE

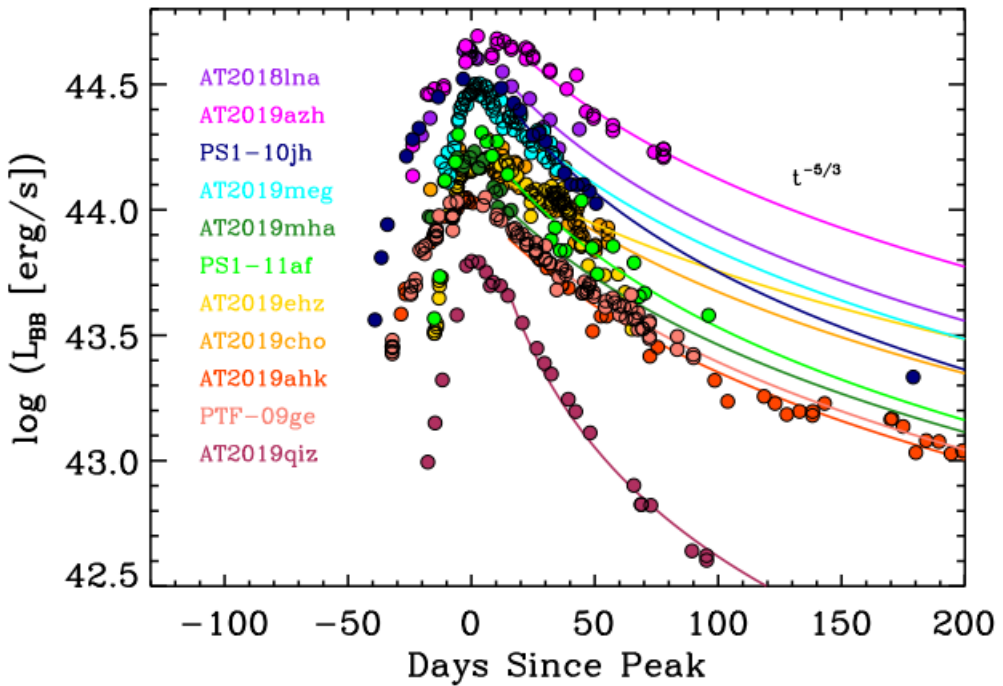


FIGURE 1.18: A compilation of bolometric luminosity curves of TDEs. The light curves are constructed by scaling the r -band light curve by the peak bolometric luminosity determined from a blackbody fit to the optical and UV photometry reported by [van Velzen et al. \(2020a\)](#) assuming no evolution in temperature. Also shown for each TDE is a $t^{-5/3}$ power law decline, fitting the curves after peak. Figure from [Gezari \(2021\)](#).

is thermal radiation from an accretion disc, which cools much more gradually. Light curves therefore only really follow the so-called fiducial power law at late times ([Lodato et al., 2009](#)). Interestingly, the rise time appears to not have any correlation to the decay time of the light curve ([van Velzen et al., 2020a](#)). If both the rise and fall timescales are related to the fallback of material, then one would expect them to have some correlation. [van Velzen et al. \(2020a\)](#) conclude that the rise time is not related to the fallback time, but is probably related to the photon diffusion time through the envelope of material.

The peak luminosity, as well as the rise and decay times, vary between TDEs, depending on a number of parameters. However, one thing which does not seem to change between TDEs is the lack of cooling implied by the inferred post-peak photospheric temperatures. Figure 1.19 shows how the temperature for 17 TDEs evolves with time. It is interesting to note that the temperature in some TDEs appear to stay constant, while in others it shows a relatively small, but still significant, increase. This lack of cooling is one way to distinguish a TDE from a supernova based on photometric properties alone.

Following from the optical classification of TDEs, [van Velzen et al. \(2020a\)](#) found correlations between the spectral type and the optical/UV photosphere size and temperature. This is shown in Figure 1.20 which plots the inferred luminosity below 228 Å (based on the photospheric temperature of the object) against the radius of the photosphere.

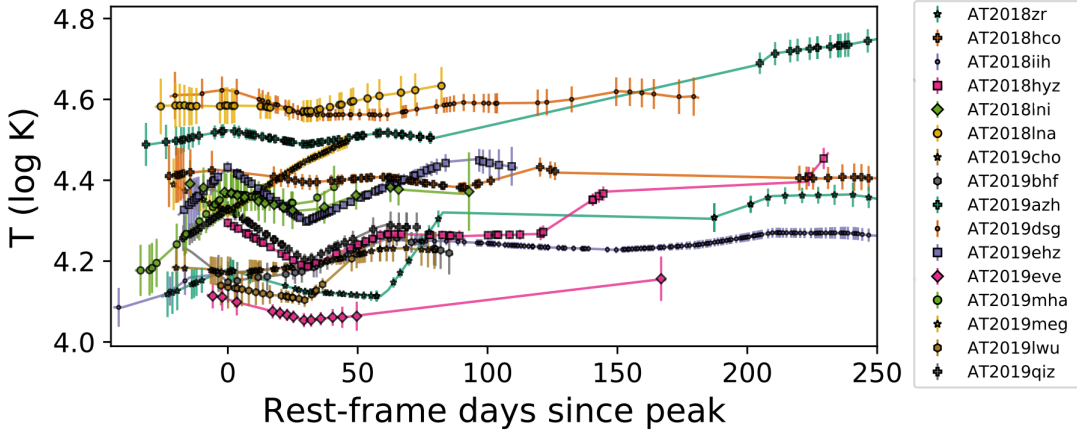


FIGURE 1.19: The rest-frame blackbody temperature for the sample of 17 TDEs presented by van Velzen et al. (2020a). Most of the TDEs show a relatively small, but significant, increase in temperature after peak brightness. Figure adapted from van Velzen et al. (2020a).

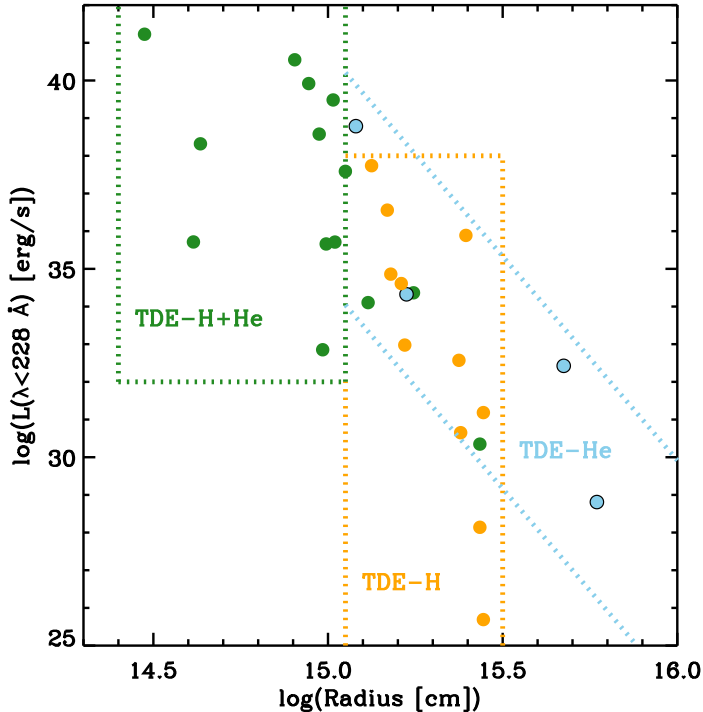


FIGURE 1.20: The blackbody luminosity below 228 Å (the helium ionizing SED) plotted against the inferred radius of the optical/UV photosphere for a sample of 28 TDEs. The points are colour-coded by their optical spectra class as labelled in the figure. It seems that TDE-H+He (TDE-H+He) events appear to occur with bright UV flares and compact photospheres, whereas TDE-H events preferentially exhibit smaller photospheres. TDE-He objects, on the other hand, appear to exist over a large range of this parameter space. Figure from Gezari (2021).

The important take away from this figure is that TDE-H+He events (labelled as TDE-H+He) appear to form compact and hot photospheres and that the same events have a longer rise time to peak light. These properties are not so surprising. Dense and hot photospheres are ideal environments for triggering the Bowen fluorescence mechanism and are also associated with longer diffusion time scales, therefore naturally produce a slower rise to peak luminosity.

The light curves of TDEs also store a wealth of information about them, and by using tools such as MOSFiT (Guillochon et al., 2018) we can indirectly measure the mass of the disrupting SMBH and the disrupted star. For this approach, we need to make a number of assumptions. First, we have to assume that the shape and brightness of the light curve is related intimately to the fallback of material (e.g. Mockler et al., 2019) and that the fallback is related to the properties of the black hole and the disrupted star (e.g. that the fallback time scales as $t_{\text{fb}} \propto M_{\text{BH}}^{1/2} M_{\star}^{-1} R_{\star}^{3/2}$). We also must assume that the debris stream is rapidly and efficiently circularized and that the soft X-ray emission from the disc is reprocessed to longer optical/UV wavelengths. With all these assumptions, a model fit to the observed light curve can provide an estimate of the mass of the black hole. Additionally, in some cases the disrupted star can affect the fallback of material just enough that it is also possible to measure the mass of the star.

1.4.7 Outflows in tidal disruption events

Given their extreme luminosities, TDEs are expected to generate significant mass loss in the form of radiation-driven winds (e.g. Poutanen et al., 2007)⁴, and outflows are, in-fact, ubiquitous in accreting systems on all scales. As I have already discussed, some of the most compelling evidence for the existence of an outflow are blueshifted BALs associated with strong UV resonance transitions. Recently, blueshifted BALs have been found in the UV spectra of iPTF15af (Blagorodnova et al., 2019), iPTF16fnl (Blagorodnova et al., 2017) and AT2018zr (Hung et al., 2019) at around $\Delta t \approx 50$ days post flare. In another TDE, ASASSN14li (Cenko et al., 2016), X-ray observations have provided evidence for more highly ionized outflowing gas (Miller et al., 2015; Kara et al., 2018). The discovery of these BALs provides unambiguous observational evidence for the presence of fast, powerful outflows in TDEs. Additionally, there is other evidence for powerful sub-relativistic outflows from blueshifted BELs (Arcavi et al., 2014; Roth & Kasen, 2018; Hung et al., 2019; Nicholl et al., 2020)

Figure 1.21 shows the UV spectrum of iPTF15af at $\Delta t = 52$ days post peak (Blagorodnova et al., 2019). The spectrum is characterized by strong blueshifted BALs in C IV, Si IV, N V and Ly α ; as labelled in the plot itself. Discussed already in Section 1.3.2, broad

⁴Although it could also be possible for an outflow to be launched hydromagnetically (e.g. Blandford & Payne, 1982).

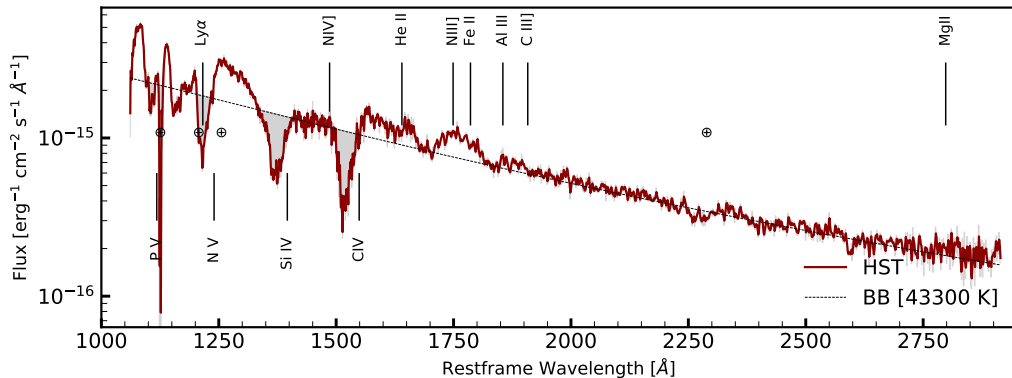


FIGURE 1.21: A rest-frame UV spectrum of iPTF15af at $\Delta t = 52$ days after discovery. Marked by the dashed black line is a best-fit blackbody spectrum for the FUV. The spectrum has been corrected for extinction and important absorption and emission lines have been labelled. This spectrum looks strikingly similar to that of a BALQSO and features broad and blueshifted absorption lines, the smoking gun signatures of outflowing material. Figure from Blagorodnova et al. (2019).

BALs in these transitions are smoking gun signatures of mildly ionized outflowing material, and the spectrum is strikingly similar to that of a BALQSO, where line formation in an accretion disc wind is usually invoked to explain these absorption features (e.g. Murray et al., 1995; Higginbottom et al., 2013; Matthews et al., 2016, 2017). In this TDE, Blagorodnova et al. (2019) measures a typical line width of $v_{\text{width}} \sim 10^4 \text{ km s}^{-1}$ and a velocity blueshift of $v_{\text{shift}} \sim 5000 \text{ km s}^{-1}$ for the absorption lines, quite similar to the inferred outflow velocities in BALQSOs.

Outflows are already a key ingredient in a number TDE models (see, e.g. Strubbe & Quataert, 2009; Lodato & Rossi, 2011; Metzger & Stone, 2016; Dai et al., 2018; Curd & Narayan, 2019). However, the physical properties of these winds remain poorly understood, even though their importance is widely acknowledged. For example, Miller et al. (2015) suggests that the slow temperature evolution and low effective temperatures measured in some TDEs may be due to a wind emanating from the accretion disc, similar to the framework proposed by Laor & Davis (2014) for AGN. In this picture, an accretion disc wind is responsible for reducing the accretion rate in the inner disc region and regulating the temperature of thermal emission. Alternatively, reprocessing of high-frequency photons by an optically thick outflow, such as an accretion disc wind, could provide an explanation for the optical and UV emission in TDEs (the so-called “optical-excess” problem: Loeb & Ulmer, 1997; Guillochon et al., 2014; Metzger & Stone, 2016; Roth et al., 2016; Roth & Kasen, 2018). In this reprocessing scenario, which is discussed in greater detail later in Section 1.4.8, high-frequency photons, generated at the inner edge of an accretion disc, are absorbed by the optically thick outflow and are re-radiated at lower optical and UV frequencies.

Quite recently, luminous *non-thermal* (synchrotron) radio emission was discovered in a sub-set of TDEs, which could be a signature of collimated radio jets. As of writing, three

TDEs have so far been observed to produce such signatures: Swift J1644+57 (Bloom et al., 2011); Swift J2058+05 (Cenko et al., 2012), and Swift J1112-82 (Brown et al., 2015). In principle, radio emission could also arise due to external shocks driven by the interaction of a non-relativistic outflow (Alexander et al., 2016) or between unbound stellar debris streams (Krolik et al., 2016). However, a jet origin is favoured by the observed correlation between the X-ray and radio light curves where $L_{\text{radio}} \propto L_X^2$, which suggests that accretion and jet power are (linearly) coupled (Pasham & Velzen, 2018).

1.4.8 Reprocessing

Reprocessing is a core component in many modern interpretations of TDE emission and is often invoked as an explanation for the large sub-set of optically bright (but X-ray weak) TDEs (Strubbe & Quataert, 2009; Metzger & Stone, 2016; Roth et al., 2016; Roth & Kasen, 2018; Lu & Bonnerot, 2019; Piro & Lu, 2020; Bonnerot et al., 2021). As briefly discussed earlier in this chapter (and later on in Chapter 4), the prevalence of optically bright, but X-ray weak emission, in some TDEs is inconsistent with simple TDE models, e.g. ones in which the observed emission is produced by a bare accretion disc. One way to account for this apparent optical excess is to invoke reprocessing. At the most basic level, “reprocessing” here simply refers to any mechanism that takes a distribution of high-frequency photons as input and produces a new distribution of typically lower-frequency photons as output.

Generally speaking, reprocessing comes in three distinct flavours: 1) atomic reprocessing; 2) bulk scatter reprocessing; and, 3) Comptonization. In the following sections, I will briefly describe these in turn.

1.4.8.1 Atomic/absorption

The first type of reprocessing to discuss is atomic/absorption reprocessing, where high frequency photons are absorbed and re-emitted at lower frequencies. This type of reprocessing has become a key part of many modern interpretations of TDE emission (Roth et al., 2016; Roth & Kasen, 2018; Dai et al., 2018, to name just a few). The key idea here is that a “reprocessing envelope” absorbs the X-rays produced (from the inner accretion disc) and re-radiates them at lower frequencies. This naturally produces the bright optical/FUV emission characteristic of a large sub-set of TDEs and accounts for the weak X-ray emission (since this is absorbed). This type of reprocessing can, in practice, happen with any atomic absorption process, such as photo-ionization or free-free absorption. Typically, then, the photons are re-remitted due to recombination or free-free emission. This type of reprocessing can only really occur in optically thick outflows, which are only mildly ionized. If the outflow is too highly ionized or if the density is too low to provide

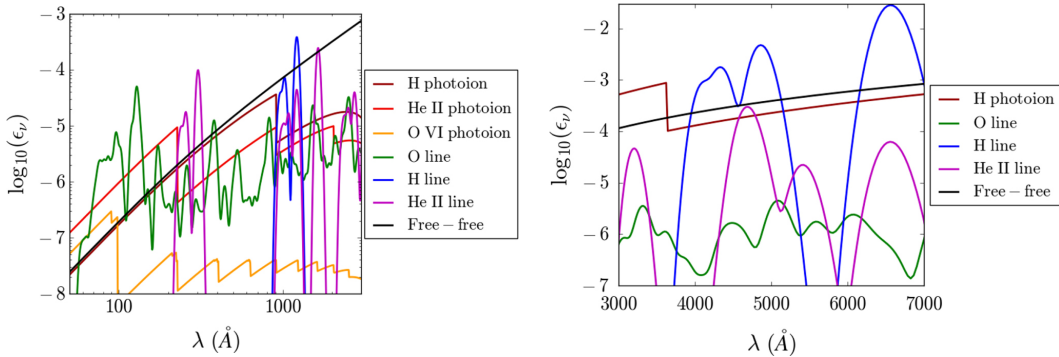


FIGURE 1.22: The ratios of various absorptive opacities (labelled in the legend) as a function of wavelength, as calculated from non-LTE radiation transport calculations for a physically motivated spherical outflow using SEDONA (Kasen et al., 2006; Roth, 2016). *Left:* soft X-ray and EUV. *Right:* optical. Figures from Roth et al. (2016).

significant opacity, then atomic absorption, and hence reprocessing via this mechanism, becomes inefficient.

So what are the dominant reprocessing mechanisms in this setting? Detailed radiative transfer calculations carried out by Roth et al. (2016), shown in Figure 1.22, show in a physically motivated, but still spherical model, the dominant absorption processes at soft X-ray and EUV wavelengths are free-free absorption, as well as photo-ionization of hydrogen and singly ionized helium. Additionally, the same processes are also responsible for efficiently reprocessing the X-ray radiation in the radiative transfer models of a super-Eddington accretion flow by Dai et al. (2018). In this case, the majority of the reprocessing responsible for producing an optically bright spectrum comes from photo-ionization of He II and O VI in the dense disc atmosphere.

1.4.8.2 Bulk scatter reprocessing

In an optically thick outflow photons are likely to become trapped. In their journey to escape, they will undergo multiple scattering events with electrons from different velocity regions of the outflow. This electron scattering leads to a decrease of their energy, and modifies the spectrum emerging from the outflow. This process has been shown to form redshifted emission and absorption lines (Titarchuk & Shrader, 2005; Laurent & Titarchuk, 2007), even sometimes with asymmetric red wings (Auer & van Blerkom, 1972; Roth & Kasen, 2018), and to modify the continuum as well (Roth & Kasen, 2018). The basic picture, of what I shall refer to as “bulk scatter reprocessing”, is depicted in Figure 1.23, which hopefully presents a simple schematic of a diverging outflow’s effect on a photon.

Bulk scatter reprocessing is a combination of two main effects: 1) the Doppler shift when boosting between the co-moving frame of the outflow and the observer frame; and

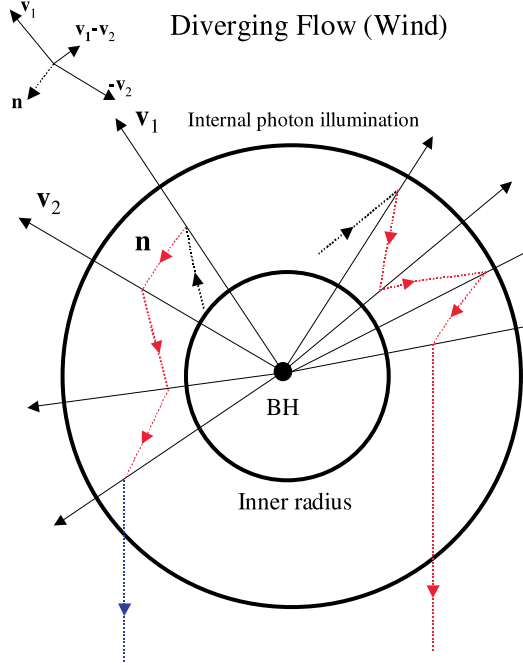


FIGURE 1.23: A diagram showing a schematic for a expanding spherical wind geometry originating from an inner radius. A photon emitted from the inner boundary is scattered by an electron with velocity \mathbf{v}_1 and is received by an electron moving with velocity \mathbf{v}_2 . The change in frequency between events is $\nu_2 = \nu_1[1 + (\mathbf{v}_1 - \mathbf{v}_2) \cdot \mathbf{n}/c]$. In a expanding (diverging) flow, $(\mathbf{v}_1 - \mathbf{v}_2) \cdot \mathbf{n}/c < 0$ and photons are redshifted. The colour of the dashed lines show the relative frequency shift in the frame of the observer. Figure adapted from Titarchuk & Shrader (2005); Laurent & Titarchuk (2007).

2) the post-scatter recoil of the electron⁵. To follow from Figure 1.23, a photon which originally scatters with an electron moving with velocity \mathbf{v}_1 may scatter again (given the flow is optically thick) with another electron with velocity \mathbf{v}_2 . At this point, the photon's frequency will be,

$$\nu_2 = \nu_1[1 + (\mathbf{v}_1 - \mathbf{v}_2) \cdot \mathbf{n}/c], \quad (1.32)$$

where \mathbf{n} is the unit vector along the path of the photon at the second scattering location. In a divergent outflow ($\nabla \cdot V > 0$, where V is the outflow speed), $(\mathbf{v}_1 - \mathbf{v}_2) \cdot \mathbf{n}/c < 0$. Therefore, in such outflows photons are successively redshifted at each scattering interaction by just the Doppler effect. Photon's can also experience a change in energy due to the electron recoil, i.e. inelastic scattering. This type of reprocessing is a natural consequence of the Doppler effect *and* Compton scattering in the presence of multiple scattering events, and does not require any particularly fine-tuned geometric arrangement or velocity profile (Auer & van Blerkom, 1972; Titarchuk & Shrader, 2005; Laurent & Titarchuk, 2007). In a converging flow ($\nabla \cdot V < 0$), the opposite happens, and photons

⁵This also can also provide some additional kick to the outflow, acting as a, albeit probably small, driving mechanism.

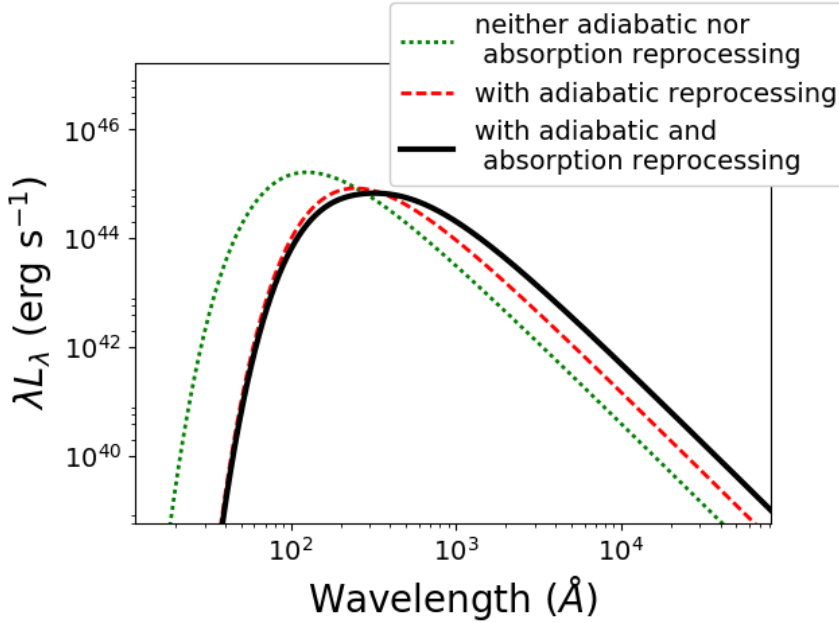


FIGURE 1.24: Synthetic spectra generated from a homologous outflow, showing how reprocessing affects the spectral energy distribution. The dashed green spectrum shows the thermal emission from a $T_{\text{bb}} = 2.95 \times 10^5$ K blackbody, whilst the dashed red line shows SED reprocessed by bulk scatter reprocessing. The solid black spectrum shows the SED when it has been reprocessed by absorption processes and bulk scatter reprocessing. Figure from Roth & Kasen (2018).

are blueshifted as $(\mathbf{v}_1 - \mathbf{v}_2) \cdot \mathbf{n}/c > 0$ (Titarchuk & Shrader, 2005; Laurent & Titarchuk, 2007).

The shift in photon energy is directly related to how many times a photon will scatter. This is shown by Laurent & Titarchuk (2007) who show that the mean energy change per scattering even is given by,

$$\Delta E \approx -\frac{\beta f}{2\tau} E_0 \sqrt{1 - (f/2\tau)^2}, \quad (1.33)$$

where E_0 is the original photon energy, $\beta = V/c$, V is the outflow speed, f is some factor which is about 1, and τ is the optical depth of the outflow. This formula directly relates the optical depth to the change in energy.

Recent simulations by Roth & Kasen (2018) have quantified the effect of their so-called *adiabatic reprocessing* (a.k.a. bulk scatter reprocessing) in the context of a spherical TDE outflow. The results of these simulations are shown in Figure 1.24. In these models, photons are injected from an inner boundary with a frequency distribution governed by a single temperature blackbody. In the absence of any reprocessing mechanisms, what comes out is what is put in: a single temperature blackbody. However, when reprocessing due to bulk scattering is included, the SED of the escaping photons (red dashed curve) is no longer a single temperature blackbody. Instead, the SED takes the form of a less luminous *stretched* blackbody and extends to lower photon energies,

due to being redshifted. Roth & Kasen (2018) show that the mean shift of the photon energies can be estimated by calculating the integral of the velocity divergence, $dW/dt = \int P_{\text{rad}}(\nabla \cdot \mathbf{v}) dV$. When atomic (absorption) reprocessing is also included, the SED at lower photon energies is further enhanced.

1.4.8.3 Comptonization

Compton scattering is the inelastic scattering of a photon by a charged particle, usually an electron. Upon impact, energy from the photon is transferred to the recoiling electron and the photons loses energy and is shifted to a longer wavelength. But instead, if the electron has significant kinetic energy in comparison to the scattering photon, then the inverse occurs. That is that the photon *gains* energy, in a process known as inverse-Compton scattering.

In many accreting black hole systems, inverse Compton scattering of soft photons by hot, thermal electrons results in photons being “up-scattered” to harder, X-ray frequencies. Such a process has been found to be important in low-mass X-ray binaries (White et al., 1988) but is also thought to be important in TDEs. For example, Bloom et al. (2011) suggests the hard X-ray emission in Swift J1644 is created by photons which are Compton up-scattered by relativistic electrons in a relativistic jet. From a theoretical stand point, simulations have also shown that inverse Compton scattering in a TDE outflow results in bright and beamed X-ray emission (Dai et al., 2018; Curd & Narayan, 2019).

But it is also important to consider the role of direct Compton scattering on shaping the SED, at least at soft X-ray and UV wavelengths. This involves the transfer of energy from photons to electrons. So if photons Compton scatter a significant amount of times, then we expect those photons to have their energies continuously shifted toward longer wavelengths, creating a softer spectrum. Dai et al. (2018) found this exact condition in their simulations of a TDE. The majority of soft X-ray photons produced in the optically thick disc atmosphere, close to the SMBH, were redshifted by repeated Compton scattering.

1.4.9 Unifying X-ray and optically bright TDEs

As I have already mentioned several times, TDEs with optically bright components and weak X-ray components are inconsistent with the simplest TDE models, in which we directly observe thermal X-ray emission from a hot and compact accretion disc. However, recent state-of-the-art models fare much better. For example, Dai et al. (2018) performed general relativistic radiation magnetohydrodynamic simulations of the super-Eddington accretion phase, which TDEs with $M_{\text{BH}} \lesssim 10^7 M_{\odot}$ are expected to undergo in their infancy. Based on their results, they propose a unified model for TDEs that explains the

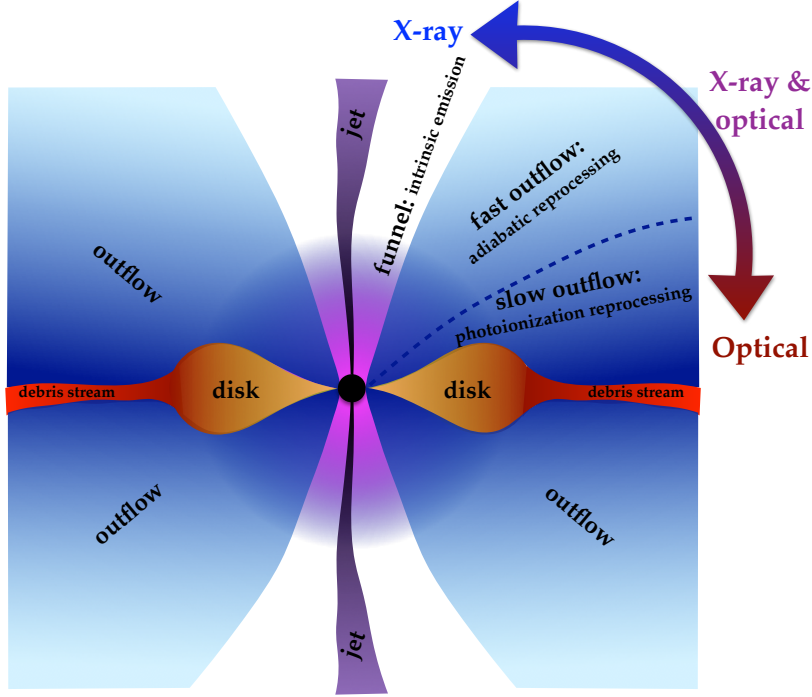


FIGURE 1.25: A schematic picture showing the viewing-angle dependence for the observed emission from a super-Eddington TDE accretion disc. The emission from the inner disc is reprocessed by the optically thick outflows and outer disc. Only when an observer is looking into the optically thin funnel is the inner disc exposed, which can reveal strong, beamed X-ray and EUV radiation. Otherwise, the disc X-ray emission is reprocessed into optical/NUV emission via photo-ionization or bulk scatter reprocessing. Figure from Dai et al. (2018).

relative X-ray brightness as an inclination effect. This model is shown in Figure 1.25. The key takeaway is that observers who look at a TDE from a polar inclination will see an X-ray bright TDE, while observers who instead look closer to the disc plane will see an optically bright TDE. This inclination dependence results entirely from the angle-dependent properties of the outflow that is driven from the system.

Reprocessing of disc radiation by this outflow is thus a key component in this model. More specifically, observers looking along the disc plane look at (and through) a dense and slow outflow that obstructs their direct view of the central engine. Along these sight lines, the outflow reprocesses the accretion disc continuum via absorption by photo-ionization of He II and O VI, which re-radiates photons at longer wavelengths via recombination. At intermediate inclinations, the outflow is faster and diffuse, and the outflowing material is characterized by a higher ionization state. In this part of the outflow, photons are mainly bulk scatter reprocessed due to repeated electron scattering. This causes the SED to be redshifted toward longer, optical wavelengths. Finally, polar viewing angles cut through a largely evacuated region in which there is no outflow at all. TDEs viewed along these orientations would appear X-ray bright, since the inner edge of the accretion disc is now exposed.

1.5 The aims of this thesis

The main aim of this thesis is to explore how optically thick winds, launched from an accretion disc, impact the observable features of TDEs at optical and UV wavelengths. To do this, I conduct radiative transfer simulations with the state-of-the-art Monte Carlo radiative transfer and ionization software **PYTHON**, modelling the physical conditions of the outflows and using that to predict the emergent spectra of these events. The main result is that line formation in an optically thick outflow can account for the BAL vs. BEL dichotomy seen in the diverse UV spectra of TDEs, and that reprocessing of thermal disc emission can form the distinctive optical spectra and continua for TDEs in the growing population of optically bright, but X-ray weak, TDEs.

This research is split into three main directions of work. In the first and second, I explore the outflows associated with the sub-Eddington phase of accretion. I first explore the UV line spectra and how line formation in an accretion disc wind could explain the diverse UV spectra of TDEs. Then, I extend my research to longer wavelengths and examine how reprocessing in an optically thick accretion disc wind could produce the distinctive optical/UV continuum and line spectra of TDEs. In the final research direction, I switch my focus to the super-Eddington accretion phase. Here, I model the emergent spectrum for an outflow derived from a realistic hydrodynamic model of the super-Eddington phase. In addition to predicting the spectrum, I apply the same techniques used in the previous sub-Eddington work and use them to understand how reprocessing, by the outflow, matters in the super-Eddington regime.

The thesis is structured as follows. In the next chapter, I introduce the core radiative transfer and numerical techniques crucial to the research I have done. Then, in the next three chapters, I present the methodology and results of my research, discussing how outflows shape how we perceive TDEs. Finally, in Chapter 6 I summarize my key findings and suggest promising future research directions.

In addition to the core of this thesis, I have included an appendix which outlines four methods to accelerate radiation transport in optically thick media. Accelerating and dealing with optically thick photon transport and the numerical difficulties therein, is quite important when modelling optically thick (TDE) outflows. A number of acceleration techniques were explored early on, but were either unfortunately not applicable to **PYTHON**, or presented computational and numerical complications upon implementation, with no simple solution. Even so, the numerical stability and efficiency of **PYTHON** has still been vastly improved so that this research could be completed. For completeness sake, a description of the most promising techniques has been included in Appendix A.

Chapter 2

Monte Carlo Radiative Transfer and Ionization

Life is really simple, but we insist on making it complicated.

Confucius

In this chapter, I outline the key physics and concepts underpinning the numerical techniques used for the work presented in this thesis. The first section outlines the fundamentals of radiative transfer, and is followed by an introduction to the Monte Carlo method. Finally, in the last section, I introduce the software used in this thesis, PYTHON, and describe its operation, as well as some of its relevant quirks and features.

2.1 Fundamentals of radiative transfer

The term “radiative transfer” refers to the transport of energy via electromagnetic radiation. The propagation of a beam of light through a medium is affected by absorption, emission and scattering processes, all of which can change the intensity of said beam. In the following section, the key fundamental processes and quantities of radiative transfer are defined.

The following section is based on content from the textbooks Mihalas (1978); Bowers & Deeming (1984); Carroll & Ostlie (1996); Rybicki & Lightman (1985).

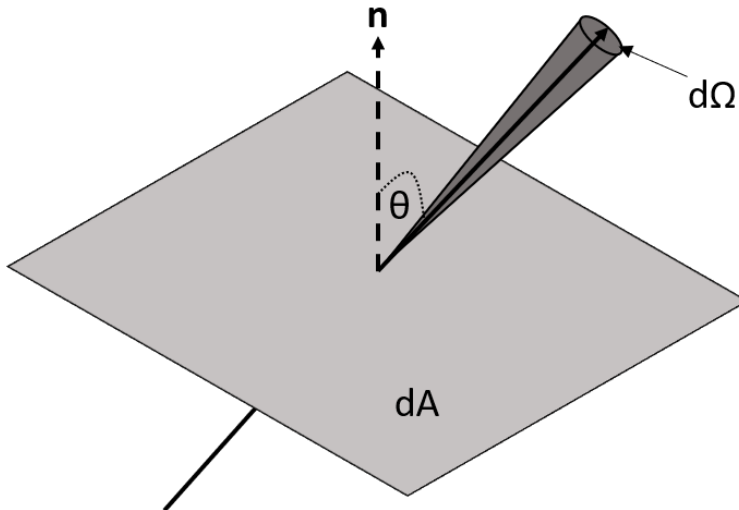


FIGURE 2.1: A cartoon of a beam of light passing through a medium of area dA , at an angle θ into a cone of solid angle $d\Omega$. The angle θ is measured from the direction of the normal of the surface.

2.1.1 The radiation field

Consider a beam of light emerging from a surface travelling at an angle θ to the normal of that surface (as shown in Figure 2.1). Over a specific frequency and time interval, we can define the *specific intensity* of the beam, which is the amount of energy of that beam, per unit frequency, passing through a unit area, into a unit solid angle over one unit of time. Mathematically, we write this as,

$$I_\nu = \frac{dE_\nu}{d\nu dt \cos(\theta) dA d\Omega}, \quad (2.1)$$

where dE is the energy of the beam and $\cos(\theta) dA = \mathbf{n} \cdot d\mathbf{A}$. The subscript ν denotes that the quantity is frequency dependent. The units of specific intensity, in the centimetre-grams-second (CGS) unit system, are $\text{ergs s}^{-1} \text{ cm}^{-2} \text{ Hz}^{-1} \text{ sr}^{-1}$.

In the mathematical description of the radiation field, it is often useful to employ various angular averages, or *moments*, of the specific intensity. In general, the definition for the n^{th} moment is,

$$M_\nu^{(n)} = \frac{1}{2} \int I_\nu \cos^n(\theta) d\Omega. \quad (2.2)$$

However, we will only consider the first two moments – the zeroth and first. The zeroth order moment is the (angle averaged) mean intensity of the radiation field J_ν , given by,

$$J_\nu = \frac{1}{4\pi} \int I_\nu d\Omega, \quad (2.3)$$

with units ergs s⁻¹ cm⁻² Hz⁻¹. The next moment is the flux F_ν which is the amount of power radiated over a given area and can be written as,

$$F_\nu = \int I_\nu(\theta) \cos(\theta) d\Omega, \quad (2.4)$$

with units ergs s⁻¹ cm⁻² Hz⁻¹. To further complicate this matter, there are actually three definitions of the flux. What is defined in Equation 2.4 is the *observed monochromatic flux* and is the flux used throughout this thesis. Sometimes, the *Eddington flux* is used instead, defined as $H_\nu = \frac{1}{4\pi} F_\nu$. The final type of flux is the *astrophysical flux*: $\mathcal{F}_\nu = \frac{1}{\pi} F_\nu$.

2.1.2 Absorption and emission processes

As a beam of light propagates through a medium, the intensity will be changed due to absorption processes attenuating its intensity, and by emission processes which boost the intensity. Photons can also be scattered into and out of the beam which will change the intensity of the beam. For now, however, this will be ignored and discussed later in Section 2.1.6.

2.1.2.1 Emission

The spontaneous monochromatic emission coefficient j_ν is defined as the energy emitted per unit time, per unit solid angle, per unit volume, and per unit frequency. The energy change of a beam due to spontaneous emission is,

$$dE = j_\nu dv dV d\Omega dt, \quad (2.5)$$

which has units ergs cm⁻³ s⁻¹ ster⁻¹ Hz⁻¹. For a beam of light, with a cross section dA , which travels a distance ds through some medium with a volume $dV = dA ds$, then the intensity added to the beam by spontaneous emission is

$$dI_\nu = j_\nu ds. \quad (2.6)$$

2.1.2.2 Absorption

The change in intensity of a beam of light, due to (monochromatic) absorption, is given by,

$$dI_\nu = -\alpha_\nu I_\nu \, ds, \quad (2.7)$$

where α_ν is the absorption coefficient with units cm^{-1} . The common convention is that positive α_ν corresponds to energy removed from the beam. The absorption coefficient is often also written as,

$$\alpha_\nu = \rho \kappa_\nu, \quad (2.8)$$

where ρ is the density of the medium and κ_ν is the mass absorption coefficient, commonly known as the opacity coefficient with units $\text{cm}^{-2} \text{ g}^{-1}$.

2.1.3 Random walk of photons

As photons travel through a medium, they do so along a random path known as a *random walk*. The mean free path, λ , of a photon measures the average distance photons travel between interactions, and depends strongly on the density and composition of the medium the photon is travelling through. For photons interacting with a particular type of matter particle – e.g. photons scattering off of electrons – we can define the mean free path as,

$$\lambda = \frac{1}{n\sigma}, \quad (2.9)$$

where n is a number density of the particles, and σ is their interaction cross section. Along their random walk, photons will travel a net displacement of \mathbf{L} , given by the sum of the individual N paths $\boldsymbol{\lambda}_i$, i.e.,

$$\mathbf{L} = \boldsymbol{\lambda}_1 + \boldsymbol{\lambda}_2 + \boldsymbol{\lambda}_3 + \cdots + \boldsymbol{\lambda}_N. \quad (2.10)$$

Taking the vector dot product of \mathbf{L} with itself gives,

$$\mathbf{L} \cdot \mathbf{L} = \boldsymbol{\lambda}_1 \cdot \boldsymbol{\lambda}_1 + \boldsymbol{\lambda}_1 \cdot \boldsymbol{\lambda}_2 + \boldsymbol{\lambda}_1 \cdot \boldsymbol{\lambda}_N + \cdots + \boldsymbol{\lambda}_N \cdot \boldsymbol{\lambda}_1 + \boldsymbol{\lambda}_N \cdot \boldsymbol{\lambda}_2 + \boldsymbol{\lambda}_N \cdot \boldsymbol{\lambda}_N, \quad (2.11)$$

$$L^2 = N\lambda^2 + \lambda^2 \left[\cos \theta_{12} + \cos \theta_{1N} + \cdots + \cos \theta_{N1} + \cos \theta_{N2} + \cdots + \cos \theta_{N(N-1)} \right], \quad (2.12)$$

where $\theta_{i,j}$ is the angle between λ_i and λ_j . In the limit of a large number of steps, the sum of the cosines will tend toward zero, and the net displacement across the random walk is given by a simple equation,

$$L = \lambda \sqrt{N}. \quad (2.13)$$

2.1.4 The optical depth

The optical depth, τ , of a medium is a measure of the opacity of a medium and is closely related to the photon mean free path. To determine an expression for the optical depth, we first consider the probability of a photon interacting as it travels a path ds ,

$$P = n\sigma ds.$$

Therefore, the probability of a photon not interacting is,

$$P = 1 - n\sigma ds.$$

For a photon travelling a distance L , split into N equal sections, the probability of travelling that distance without any interactions is

$$P = \left[1 - \frac{n\sigma L}{N}\right]^N.$$

As $N \rightarrow \infty$,

$$P = e^{-n\sigma L} = e^{-\tau}, \quad (2.14)$$

where τ is the optical depth defined by,

$$\tau = n\sigma L. \quad (2.15)$$

To interpret Equation 2.14 physically, the optical depth is the number of mean free paths *available* between a photon's initial and final position. We can also estimate the number of interactions a photon will undergo along an optically thick path by substituting Equation 2.15 into Equation 2.13,

$$\tau = \sqrt{N}. \quad (2.16)$$

Equation 2.16 shows that the number of interactions a photon will undergo in a region is, on average, equal to the square of the optical depth of that region. In situations where there is a large optical depth ($\tau \gg 1$) photons undergo a large number of interactions. In an optically thin medium, the number of scatters is instead,

$$N \sim \tau. \quad (2.17)$$

In any sort of realistic medium, the cross section and density are not constant over the photon's path, and therefore Equation 2.15 is not always valid. If we consider a beam of photons propagating along a path ds through a medium of number density n , then the combination of absorbing particles (with cross section σ_ν) will present an effective absorbing area $n\sigma_\nu dA ds$. The change in intensity, due to absorption is,

$$dI_\nu = -n\sigma_\nu I_\nu ds. \quad (2.18)$$

Which, following from Equation 2.7, defines,

$$\alpha = n\sigma_\nu. \quad (2.19)$$

We can therefore define the optical depth along a path S as,

$$\tau_\nu = \int_0^S \alpha_\nu ds. \quad (2.20)$$

2.1.5 The equation of radiative transfer

We can use the radiative transfer equation (RTE) to calculate the fractional change in intensity of a photon beam as it travels along a path. The change in intensity at any point along a path is equal to the intensity removed from the beam due to absorption and intensity added due to emission. The net change in intensity dI_ν over a small path length ds is given by,

$$dI_\nu = j_\nu ds - \alpha_\nu I_\nu ds. \quad (2.21)$$

Whilst Equation 2.21 is already useful, it is generally more insightful to consider the rate at which the competing absorption and emission processes occur, as this controls how rapidly the beam changes in intensity. By dividing through with α_ν , we can re-write Equation 2.21 as,

$$\frac{dI_\nu}{d\tau_\nu} = -I_\nu + S_\nu, \quad (2.22)$$

where we have used $d\tau_\nu = \alpha_\nu ds$ and $S_\nu \equiv j_\nu / \alpha_\nu$ is the *source function* of the medium. The source function describes how photons are removed and replaced and has the same units as the specific intensity. By integrating Equation 2.22 over the entire path the intensity at any point can be calculated,

$$I_\nu = I_{\nu,0} e^{-\tau_\nu} + \int_0^{\tau_\nu} S_\nu e^{\tau'_\nu - \tau_\nu} d\tau'_\nu. \quad (2.23)$$

This is a difficult equation to solve. However, with a constant source function, Equation 2.23 simplifies to,

$$I_\nu = I_{\nu,0} e^{-\tau_\nu} + S_\nu [1 - e^{-\tau_\nu}], \quad (2.24)$$

where both I_ν and S_ν are functions of τ . In the optically thick limit, Equation 2.24 simplifies even further. When $\tau \gg 1$, then $e^{-\tau} \rightarrow 0$ and Equation 2.24 simplifies to,

$$I_\nu = S_\nu. \quad (2.25)$$

Equation 2.25 shows that a radiation beam illuminating an optically thick medium is completely absorbed by the medium and redistributed as the source function. In an optically thick medium, photons are effectively trapped as they undergo multiple interactions and the medium eventually reaches thermodynamic equilibrium. The emergent spectrum of an optically thick region is hence expected to be that of a blackbody as,

$$I_\nu = S_\nu = B_\nu(T), \quad (2.26)$$

where $B_\nu(T)$ is the Planck function at the local temperature T . Following from Equation 2.26 we can also note the relation,

$$j_\nu = \alpha_\nu B_\nu(T), \quad (2.27)$$

known as *Kirchoff's law* (Kirchhoff, 1860), which implies that there is some relationship between emission and absorption at a *microscopic* level. We can use this relation to write the transfer equation for thermal radiation as

$$\frac{dI_\nu}{d\tau_\nu} = -I_\nu + B_\nu(T). \quad (2.28)$$

2.1.6 Scattering

In addition to the processes described in Section 2.1.2, the intensity of a beam can also be modified by photons being scattered into and out of a photon beam. This is different in that the change in intensity due to scattering is not “true” emission or absorption. A scattering processes is an interaction between a photon and a “scatterer”, which results in a new direction for the photon and, sometimes, a different frequency. This is different to “true” processes, which either destroy or emit photons.

The important distinction is that scattering processes basically depend only upon the properties of the radiation field, and have a weak dependence on the thermodynamic properties of the medium in which photons are scattering in. True absorption, on the other hand, depends on the thermal properties of the medium, as it feeds energy from the radiation field into the thermal kinetic energy of the medium. Conversely, true thermal emission directly couples the thermal properties of the gas and the radiation field.

By far the most common scattering mechanism, in astrophysical situations, is scattering by non-relativistic electrons. The emission coefficient due to scattering can be derived by equating the power absorbed by a medium to the (thermal) power emitted. In the simple case of (elastic) isotropic scattering,

$$j_\nu = \sigma_\nu J_\nu, \quad (2.29)$$

where J_ν is the mean intensity following from Equation 2.3 and σ_ν is the scattering coefficient. The scattering source function is then derived by dividing through by α_ν ,

$$S_\nu = J_\nu, \quad (2.30)$$

which shows that the scattering source function, for isotropic scattering, is equal to the mean intensity of the medium. Of course, this is not true for all scattering processes. As an example, non-coherent (Compton) scattering changes the frequency of a photon and the scattering direction is not isotropic, therefore, in this case, S_ν will diverge from J_ν .

The addition of scattering processes significantly complicates the radiative transfer. For example, consider a medium with absorption coefficient α_ν corresponding to thermal emission and an isotropic electron scattering coefficient σ_ν . In this case, the source function is,

$$S_\nu = \frac{\alpha_\nu B_\nu + \sigma_\nu J_\nu}{\alpha_\nu + \sigma_\nu}. \quad (2.31)$$

Clearly, this is more complicated than when dealing with only true absorption and emission processes. To differentiate true absorption from the absorption by scattering, we often define the extinction coefficient, which is the sum $\epsilon = \alpha_\nu + \sigma_\nu$. When scattering is included, the optical depth, following from Equation 2.20, is therefore given by,

$$\tau_\nu = \int_0^S (\alpha_\nu + \sigma_\nu) \, ds. \quad (2.32)$$

2.1.7 Radiative equilibrium

In the case where all energy transport in a medium is done via radiation, then the medium is in *radiative equilibrium*. When a medium is in radiative equilibrium, the total energy absorbed by a volume is equal to the total energy emitted by the same volume and the total energy flux is conserved. In, for example, a stellar atmosphere in radiative equilibrium, the atmosphere merely transports the total energy it receives outwards. The atmosphere may alter the frequency distribution but the total energy flux will be conserved.

2.1.8 Local thermodynamic equilibrium

LTE is an important approximation and acts as a first-order *best-guess* to describe the physical conditions of a medium. Under LTE, we assume that in a small volume of material all thermodynamic processes and properties, such as the level population of atoms, are the same as their thermodynamic equilibrium values at the local temperature T and electron density n_e . We also make the assumption that the local thermodynamic temperature, typically the electron temperature, is equal to the radiation temperature T_R , representing the mean energy of a photon from a blackbody radiation field. We also assume that the medium is in radiative equilibrium and that the principle of *detailed balance* applies, such that electrons transitioning between different energy states is balanced exactly by electrons doing the inverse processes.

The electrons and ions are governed by Maxwell-Boltzmann statistics. We can easily calculate the excitation state of an ion, i.e. how the bound levels are populated, using the Boltzmann distribution,

$$\frac{n_{i,j}}{n_{0,j}} = \frac{g_i}{g_0} e^{-\chi_i/k_B T}, \quad (2.33)$$

where i denotes the level, j the ionization state of atom and subscript 0's the ground level. I have used n to denote the level population/density, χ_i the energy between the level i and the ground state, g the statistical weight and k_B the Boltzmann constant. We

can also calculate the ionization state of a medium by calculating relative population of two ions using the Saha equation,

$$\frac{N_{j+1}}{N_j} = \frac{2}{n_e} \left[\frac{2\pi m_e k_B T}{h^2} \right]^{3/2} \frac{g_{j+1}}{g_j} e^{-\chi_I/k_B T}, \quad (2.34)$$

where N is the density of the ion, m_e the electron rest mass, h is Planck's constant and χ_I is the ionization potential of the atom.

Unfortunately, whilst LTE is (relatively) simple, the universe is not. In many astrophysical systems, there is a large difference between the LTE and real solution. For example, if a medium is not illuminated by a blackbody or heavily absorbing then we will see large departures from the LTE solution. Such situations require more complex analysis and mathematics.

2.1.9 The dilute blackbody approximation

One method to deal with non-LTE conditions is the dilute blackbody approximation. We no longer assume that the thermodynamic temperature is equal to the radiation temperature and also assume that the mean intensity of the radiation field is given by a *dilute* blackbody,

$$J_\nu = W B_\nu(T_R), \quad (2.35)$$

where W is the dilution factor. This factor is usually based on the properties of the radiation field, but can also be a purely geometric parameterization. With the dilute approximation, the excitation state of an ion is given by a modified Boltzmann distribution (Abbott & Lucy, 1985),

$$\frac{n_{i,j}}{n_{0,j}} = \xi W \left[\frac{n_{i,j}}{n_{0,j}} \right]_{T_R}^*, \quad (2.36)$$

where the last term is calculated using the regular Boltzmann distribution at the radiation temperature and ξ is the fraction of recombining electrons which go directly to the ground state. We can also use a modified version of the Saha equation to calculate the ionization state (Abbott & Lucy, 1985),

$$\frac{N_{j+1}}{N_j} = \frac{\xi W}{n_e} \left[\frac{T}{T_R} \right]^{1/2} \left[n_e \frac{N_{j+1}}{N_j} \right]_{T_R}^*, \quad (2.37)$$

where the last term is calculated using the Saha equation at the radiation temperature.

2.2 The Monte Carlo method

Calculating the ionization and excitation state of a medium, as well as the radiative transfer through it, is difficult. To obtain accurate values for the properties of the medium, we need to deal with all the relevant processes at play. Considering the form of the solution to the RTE (Equation 2.23), it very quickly becomes very difficult to analytically (and numerically) calculate the full radiative transfer, when any number of important processes are included. In mathematics, one convenient way to solve a horribly complicated and coupled system of equations is by using Monte Carlo methods. Therefore one way to solve the horribly complicated equations governing the ionization and excitation state and the radiative transfer of a medium, is also by using a Monte Carlo approach.

The Monte Carlo (MC) method is a range of mathematical techniques which compute numerical results, through the repeated use of random sampling. It is often used for problems where deterministic techniques are either impossible or inefficient. In principle, an MC method can be used to solve any problem which has a probabilistic interpretation.

The earliest known use of the MC technique dates back to the 18th century by the French naturalist Buffon, with their needle experiment. In this experiment, Buffon determined the probability that a dropped needle would overlap a line on a striped sheet of paper. Although not the original point of the experiment, due to the geometry of the problem, it is possible to approximate the value of π from this experiment by counting the number of times a needle overlaps a line.

Unwittingly the MC method was seemingly forgotten about and was eventually “re-discovered” and formalised in the 1940’s by Stanislaw Ulman at the Los Alamos National Laboratory. Here, the MC technique was applied to model the random walk of neutrons to understand neutron diffusion and shielding requirements for nuclear reactors.

MC methods have found a wide range of applications in multiple fields including mathematics, the physical sciences, modern computer graphics and finance. Some of the more common techniques include Monte Carlo integration, used to evaluate difficult integrals, and Markov Chain Monte Carlo. The latter has turned out to be especially important, finding a plethora of applications from computational linguistics and parameter optimisation to statistical mechanics (such as the famous Metropolis-Hastings algorithm; Metropolis et al., 1953; Hastings, 1970).

Suppose we want to know the average value of a quantity X , that is distributed according to some probability distribution function (PDF) $P(X)$. The most simple way to do this, using MC methods, is by drawing N random values from $P(X)$ and constructing the “mean-value estimator” from that. Estimators are actually the basic building blocks of

the MC method, and are what is used to “estimate” and get numbers out of the MC approach. Mathematically, we write this estimator as

$$\hat{X} = \frac{1}{N} \sum_{i=0}^{N-1} x_i, \quad (2.38)$$

where \hat{X} is the estimated value of X and x_i are the random sample points used to evaluate $P(X)$. MC methods are, therefore, all about sampling from a PDF. In the most simple case, to sample uniformly from a PDF we can use the inversion method, which requires a cumulative probability distribution (CPD) of the PDF. To construct a CPD $\psi(x)$, the PDF has to be integrated and normalised such that,

$$\xi = \psi(X_0) = \frac{\int_a^{X_0} P(X) dX}{\int_a^b P(X) dX} \quad (2.39)$$

where x_0 ranges from a to b and $\psi(X_0) = \xi$ ranges from 0 to 1 uniformly (a proof for this can be found in [Duderstadt & Martin, 1979](#)). To now sample a random variable X_0 from a PDF, a uniform random deviate $\xi \in [0, 1]$ is generated and Equation 2.39 is inverted to solve for X_0 . However, it is not always possible to analytically invert Equation 2.39, so a numerical approach can be required.

2.3 Monte Carlo radiative transfer and ionization

The RTE equation can be quite difficult to solve, but it can be solved relatively straightforwardly using a Monte Carlo approach. In Monte Carlo radiative transfer (MCRT), individual and independent photon packets are used to represent the radiation field. Each photon is individually tracked along its random walk from emission to escape, simulating each interaction, be that an absorption, emission or scattering process. MCRT has become a widely adopted technique due to its flexibility, accuracy, stability and the simplicity with which complicated geometries and interactions can be implemented. The underlying procedure in any MCRT simulation is to generate a large generation of independent photons and transport them through a random walk through a (usually spatially discretised) simulation grid, randomly deciding what happens to a photon at each interaction point.

MCRT simulations can, however, be computationally expensive. But since each photon is independent, MCRT falls under the class of “embarrassingly parallel” algorithms and is easily accelerated by a range of parallel computing techniques, such as the [Message Passing Interface](#) (MPI; [MPI Forum, 1994](#)) or the [Compute Unified Device Architecture](#) (CUDA; [Nickolls et al., 2008](#)).

I will now describe PYTHON¹, a state-of-the-art piece of software for modelling the radiative transfer and ionization of accretion disc outflows. The somewhat confusingly named PYTHON has been in development since the early 1990s and is written in the *C* programming language, to a mostly ANSI-*C* standard. PYTHON is parallelised using the OpenMPI implementation of the **Message Passing Interface**. Although PYTHON has been well described multiple times in the literature (e.g. Long & Knigge, 2002; Higginbottom et al., 2013, 2014; Matthews et al., 2015; Matthews, 2016), as it is central to the work in this thesis, this section aims to describe the key physics and numerical techniques built into PYTHON.

2.3.1 Basics

PYTHON consists of two separate calculation stages. The first stage determines the ionization state, level populations and temperature structure of an outflow on a spatially discretised grid. This is done iteratively by tracking a population of photon packets and simulating their random walk through the grid. The photon packets are randomly generated over a wide frequency range, sampled from the spectral energy distribution (SED) of the radiation sources included in a simulation. As photon packets travel through the grid, they interact with the plasma and update Monte Carlo estimators used to describe the radiation field in each grid cell. The heating effect of photon packets is recorded and used to iterate the temperature towards thermal equilibrium, where the amount of heating and cooling in each grid cell is eventually balanced.

Once the photon packets have been transported through the grid, updated temperature and radiation field estimators are used to recalculate level populations and an updated ionization state of the outflow. This process is repeated until the simulation has converged. A grid cell is considered converged when i) the electron and radiation temperature have stopped changing between iterations to within 5%, and, ii) when the heating and cooling rates are balanced to within 5%. It is usually not necessary, or expected, for all grid cells to converge. Typically, cells with poor photon statistics or noisy Monte Carlo estimators tend to not converge. These cells are usually located near the outer edge of the computational domain and are relatively unimportant; they typically contribute little to the final result.

The second calculation stage produces synthetic spectra for a converged simulation. Additional populations of photon packets are generated, typically over a narrow frequency range to give high signal-to-noise, and are flown through the *converged* grid to generate spectra for a selection of sight lines. Figure 2.2 shows a flowchart of the “top-level” details, showing the basic processes and the order in which they occur during a simulation.

¹PYTHON is an open source project, available at <https://github.com/agnwinds/python>.

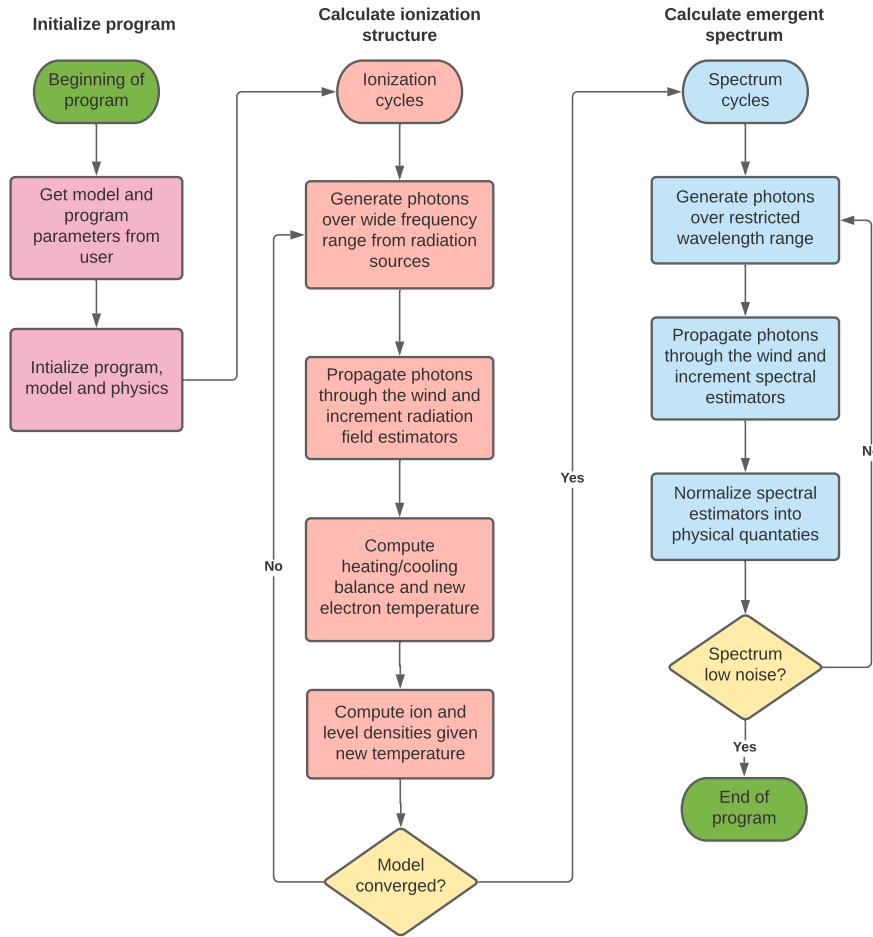


FIGURE 2.2: A flowchart showing the basic steps carried out in a PYTHON simulation.

2.3.2 Wind models

To model an outflow, PYTHON requires a model where the spatial, density and velocity structure have been defined. As part of the program, multiple parameterisable wind models are included, such as a simple homologous model or more complex models such as the infamous Knigge et al. (1995) or Shlosman & Vitello (1993) wind models. PYTHON also allows a user to read in a “custom” grid which, for example, could be the output from another simulation.

2.3.2.1 The Shlosmann & Vitello wind model

Throughout this thesis, I have modelled TDE outflows using the kinematic biconical wind prescription presented originally by Shlosman & Vitello (1993). This model is illustrated in Figure 2.3. In this prescription, streamlines emerge from disc radii between r_{\min} and r_{\max} at angles relative to the disc normal given by,

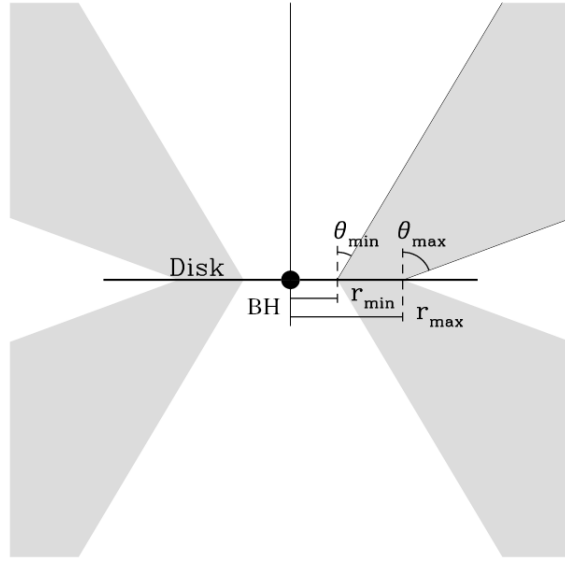


FIGURE 2.3: A cartoon showing the basic geometry of the Shlosman & Vitello (1993) biconical disc wind model. Adapted from Long & Knigge (2002).

$$\theta(r_0) = \theta_{\min} + (\theta_{\max} - \theta_{\min})x^{\gamma}, \quad (2.40)$$

where,

$$x = \frac{r_0 - r_{\min}}{r_{\max} - r_{\min}}. \quad (2.41)$$

Here, r_0 is the launch radius of a streamline, θ_{\min} and θ_{\max} are the minimum and maximum opening angles of the wind, and γ controls the concentration of streamlines towards either of the two boundaries r_{\min} and r_{\max} .

The launch velocity, v_0 , and terminal velocity, v_{∞} , of a streamline are set to the local sound speed and a multiple of the escape velocity, v_{esc} , at the streamline footpoint, respectively. The poloidal velocity, v_l , at a distance l along a streamline, is assumed to follow,

$$v_l(r_0) = v_0 + (v_{\infty} - v_0) \left[\frac{(l/R_v)^{\alpha_v}}{(l/R_v)^{\alpha_v} + 1} \right], \quad (2.42)$$

where R_v is the acceleration length scale, i.e. the distance where $v = 0.5v_{\infty}$ is reached. The value of this parameter directly influences the mass continuity of the wind, playing a crucial role in setting the density and the scale length over which the wind is accelerating. Its value is typically set by observations or by physically motivated “back-of-the-envelope” calculations. But in the absence of such informed decisions, R_v is either typically set, by *intuition*, to be an order or two magnitudes smaller than the spherical

extent of the wind, or multiple values are experimented with. The parameter α_v controls the shape of the velocity law along the streamline, with larger values corresponding to slower initial acceleration. The rotational velocity, v_ϕ , is Keplerian at the footpoint of a streamline and is assumed to conserve specific angular momentum as it rises above the disc. At a cylindrical radius r , v_ϕ is given by,

$$v_\phi(r) = v_k r_0 / r, \quad (2.43)$$

where v_k is the Keplerian velocity at r_0 . The density at any point in the wind is obtained by enforcing mass continuity, giving,

$$\rho(r, z) = \frac{r_0}{r} \frac{dr_0}{dr} \frac{\dot{m}'}{v_z(r, z)}, \quad (2.44)$$

where \dot{m}' is the mass-loss rate per unit surface area of the accretion disc,

$$\dot{m}' \propto \dot{M}_{\text{wind}} r_0^\lambda \cos[\theta(r_0)]. \quad (2.45)$$

The parameter λ controls where mass is lost from the disc, and \dot{M}_{wind} is the total mass loss rate of the wind. A value of $\lambda = -2$ results in roughly uniform wind densities at the base of the outflow, across the disc surface. Both λ and γ are similar in that they influence the density distribution of the wind. A value of $\gamma = 0$, for example, strongly skews the streamlines toward the outer wind boundary (r_{\max}), creating a highly collimated and dense equatorial flow (even if the opening angles define a wide-angled wind) because of the increased concentration of streamlines at the outer boundary. On the other hand, λ can also be used to enhance the density at either wind boundary, but does not influence the creation of a collimated flow as much.

2.3.3 Micro-clumping

PYTHON was originally developed to model smooth outflows, such that the density at any given point is determined by only the kinematic parameters and the mass loss rate of the wind. In reality, various instabilities are likely to break up a smooth flow into clumps. In-fact, multiple clump forming mechanisms have been identified in various astrophysical settings including, radiation (line-)driven instabilities (Owocki et al., 1983; Krolik & Raymond, 1985), magnetic confinement (Emmering et al., 1992; de Kool & Begelman, 1995) and various types of thermal and hydrodynamic instabilities (McCourt et al., 2018; Waters & Proga, 2019; Dannen et al., 2019) such as the Rayleigh-Taylor and Kelvin-Helmholtz instabilities (e.g. Wang & Chevalier, 2001; Ellinger et al., 2012).

From both a computational and astrophysical standpoint, addressing the problem of clumping is difficult. First and foremost, in most astrophysical outflows, the scale length and density contrast of clumps are not well-constrained from observations, or theory. Nor is it simple to know where to place clumps in a kinematic model, or how the shape, size and density could change as a function of, for example, radius. Secondly, not only does clumping introduce additional complexity into already complex models, the spatial resolution of the computational grid is required to be fine enough to resolve each individual clump. In PYTHON, this is not yet feasible due to current memory restrictions limiting the size of the simulation grid.

As a first step, PYTHON uses a necessarily simple approximation known as *micro-clumping* (Hamann & Koesterke, 1998; Hillier & Miller, 1999; Oskinova et al., 2008), a parameterization commonly used in stellar wind modelling. The key assumption in the micro-clumping approximation is that clumps are optically thin and smaller than all relevant length scales. In PYTHON, for example, a photon can interact with a bound-bound transition only in a narrow resonance region defined by the Sobolev length l_s (Equation 2.52). In a simulation where $l_s \sim 10^{10} - 10^{12}$ cm and where the optical depth for a resonance can reach upwards of $\tau \sim 10^6$, in order for clumps to remain optically thin, even in optically thick lines, the clump length scale would need to satisfy $l_c \ll l_s/\tau \sim 10^4$ cm.

In the micro-clumping approximation, clumps are embedded within a vacuum and are treated simply in terms of a volume filling factor, f_v . The clumps are not resolved by the grid, hence this framework is easily applied to a wide range of wind models without any modification to the grid. The density of the clumps is enhanced by a factor $D = 1/f_v$ relative to the equivalent smooth outflow. The opacities, κ , and emissivities, ϵ , are then given by,

$$\kappa = f_v \kappa_c(D) \text{ and } \epsilon = f_v \epsilon_c(D), \quad (2.46)$$

where the subscript c denotes that the quantity is calculated using the enhanced density of the clump. At a fixed temperature, processes which scale linearly with density (e.g. electron scattering) remain unchanged as f_v and D will cancel one another out. Processes which scale with the square of the density (e.g. collisional excitation or recombination) are enhanced by a factor D . For a simulation where the temperature is not constant, the ionization state is moderated due to a decrease in the ionization state resulting from the enhanced density of clumps.

2.3.4 Atomic data

By default PYTHON assumes solar abundances for H, He, C, N, O Ne, Na, Mg, Al, Si, S, Ar, Ca and Fe following Verner et al. (1995). However, PYTHON is extremely flexible in terms of the elements that can be included and the relative abundance that can be adopted in a simulation. Throughout this thesis, I use the same atomic data outlined originally by Long & Knigge (2002), with the subsequent improvements described by Higginbottom et al. (2013) and Matthews et al. (2015). Hydrogen and helium are described with a multi-level model atom, treated using the “macro-atom” formalism of Lucy (2002, 2003); see Section 2.3.8.3.2. Metals, on the other hand, are treated with a two-level atom formalism (see, e.g. Mihalas, 1978, 1982).

2.3.5 Radiation sources

PYTHON is intended to model the radiative transfer in accretion disc systems of all scales, comprised of a central source, such as a white dwarf or black hole, and an optically thick, geometrically thin accretion disc. A typical PYTHON model will include multiple radiation sources, each of which produces a distinct photon population whose properties are controlled by the source SEDs. In the simulations for this thesis, I include either one, or two, of the following three radiation sources: (i) the outflow, (ii) an accretion disc, and, (iii) a central source.

2.3.5.1 Accretion disc

The accretion disc is assumed to be both geometrically thin and optically thick, and is treated as an ensemble of constant temperature annuli, radiating either as a stellar atmosphere or as a blackbody with a temperature defined by a standard α -disc temperature profile (see Section 1.2.1 or Shakura & Sunyaev, 1973). The SED of the disc is therefore specified almost entirely by the mass accretion rate and the mass of the black hole, as well as the inner and outer radii of the disc. In principle, both of these are free parameters, but the former is often set to the innermost stable circular orbit of a Schwarzschild black hole. The angular distribution of emitted photons is determined using the Eddington approximation, including fore-shortening and limb-darkening resulting in a highly anisotropic radiation field.

It is also possible to model the accretion disc as either a flared or vertically extended disc. However, this still assumes a standard α -disc temperature profile, i.e. this is not an implementation of, for example, a detailed model of a super-Eddington accretion disc. But, it is possible to provide a “non-standard” temperature distribution via an external file, or to use a slim disc temperature profile as discussed in Section 1.2.2.

2.3.5.2 Central source

The central source can be a star, white dwarf or even a black hole, specified by their respective mass, radius and, where appropriate, their temperature. The SED for the central source can either be a blackbody or Bremsstrahlung spectrum for a given temperature, a power law specified by an X-ray luminosity and spectral index, or as model read in from an external file. The angular distribution of emitted photons is, again, determined using the Eddington approximation, if it is appropriate. In, for example, the case of Bremsstrahlung, which can included to model compact coronae, photons are emitted isotropically.

2.3.5.3 The outflow

The outflow is assumed to be in radiative equilibrium, modulo non-radiative heating/-cooling processes such as adiabatic cooling or shock heating (both of these can be included in a simulation). The outflow itself, however, is not a *net* source of photons, but acts as a reprocessing medium. Energy absorbed is either reprocessed or re-radiated due to Comptonization, radiative recombination, free-free emission or line emission. It could also be converted to $P dV$ work due to adiabatic expansion. As these processes depend upon the temperature and ionization state of the outflow, the number of “wind” photons and their frequency distribution is updated as these quantities change.

2.3.6 Photon packets

When a photon is generated, it is assigned both a weight and frequency determined by the particular nature and SED of the radiation source from which it is being emitted. The total weight of all the photon packets in a simulation is equal to the total luminosity of all the radiation sources. Hence, the weight of a photon, w_i , represents the amount of luminosity carried by that particular photon packet given by.

$$w_i = \frac{L_{\text{tot}}}{N_p}, \quad (2.47)$$

where L_{tot} is the total luminosity in the simulation and N_p is the number of photons.

In the simplest approach, the frequency distribution of the photons is sampled uniformly across the frequency range of the SED. This can be inefficient, however. For example, generating a *sufficient* number of photons from the Wien tail of a blackbody spectrum is often impossible with uniform sampling for any realistic number of photon packets. One solution to this problem is *importance sampling*, where the frequency distribution is split into multiple bands, each of which is allocated a user-defined fraction f_i of the

total number of photon packets. In order to draw a random frequency for a photon in band i with the frequency range $[\nu_i, \nu_{i+1}]$, a CPD is constructed using the SED of each band. Following from Equation 2.39, the CPD for a band i is,

$$\psi_i(\nu) = \frac{\int_{\nu_i}^{\nu} L_i \, d\nu}{\int_{\nu_i}^{\nu_{i+1}} L_i \, d\nu}, \quad (2.48)$$

where L_i is the SED of the band i . The frequency of a random photon packet can then be drawn by drawing a uniform random deviate $\xi \in [0, 1]$, setting $\xi = \psi_i(\nu)$ and solving for ν . The weight of the photons in each band is no longer equal, but is given by

$$w_i = \frac{\sum_{N_s} \int_{\nu_i}^{\nu_{i+1}} L_{i,s} \, d\nu}{f_i N_{\text{tot}}}. \quad (2.49)$$

The term \sum_{N_s} indicates a sum across all radiation sources, therefore $L_{i,s}$ is the total luminosity in band i from source s , and $N_i = f_i N_{\text{tot}}$ is the number of photons assigned to this band, with N_{tot} photons across all bands.

2.3.7 Radiative transfer

As a photon is transported through the grid after being emitted, it has a finite chance to interact with the plasma making up the outflow. Interactions in PYTHON are implemented in much the same way as outlined by [Mazzali & Lucy \(1993\)](#). The optical depth to a photon's next interaction is determined by substituting the probability a photon won't interact (Equation 2.14) into Equation 2.39 and inverting to get,

$$\tau = -\ln(1 - \xi). \quad (2.50)$$

Here, ξ is a uniform random deviate, $\xi \in [0, 1]$. As a photon is transported from point to point through the grid, the run of optical depth along its path s , τ' , is recorded. Along the path s , if the photon comes into resonance with a bound-bound transition, then the opacity due to line scattering is included. The optical depth along a photon's path is influenced by opacity from electron (ES) scattering, line scattering (BB), bound-free absorption (BF) and free-free absorption (FF). Thus, along the total optical depth a photon will see along its path s can be calculated using

$$\tau'(s) = \int_{s'=0}^{s'=s} [\sigma_{\text{KN}} n_e + \sum_{N_{\text{ions}}} \rho(\kappa_{\text{bb}} + \kappa_{\text{bf}} + \kappa_{\text{ff}})] \, ds', \quad (2.51)$$

where σ_{KN} is the Klein-Nishina cross section (Klein & Nishina, 1929), n_e is the electron density along the path, ρ_i the mass density of an ionic species and κ_{bb} , κ_{bf} and κ_{ff} are the opacities due to line scattering, bound-free absorption (photoionization) and free-free absorption respectively. It is important to note that the total opacities for the BB, BF and FF processes are summed over all of the ions in the simulation.

A photon will interact with the plasma at the first location S for which $\tau'(s) \geq \tau$. At the interaction point, the photon will either be resonance scattered by a bound-bound line, or will be scattered by the continuum by a random scattering process. If the photon has scattered it is given a new direction sampled from the appropriate distribution for the process. Finally, the weight of the photon is attenuated due to absorption from photoionization and free-free processes between its starting and end points, i.e. between $s' = 0$ and $s' = s$.

2.3.7.1 Sobolev approximation

PYTHON uses the Sobolev approximation (see, e.g. Sobolev, 1957; Rybicki & Hummer, 1978; Hummer & Rybicki, 1985) to considerably simplify the line interaction process and its contribution to the opacity. The Sobolev approximation applies in the limit where the velocity gradient in a region dominates over the thermal broadening. In this limit, photons no longer interact with a line in a volume and instead interact only at points lying on a thin *resonance surface*, known as the Sobolev surface.

To see this, consider the interaction of a photon of frequency ν with a bound-bound transition of frequency ν_0 . The photon will be able to interact with the line if it comes into resonance with it, i.e. if the bulk velocity of the material it travels through, projected along the photon's line-of-flight, v , satisfies $\nu_0 \simeq \nu(1 - v/c)$. When this condition is met, the photon's frequency is Doppler-shifted into the rest frequency of the transition. In reality, ions in the flow will have typical random thermal velocities, v_{th} , so the resonance condition does not have to be met exactly. We can thus estimate the physical width of the volume across which a photon can interact with a particular bound-bound transition – the so-called Sobolev length – by considering the distance over which v changes by $\simeq v_{th}$

$$l_s \approx \frac{v_{th}}{|dv/ds|}. \quad (2.52)$$

Here, $|dv/ds|$ is the velocity gradient along a path s . For the Sobolev approximation to be valid, l_s must be sufficiently small that the physical conditions in the flow do not change significantly on this length scale. If they do, then the Sobolev approximation is not valid.

If the Sobolev approximation *is* valid, the integral for the line optical depth (c.f. Equation 2.20) can be simplified dramatically. Schematically, $\int f(s) ds \simeq f(s_{\text{res}}) l_s$ in this limit, where s_{res} is the location of the resonance point. The optical depth due to line scattering at the resonance point can thus be calculated immediately as,

$$\tau_s = \frac{\pi q_e^2}{m_e c} \frac{f \lambda}{|dv/ds|} \left(n_l - n_u \frac{g_l}{g_u} \right), \quad (2.53)$$

where q_e and m_e are the electron charge and mass, f and λ are the oscillator strength and the wavelength of the line, and n_l , n_u , g_l and g_u are the densities and statistical weight of the upper and lower levels of the bound-bound transition.

If the line is optically thick, then a photon could undergo multiple line scatterings. The excited electron could also potentially be de-excited collisionally, resulting in the absorption of that photon. In order to avoid having to simulate these multiple interactions within a single Sobolev region, PYTHON implements the escape probability approximation of Rybicki & Hummer (1978). Fundamentally, Rybicki & Hummer (1978) show that a photon is more likely to *escape* the resonant zone along the direction of largest velocity gradient, where the photon will be Doppler shifted out of resonance with the line. The probability that a photon will escape in a direction \mathbf{n} is given by,

$$P_{\text{esc}} = \frac{1 - \exp(-\tau_{s,n})}{\tau_{s,n}}, \quad (2.54)$$

where $\tau_{s,n}$ is the Sobolev optical in the direction \mathbf{n} . The probability that a photons escapes from the Sobolev region is thus found by taking the angle average,

$$\langle P_{\text{esc}} \rangle = \int P_{\text{esc}} d\Omega, \quad (2.55)$$

and therefore the probability that a photon does not escape is $1 - \langle P_{\text{esc}} \rangle$. The photons which do not escape, as already mentioned, collisionally de-excite an electron and are absorbed. Therefore PYTHON is able to convert multiple interactions into an effectively single step, through immediate knowledge of how likely a photon is absorbed in or escapes the resonance region.

2.3.7.2 Doppler shifts

When a photon interacts with the plasma, or when the opacities in Equation 2.51 are evaluated, the photon's frequency must be transformed from the observer into the local rest frame of the outflow. The Doppler shift a photon experiences depends on the

projected velocity of the photon, $v = \mathbf{v} \cdot \mathbf{n}$ where \mathbf{n} is the unit vector of the photon. The photon will come into resonance with a line, if the outflow velocity is

$$v = c \left(1 - \frac{\nu_{\text{line}}}{\nu} \right), \quad (2.56)$$

where v is the velocity at which the photon comes into resonance with a line, ν_{line} the frequency of the line and ν the frequency of the photon.

2.3.7.3 Special relativity

Prior to this thesis, PYTHON made the assumption that outflow velocities were small compared to the speed of light. Doppler shifts were therefore treated “classically” (proportional to linear order in v/c), and no other corrections associated with relativistic effects were considered. However, the outflows of TDEs can approach speeds where relativistic effects need to be considered (e.g. [Dai et al., 2018](#)), and so PYTHON has been updated to fully incorporate special relativistic effects. PYTHON now explicitly distinguishes – and correctly transforms between – the co-moving (local/fluid) and observer frames. Energy is conserved in the co-moving frame, and the correct special relativistic transforms are applied when transforming between the two frames (see, e.g. [Castor, 1972](#); [Mihalas & Mihalas, 1984](#)). To be more specific, PYTHON implements relativistic Doppler transformations and takes into account the angular aberration of the photon direction when transforming between frames.

The coordinate grid is defined in the observer frame, so that the location of cells and the grid boundaries are defined as an observer would see them. By definition, then, photon transport takes part wholly in the observer frame, and the synthetic spectra generated are also as seen in the observer’s frame of reference. Additionally, the kinematic model properties of the outflow, such as the mass loss rate and velocity, are defined in the observer frame, but the properties of the plasma, such as the ion density, are correct only for the co-moving frame. When a photon packet interacts with an outflow, this is handled in the local co-moving frame of the fluid. Photon packets are therefore transformed into the local fluid frame during, e.g., scattering or photo-ionization events. In general, estimators of the radiation field as well as the atomic heating/cooling processes are calculated in the fluid frame.

2.3.8 Calculating the ionization state

Multiple populations of photons are flown through the grid, over multiple cycles, to iterate toward a converged state, where the heating and cooling processes of the outflow are balanced against one another. As the photon packets traverse through the outflow,

MC estimators are used to model the radiation field of the photon packets and atomic processes in the outflow. Once a complete population of photon packets has been transported, a revised temperature for each grid cell is calculated balancing the heating effect of the photon packets to the cooling rate of the outflow. Using the new temperature and models of the radiation field, the ionization state of each grid cell is then updated to reflect the current conditions of the outflow.

2.3.8.1 Heating and cooling balance

Once all photons in a given cycle have been transported through the outflow, PYTHON will calculate a new electron temperature assuming that cell is in thermal equilibrium. Thus the new temperature is chosen such that the heating rate is equal to the cooling rate, i.e. by solving the equation,

$$H_{\text{tot}}(T) - C_{\text{tot}}(T) = 0, \quad (2.57)$$

where H_{tot} and C_{tot} are the total heating and cooling rates in that cell. Unfortunately, both the heating and cooling rates are themselves functions of temperature and also depend on the ionization state of the outflow (which in turn depends on the temperature). The equation is therefore non-linear, meaning that it cannot be solved in one step. An iterative procedure must be used to *converge* toward the final cell temperature. This non-linearity is the underlying reason why multiple ionization cycles are required in a PYTHON simulation.

The outflow is heated when a photon packet loses weight due to absorption by either bound-free or free-free interactions, or due to collisional de-excitation occurring during a line scattering interaction. In the case of bound-free and line scattering processes, only a fraction of the photon's luminosity is transferred into the outflow. By contrast, free-free absorption transfers the entire photon luminosity into heat.

Non-radiative processes can also be included in the heating rates. At present, PYTHON is capable of handling two such processes: adiabatic heating/cooling and shock heating. Only the first of these is included by default.

As the outflow is assumed to be in thermal equilibrium, the cooling rates of the plasma are required to balance the heating rates exactly. There are three radiative cooling processes in PYTHON, free-free, free-bound and collisional excitation. The cooling effect due to these processes is calculated by integrating the frequency and temperature dependent luminosity for each process to calculate a total cooling rate. As already noted above, adiabatic cooling due to the expansion of the outflow is also included in the total rate.

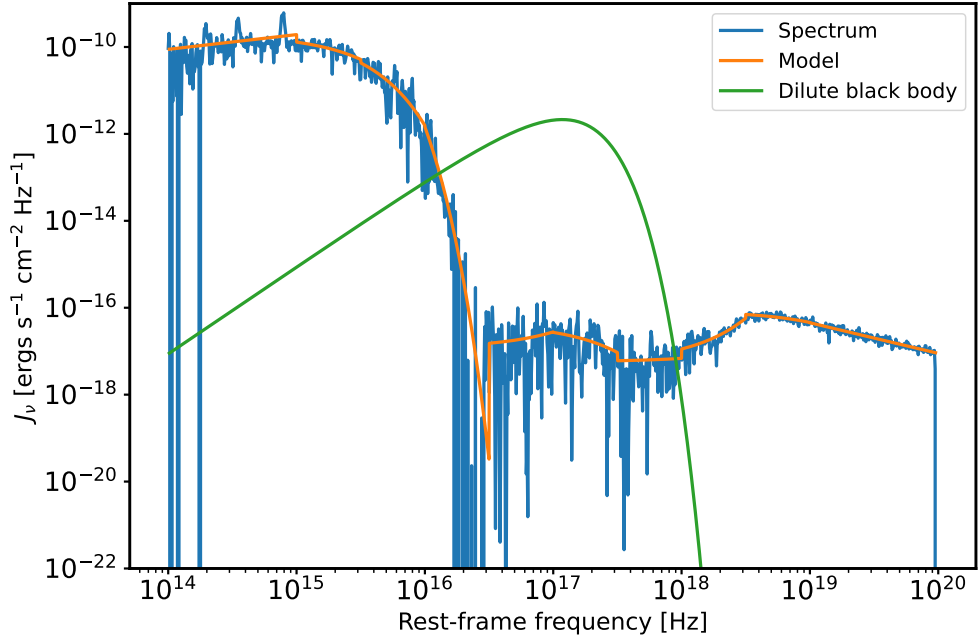


FIGURE 2.4: An example of a modelled cell spectrum, compared to both the “true” MC spectrum and to a dilute blackbody approximation. The modelled spectrum accurately reproduces the MC spectrum, whilst the dilute blackbody does not.

2.3.8.2 Modelling the radiation field

Using the properties of the photon packets, we can use MC estimators to calculate the properties of the radiation field such as the mean intensity or the flux. Following Lucy (1999), PYTHON uses the path-length formulation to estimate the mean intensity, on a cell-by-cell basis, by tracking the contribution of each *individual photon path*, in each frequency band, toward the mean intensity,

$$J_\nu = \frac{1}{4\pi V} \sum_{\text{paths}} w_i \Delta \ell, \quad (2.58)$$

where V is the volume of a cell the photon passed through, w_i is the weight of the photon and $\Delta \ell$ is the distance the photon moved in the cell, known as the path length. This estimator takes the form of the mean-value estimator of Equation 2.38, hence a sufficiently large number of photons are required to pass through a grid cell for an accurate and low noise estimator.

To combat the noise associated with mean-value estimators, PYTHON creates a series of frequency banded models of the mean intensity. The key advantage of this approach is that it is possible to create a good model of a grid cell’s SED, even when only a small

number of photons of a specific frequency band passed through that cell. Both power law and exponential fits are used,

$$J_\nu = K_{\text{pl}} \nu^{\alpha_{\text{pl}}}, \quad (2.59)$$

and,

$$J_\nu = K_{\text{exp}} e^{-h\nu/kT_{\text{exp}}}. \quad (2.60)$$

The parameter α_{pl} and the constants K_{pl} and K_{exp} are adjusted to ensure that the mean intensity of each model fits the recorded intensity by the J_ν estimator of that band. Essentially, the use of models means that the SED in a given band can be characterized by just two parameters (e.g. power law slope and normalization), which can be estimated fairly well even if the number of available photons is small. At the same time, these banded models are able to capture large departures from LTE, since the overall model SED can be far from a blackbody. Figure 2.4 shows an example of a modelled SED compared to the *true* SED of a cell, showing that the model can reproduce the SED well, even in a situation far from LTE where something like a dilute blackbody fails.

In an analogous way, estimators for higher order moments of the radiation field, such as the flux, and other quantities, such as the mean frequency of photons, can be constructed.

2.3.8.3 Ionization fractions and level populations

After a population of photons have been transported through the wind, and the estimators and outflow temperature have been updated, PYTHON computes revised ionization fractions and level populations for each ion. As mentioned previously in Section 2.3.4, metals are modelled using a two-level atom approximation, known in PYTHON as “simple atoms.” Hydrogen and helium, on the other hand, are modelled using the “macro atom” approach of Lucy (2002, 2003). Both of these schemes are greatly different from one another in how they treat and model atomic processes, and how photon packets interact with them. As such, a hybrid scheme is required to compute the ionization fractions and level populations depending on how an ion is modelled.

2.3.8.3.1 Simple two-level atoms

In the simple atom limit, line transfer is treated as a pure resonance interaction – i.e. transitions where the lower level is the ground state – even if the interaction is not a resonance interaction itself. In this case, only accurate knowledge of the ground state populations are required to sufficiently describe line formation, considerably simplifying

the situation. However, not all lines can be described by simple resonance interactions. One prime example of this is the Balmer series, which is created by recombination cascades down the various excited levels of hydrogen. In such cases, the simple two level approach fails, and another approach is required.

Throughout the photon transport, simple atoms are assumed to be in their ground state. This is done as PYTHON cannot currently compute the level population for any arbitrary mean intensity. But given that the radiation fields are often very dilute, the ground state assumption is not that bad. However, during the ionization state calculations, the level populations of simple atoms are updated assuming LTE conditions (see Section 2.1.8) or by using an alternative method to LTE, such as a dilute blackbody approximation (see Abbott & Lucy, 1985; Mazzali & Lucy, 1993; Lucy, 1999; Higginbottom et al., 2013, or Section 2.1.9). Since the outflow is assumed to be in detailed balance, any photoionization is accompanied by its inverse processes, recombination. The rates of these two competing processes are thus balanced as,

$$\gamma_{i,i+n} n_i = \alpha_{i,i-n} n_i n_e, \quad (2.61)$$

where $\gamma_{i,i+n}$ is the photo-ionization rate coefficient from an ionization state i to $i + n$ (where $n \geq 1$), $\alpha_{i,i-n}$ is the stimulated recombination coefficient from ionization state i to $i - n$ and n_i is the density of the ion.

This equation can be solved to calculate the density of an ion. To solve it, however, the ionization and recombination rates are required. The ionization rate is calculated by using a model of the mean intensity (Section 2.3.8.2),

$$\gamma_{i,i+1} = \sum_i^{\text{bands}} \int_{\nu_i}^{\nu_{i+1}} \frac{J_\nu \sigma_\nu}{h\nu} d\nu, \quad (2.62)$$

where σ_ν is the bound-free cross section for the ion. The recombination rates are obtained either from tabulated data (taken from the CHIANTI database; Dere et al., 1997; Landi et al., 2011) or, if the coefficient is not within the table's range, it is calculated using the Milne relation (see, e.g. Mihalas, 1978, 1982; Rybicki & Lightman, 1985).

By constructing a matrix of these rate equations, the ion density for all the ions included in a simulation can be found by substituting in values for the photoionization and recombination rates and solving the matrix. The matrix, taking the form $A\mathbf{x} = \mathbf{b}$, is easily solvable using a direct method such as LU decomposition (e.g. Vetterling et al., 1993). As an example, a simulation including only hydrogen and helium would have a rate matrix,

$$\begin{bmatrix} 1 & 1 & 0 & 0 & 0 \\ \gamma_{H_I, H_{II}} & -n_e \alpha_{H_{II}, H_I} & 0 & 0 & 0 \\ 0 & 0 & 1 & 1 & 1 \\ 0 & 0 & \gamma_{He_I, He_{II}} & -n_e \alpha_{He_{II}, He_I} - \gamma_{He_{II}, He_{II}} & 0 \\ 0 & 0 & 0 & \gamma_{He_{II}, He_{III}} & -n_e \alpha_{He_{III}, He_{II}} \end{bmatrix} \begin{bmatrix} n_{H_I} \\ n_{H_{II}} \\ n_{He_I} \\ n_{He_{II}} \\ n_{He_{III}} \end{bmatrix} = \begin{bmatrix} N_H \\ 0 \\ N_{He} \\ 0 \\ 0 \end{bmatrix}. \quad (2.63)$$

2.3.8.3.2 Macro atoms

The simple atom treatment is perfectly adequate for modelling resonance interactions, where the lower level of the transition is the ground state. However, it is not so good when dealing with transitions to and from excited states, such as with the Balmer series of hydrogen. For transitions like this, accurate level populations are normally required but these are not always easy to calculate. Iterative schemes for solving for the level populations are often slow and can be numerically unstable. This means simple atoms are quite unsuited to model transitions from excited states, or any line formation processes which is more complex than a single transition to and from the ground state. Recombination cascades are an obvious example of such a process.

In cases where an accurate treatment of excited levels is important, macro atoms are therefore used instead. Macro atoms are designed, by definition, to rigorously conserve energy and enforce thermal, radiative and statistical equilibrium of a system. A macro atom can be thought of as a model of an ensemble of atoms, containing the same energy levels as the *true-to-life* atom being modelled. One of the benefits of using a macro atom, is that one can obtain accurate excited state emissivities, even with a relatively poor knowledge of the populations.

Macro atoms require something of a conceptual shift to understand when compared to the simple atom approach. At a top conceptual level with simple atoms, one can imagine what is going on by thinking of photon packets striking atoms and imparting some of their energy onto the bound electrons. In macro atoms, instead of tracking photon packets interacting with electrons, the flow of radiant and kinetic energy is followed as it interacts with the levels of a macro atom.

The rate at which radiant energy is absorbed and emitted by some macro atom level i is

$$\dot{A}_i^R = R_{\ell,i} \epsilon_{i,\ell} \text{ and } \dot{E}_i^R = R_{i,\ell} \epsilon_{i,\ell}, \quad (2.64)$$

where ℓ denotes a sum over all the lower levels $< i$, ϵ is the excitation level where $\epsilon_{i,\ell} = \epsilon_i - \epsilon_\ell$, R are the radiative transition rates between levels, and \dot{A}_i^R and \dot{E}_i^R are the rates of radiative absorption and emission. Almost analogously, the rates at which

collisional (kinetic) energy, from the electron and ion thermal energy pool, is absorbed, \dot{A}_i^C and emitted, \dot{E}_i^C , is,

$$\dot{A}_i^C = C_{\ell,i}\epsilon_{i,\ell} \text{ and } \dot{E}_i^C = C_{i,\ell}\epsilon_{i,\ell}, \quad (2.65)$$

where C is the collisional rate between levels. By defining the total rate for a transition $i \rightarrow j$ as $\mathcal{R}_{i,j} = R_{i,j} + C_{i,j}$, the net rate at which a level i absorbs energy is,

$$\dot{A}_i^R + \dot{A}_i^C - \dot{E}_i^R - \dot{E}_i^C = (\mathcal{R}_{\ell,i} - \mathcal{R}_{i,\ell})(\epsilon_i - \epsilon_\ell). \quad (2.66)$$

Macro atoms are formulated under the assumption that they are in statistical equilibrium. This means that the net transition rate into and out of a macro atom level are the same. By imposing statistical equilibrium, the rate of transitions into a level is balanced by the rate of transitions out of that level, such that,

$$\mathcal{R}_{\ell,i} + \mathcal{R}_{u,i} = \mathcal{R}_{i,\ell} + \mathcal{R}_{i,u}, \quad (2.67)$$

where u denotes the sum over all upper levels $> i$. By multiplying by ϵ_i and substituting in Equation 2.66, we can write,

$$\dot{E}_i^R + \dot{E}_i^C + \mathcal{R}_{i,u}\epsilon_i + \mathcal{R}_{i,\ell}\epsilon_\ell = \dot{A}_i^R + \dot{A}_i^C + \mathcal{R}_{u,i}\epsilon_i + \mathcal{R}_{\ell,i}\epsilon_\ell. \quad (2.68)$$

This shows that when a system is in statistical equilibrium, the energy flow into a given level is matched by the energy flowing out of that level and that the energy flow depends *entirely* on the transition probabilities and the atomic physics associated with the level.

By quantifying the energy flow through a macro-atom into indivisible radiant and kinetic energy packets (*r*- and *k*-packets respectively), a Monte Carlo approach can be formulated to determine the transition rates between levels and also the population of each level of a macro atom. When an energy packet is absorbed by a macro atom level, it becomes “activated.” The macro atom can then “jump” between multiple levels (given favourable transition probabilities into a different level) before “deactivating” and emitting a *r*- or *k*-packet with the same energy as the original activating energy packet; it could also deactivate immediately without any internal jumps. The internal jumps are essentially a Monte Carlo way to record where energy is coming from in the macro atom, as the level of the final internal jump is where a packet is emitted from. Crucially, the energy packets are not modified at all. They are *indivisible*, and cannot be split into smaller or joined into larger energy quanta. What comes out of the macro atom is precisely what is put into it. But, a word of caution is also required, as non-radiative processes (i.e. shock heating or adiabatic expansion) can also be included in the macro

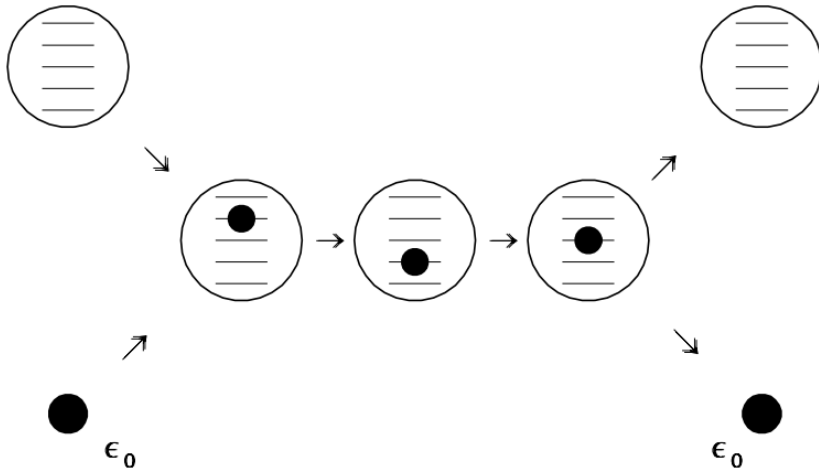


FIGURE 2.5: A schematic representation of the interaction process of an energy packet with energy ϵ_0 interacting with a macro atom. The macro atom is activated by absorbing the energy packet, makes two internal transitions, and deactivates by emitting an energy packet of equal energy ϵ_0 . Figure from Lucy (2002).

atom approach, which destroy energy packets causing a divergence from statistical equilibrium (see, e.g. Matthews, 2016). However, non-radiative processes are not enabled by default in PYTHON.

To remove the jargon, an activated macro atom can be thought as a machine which allows us to determine, in a purely statistical sense, where energy comes out when it is activated into a given level. In this sense, when a macro atom becomes activated, it has moved from one machine state into another. If this machine only had two states, then it would be activated before deactivating back into its original state. If there are multiple states, then the machine can switch (jump) between these other states, before it reaches its final state where it will deactivate, emitting an energy packet. In more basic terms: 1) activation means energy is absorbed, 2) the internal jumps are a way to determine where energy is being emitted from, 3) deactivation means energy is emitted, and 4) the state is the configuration of the machine. A basic schematic of a possible interaction process is shown in Figure 2.5. In this figure, a macro atom is activated, makes two internal jumps and then deactivates, emitting an energy packet and returning to its original state.

Since macro atoms are in statistical equilibrium, the transition probabilities (governing the activation, deactivation and jumping probability between levels) depend on the conditions of the outflow and the radiation field, which can be quantified using Monte Carlo estimators, as well as the governing atomic physics. In this sense, the macro atom and simple atom schemes are somewhat similar. However, each scheme has a separate system of estimators due to the difference in how energy packets are represented and interact. With the transition probabilities and thus transition rates between levels known, in a similar way to the simple atom scheme outlined earlier, a system of rate equations,

taking the same $A\mathbf{x} = \mathbf{b}$ form, is constructed and solved for the level populations of a macro atom with n ions and m levels,

$$\begin{bmatrix} 1 & 1 & 1 & \dots & 1 \\ \mathcal{R}_{1,2} & -(\mathcal{R}_{2,\ell} + \mathcal{R}_{2,u}) & \mathcal{R}_{3,2} & \dots & \mathcal{R}_{m,2} \\ \mathcal{R}_{1,3} & \mathcal{R}_{2,3} & -(\mathcal{R}_{3,\ell} + \mathcal{R}_{3,u}) & \dots & \mathcal{R}_{m,3} \\ \vdots & \vdots & \vdots & \ddots & \vdots \\ \mathcal{R}_{1,m} & \mathcal{R}_{2,m} & \mathcal{R}_{3,m} & \dots & -\mathcal{R}_{m,\ell} \end{bmatrix} \begin{bmatrix} n_1/N_{\text{elem}} \\ n_2/N_{\text{elem}} \\ n_3/N_{\text{elem}} \\ \vdots \\ n_m/N_{\text{elem}} \end{bmatrix} = \begin{bmatrix} 1 \\ 0 \\ 0 \\ \vdots \\ 0 \end{bmatrix}, \quad (2.69)$$

where n_i is the level population of the level m and $N_{\text{elem}} = \sum_m n_m$. Note that the first row of the A matrix and \mathbf{b} vector is set such that the calculated populations are normalised into fractional populations where $\sum_m n_m/N_{\text{elem}} = 1$. The diagonal $-(\mathcal{R}_{m,\ell} + \mathcal{R}_{m,u})$ entries represent the rate out the level, whilst off-diagonal represent the rate into the level.

2.3.8.3.3 A hybrid scheme

The macro atom formalism is seldom used by itself. Not only because PYTHON has, so far, only implemented the machinery for hydrogen and helium macro atoms, but more importantly because with current computer hardware, it is far too computationally expensive, except in the most simple of models, to model each atomic species as a macro atom. Additionally, there are numerous numerical and atomic data challenges which need to be overcome. As somewhat of a stop-gap solution, and also because the majority of models do not need every atomic species to be a macro atom, a hybrid scheme using both simple and macro atoms has been implemented.

In this scheme, hydrogen and helium are treated as macro atoms, but metals are modelled using the simple two-level atom formalism. The advantage of this is that the accurate treatment of complex hydrogen and helium line formation processes (such as recombination cascades and transitions between excited states) are accurately modelled, whilst the fast treatment of, for example, metal resonance lines is retained.

The ionization state in these two approaches are calculated using the same matrix approach detailed earlier, but separate sets of estimators are used for the different atomic models. The r - and k -packets in the macro atom approach interact with simple atoms, but since they do not possess any internal transitions any interaction with a simple atom is essentially an activation followed immediately by a deactivation into an r - or k -packet. The exact interaction and interface between simple and macro atoms is quite complex, but has been tested and described in extensive detail in, for example, Matthews et al. (2015) and Matthews (2016).

2.3.9 Synthetic spectrum generation

When the wind has reached a converged state, additional populations of photon packets are transported through the outflow whose properties are used to create synthetic spectra for a set of user-defined inclination angles. The photon packets are generated using the same radiation sources as when determining the ionization state of the wind. This time, however, the frequency distribution is sampled uniformly from a, typically narrow, frequency band of interest to create high signal-to-noise spectra.

PYTHON uses the “viewpoint” technique developed by Woods (1991) to construct spectral estimators for each defined inclination angle. Photons are tracked from emission to their eventual escape. At each interaction, the probability of a photon being scattered or re-emitted along a given inclination angle. The optical depth to escape is then calculated, and the spectral estimators are incremented by,

$$\Delta L = w f_{\theta_i} e^{-\tau_{\theta_i}} \quad (2.70)$$

where w is the weight of the photon and f_{θ_i} and τ_{θ_i} are a re-weighting function and the optical depth to escape for the inclination θ_i , respectively. When all of the photon packets have been transported through the outflow, the spectral estimators are normalised either as a luminosity or as a flux density.

Chapter 3

Ultraviolet Spectral Lines as Orientation Indicators

As for me, I'm a gurgling wizard of calorific excess.

Martin Amis

This chapter is based on the publication:

Edward J Parkinson, Christian Knigge, Knox S Long, James H Matthews, Nick Higginbottom, Stuart A Sim, Henrietta A Hewitt, Accretion disc winds in tidal disruption events: ultraviolet spectral lines as orientation indicators, Monthly Notices of the Royal Astronomical Society, Volume 494, Issue 4, June 2020, Pages 4914–4929.

3.1 Introduction

It seems that not all TDEs display UV broad absorption lines (BALs) at similar stages of their outburst evolution. For example, as illustrated in Figure 3.1, the UV spectrum of ASASSN-14li at $\Delta t = 60$ days post flare exhibits predominantly broad emission lines (BELs), whilst iPTF15af at $\Delta t = 52$ days displays BALs. This BEL vs BAL dichotomy is reminiscent of Type I QSOs. Most of these display BELs in their UV spectra, but $\simeq 20\%$ of the population display prominent BAL features (the so-called Broad Absorption Line Quasars (BALQSOs); e.g. Weymann et al., 1991; Knigge et al., 2008; Dai et al., 2008; Allen et al., 2011). In fact, as illustrated in Figure 3.1, the UV spectra of some TDEs (e.g. iPTF15af and AT2018zr in particular) show a striking similarity to those of BALQSOs. The UV spectra of TDE are unique in that the Mg II $\lambda 2796, 2804$ and C III] $\lambda 1909$ lines, commonly seen in QSO spectra, are either weak or missing entirely (Cenko et al., 2016;

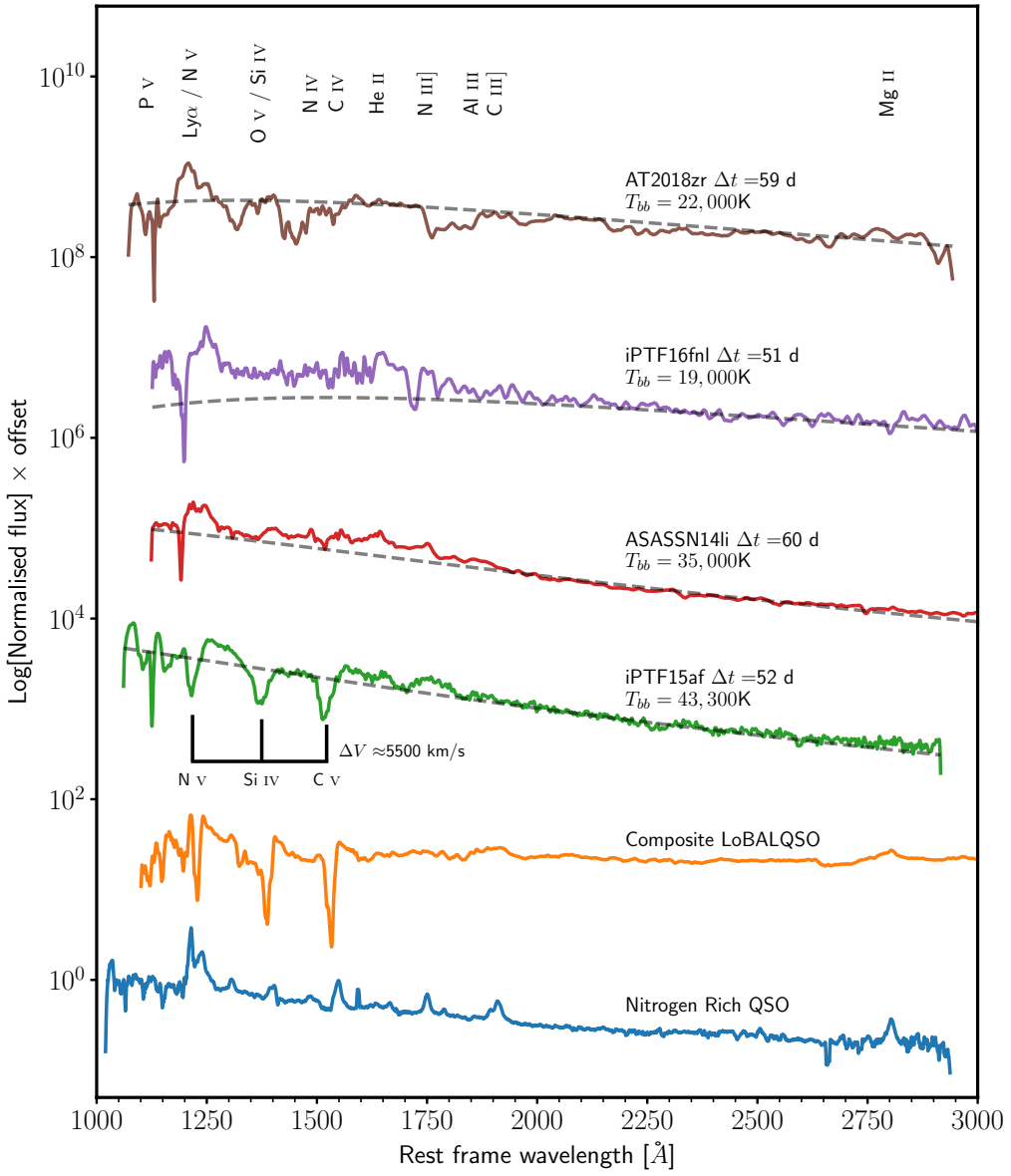


FIGURE 3.1: Rest-frame UV spectra of four TDEs: iPPTF15af (Blagorodnova et al., 2019); ASASSN14li (Cenko et al., 2016); iPPTF16fnl (Brown et al., 2017a; Blagorodnova et al., 2017); and AT2018zr (Hung et al., 2019). The spectra were all observed at similar post-flare epochs. Also included is a composite LoBALQSO spectrum (Brotherton et al., 2001) and a rest-frame UV spectrum of the nitrogen rich QSO SDSS J164148.19 +223225.22 (Batra & Baldwin, 2014). Grey dashed lines mark the continuum for each TDE spectrum, modelled using a simple blackbody of the corresponding temperature. Important line transitions identified are marked at the top. Three important transitions (C IV, Si IV and N V) are labelled for iPPTF15af with approximate blueshift as labelled.

All spectra have been smoothed using a boxcar filter.

Brown et al., 2017b; Hung et al., 2019). Conversely, TDEs also tend to display strong N III] $\lambda 1750$ emission, similar to what is seen in the rare nitrogen-rich QSOs (Batra & Baldwin, 2014; Kochanek, 2016). At least in TDEs, this enhanced nitrogen emission has been attributed to the disruption of a CNO-processed star (Kochanek, 2016; Yang et al., 2017).

In BALQSOs, line formation in an accretion disc wind can be invoked to explain the broad, blueshifted UV absorption features (Murray et al., 1995; Higginbottom et al., 2013). In fact, simple biconical disc winds can, in principle, produce both the BELs seen in “normal” QSOs and the BALs seen in BALQSOs. More specifically, BELs are always produced, via collisional excitation, in the densest parts of the outflow whereas BALs are seen *only* if the observer’s line of sight to the UV continuum source (the accretion disc) falls within the wind cone (e.g. Shlosman et al., 1985; de Kool & Begelman, 1995; Hamann et al., 2013). In such models, the BEL vs BAL dichotomy is therefore an orientation effect (e.g. Murray et al., 1995; Elvis, 2000).

Outflows are already a key ingredient in orientation-based unification schemes for TDEs. Dai et al. (2018) argues that the existence of both X-ray-bright and UV/optically-bright TDEs can be understood as an inclination effect associated with reprocessing in an optically thick disc wind. Not only that, outflows have been invoked as the line-forming region of TDEs, although detailed radiative transfer modelling has so far only been carried out using simple spherical models (Roth et al., 2016; Roth & Kasen, 2018; Dai et al., 2018).

Motivated by these considerations, the goal here is to test whether line formation in disc winds can provide a natural explanation for the BEL vs BAL dichotomy in TDEs. I also explore how the disruption of a CNO-processed star affects the emergent spectrum, testing whether the disruption of such a star can result in the nitrogen enhanced spectra of some TDEs. This chapter is structured as followed. In Section 3.2, I describe the calculations and models used. The synthetic spectra produced by my models are shown in Section 3.3. In Section 3.4 I discuss the implication of these spectra, as well as various caveats to do with my modelling, due to the limitations of the software and approach. Finally, in Section 3.5, I summarise my findings.

3.2 Model setup

Using the Shlosmann & Vitello wind parameterization described in Section 2.3.2.1, I use two sets of model parameters to create (i) a wide-angle and (ii) an equatorial disc wind, inspired by previous PYTHON models for accreting WDs and QSOs, respectively. The difference between these two geometries is illustrated in Figure 3.2. Throughout this chapter, the spectra for three inclinations are shown: 10° , 60° and 75° . These inclinations are adopted from previous work using a similar wind geometry and include at least one

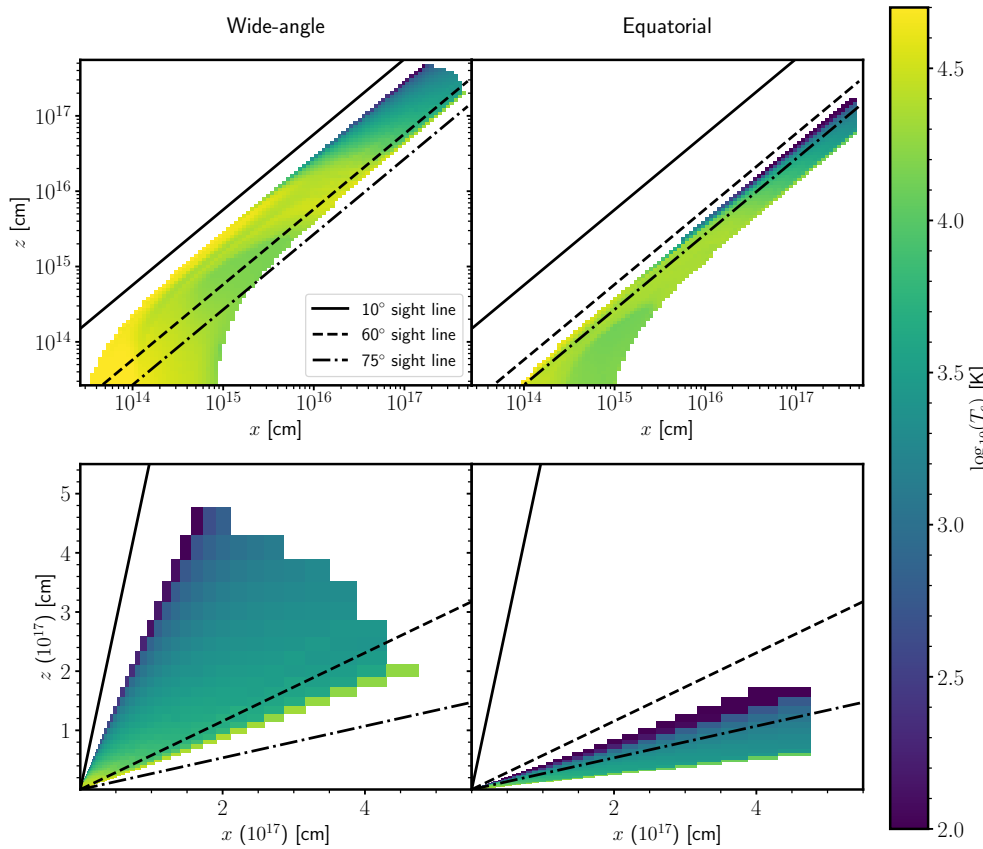


FIGURE 3.2: The geometry and temperature structure of the two adopted model geometries, described by the parameters found in Table 3.1 and in Section 3.2. The colour-map corresponds to the logarithm of the *converged* electron temperature T_e . The lines drawn over the wind show sight lines for an observer for inclination angles indicated in the legend. *Top:* the two wind geometries plotted on logarithmic axes.

Bottom: the same but are instead plotted on linear axes.

sight line which probes the properties of where most line formation is expected. The reason for the large gap between the low and medium inclination spectra is due to the main difference between the $10^\circ < \theta < 40^\circ$ spectra being the continuum normalization, caused by foreshortening, rather than spectral features.

Two radiation sources are included in the simulations, an accretion disc and the outflow. As previously discussed in Section 2.3.5, the outflow radiatively reprocesses the photons changing the frequency distribution, but it is not a *net* source of photons. The photon source, then, is a steady-state α -disc (see Section 1.2.1 or Shakura & Sunyaev, 1973), whose SED is specified entirely by the mass of the central source and accretion rate of the system, as well as the inner and outer radii of the disc. Following from mass estimates obtained by light-curve fitting of iPTF15af by Blagorodnova et al. (2019), I have assumed a black hole mass of $3 \times 10^7 M_\odot$. This mass is on the heavier side, but is at least similar to one other TDE (PS1-10jh; Gezari et al., 2012; Mockler et al., 2019). I model the accretion disc using parameters inspired by the characteristic (blackbody)

luminosity inferred for iPTF15af (Blagorodnova et al., 2019) to estimate a reasonable accretion rate. More specifically, I assumed that the blackbody luminosity of iPTF15af, $L_{\text{BB}} \sim 10^{43} \text{ ergs s}^{-1}$, roughly corresponds to the luminosity of the accretion disc, $L_{\text{acc}} = \eta \dot{M}_{\text{disc}} c^2$, for an accretion efficiency of $\eta = 0.1$. The estimated accretion rate is hence roughly $\dot{M}_{\text{disc}} \simeq 2 \times 10^{-2} M_{\odot} \text{yr}^{-1}$, corresponding to an Eddington accretion limit of 0.02 \dot{M}_{Edd} or 0.01 L_{Edd} . The outer radius of the disc for both models is set to be $R_{\text{disc}} = 10^{15} \text{ cm}$ to roughly match the continuum level of iPTF15af. As shown later in Section 3.3.1, BALs are produced by both models, but for different viewing angles. Therefore the accretion rates are adjusted for each model so that the predicted model flux for a BAL-forming sight line roughly matches the flux level of iPTF15af at $d = 350 \text{ Mpc}$. For the equatorial model, I found that the previously calculated accretion rate already matched well with observations. However, the wide-angle model required a slightly lower mass accretion rate of $\dot{M}_{\text{disc}} = 10^{-2} M_{\odot} \text{yr}^{-1}$. This difference is mainly due to foreshortening: BALs are observed for more face-on inclinations in the wide-angle model.

Based on previous experience of modelling disc winds in accreting WD and QSO systems, the mass-loss rate is initially assumed to be $\dot{M}_{\text{wind}} = 0.1 \dot{M}_{\text{disc}}$. By conducting an initial coarse parameter search, focusing on parameters which can impact line formation, i.e. the velocity law and mass-loss rate of the wind, I found that a larger mass-loss rate of $\dot{M}_{\text{wind}} = \dot{M}_{\text{disc}}$ resulted in stronger line formation for the wide-angle model, therefore adopting this scaling instead for this model. This does mean that the α -disc assumption is an even coarser approximation for the disc in this model. The substantial mass loss of the wind would most likely lower the accretion rate, producing a cooler effective temperature profile (Knigge, 1999; Laor & Davis, 2014; Miller et al., 2015). But as already shown in Section 1.2.3 by Figure 1.2 and Figure 1.4, changes to the temperature profile tend not to result in large observable differences in the spectra of the accretion disc considered.

The potential impact of clumping was also considered, not least just because the spectra of TDEs resemble those of QSOs (see Section 1.4.5.3 and Figure 3.1). A long-standing challenge for QSO line-driven wind models is that they can easily become overionized when exposed to the intense (E)UV and X-ray radiation field near the central engine (Proga, 2003; Higginbottom et al., 2013). In line-driven winds, if the wind is too highly ionized it can become impossible to sustain the wind (e.g. Proga et al., 2000; Proga, 2003). Irrespective of the driving mechanism of the wind, overionization can also prevent the formation of both absorption and emission features. Clumping is one natural way to overcome the so-called “overionization problem” and can moderate the ionization state of the outflow (Hamann et al. 2013; Matthews et al. 2016; another solution is self-shielding, e.g. Murray et al. 1995; Proga et al. 2000; Proga & Kallman 2004).

Overionization can also be expected to be a challenge for spectral models of TDEs. The range of X-ray-to-optical ratios, L_x/L_{opt} , observer in these systems at $\Delta t \approx 60$

days (Auchettl et al., 2017; Wevers et al., 2019) is broadly comparable to that seen in QSOs (Steffen et al., 2006). Clumping is therefore also an important effect to consider. However, the large dispersion in the ratio seen in both types of systems may be due to geometric effects, highlighting the need for unified models (e.g. Dai et al., 2018). With these considerations, I explored the impact of clumping using the micro-clumping framework as described in Section 2.3.3, using a volume filling factor of $f_v = 0.1$.

The final parameter choices for the two wind models are presented in Table 3.1. I also conducted a finer parameter search around the values in Table 3.1, finding that the ionization state and emergent spectra are fairly insensitive to moderate changes in these values.

In both models, the disc wind emanates from the entire surface of the accretion disc, choosing a values of $\gamma = 1$ for uniform streamline spacing and $\lambda = 0$ corresponding to uniform mass loss across the disc surface. The models use a logarithmic cylindrical grid with a greater concentration of cells at smaller radius, where most of the line formation is expected to occur. Several resolution tests were conducted. For grids with a spatial resolution lower than 50×50 cells, dramatic changes to the line profiles are observed between the low resolution grids as the line-forming region was inadequately spatially resolved, resulting in artificial and odd line profiles. For resolutions higher than 75×75 cells, only small changes between the emergent spectra were found. In the final calculations, the models use a grid with 100×100 cells to fully ensure that the emission and absorption line profiles are not affected by poor spatial resolution. The models adopt a maximum wind radius of $R_{\text{wind}} = 5 \times 10^{17}$ cm to ensure the computational domain is large enough to not affect the results. Test models where the maximum wind radius was changed by a factor of a few showed little effect on the emergent spectra. Whilst PYTHON now includes special relativistic effects, these models here predate this treatment. Hence, Doppler shifts between the observer and co-moving fluid frame are calculated using a linear approximation.

3.3 Results

In the following sections, I present the results of my simulations. In Section 3.3.1, I present a fiducial clumpy wide-angle outflow using solar abundances, discussing the physical properties of the outflow and its synthetic spectra, in the context of how an accretion disc wind could be responsible for the observed BEL vs BAL dichotomy. I then examine the effects of the different wind geometries in Section 3.3.2, followed by how microclumping and abundance variations impact the emergent spectrum in Section 3.3.3 and Section 3.3.4 respectively.

Parameters	Wide-angle	Equatorial	Units
r_{\min}	2.65×10^{13}	2.65×10^{13}	cm
	6	6	r_g
r_{\max}	7.95×10^{14}	7.95×10^{14}	cm
	180	180	r_g
α_v	1.5	1.0	-
v_∞	1.0	1.0	v_{esc}
R_v	5×10^{16}	5×10^{16}	cm
	11291	11291	r_g
θ_{\min}	20	70	°
θ_{\max}	65	82	°
\dot{M}_{wind}	10^{-2}	2×10^{-3}	$M_\odot \text{yr}^{-1}$
\dot{M}_{disc}	10^{-2}	2×10^{-2}	$M_\odot \text{yr}^{-1}$

TABLE 3.1: Parameters and their respective values adopted for the two wind geometries shown in figure 3.2.

3.3.1 A fiducial wide-angle disc wind

I will now describe a clumpy wide-angle disc wind with solar abundances and clumping factor $f_v = 0.1$ in the context of the formation of BALs and BELs. Based on the limited exploration of parameter space (see Section 3.3.2, Section 3.3.3 and Section 3.3.4 below), I use this as a fiducial disc wind ‘‘benchmark’’ model.

Figure 3.3 shows a selection of physical parameters for the wide-angle wind on a log-log distance scaling, and Figure 3.4 shows the synthetic UV spectra produced by this model, compared to the spectra of a BAL (iPTF15af) and a BEL TDE (ASASSN14li). For the BAL sight, I have adopted an inclination of $i = 60^\circ$, i.e. a sight line which looks into the wind cone. To represent BEL models, I show spectra for both face-on ($i = 10^\circ$) and edge-on ($i = 75^\circ$) sight lines, both of which lie outside the wind cone.

3.3.1.1 The physical properties

Figure 3.3 shows a selection of physical parameters for the converged wide-angle wind. Considering first the electron number density of the wind, the base has a high density with $n_e \sim 10^{11} \text{ cm}^{-3}$. The electron density declines gradually with radius due to the expansion and acceleration of the wind, resulting in line formation processes which scale with density decreasing in the outer wind regions. The velocity at the base of the wind is dominated by rotation, where it is effectively Keplerian. Here, the velocity is $v_\phi \sim 10^5 \text{ km s}^{-1}$ at the inner disc edge and $v_\phi \sim 10^4 \text{ km s}^{-1}$ at the outer edge. Further out in the wind, the rotational velocity decreases linearly due to the wind material conserving specific angular momentum. The poloidal velocity of the outflow, however, increases

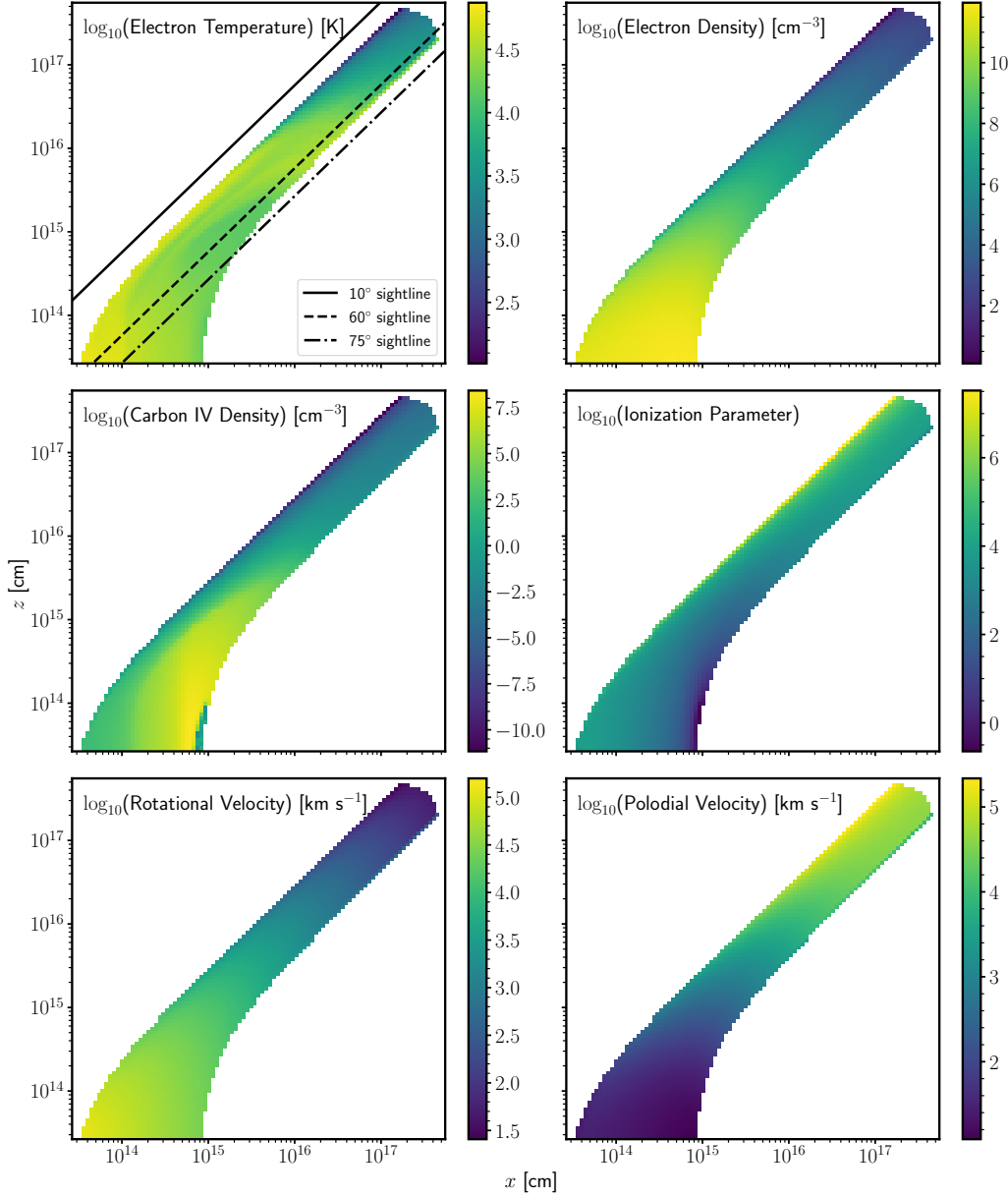


FIGURE 3.3: Contour plots showing a selection of physical properties for the clumpy wide-angle disc wind, with clumping factor $f_v = 0.1$. Only the x - z plane is shown where the wind is rotationally symmetric about the z -axis. The lines drawn over the wind show sight lines for an observer for the inclination angles indicated in the legend. The spatial scales and colour maps are logarithmic. *Top left:* the electron temperature. *Top right:* the electron number density. *Middle left:* the C IV ion density. *Middle right:* the ionization parameter. *Bottom left:* the rotational velocity. *Bottom right:* the poloidal velocity.

with distance, as determined by the velocity law exponent. At the base of the wind, streamlines are launched from the surface of the disc with a velocity set by the local sound speed, corresponding to $v_l \sim 10 \text{ km s}^{-1}$. At the very top of the wind, the streamlines have accelerate to $v_l \sim 10^5 \text{ km s}^{-1}$ ($0.3c$). Doppler broadening of emission and absorption lines is dominated by rotation near the disc-plane and by the poloidal outflow velocity further out.

The hottest region of the wind is at the base, where it is exposed directly to the radiation field from the accretion disc. Here, the electron temperature is $T_e \sim 3 \times 10^4 \text{ K}$. At larger radii, near the outer edges, where adiabatic cooling dominates, the wind is cooler with $T_e \sim 10^3 \text{ K}$ and can be as low as $T_e \sim 10^2 \text{ K}$ where the density of the wind is lowest. In these regions, the wind is illuminated by the reprocessed disc SED. The flux of high-frequency photons is reduced significantly in these regions, resulting in less energy being dumped into the wind and subsequently less heating. In reality, dust and/or molecules could potentially form in this region. However, since PYTHON does not include any dust or molecular physics, the treatment of these regions is highly approximate. But should not contribute significantly to the formation of the UV features of interest. It is also worth noting that the ionization state of these cells could be *frozen-in*, i.e. set by the advection of the physical properties and ionization state of the outflow at smaller radii (see, e.g. Owocki et al., 1983). In PYTHON, the ionization state is always computed based on the local properties of the radiation field and grid cell, i.e. this kind of freezing-in is not modelled. However, at the large radii where this is relevant, the ionization state is roughly constant along flow lines in the models.

It is possible to characterise the ionization state of the wind by using an ionization parameter, U_H , given by,

$$U_H = \frac{4\pi}{n_H c} \int_{13.6 \frac{\text{eV}}{h}}^{\infty} \frac{J_\nu}{h\nu} d\nu, \quad (3.1)$$

where ν denotes frequency, n_H is the number density of hydrogen, c is the speed of light, h is Planck's constant and J_ν is the monochromatic mean intensity. The ionization parameter measures the ratio of the number density of hydrogen ionizing photons to the local hydrogen matter density. For values of $U_H > 1$, hydrogen is ionized making it a useful predictor of the global ionization state. Throughout most of the wind, U_H is roughly constant with $U_H \sim 10^4$. As $U_H > 1$, this indicates that hydrogen is ionized throughout the wind and suggests that $n_H \simeq n_e$. The “top” of the wind is highly ionized with $U_H \sim 10^7$. The UV absorption lines form along sight lines where the relevant ion density is large, i.e. where the C IV ion density $n_{\text{C IV}} \gtrsim 10^6 \text{ cm}^{-3}$, approximately traced along the 60° sight line (middle left panel of Figure 3.3). The UV emission lines, on the other hand, preferentially form in the base of the wind, where the electron density is high.

3.3.1.2 The emergent spectrum

The top panel of Figure 3.4 shows the spectrum for BAL case of the fiducial model. This model produces broad absorption in the strong resonance lines of C IV, Si IV and N V. The wide-angle BAL model, however, is clearly far from a perfect match to iPTF15af. It is encouraging, however, that it produces BALs in essentially the correct set of transitions, for a UV continuum that reasonably matches observations in both shape and normalisation.

One interesting feature of the BAL model is that the profiles of C IV and N V are significantly blueshifted, whereas the Si IV absorption feature is centred close to the rest wavelength of the rest transition. This reflects the ionization state of the model. The dominant ionization stage of silicon throughout most of the outflow is actually Si V. As a result, Si IV is typically formed only in the dense, low velocity base of the wind resulting in a small blueshifting of the Si IV absorption line. The model spectrum also features broad and blueshifted O VI $\lambda 1034$, representing an even higher ionization potential than N V.

The bottom panel of Figure 3.4 shows the BEL spectra produced for face-on and edge-on sight lines. At $i = 10^\circ$, the model produces strong C IV, N V and Ly α emission lines. The same transitions are also seen in emission at $i = 75^\circ$, but the lines are now so broad that N V and Ly α are blended. Neither spectrum produces Si IV emission, again reflecting that Si V dominates throughout most of the outflow. However, a weak absorption trough associated with Si IV can be identified in the edge-on spectrum, which cuts through the dense, low velocity base of the wind where Si IV ions are preferentially found. The BELs seen in ASASSN14li are considerably narrower than those produced by the wide-angle model for $i = 75^\circ$, favouring the association of BEL TDEs with a face-on system.

3.3.2 Wide-angle vs equatorial winds

The spectra produced by both wide-angle and equatorial wind models are shown in Figure 3.5 (for smooth vs clumpy outflows) and Figure 3.6 (for solar vs CNO-processed abundances). The dependence of the spectra on clumpiness and abundances will be discussed in Section 3.3.3 and Section 3.3.4, respectively. Here, I will first briefly comment on the basic differences between the spectra produced by the two types of outflow geometry. The implications of these differences is discussed in more detail in Section 3.4.1.

In principle, both wide-angle and equatorial winds are able to produce BALs and BELs. In both geometries, BALs are observed preferentially for sight lines looking into the wind cone. However, wide-angle flows produce BELs for both low and high inclinations, whereas the equatorial model only produces BELs at low inclinations. Perhaps more importantly, in terms of line-to-continuum contrast, the equatorial model only produces

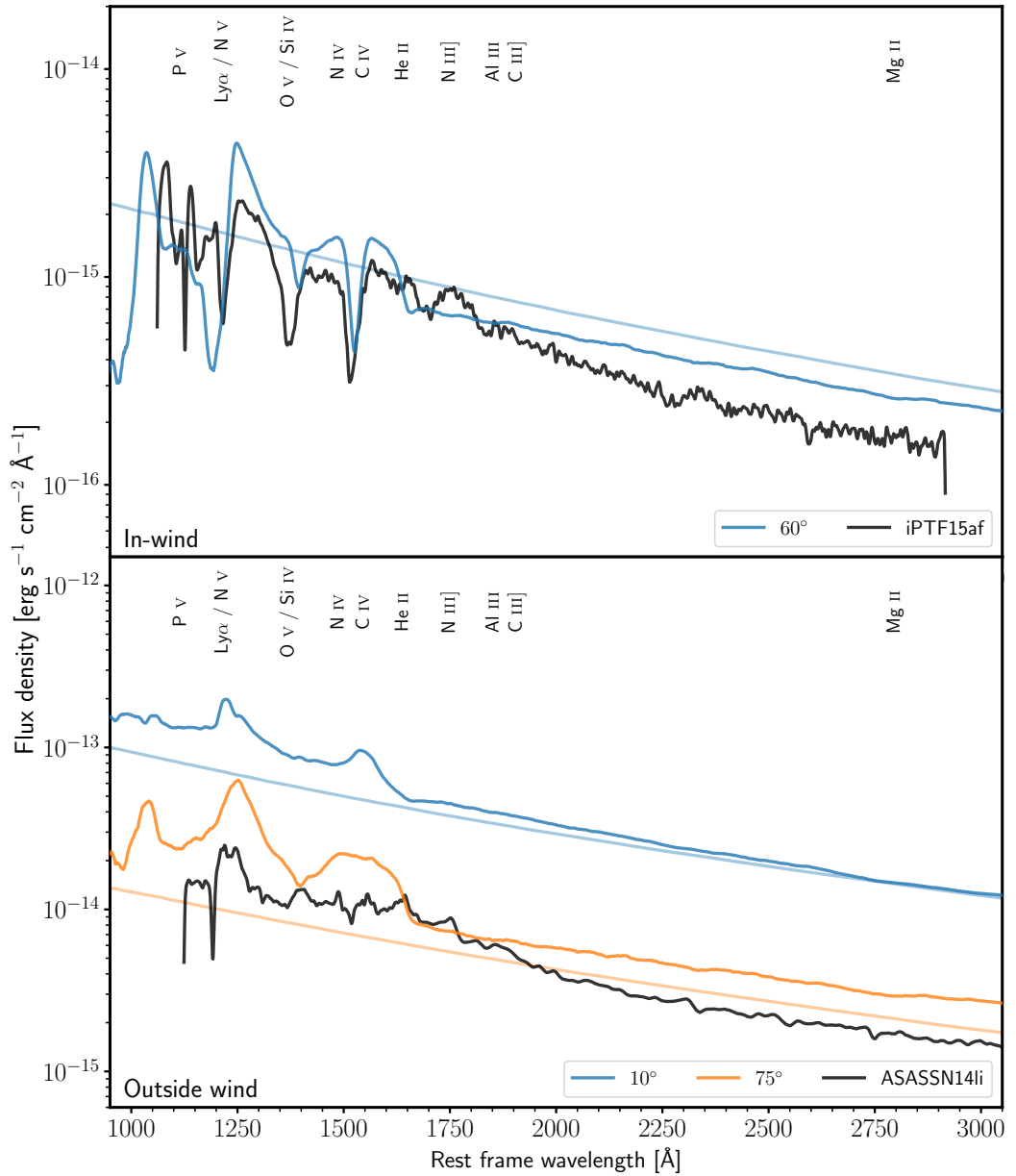


FIGURE 3.4: Synthetic UV spectra of a clumpy ($f_v = 0.1$) wide-angle disc wind for three sight line angles. Over-plotted are both a *characteristic* BAL (iPTF15af) and BEL TDE (ASASSN14li) for comparison. Marked by faded lines is the accretion disc SED. The flux of the model has been scaled to the distance of the relevant TDE which it is compared to. Important line transitions in the spectra have been marked at the top of each panel. *Top panel:* an observer with a line of sight through the wind cone, which observes BALs. *Bottom panel:* an observer with a line of sights not looking through the wind cone, observing, instead, BELs.

very weak emission lines. This is partly due to the anisotropic radiation pattern produced by the disc in the model. As a result, the continuum level is much higher for the face-on orientations that can produce BELs in the equatorial wind model. The line emission produced by the wind is always more isotropic than the disc continuum, so it is harder to achieve high line-to-continuum contrasts in equatorial models. As discussed further in Section 3.4, it is actually not clear if real TDE discs emit this anisotropically. For a more isotropic continuum source, the *emission* line-to-continuum contrast will be considerably more uniform across all orientations. However, *absorption* features would still be formed preferentially for sight lines looking into the wind cone.

3.3.3 Clumping

Figure 3.5 illustrates the effect of clumping on the emergent spectra. More specifically, it compares the spectra produced by smooth winds ($f_v = 1$) to those produced by (micro-)clumpy winds, with a clump to inter-clump density ratio of 10 (i.e. $f_v = 0.1$).

The main effect of clumping is to strengthen the UV resonance transitions. This happens because clumping increases the density of the line-forming gas and hence lowers its ionization state. In the wind models presented here, which tend to be somewhat overionized, this increases the abundance of the ionic species responsible for the UV lines. For the “in-wind” (BAL) spectra, this manifests as deeper and broader absorption troughs. The BALs are also more highly blueshifted, as the abundance of the relevant ions in the high velocity regions of the wind is increased. Emission lines are additionally strengthened in clumpy winds, because collisional excitation scales as the *square* of the density in the line-forming region.

The presence of clumps is particularly important for the formation of Si IV. As noted before, Si V tends to be the dominant ionization stage of silicon in the models, but clumpy winds contain enough Si IV to produce BAL features for sight lines looking into the outflow. This feature is not generally observed in the smooth wind models.

3.3.4 Abundances

Some UV spectra of TDEs present strong nitrogen emission lines, but weak or undetectable carbon lines; e.g. iPTF15af and ASASSN14li. This has been attributed to an enhanced nitrogen to carbon ratio in the line-forming region, as expected from TDEs associated with stars that have undergone CNO-processing (Kochanek, 2016; Yang et al., 2017). I therefore carried out some simulations with abundances representing CNO-processed material. In these, the relative abundances of helium, carbon and nitrogen were changed to $(X/X_\odot)_{^2\text{He}} \approx 2$, $(X/X_\odot)_{^6\text{C}} \approx 0.5$ and $(X/X_\odot)_{^7\text{N}} \approx 7$, where X_\odot is the relevant solar abundance. These values are based on abundances calculated by

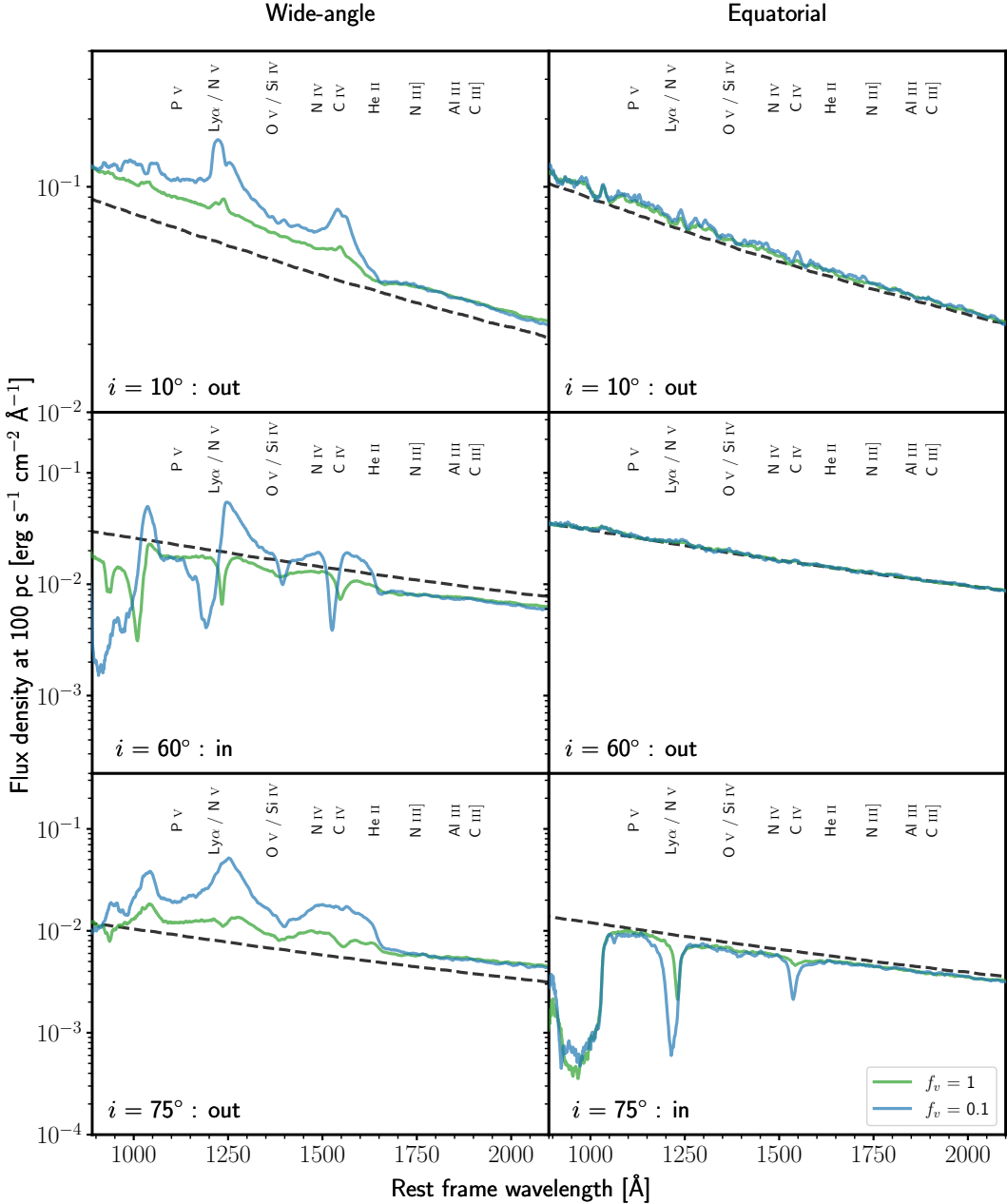


FIGURE 3.5: Synthetic UV spectra of a smooth and clumped wind for the two wind geometries at characteristic low, medium and high inclination angles. Important line transitions have been marked at the top of each panel and the accretion disc SED is shown using a dashed line. Clumped winds produce stronger absorption and emission features, due to the increased density of the clumps increasing the abundance of the relevant ions.

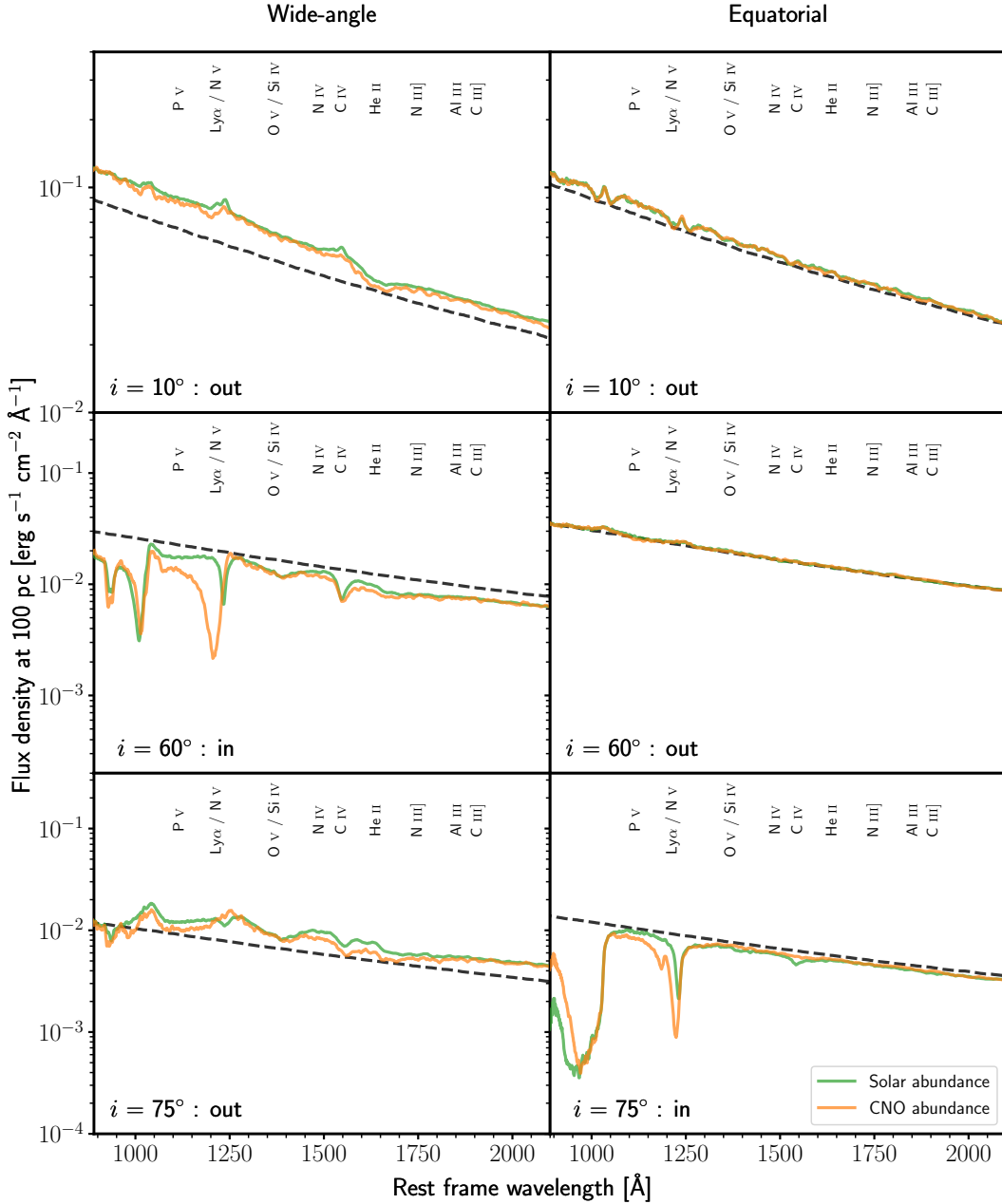


FIGURE 3.6: Synthetic UV spectra generated for smooth winds of both wind geometries using both Solar and CNO-processed abundances for a low, medium and high inclination angle. The accretion disc SED is also shown with a dashed line and important line transitions are marked at the top. By switching to CNO-processed abundances, the N V absorption line is strengthened but the rest of the spectrum is relatively unchanged.

Gallegos-Garcia et al. (2018) for a $\simeq 1.8M_\odot$ star near the terminal main sequence. In Figure 3.6 and Figure 3.7, I explore the impact of abundance variations by showing synthetic spectra produced by smooth and clumpy winds with solar and CNO-processed abundances, respectively.

For smooth equatorial winds, the change to CNO-processed abundances results in a slight

suppression of the C IV line. The temperature and ionization structure of the wind is roughly the same for both abundance patterns, suggesting that this suppression is due to the change in the abundance of carbon atoms, rather than a change in the ionization state. This suppression is less obvious in the wide-angle wind model, probably because C IV is more dominant, resulting in the line being more optically thick here. In any case, the effect of the CNO-processed abundances on the N V BAL is much greater. In both wind geometries, this feature becomes both deeper and broader as the density of nitrogen atoms increases in the wind.

The effect of CNO-processed abundances on clumpy winds is similar, but stronger. Figure 3.7 shows a comparison between the two abundances for a clumping factor $f_v = 0.1$. For the equatorial wind, again, the C IV absorption has weakened, whereas it remains unchanged for the wide-angle wind. As before, the strongest effect is on the N V BAL, which is once again deeper and broader with CNO-processed abundances.

3.4 Discussion

3.4.1 UV lines as geometry and orientation indicators

BALs have been (at time of writing) detected in three out of four UV spectra of TDEs. As pointed out by Hung et al. (2019), this suggests that the appearance of these outflows is less sensitive to viewing angle than that of the outflows in QSOs, where BALs are seen in only $\simeq 20\%$ of sources (e.g. Knigge et al., 2008; Allen et al., 2011). If BALs are observed preferentially for sight lines to the central engine that pass through the outflow, the fraction of systems displaying them is a measure of the wind “covering factor”, i.e. the solid angle subtended by the wind, as seen by the central engine. In practice, selection effects will complicate this picture. For example, if bright systems are over-represented in observational samples, fore-shortening, limb-darkening and attenuation by the wind itself will all lead to orientation-dependent incompleteness. Moreover, TDEs are evolving systems, so their outflows and associated BALs are bound to be transient features. Nevertheless, for TDEs observed at similar stages of their eruptions, as is the case for the objects shown in Figure 3.1, the incidence rate of BALs should provide a reasonable initial estimate of the outflow covering fraction.

The finding that a wide-angle wind model seems to match the observations better than an equatorial one is in line with this picture. The covering factor, $f_\Omega = \int_{\theta_{\min}}^{\theta_{\max}} \sin(\theta) d\theta$, of the wide-angle wind model is $f_\Omega = 0.52$, whereas that of the QSO-inspired equatorial model is $f_\Omega = 0.20$. A wide-angle wind model spanning an even wider range of opening angles is clearly worth exploring in future.

In the context of the wide-angle wind model, where $\theta_{\min} > 0^\circ$ and $\theta_{\max} < 90^\circ$, BELs are seen for both very low and very high inclinations. Do TDEs displaying BELs correspond

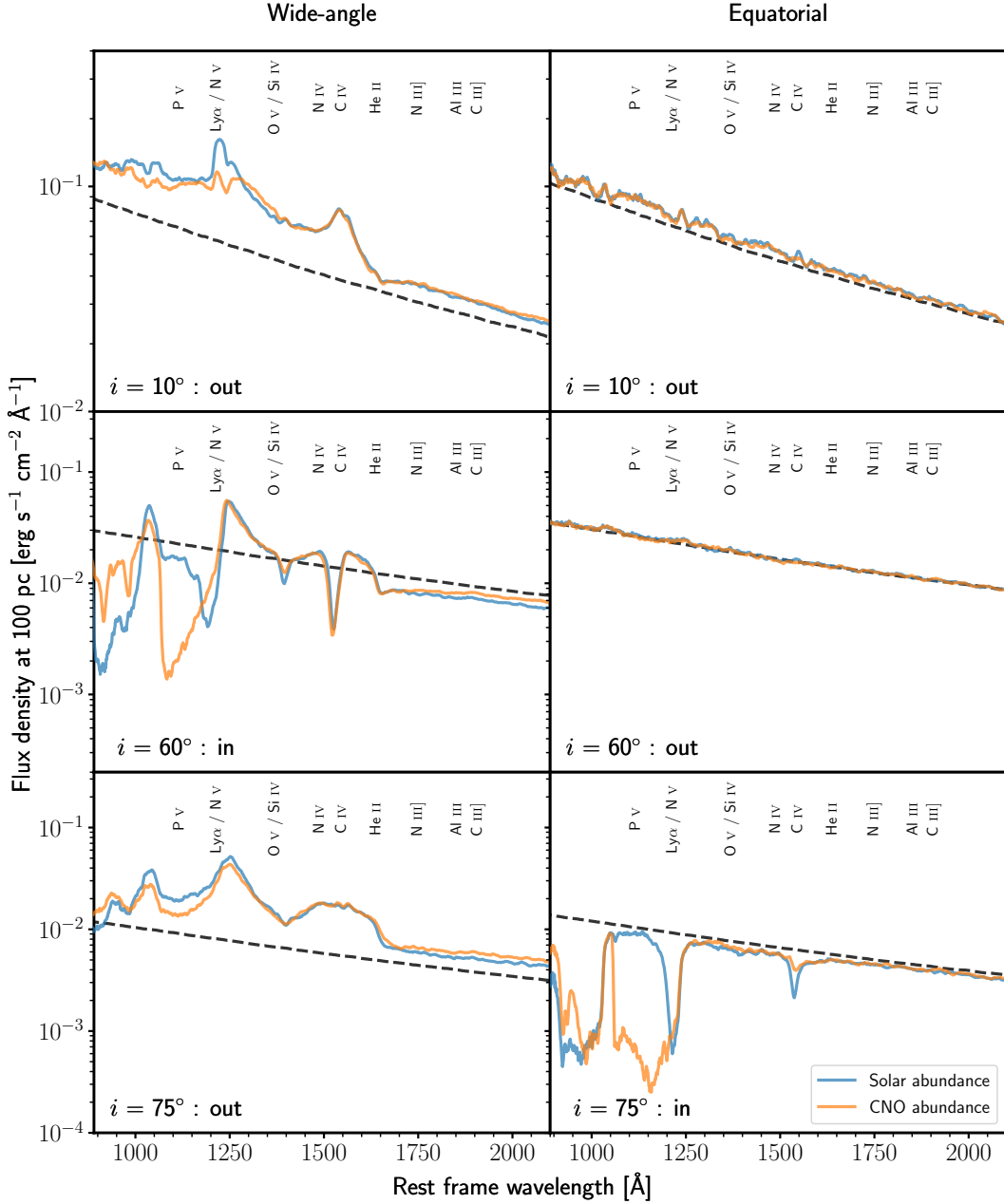


FIGURE 3.7: Synthetic UV spectra generated for clumped winds for both of the wind geometries using Solar and CNO-processed abundances at a low, medium and high inclination angle. The accretion disc SED is also shown with a dashed line and important line transitions are marked at the top. As in Figure 3.6, the most significant change is the N v absorption line which is stronger with CNO-processed abundances.

to extremely face-on systems, extremely edge-on ones, or both? For the fiducial model, the narrower line widths seen for face-on orientations appear to be more in line with the very limited observational data (c.f. Figure 3.4). On the other hand, extremely face-on orientations are *a priori* unlikely. As assuming random orientations for an accretion disc system, i.e. equal probability per unit solid angle, then only 6% of randomly oriented systems would be viewed at inclinations $i < 20^\circ$, whereas 42% would be viewed at $i > 65^\circ$. In any case, the detailed line shapes produced by the models should not be over-interpreted: the parameter space of even just wide-angle models is large, and, as discussed in Section 3.4.3 below, the models still have significant limitations that are likely to affect the line profiles. As the sample of TDEs with UV spectroscopy grows, it will be interesting to check for correlations between the incidence of BALs/BELs and other system properties that might depend on orientation (such as the X-ray to optical ratio; Dai et al., 2018).

3.4.2 The optical depth of disc winds in TDEs

Several lines of evidence suggest that the outflows of TDEs may be optically thick. For example, the likely presence of P v $\lambda 1118^1$ in iPTF15af suggests a column density of $N_H > 10^{23} \text{ cm}^{-2}$ (Blagorodnova et al., 2019). A similar constraint has been obtained for AT2018zr from the detection of BAL signatures in Balmer and metastable helium lines (Hung et al., 2019). From a modelling perspective, Roth & Kasen (2018) have shown that the detailed line profile shapes seen in TDEs can be understood if these features are formed in an optically thick outflow. Finally, the reprocessing of radiation produced by the central engine in an optically thick, non-spherical wind is also central to the unification scenario presented by Dai et al. (2018), which is based on 3D general relativistic magneto-hydrodynamic simulations of the super-Eddington accretion phase near the peak of TDE flares.

How optically thick is the fiducial clumpy wide-angle wind model? Figure 3.8 shows the continuum (free-free, bound-free and electron scattering) optical depth through this model, as a function of frequency, for several lines of sight. Starting from a point at the inner disc edge, each sight line runs radially outward, making an angle i with the normal to the disc plane. At low frequencies, electron scattering is the dominant source of opacity. The electron scattering optical depth is $\tau_{es} > 1$ for all of the sight lines shown ($30^\circ \leq i \leq 85^\circ$). For $i = 30^\circ$, the optical depth is moderate, $\tau_{es} \simeq 3$, but it increases monotonically with inclination, reaching $\tau_{es} \simeq 30$ for $i = 85^\circ$. This increase continues even for sight lines that exit the wind cone, i.e. $i > \theta_{max}$, because the shorter path through the wind for these sight lines is more than compensated by the higher densities found at the base of the wind.

¹Note that this transition is currently not included in PYTHON's line list.

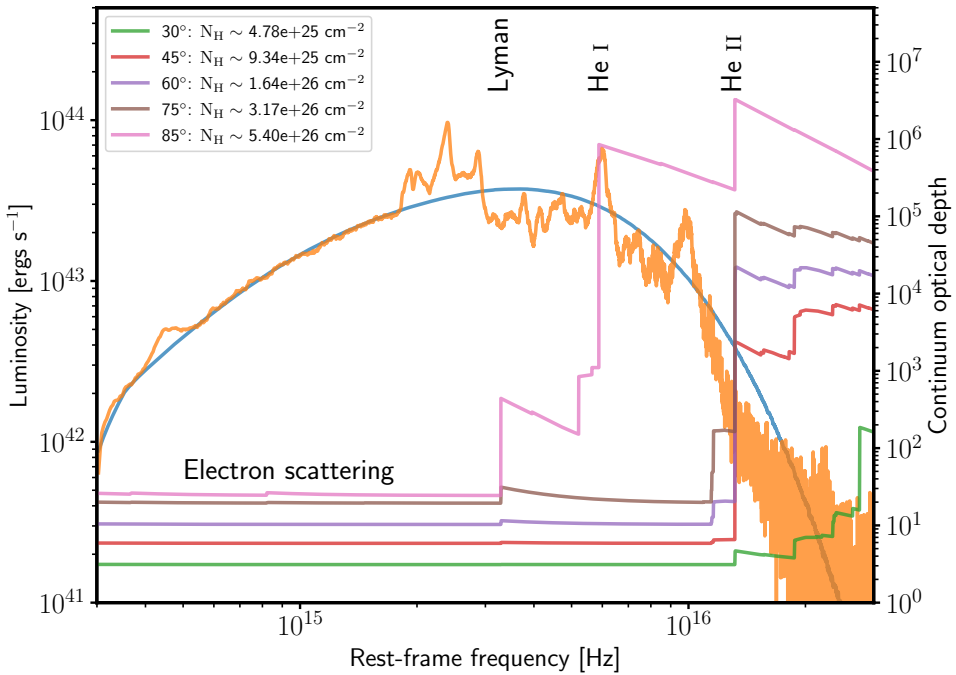


FIGURE 3.8: The continuum optical depth of the fiducial model shown in Figure 3.4. Marked by the solid blue is the angle averaged accretion disc SED for the model and shown by the solid orange line is the angle averaged emergent luminosity for the model. Included in the legend are the hydrogen column densities of each sight line. Important absorption edges are marked at the top of the figure. High frequency flux from the accretion disc is absorbed and re-radiated at longer wavelengths.

At higher frequencies, the opacities are dominated by photo-ionization. In particular, the He II edge at 54.4 eV (228 Å) is highly optically thick for essentially all inclinations. The Lyman edge at 13.6 eV (912 Å) and the He I edge at 24.6 eV (504 Å) only start to make a noticeable contribution to the opacity for high-inclination lines of sight that pass through the dense, less ionized wind base. Figure 3.8 also includes the angle-averaged input disc SED and the angle-averaged emergent flux of the model for comparison. This shows that the contribution of He II ionizing photons, which will be almost completely reprocessed by the wind, is not dominant, but still significant in the fiducial model. The majority of the reprocessed emission in the model is emitted at optical wavelengths and at high inclination angles. The column densities along the sight lines shown in Figure 3.8 range from $N_H \simeq 5 \times 10^{25} \text{ cm}^{-2}$ (at $i = 30^\circ$) to $N_H \simeq 5 \times 10^{26} \text{ cm}^{-2}$ (at $i = 85^\circ$). These values are compatible with the lower limits suggested by Blagorodnova et al. (2019) and Hung et al. (2019).

3.4.3 Limitations and future work

As is the case for any computational model, the calculations here have several limitations. First, PYTHON is time-independent, so it implicitly assumes that the flow is in

a steady-state on time-scales short to the time-scales over which the TDE luminosity and SED evolve significantly. Perhaps most importantly, however, is that these models were created when PYTHON was a purely Newtonian code. In particular, this means general relativistic effects are neglected on the photon paths in my simulations. Whilst the full random walk of photons is simulated, photons travel in straight lines between interaction points throughout the computational domain. There is no concept of an event horizon. As a simple test of this approximation, I repeated the simulation of the fiducial wide-angle wind removing all photons which intersected a sphere of radius R_{ISCO} centred on the BH. The ionization state and emergent spectra changed only marginally relative to the fiducial model. PYTHON also did not at this point take into account the full detailed effects of special relativity, which will have an effect on the Doppler shifts experienced by photons and hence on the emergent line profiles. However, this should not affect the overall ionization state of the flow, nor the qualitative appearance of the emission and absorption line spectra.

Another clear limitation in the model is the description of the accretion disc as a standard steady state α -disc (Shakura & Sunyaev, 1973). In reality, the inner discs in these systems are dominated by radiation pressure and are almost certainly vertically extended. However, the structure, evolution, and even the stability, of such discs are the subject of intense research in radiation-dominated regimes (e.g. Hirose et al., 2009; Jiang et al., 2013; Shen & Matzner, 2014). Additionally, relativistic effects of accretion onto a Kerr black hole is also likely to play a crucial role in TDEs (Balbus & Mummery, 2018; Mummery & Balbus, 2020), particularly at late times (Mummery & Balbus, 2020). In the absence of a simple, physically realistic description of such discs, the reliance on the standard α -disc picture is mainly a practical choice. From the perspective of modelling the outflow, the most important aspect of this approximation may be the angular distribution it imposes on the photons produced by the disc. Due to fore-shortening and limb-darkening, geometrically thin and optically thick discs generate a highly anisotropic radiation field. PYTHON adopts the Eddington approximation for limb-darkening, so that the specific intensity produced by the disc scales as $I \propto \cos i(1 + \frac{3}{2} \cos i)$. This degree of anisotropy is likely to be an overestimate for the vertically extended inner discs in rapidly accreting TDEs. Given that the outflow itself reprocesses, and hence isotropises the disc radiation field, it should not change the results qualitatively. However, a more physically realistic description of the accretion discs in TDEs may be needed to enable meaningful *quantitative* modelling of observational data.

Finally, in PYTHON, only hydrogen and helium are self-consistently described with full, multi-level model atoms. By contrast, bound-bound transitions in metals are currently treated via a 2-level atom approximation that is reasonable for resonance lines, but not for transitions involving excited and/or meta-stable states. As a result, the simulations are unable to produce semi-forbidden transitions at the moment, such as N III] or C III], which are present in the data and could, in future, be useful outflow diagnostics.

3.5 Summary

Line formation in an accretion disc wind may account for the BEL vs BAL dichotomy observed in the UV spectra of TDEs. In order to test this hypothesis, I conducted MCRT simulations to generate synthetic UV spectra of wind- and disc- hosting TDEs, based on a simple biconical disc wind parameterization. The models cover a wide range of wind geometries and kinematics. I also studied the effects of wind clumping and CNO-processed abundances on the spectra. The main results are as follows:

1. Disc winds are naturally able to produce both BALs and BELs, depending on the sight line of the observer. Sight lines which look through the wind cone preferentially produce BALs, whereas other orientations, which do not look through the wind, tend to produce BELs.
2. The “best-bet” fiducial model is a clumpy wide-angle accretion disc wind that subtends more than 50% of the sky as seen from the central engine. Such a geometry is consistent with the high covering factor implied by the detection of BALs in three out of four TDEs with UV spectra to date.
3. Clumping is required to lower the ionization state of the wind and results in an increased abundance of the relevant ionic species. Both absorption and emission lines are broader and stronger in clumpy wind models, relative to the same lines produced by smooth wind models.
4. The main effects of switching from solar to CNO-processed abundances is a weakening of C IV $\lambda 1550$ features and a strengthening of N V $\lambda 1240$ ones. Both of these effects are due to the change in the abundances of the relevant species, rather than a major change in the ionization state of the wind.
5. At long wavelengths, the dominant source of continuum opacity in the models is electron scattering. At shorter wavelengths, and especially for sight lines passing through the dense base of the outflow, the dominant source of opacity is photo-ionization. In particular, the He II edge is highly optically thick for all sight lines in the fiducial model.
6. The column densities presented by the fiducial model are within the range of $3 \times 10^{25} \text{ cm}^{-2} \lesssim N_H \lesssim 3 \times 10^{26} \text{ cm}^{-2}$ for inclinations between $i = 30^\circ$ and $i = 85^\circ$, with higher columns corresponding to higher inclinations. This is consistent with the empirically inferred lower limits of $N_H \gtrsim 10^{24}$ in BAL-hosting TDEs.

3.6 Data availability

The models and their synthetic spectra from this chapter are publicly available online at https://github.com/saultyevil/tde_uv_disc_winds_2020.

Chapter 4

Optical Line Spectra from Reprocessing in Optically Thick Outflows

Men of Tanith! Do you want to live forever?

Colonel-Commissar Ibram Gaunt

This chapter is based on the publication:

Edward J Parkinson, Christian Knigge, James H Matthews, Knox S Long, Nick Higginbottom, Stuart A Sim, Samuel W Mangham, Optical line spectra of tidal disruption events from reprocessing in optically thick outflows, Monthly Notices of the Royal Astronomical Society, Volume 510, Issue 4, January 2022, Pages 5462-5443.

4.1 Introduction

In the last chapter I showed that line formation in an accretion disc wind could explain the existence of both BELs and BALs in the UV spectra of TDEs. I proposed that the BEL vs. BAL dichotomy arises naturally as a consequence of the orientation of an observer, with respect to the accretion disc. I found that BALs are preferentially seen for sight lines looking into the outflow, whereas BELs are more likely to be observed for viewing angles which are above or below the wind cone. In this chapter, I extend that same modelling to longer wavelengths.

An increasing number of UV and optically bright TDEs with a weaker than expected soft X-ray component have been discovered over the past decade. The exact source of

the optical emission is still uncertain, but it is clearly inconsistent with the SED of a hot accretion disc. In early TDE models, the stellar debris is assumed to fall back onto the black hole typically at a super-Eddington rate. The luminosity of these events is then generated via thermal blackbody radiation from a hot, quasi-circular accretion disc (see, e.g. Rees, 1988). Two mechanisms have been proposed to explain this “optical excess.” In the first, the optical emission is powered by shocks associated with collisions between infalling stellar debris streams (e.g. Dai et al., 2015; Piran et al., 2015; Shiokawa et al., 2015). In the second, the optical excess is due to the reprocessing – and consequent softening – of the disc’s X-ray radiation in a surrounding optically thick medium, such as an outflow (Strubbe & Quataert, 2009; Metzger & Stone, 2016; Roth et al., 2016; Roth & Kasen, 2018; Lu & Bonnerot, 2019; Piro & Lu, 2020; Bonnerot et al., 2021).

Reprocessing is a core component in a number of TDE models (Strubbe & Quataert, 2009; Metzger & Stone, 2016; Roth et al., 2016; Dai et al., 2008; Roth & Kasen, 2018; Piro & Lu, 2020; Matsumoto & Piran, 2021b; Bonnerot et al., 2021). Notably, Roth et al. (2016) showed that reprocessing in an optically thick outflow plays a key role in the formation of the optical spectrum. They identified two distinct reprocessing regimes, which can explain why some TDEs can still retain their soft X-ray component. Reprocessing also plays a key role in the unification scenario proposed by Dai et al. (2018). In their model, a given TDE could be observed as either optically or X-ray bright, depending on the inclination of the observer. Intermediate and high-inclination observers see an optically bright SED, since the disc emission is reprocessed via repeated scattering and photo-ionization along these sight lines. By contrast, observers viewing the TDE face-on see an X-ray bright TDE, since they are looking directly at the exposed inner accretion disc.

Accretion disc emission reprocessed by an accretion disc wind is a promising mechanism for the formation of the distinctive *optical* emission line spectra seen in TDEs. So far reprocessing has been investigated with somewhat artificial geometries relying on simple 1D spherically symmetric models, neglecting any possibility of clumping. The goal here, then, is to test the outflow reprocessing model for a more realistic geometry (a biconical accretion disc wind), to see if reprocessing in this outflow produces the optical (and UV) emission line spectra and broadband SED of TDEs. This is quite a natural scenario, since strong, radiation-driven mass loss is almost inevitable, given the extreme luminosities of TDEs.

This chapter is structured as follows. In Section 4.2, I describe the model setup. I then present the key results in Section 4.3 and discuss their implications in Section 4.4. Finally, I summarize my findings in Section 4.5.

4.2 Model setup

The masses of the black holes in TDEs are expected to fall within a broad, but well defined mass range. If the black hole is too large, i.e. $\gtrsim 10^8 M_\odot$, then the disruption radius will be within the event horizon of the black hole. In this case the star will be completely swallowed before it is disrupted (MacLeod et al., 2012), resulting in no observable TDE. At the opposite end of the mass scale, the lowest inferred black hole masses are $\simeq 5 \times 10^5 M_\odot$ (Wevers et al., 2017; Mockler et al., 2019; Ryu et al., 2020; Zhou et al., 2020). It is worth noting that several different methods are being used to estimate black hole masses in TDEs. For example, if the velocity dispersion can be measured from the stellar kinematics of the host galaxy, the $M_{\text{BH}} - \sigma$ relation can be used (e.g. Wevers et al., 2017). Alternatively, a multi-parameter model can be fit to the observed light curve to extract the physical properties of the TDE (Guillochon et al., 2018; Mockler et al., 2019)¹.

In order to settle on a reasonable range of black hole masses and Eddington ratios for the simulation grid, I used the largest compilation of these parameters by (Ryu et al., 2020). Their estimates are based on TDEMASS² (Ryu et al., 2020), which assumes a *slow circularization* scenario for the in-falling stellar debris. In this model, the optical emission is generated from stream-stream collisions; both black hole and stellar mass can then be estimated from the optical luminosity and colour temperature at peak flare. Even though their underlying physical picture is quite different from that envisaged in my simulations – where the reprocessed accretion disc radiation dominates the optical light – the black hole masses inferred via this method are in agreement with those obtained by MOSFIT (Mockler et al., 2019), which remains agnostic about the origin of optical emission.

Figure 4.1 shows the black hole masses and Eddington fractions for a sample of 20 TDEs, provided by Ryu et al. (2020). Based on Figure 4.1, I consider three black hole masses (with spin $a = 0$) in the simulations: $M_{\text{BH}} = 10^6$, 3×10^6 , and $10^7 M_\odot$. These cover the vast majority of the observationally inferred black hole parameter space. In terms of accretion rates, I have only considered the sub-Eddington regime in the present work with an accretion efficiency of $\eta = 0.1$: the highest accretion is $\dot{M}_{\text{acc}} = 0.5 \dot{M}_{\text{Edd}}$. Early on in their evolution, some TDEs with $M_{\text{BH}} \lesssim 10^7 M_\odot$ are expected to undergo a super-Eddington accretion phase, transitioning eventually to sub-critical accretion rates as the fallback rate of stellar debris diminishes (Strubbe & Quataert, 2009; Wu et al., 2018; Roth et al., 2020). However, most TDEs in the Ryu et al. (2020) sample appear to be sub-critical even at peak. Moreover, the TDE spectra to which I compare my models to have typically been obtained $\simeq 2$ months post-peak. Many super-Eddington TDEs

¹The widely used MOSFIT light curve modelling package is available at <https://github.com/guillochon/MOSFiT>.

²Available at <https://github.com/taehoryu/TDEmass>.

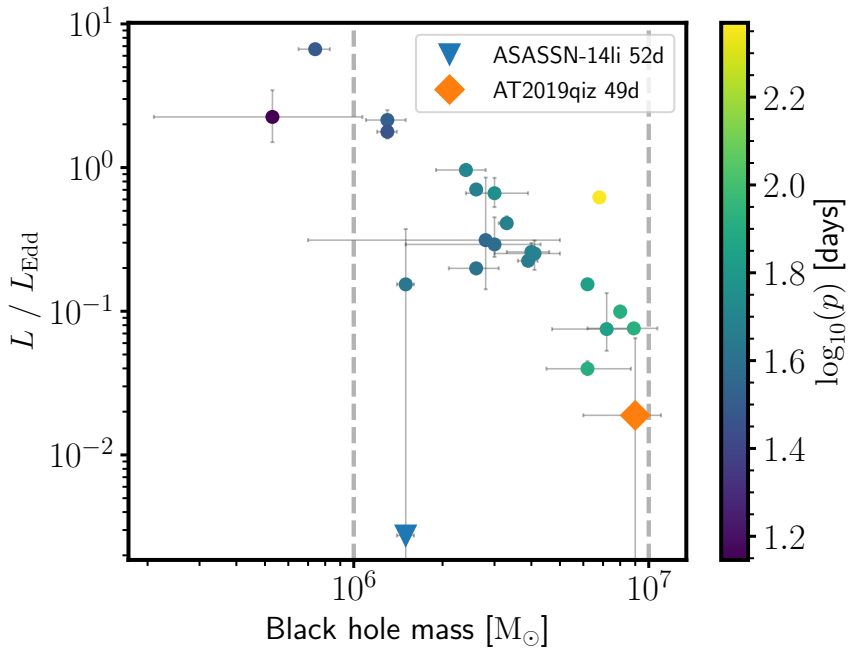


FIGURE 4.1: The Eddington luminosity fraction against inferred black hole masses for a sample of 20 TDEs taken from Ryu et al. (2020) and the spectra included in Figure 4.8, labelled in the legend. Each point from the Ryu et al. (2020) sample has been coloured depending on the mass return time p since disruption, measured in days. The Eddington luminosity is estimated using the inferred black hole masses. The bounded region represents the black hole mass parameter space covered by the grid.

are expected to have transitioned to the sub-critical regime by this point (Strubbe & Quataert, 2009). The structure and radiative properties of super-Eddington accretion discs are still poorly understood. By restricting to the sub-Eddington regime, I am able to avoid some of the resulting uncertainties. I have made the assumption that all the luminosity generated in the TDE is (initially) emitted by the accretion disc. For the model with the largest accretion rate (with $M_{\text{BH}} = 10^7 M_{\odot}$), this places the maximum disc luminosity of the grid at $L_{\text{disc}} \approx 5 \times 10^{44} \text{ ergs s}^{-1}$.

Not only does the grid explore the black hole mass dependence on the optical spectra with the simulation grid, but it also explores the effects of three key parameters: (1) the disc accretion rate, (2) the wind mass-loss rate, and, (3) the terminal velocity of wind streamlines. For each parameter, I also explore three values for each black hole mass. The values of these parameters are contained within the upper section of Table 4.1.

Each model has two radiation sources, 1) a steady-state α -disc, and 2) the outflow. As in the previous chapter, the outflow is not a source of photons, but radiatively reprocesses the photons in the simulation. For an α -disc, the SED is specified by the SMBH mass and accretion rate of the disc, as well as the inner and outer disc radii. The inner radius of the accretion disc in each model is set to the location of the innermost stable circular orbit (ISCO), for a non-rotating black hole. The outer disc radius is set to $R_{\text{disc}} = 10R_t$

for a solar-like star and the relevant black hole mass, a value which is inspired by the hydrodynamic simulations of Bonnerot et al. (2021). The outflow is wide-angled and characterised by opening angles $\theta_{\min} = 20^\circ$ and $\theta_{\max} = 65^\circ$ and emanates from the entire accretion disc surface. The mass-loss rate per unit area from the disc is slightly enhanced at larger disc radii ($\lambda = 2$), meaning the density at the base of the wind increases with radius.

The acceleration length scale for each wind model is set to $2000 R_g$, a value motivated by the radiation-hydrodynamic simulations presented by Dai et al. (2018). In their model, the outflow is still accelerating at distances of $\sim 1500 - 3000 R_g$. The launch velocities of the streamlines are set to the local sound speed at the footpoint of the streamline and are uniformly spaced at the base of the outflow ($\gamma = 1$). Importantly to note is that the Dai et al. (2018) model is a snapshot of a super-Eddington TDE, whilst the models here are sub-Eddington. The choice to base the acceleration length on this model are mainly a practical choice, given the lack of constraints available from observations. Since the purpose of my models are not to exactly model the dynamics of a TDE outflow, but rather model its radiative reprocessing capabilities, the choice of acceleration length should not significantly influence the qualitative picture. From a quantitative standpoint, this choice would clearly matter for any detailed comparison to a TDE. But given the idealised choice for a continuum source, there are other parts of the models which would make a far more significant impact and require improvement first.

The outflows are logarithmically discretised onto a 2D cylindrical rotationally symmetric grid. Photons are transported in 3D, to account for effects due to the rotational velocity field and structure. The grid has a resolution of 100×100 grid cells with a greater concentration of cells at smaller radii, where line formation typically occurs. The total volume covered by the grid is a sphere of radius 5×10^{17} cm. Tests in the previous chapter indicate that the grid resolution and spherical extent of the wind are sufficient to resolve the line forming region. A complete summary of the grid and parameter values is shown in Table 4.1.

4.3 Results

In the following section, I present the results of the simulation grid. First, I describe the physical characteristics and synthetic spectra for a reference fiducial model that lies at the centre of the parameter space covered by the grid. I then explore how the synthetic spectra depend on the four key parameters covered by the grid (accretion rate, mass-loss rate, terminal velocity and black hole mass).

Grid parameters				
Parameters	Values		Units	
\dot{M}_{disc}	0.05	0.15	0.50	\dot{M}_{Edd}
\dot{M}_{wind}	0.1	0.3	1.0	\dot{M}_{disc}
v_{∞}	0.1	0.3	1.0	v_{esc}
Geometry parameters				
Parameters	Values		Units	
M_{BH}	10^6	3×10^6	10^7	M_{\odot}
R_{co}, r_{\min}	8.85×10^{11}	2.66×10^{12}	8.85×10^{12}	cm
	6	6	6	r_g
$R_{\text{disc}}, r_{\max}$	7×10^{13}	10^{14}	1.5×10^{15}	cm
	473	228	102	r_g
α_v	4	4	4	-
R_v	3×10^{14}	8.9×10^{14}	3×10^{15}	cm
	2000	2000	2000	r_g
θ_{\min}	20	20	20	°
θ_{\max}	65	65	65	°
R_{\max}	5×10^{17}	5×10^{17}	5×10^{17}	cm
	3.39×10^6	1.13×10^6	3.39×10^5	r_g
γ	1	1	1	-
λ	2	2	2	-
f_v	0.1	0.1	0.1	-
Eddington ratio conversions				
Ratio	Values		Units	
M_{BH}	10^6	3×10^6	10^7	M_{\odot}
$0.05 \dot{M}_{\text{Edd}}$	1.11×10^{-3}	3.33×10^{-3}	1.11×10^{-2}	$M_{\odot} \text{ yr}^{-1}$
$0.15 \dot{M}_{\text{Edd}}$	3.33×10^{-3}	9.99×10^{-3}	3.33×10^{-2}	$M_{\odot} \text{ yr}^{-1}$
$0.50 \dot{M}_{\text{Edd}}$	1.11×10^{-2}	3.33×10^{-2}	1.11×10^{-1}	$M_{\odot} \text{ yr}^{-1}$

TABLE 4.1: Key parameters for the models presented. The top sub-table shows the values for the parameter grid as described in section 4.2, whilst the middle sub-table defines the parameters which control the geometry for each black hole mass. The bottom table shows conversion values of the Eddington accretion rate into solar masses per year for each black hole mass.

4.3.1 A fiducial model

I begin by first considering a fiducial ‘‘benchmark’’ model, in which all parameters are set to their central values on the grid: $M_{\text{BH}} = 3 \times 10^6 M_{\odot}$; $\dot{M}_{\text{disc}} = 0.15 \dot{M}_{\text{Edd}}$; $\dot{M}_{\text{wind}} = 0.3 \dot{M}_{\text{disc}}$ and $v_{\infty} = 0.3 v_{\text{esc}}$. I now present and describe both the physical properties of the outflow and its optical spectrum. Figure 4.2 shows colour plots for a selection of physical parameters in the fiducial model and five lines showing how and where different sight lines intersect the wind, as well as additional contours showing the relative number density of H α photon emission.

4.3.1.1 Physical properties

At the base of the wind, the velocity field is rotation dominated and effectively Keplerian, with $v_\phi \sim 10^5 \text{ km s}^{-1}$ near the inner wind edge and $v_\phi \sim 10^4 \text{ km s}^{-1}$ at the outer edge. The launch velocities of streamlines at the inner and outer edges of the wind are $v_0 \sim 40 \text{ km s}^{-1}$ and $v_0 \sim 10 \text{ km s}^{-1}$, respectively. Along the disc plane, the matter density increases with radius (due to the choice of $\lambda = 2$) and is $n_H \sim 10^9 \text{ cm}^{-3}$ at the inner edge which increases to $n_H \sim 10^{12} \text{ cm}^{-3}$ at the outer edge. At increasing cylindrical radii, both the hydrogen density and rotational velocity decrease. As the electron density is also decreasing, line formation processes which scale with the electron density, such as collisional excitation, also decrease in strength. The rotational velocity decreases linearly with radius, since material in the outflow is assumed to conserve specific angular momentum. However, the poloidal velocity of the wind increases with radius. The result of this is that Doppler broadening of lines is dominated by rotation close to the disc surface, but by the poloidal velocity field at larger radii.

At the base of the wind, where it is exposed directly to the radiation generated by the accretion disc, the electron temperature is the highest. The temperature at the very inner edge is in excess of $T_e \sim 3 \times 10^5 \text{ K}$, but is closer to $T_e \sim 3 \times 10^4 \text{ K}$ at the outer edge. At large radii, near the far outer edges of the wind, adiabatic cooling dominates, and the temperature is cooler ($T_e \sim 10^3 - 10^4 \text{ K}$). Since PYTHON does not implement any dust or molecular physics, the treatment of this region of the wind is highly approximate. However, the majority of the line formation of interest does not occur in this region. Neglecting this physics, then, should not affect the emergent spectrum to a significant degree.

As in Chapter 3, I use the ionization parameter (Equation 3.1) which measures the ratio of the number density of hydrogen ionizing photons to the number density of hydrogen, to measure the ionization state of the outflow. Figure 4.2 shows that the ionization parameter is fairly constant throughout the wind, with $U_H \sim 10^5$ meaning hydrogen is ionized almost everywhere. At the very top of the wind, the wind is very highly ionized, with $U_H \sim 10^7$. There is a portion of the wind where $U_H \lesssim 10$. This part of the wind is located close to the dense base of the wind, at the outer edge. In this region, the wind has been somewhat shielded by the large column of wind material closer in, meaning it is exposed to a softer, reprocessed SED. This results in this part of the wind being cooler. The reduced ionizing flux also means that the neutral hydrogen population is enhanced in this region. This is where the majority of H α photons are produced, as shown by the contour lines on the middle right panel of Figure 4.2.

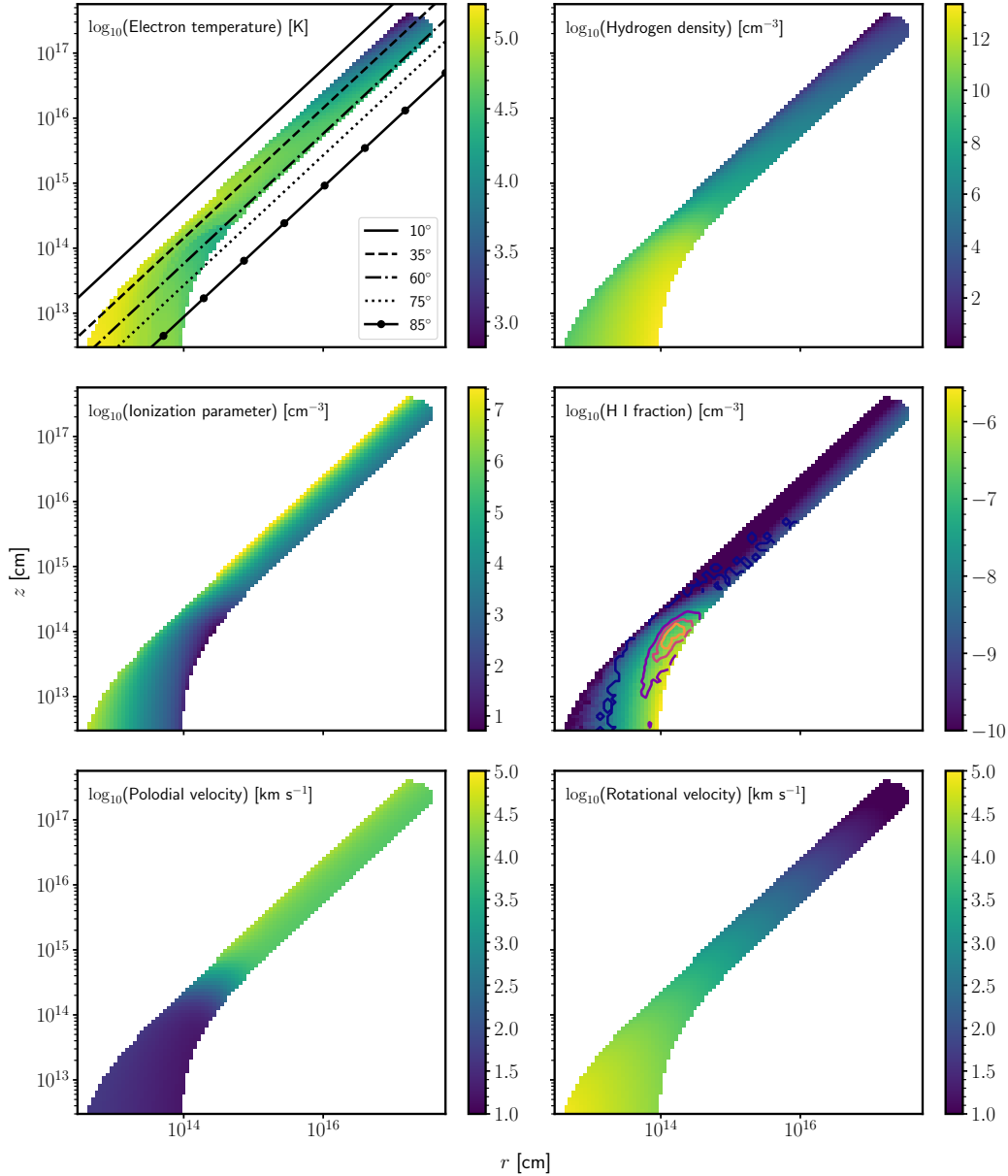


FIGURE 4.2: Colour plots showing a selection of physical properties for the fiducial model on logarithmic axes. The $r - z$ plane, where r is the cylindrical radius, is shown and the wind is rotationally symmetric about the z -axis. The lines drawn over the wind show sight lines for an observer for inclination angles indicated in the legend. The spatial scales and colour maps are both logarithmic. *Top left:* the electron temperature. *Top right:* the Hydrogen number density. *Middle left:* the ionization parameter. *Middle right:* H I ionization fraction. The contour lines show the origin of $\text{H}\alpha$ photons contributing to the spectra from a cylindrical radius $r < 10^{16}$ cm. From darkest to lightest colour, the contours are regions where the photon count is 0 N_{tot} , 0.25 N_{tot} , 0.5 N_{tot} , 0.75 N_{tot} and 1.0 N_{tot} and where N_{tot} is the total number of $\text{H}\alpha$ photons. *Bottom left:* the poloidal velocity. *Bottom right:* the rotational velocity.

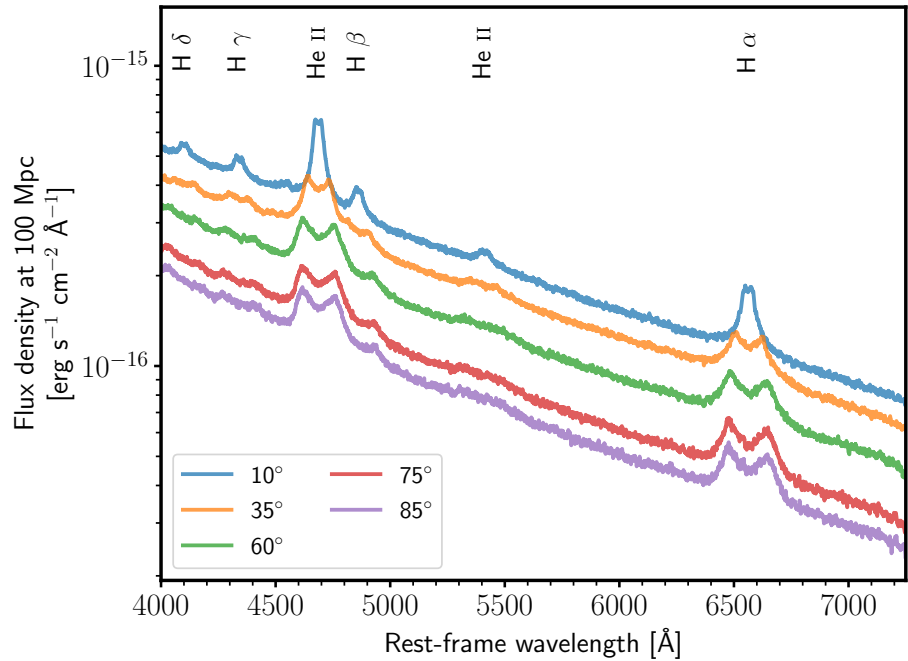


FIGURE 4.3: Synthetic optical spectra of the fiducial model. The spectra for five inclination angles are shown, each coloured as labelled by the legend. For each inclination angle, the model produces broad Balmer and helium recombination features. At low inclinations, the emission lines are single peaked but transition into double peaked lines as the inclination angle increases. Notably, the intermediate and high inclination spectra are almost identical as the base of the wind, which these sight lines cut through, dominates spectrum generation. The spectra are plotted on a log-linear axes and have not been smoothed. Labelled at the top of each panel are important line transitions.

4.3.1.2 Optical spectra

The synthetic optical spectra produced by the fiducial model for five sight lines are shown in Figure 4.3. For each inclination angle, the model produces broad, double peaked, recombination emission in $H\alpha$ and $H\beta$. The spectra also include other He II recombination lines commonly seen in the spectra of TDEs. The He II emission line is clearest at low inclination; it becomes very broad and blended with $H\beta$ for intermediate and edge-on inclinations, as these probe higher projected velocities. In comparison to observations, only one TDE so far (AT2018hyz; Short et al., 2020) has been observed to exhibit double peaked lines.

The line widths and peak-to-peak separations of the double-peaked emission lines increase with inclination. This happens because rotation is the dominant line broadening mechanism, and edge-on sightlines see higher projected rotational velocities. This also explains the double-peaked nature of the emission lines. Rotational kinematics dominate in the line-forming regions. The emissivity of recombination lines scales with density squared, so these features are formed preferentially in the dense base of the wind where

Inclination (°)	Column density (cm ⁻²)		Optical depths		
	Hydrogen	Lyman	He I	He II	Electron
35	1.02×10^{25}	1.13×10^{-3}	2.4×10^{-4}	4.00×10^{-4}	0.82
60	2.46×10^{26}	2.75	0.58	4.01×10^3	19.8
75	8.19×10^{26}	190	5.5	3.41×10^5	56.2
85	8.42×10^{26}	5.49	1.17	1.48×10^4	54.2

TABLE 4.2: The hydrogen column density and the integrated optical depth for three frequencies corresponding to three photo-ionization edges and the electron scattering optical depth for the fiducial model in Section 4.3.1. In cases where the optical depth are constant across multiple frequencies, the electron scattering opacity is dominating the opacity from photo-absorption.

the poloidal velocities are still relatively low. In fact, the lines are mostly formed near the outer edge of the wind base, where the outflow is both dense and relatively more neutral (since it is exposed to the redder, reprocessed SED, instead of the ionizing disc SED). If this line forming region was located at larger radii, where the poloidal velocity dominates, then the emission lines are expected to be single peaked. This would be more inline with the majority of observations.

The emission lines are asymmetric and display an extended red wing, although this is hard to see due to how broad some of the emission lines are. TDEs, such as ASASSN-14ae (Holoiien et al., 2014), AT2019qiz (Hung et al., 2020; Nicholl et al., 2020) or AT2018zr (Holoiien et al., 2019; Hung et al., 2019), often exhibit the same asymmetry, deviating from a Gaussian line profile. Roth & Kasen (2018) proposes that the origin of this asymmetry is from line formation in an optically thick outflow. Photons which scatter in an optically thick, diverging outflow lose energy resulting in an extended red wing in emission lines (e.g. Laurent & Titarchuk, 2007; Strubbe & Quataert, 2009; Metzger & Stone, 2016; Roth & Kasen, 2018), in a process known as bulk scatter reprocessing. Other than through energy losses due to this, extended red wings could instead form due to (general) relativistic effects (e.g. Eracleous et al., 2009).

The spectra produced by the fiducial model at high inclinations are very similar, with similar line strengths and widths. These sight lines intersect the dense base of the wind, and are probing parts of the wind which have very similar conditions. Table 4.2 shows the hydrogen column density and integrated optical depths for three photo-ionization edges and the electron scattering optical depth along four of the sight lines shown in the top left panel of Figure 4.2. Along these sight lines, the integrated optical depths and column densities are very high ($N_H \sim 10^{26} \text{ cm}^{-2}$) and are so high, in-fact, that this region of the wind actually dominates the formation of the optical spectrum.

As an example, for inclinations close to the disc plane, the optical depth of the He II edges is around $\tau \sim 10^4 - 10^5$, suggesting that photo-ionization of helium ions in the

base of the wind is contributing significantly to reprocessing the disc emission. In fact, this is the main reprocessing mechanism. Electron scattering optical depths are also fairly large for these inclinations, with $\tau \simeq 55$. By contrast, at low inclinations, the electron scattering optical depth is only $\tau \lesssim 1$, and the optical depths associated with the photo-ionization edges are broadly comparable. Even so, these sight lines can still intersect a small fraction of the dense wind base and thus see a substantial column density (e.g. $N_{\text{H}} \sim 10^{25} \text{ cm}^{-2}$ for $i = 35^\circ$). Electron scattering is the dominant global source of opacity along low and intermediate inclination sight lines, since the reduction in photo-ionization opacity means electron scattering reprocesses across a wider frequency range.

4.3.2 Synthetic spectra across the simulation grid

Figure 4.4 shows an intermediate in-wind inclination spectrum for each model in the simulation grid (as labelled in the legends). Note that the viewing angle adopted for these plots, $i = 60^\circ$, corresponds to a sight line which looks into the wind cone. Additionally, in Figure 4.5, I show angle-integrated disc and emergent reprocessed SEDs for the same models, along with the continuum optical depths they present along several sight lines.

For all of the models, the optical spectra feature broad Balmer and helium recombination lines that are strongly reminiscent of the TDE-H+He class of spectra.³ However, the He II and H β emission lines can often become blended with one another, making them difficult to distinguish from each other.

All the synthetic spectra shown in Figure 4.4 feature double-peaked lines and asymmetric red-skewed line wings, for the same reasons as the fiducial model discussed earlier in Section 4.3.1. No model on the simulation grid creates the pure Balmer recombination spectra (without helium lines) that are characteristic of the TDE-H class. This is could be a signature of the radiation field in the optical line-forming region. The absence of helium recombination features in TDE-H systems suggests a lack of photons with energies sufficient to ionize helium (24.6 eV). By contrast, all of the models contain regions whose ionization state and emission measure are both high enough to create observable He I and He II features. In recent work, Nicholl et al. (2022) proposed that the emission from TDE-H events could be powered by a collisionally induced outflow, launched by the intersection of the debris stream; e.g., a stream-stream collision scenario. They further propose that the lack of helium emission could be a signature of a shallow impact parameter and a partial disruption, resulting in larger photosphere radii and lower radiative and disc circularization efficiencies. This is the opposite scenario I have envisioned for my models, which assume a circular accretion disc and that the optical emission is reprocessed thermal disc emission. The lack of helium free spectra across the

³Note that PYTHON does not currently include the Bowen fluorescence process, so the models cannot produce the Bowen features themselves.

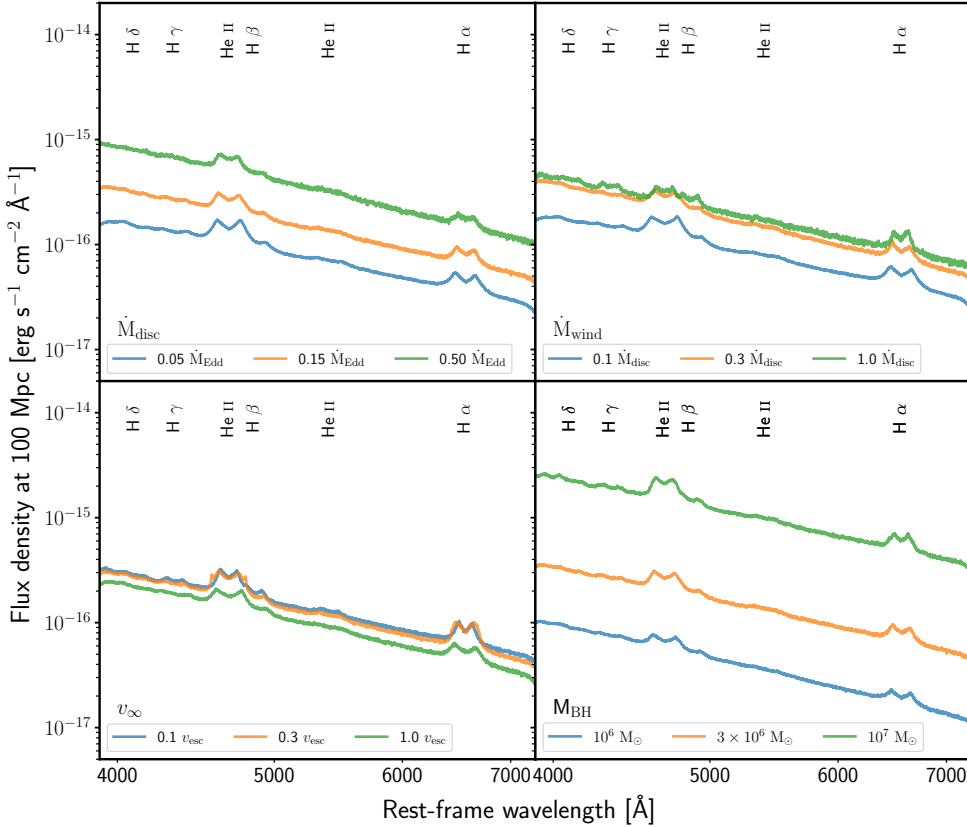


FIGURE 4.4: Synthetic optical spectra for the four parameter grids on log-linear axes. The first three panels show spectra for the mass accretion rate (\dot{M}_{disc}), the wind mass-loss rate (\dot{M}_{wind}) and the terminal velocity of wind streamlines (v_∞) grids, using a black hole mass of $M_{\text{BH}} = 3 \times 10^6 M_\odot$. The bottom right panel shows spectra of the fiducial model for three black hole masses (M_{BH}). In each panel, the orange spectrum corresponds to the fiducial model in Section 4.3.1. All of the spectra exhibit broad Balmer and helium recombination features, strongly reminiscent of TDE-H+He objects. The emission lines are double peaked and feature an extended red wing. Each spectrum is for an intermediate, in-wind, inclination angle of 60° . The spectra have not been smoothed. Labelled at the top of each panel are important line transitions.

models may then be due to the picture adopted. If TDE-H events really do preferentially form from a stream-stream collision scenario, then we may not expect the models here to have the conditions required to generate helium free spectra.

Figure 4.5 shows that each of the wind models, regardless of its detailed parameters, strongly reprocesses the accretion disc continuum (labelled as “disc” in Figure 4.5), producing a much redder observed SED (labelled as “emergent”). Thus reprocessing of the disc continuum in an outflow can, rather naturally, result in an optically bright emergent SED.

Qualitatively, the line spectra and SEDs do not change drastically with different parameter values or with inclination. More specifically, all the synthetic line spectra produce broadly the same set of transitions, accompanied by a continuum with roughly similar colour temperatures. The ionization state of the wind, in particular that of hydrogen

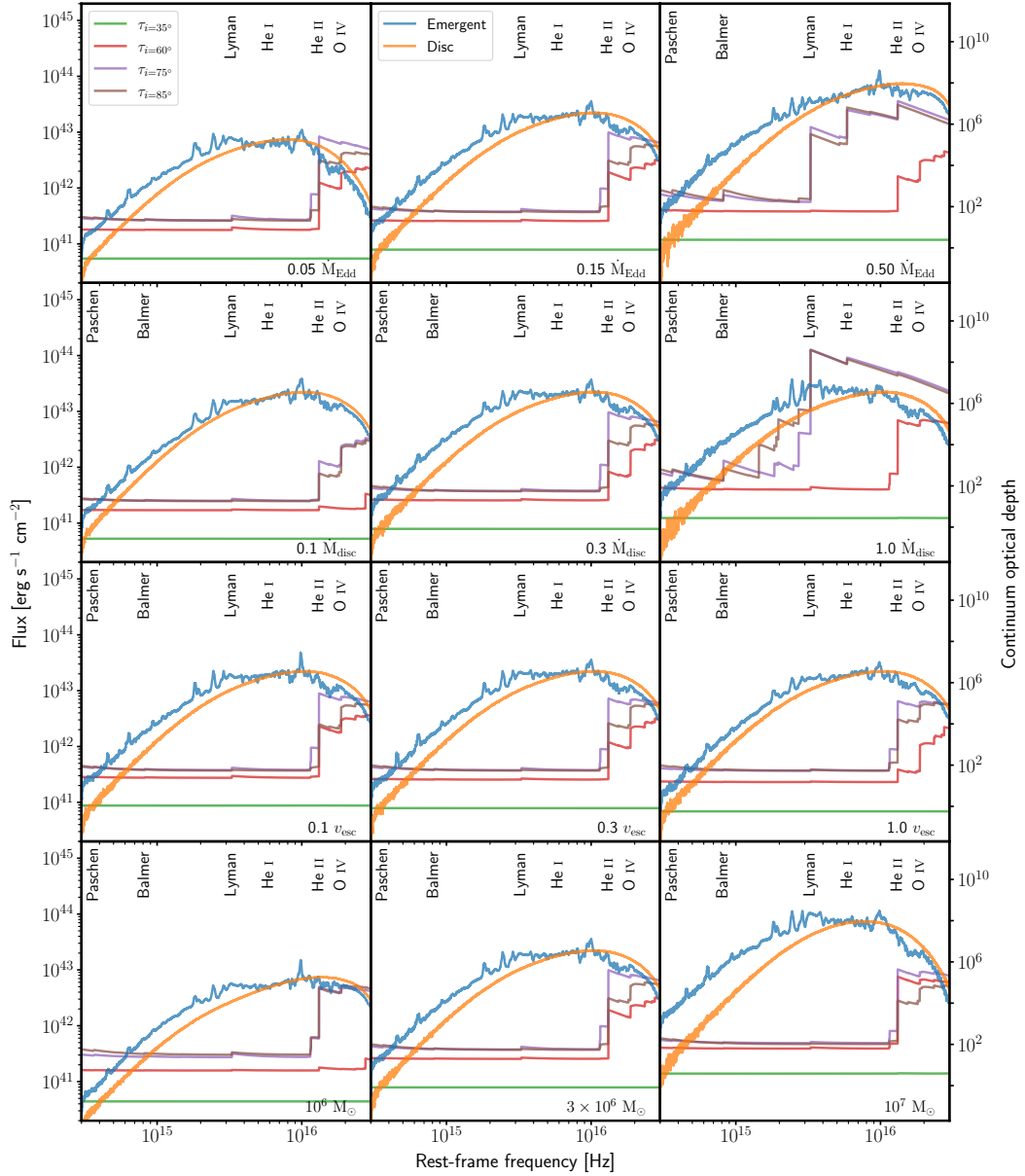


FIGURE 4.5: The continuum optical depth as a function of frequency for various sight lines (right axis) and both the emergent and disc SEDs for the same models as in Figure 4.4. The middle column corresponds to the fiducial model from Section 4.3.1. The spectra have been plotted on logarithmic axes and important photo-ionization edges have been labelled at the top. Each model is producing a redder (reprocessed) SED relative to the input *disc* SED. In general, denser winds are more efficiently reprocessing the disc SED and result in optically bright spectra. The main reprocessing mechanism is photo-ionization of He I and He II, but in some winds H I also contributes significantly. The electron scattering optical depth (corresponding to the “flat” region of the optical depth spectra) is roughly the same between models.

and helium, is insensitive to moderate changes in the input SED, the mass-loading of the wind or its kinematics. The ionization state of the dense base of the wind, which is the main line-forming region, does not change all that much between models. This suggests that reprocessing, and the production of Balmer and helium recombination features, can happen over a fairly broad range of conditions in TDEs. Quantitatively, the spectra do, of course, depend on the model parameters. In the following sections, I will outline the main effect of the different parameters explored on the resulting line spectra and emergent SEDs.

4.3.2.1 Disc mass-accretion rate

The top left panel of Figure 4.4 shows three models with different disc accretion rates. In all of these models, the wind mass-loss rate is 30% of the accretion rate. The main difference between the spectra is the continuum normalization and the strength of the H α line. The highest accretion rate model produces the most luminous spectrum. The increase in the continuum level is mostly due to a more luminous disc, but also because of greater reprocessing associated with the higher density of the wind. This is clear by looking at the top row of Figure 4.5, which shows the reprocessed SED relative to the input SED for the three accretion rates. In the highest accretion rate model, the high frequency region of the disc continuum is slightly less attenuated, but there is significant optical depth from lower frequency edges contributing to reprocessing the SED. So while the higher continuum luminosity can mostly be attributed with the higher accretion rate, it does appear this wind reprocesses more radiation and re-emits it at longer wavelengths.

The spectrum produced with the lowest accretion rate in Figure 4.3 has the strongest emission lines. In general, the strength of the emission lines decreases with accretion rate, even though the higher accretion rate models are reprocessing (and re-emitting via recombination) more emission and that the emissivity of these lines scales with the density squared. In this situation, the lines appear weaker because of the stronger optical continuum due to stronger reprocessing decreasing the line-to-continuum contrast.

4.3.2.2 Wind mass-loss rate

The top right panel in Figure 4.4 shows how changing the mass-loss rate of the wind affects the line spectrum, and the second row of Figure 4.5 shows how the reprocessed SED changes. The model featuring the highest mass-loss rate (and thus highest densities) has the strongest recombination features, since, stating this once again, the emissivity of recombination scales with the density squared. This model also produces the brightest optical spectrum, since it reprocesses the largest fraction of the disc emission.

Quite generally, denser winds tend to be more efficient at reprocessing disc emission, generating optically brighter spectra. This derives from the dominant reprocessing mechanisms being photo-ionization and free-free absorption, and since the optical depth of edges, specifically He II, and the electron/ion density, which free-free opacity scales with, are enhanced in a denser wind, the reprocessing becomes stronger. In the lowest mass-loss rate model, the input SED is reprocessed less (refer to Figure 4.5) and the emergent SED is the least red, although not by much. The opacity of the Lyman and He I photo-ionization edges are considerably diminished and comparable to the scattering optical depth, resulting in a reduction in the overall amount of reprocessing via photo-ionization. However, as the He II edge is still comparably strong there is still enough reprocessing via photo-absorption to create an optically enhanced spectrum. It appears that this edge is very important in reprocessing high frequency disc emission.

4.3.2.3 Terminal velocity

The terminal velocity is one of the parameters which controls the wind kinematics. Larger terminal velocities imply higher velocities *along* streamlines, as well as lower densities (via the continuity equation). Thus slower outflows are denser and produce redder reprocessed SEDs (third row down of Figure 4.5). However, the effect of the terminal velocity on the optical continuum luminosity and colour temperature is relatively modest.

The bottom left panel of Figure 4.4 shows the synthetic spectra for the three different values of v_∞ on the grid. Since the density is modified by the velocity, the two models with the lowest terminal velocities, i.e. which have largest densities at the base of the wind, produce the strongest recombination lines and the brightest optical continuum. Much like changing the mass-loss rate of the wind, varying v_∞ from $0.1 - 1 v_{\text{esc}}$ does not significantly affect the overall optical spectrum, producing only modest changes in the normalisation. However, as noted previously, changing the acceleration length scale has a more significant impact.

4.3.2.4 Black hole mass

The bottom right panel of Figure 4.4 shows the optical spectra produced by the fiducial wind model for three different black hole masses. Changing the black hole mass indirectly affects other parameters of the models as well, such as the three other parameters comprising the grid (since these parameters all scale with black hole mass).

The most significant differences between the spectra, associated with different black hole masses, is their continuum luminosities and their line strengths. The model with the most massive black hole produces the strongest lines, as expected since recombination

scales with the density squared. The same model produces the brightest optical spectrum, in this case because the accretion disc is the brightest in the grid, rather than because of any significantly greater level of reprocessing relative to the rest of the grid. In the case of the highest black hole mass model, there are simple “more” photons to reprocess. Figure 4.4 also shows that the same Balmer and helium recombination features are produced for all three black hole masses. Otherwise, the spectra remain relatively unchanged in terms of distinct spectral features.

4.4 Discussion

4.4.1 The origin of optical emission

In Section 4.3, I showed how reprocessing in an optically thick accretion disc wind, with plausible parameters, results in an optically bright spectrum, significantly redder than the original accretion disc SED. The main reprocessing mechanism in the simulation grid is photo-ionization, similar to the [Dai et al. \(2018\)](#) unification model. Even so, free-free absorption is *still* important, with $\tau_{\text{ff}} \sim 10^2$ for intermediate and high inclinations in the fiducial model. The majority of the photo-ionization reprocessing is associated with the ionization of He II; in some models, He I and H I are also important (Figure 4.5). When the opacity in both helium edges is high, high frequency radiation is efficiently absorbed and reprocessed, softening the SED and reducing the EUV/X-ray brightness. The absorbed luminosity is re-emitted at longer wavelengths via recombination, free-free and line emission.

The photo-ionization of He II seems to be particularly important for the reprocessing efficiency. For instance, the optical brightness in the wind mass-loss rate sub-grid (second row down in Figure 4.5) increases as the optical depth (and hence absorption) of this edge increases, as is clear by comparing the $0.1 \dot{M}_{\text{disc}}$ and $0.3 \dot{M}_{\text{disc}}$ models. This is, in-fact, a common trend across all of the models in Figure 4.5. But additionally, models with high optical depths for lower frequency edges (e.g. He I and Lyman) also have optically brighter spectra (see the top right panel of the first and second row in Figure 4.5). It seems that reprocessing of not just the soft X-ray photons, but also of the EUV photons is important for the production of optically bright spectra.

As mentioned previously, photons undergoing repeated scattering events in a divergent flow lose energy and are redshifted as they do work on the outflow (see, e.g., [Laurent & Titarchuk, 2007](#); [Roth & Kasen, 2018](#)). This effect, sometimes referred to as “bulk scatter reprocessing,” can be important (see figure 14 in [Roth & Kasen, 2018](#)). The integrated electron scattering optical depth in the winds are significant ($\tau \gtrsim 50$ for intermediate and high inclinations in the fiducial model) and photons are almost certain to undergo multiple scatters before reaching an observer. However, compared to outflow models in

which bulk scatter reprocessing is known to dominate, the scattering optical depth in the winds here are fairly modest. For example, Roth & Kasen (2018) report a scattering optical depth of $\tau \simeq 130$ for their spherical outflow, in which repeated scatterings in the outflow play a major role in redshifting the SED. Additionally, as the models here are 2D, photons are able to scatter around highly optically thick regions and do not become trapped, as they would in a spherical model such as by Roth & Kasen (2018).

In the fiducial model, the role played by bulk scatter reprocessing is minor. The scattering optical depths are similar between the models in Figure 4.5, but the amount of reprocessing is not. It is clear, then, that whilst bulk scatter reprocessing can modify the SED, in the models here it is not an important process for the creation optically bright spectra. To see this, consider the $\dot{M}_{\text{wind}} = 0.1 \dot{M}_{\text{disc}}$ panel in Figure 4.5. Here, the scattering optical depth is similar to other models, but the optical depth of the He I edge is greatly reduced and comparable to the scattering optical depth. The optical luminosity in this model is low, showing that it tracks the photo-ionization optical depth, rather than the scattering one. Hence why bulk scatter reprocessing is not important.

In contrast to the dense, spherically symmetric model of Roth et al. (2016), the disc wind models in this work typically do not completely absorb the soft X-ray flux. This difference is likely a geometric effect, as photons are able to escape along paths with lower optical depths in the biconical outflows. Thus, similar to Dai et al. (2018), the ratio of optical to X-ray fluxes increases with inclination angle. At polar angles, the SED is more akin to a underlying disc spectrum, since the optical depth is lower – and reprocessing less efficient – along these sight lines.

Additionally, the emergent optical luminosity is also affected by the SED of the accretion disc. If the SED does not have enough high frequency flux, then there is nothing to reprocess to create a red optical spectrum. This effect is illustrated in Figure 4.6, with the fiducial model I used in Chapter 3 and the fiducial model in this chapter. Clearly, the new fiducial model reprocesses a great deal more of the underlying disc continuum. This is despite the fact that the photo-ionization optical depths for He II is not too dissimilar between the models. But there is a disparity between the optical depths for the He I and Lyman edges in the old fiducial model, where they are larger.

So what is responsible for the higher reprocessing efficiency of the *new* fiducial model, compared to the fiducial model in Chapter 3? Crucially, the disc continuum in this model peaks at a higher frequency, which means a higher fraction of its luminosity is susceptible to reprocessing by the He II edge. The reprocessing efficiency is not just related to the physical properties of the wind, notably its (column) density, but it also depends on the underlying SED. If this SED does not include enough *ionizing* photons, reprocessing via photo-ionization becomes inefficient (as does free-free reprocessing). Of course, bulk scatter reprocessing can still reprocess the continuum if the outflow is optically thick, even if this is a relatively small effect in the models here.

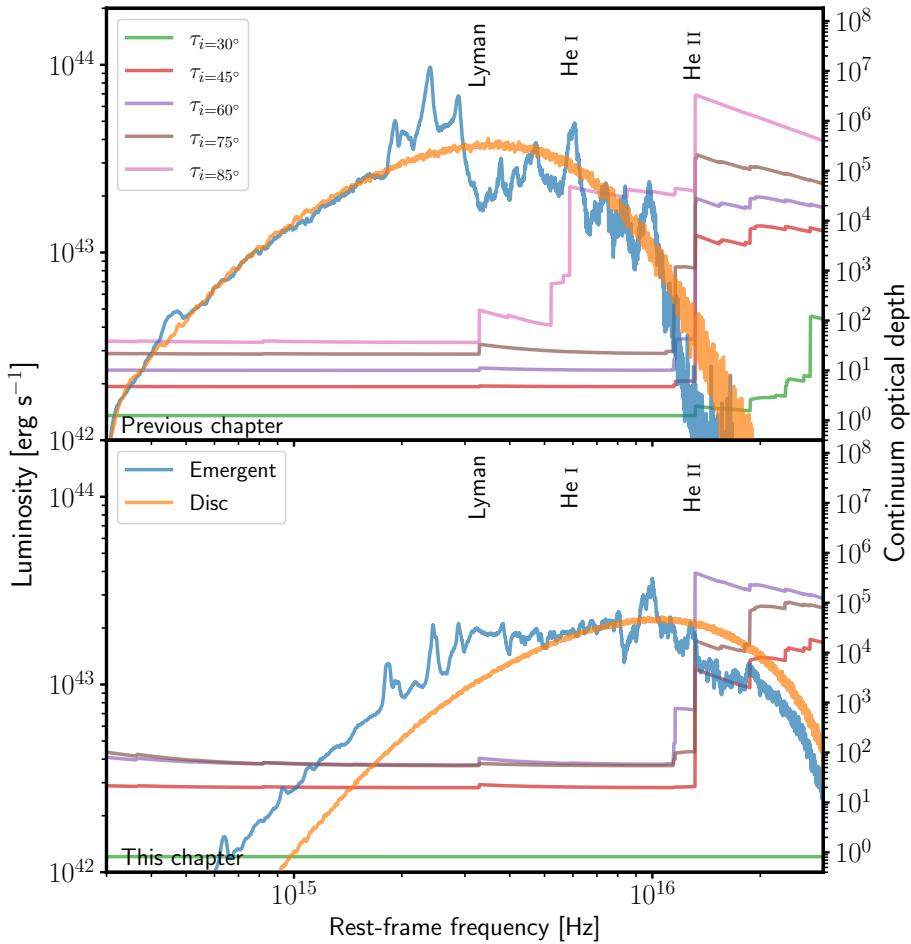


FIGURE 4.6: The continuum optical depth as a function of frequency for various sight lines (right axis) and both the emergent and disc SEDs (left axis) for the fiducial model in Chapter 3 and in this work (Section 4.3.1). Both axes are logarithmically spaced and important photo-ionization edges have been labelled at the top. Relative to the (Chapter 3) fiducial model, reprocessing is more efficient in the fiducial model presented in this work. Crucially whilst the both models have similar optical depth for the same photo-ionization edges, the disc continuum peaks at a higher frequency in the “new” fiducial model. In the Chapter 3 model, the disc SED does not include enough *ionizing* photons resulting in reprocessing via photo-ionization becoming inefficient.

4.4.2 Formation of optical lines

When the density of the wind is low, the Balmer and He II optical features become weak. If the density is too low to shield or soften the disc emission via reprocessing, the recombination features are greatly diminished as the wind becomes overionized, preventing the formation of absorption and emission lines (e.g. Proga et al., 2000; Proga, 2003; Higginbottom et al., 2013). More generally, however, the strength recombination features scales with emission measure, $EM = \int n_e^2 dV$. This depends not only the local density, but also on the emitting volume, so where in the outflow these lines form is also

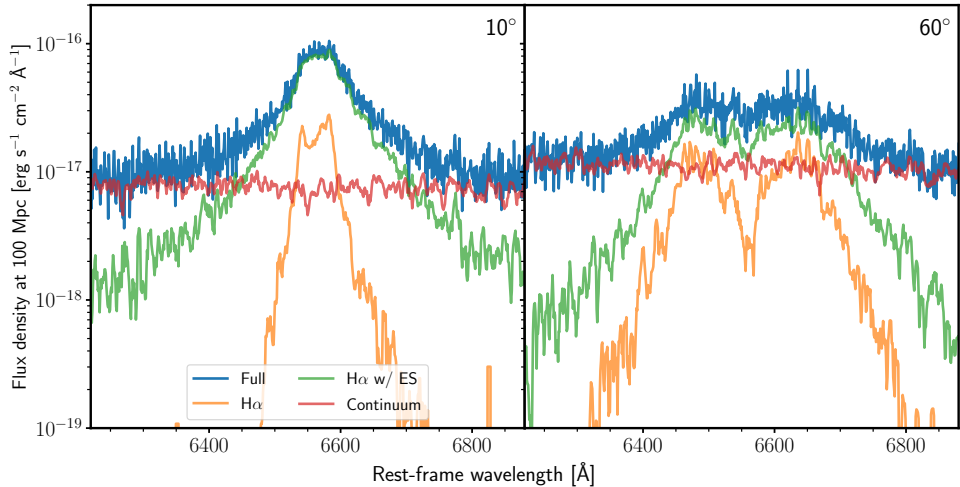


FIGURE 4.7: Synthetic spectra for two inclinations (labelled in the top right of each panel) of photons contributing toward the emergent spectrum (labelled as full as in the figure) of the H α line profile for the fiducial model. Included are “pure” continuum photons (free-free, bound-free and electron scattered), as well as H α photons and H α photons which have electron scattered at least once between emission and escape (H α w/ ES). The spectra have been smoothed by a six pixel boxcar filter. Importantly, electron scattering is responsible for the broad wings of the emission lines. It also smooths out the double peaked line profile at low inclinations. *Left:* a low inclination spectrum (10°). *Right:* an intermediate inclination spectrum (60°).

important. For example, emission lines will preferentially form near the base of the wind where the density is largest. But, if H α photons were being emitted over an extended region in the sparse, outer portion of the outflow, this emission could still be significant, since the volume of this region is so large.

One way to modify the density of the outflow in this kinematic approach (other than by modifying the mass loss rate) is by changing the acceleration length scale or the acceleration exponent. Together, these variables control how quickly the outflow accelerates. By increasing the acceleration length and increasing the exponent, the outflow density increases and the ionization state is lowered. Both effects result in stronger recombination features, so the appearance of the optical spectra is sensitive to these kinematic model parameters. However, some lines, such as H α , are insensitive to changes in the velocity structure. This suggests these line photons are produced in the very base of the wind, whose kinematic properties remain fairly constant with the change in parameters.

4.4.3 The effect of electron scattering on the line profiles

Figure 4.7 is a break down of the contribution of different physical processes on the spectrum produced by the fiducial model in the vicinity of the H α line. First, it isolates the contribution of “continuum photons” to this region. These are photons that have never undergone any bound-bound interaction in the outflow. This category includes

photons emitted directly by the disc and photons produced via bound-free or free-free processes. It also includes such photons if they subsequently underwent one or more electron scatters. Second, it separates out the contribution of “pure” H α photons, i.e. photons whose last interaction in the wind was in the bound-bound H α transition. Third and finally, it also shows the spectra associated with H α photons that subsequently underwent one or more electron scatters (H α w/ ES).

Figure 4.7 shows very clearly that electron scattering is responsible for the broad wings of the emission line. This is in line with the results of Roth & Kasen (2018). In their simulations, higher electron scattering optical depths resulted in broader emission lines. In the models here, electron scattering can also smooth out the double peaked line profile, at least at low inclinations (left panel). The asymmetric red wing of the emission lines is less prominent at polar inclinations. This will be due to photons scattering less along these inclinations, as they travel through less optical depth before escaping and reprocessed less.

4.4.4 Comparison to observations

In Figure 4.8, I show comparisons of two models to the optical spectra of ASASSN14-li and AT2019qiz. Other than the choice of inclination angles and re-scaling the spectra to the relevant distance, the model parameters used to generate the synthetic spectra have not been tailored and/or fine-tuned to fit either object. The observed spectra were taken at roughly the same time post peak, at $\Delta t \approx 50$ days, and have been corrected for foreground extinction assuming a Cardelli et al. (1989) extinction curve with $R_v = 3.1$ with $E(B - V) = 0.0225$ and $E(B - V) = 0.0939$ for ASASSN14-li and AT2019qiz, respectively. For ASASSN-14li, I have also included photometry, provided by Holoi en et al. (2016), from both the *Swift* UltraViolet and Optical Telescope (Roming et al., 2005) and from the 2-m Liverpool telescope (Steele & Oschmann, 2004). For the comparison with ASASSN-14li, I use a black hole with mass $M_{\text{BH}} = 3 \times 10^6 M_\odot$ and a mass loss rate of $\dot{M}_{\text{wind}} = \dot{M}_{\text{disc}}$. For AT2019qiz I use a model with $\dot{M}_{\text{disc}} = 0.5 \dot{M}_{\text{Edd}}$ and a black hole mass $M_{\text{BH}} = 10^6 M_\odot$. The rest of the model parameters are set to their “fiducial” values.

Both TDEs belong to the TDE-H+He spectroscopic class in the van Velzen et al. (2020b) taxonomy, as they display broad Balmer and helium emission, along with complex of lines due to Bowen fluorescence. TDE-H+He objects present the strongest case for reprocessing, as Bowen fluorescence requires both large densities and a high flux of EUV photons. As noted earlier, none of the models produce pure Balmer emission spectra, so I have not made any comparisons to TDE-H objects such as AT2018zr, and also do not make any comparisons to TDE-He objects. These helium enhanced transients could be associated with the disruptions of helium-rich stars. However, both Guillochon et al.

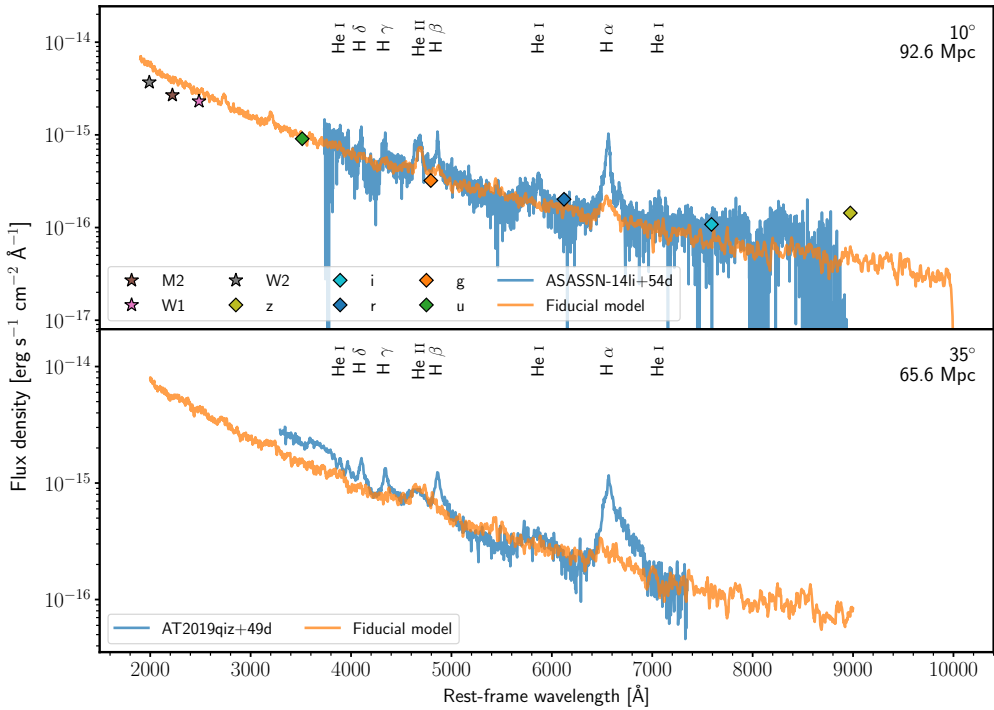


FIGURE 4.8: Rest frame synthetic optical spectra for two models (labelled in the legend) plotted on linear axes and against the optical spectra of ASASSN14-li bat $\Delta t = 54$ days (Holoien et al., 2016) and AT2019qiz at $\Delta t = 49$ days (Nicholl et al., 2020). The spectra for the objects have been corrected for foreground extinction assuming a Cardelli et al. (1989) extinction curve with $R_v = 3.1$ for both TDEs and $E(B - V) = 0.0225$ and $E(B - V) = 0.0939$ for ASASSN14-li and AT2019qiz respectively. Photometry for ASASSN-14li, taken from Holoien et al. (2016), has also been included with the filters labelled in the legend. The distance of the object and inclination of the model are labelled in the top right of each panel. The spectra have not been smoothed. Important line transitions are marked at the top of each panel. The synthetic spectra are in rather excellent agreement with the observations, especially considering neither model has been tailored to fit the specific observation, producing the same recombination features with similar continua.

(2014) and Roth et al. (2016) have shown how the disruption of a star with a solar-like composition also results in hydrogen free spectra. In this preferred interpretation, hydrogen Balmer lines are self-absorbed in a very compact and optically thick spherical emitting region (Roth et al., 2016). Whilst my models adopt a more realistic geometry for the emitting region and outflow, they can still fit into this self-absorption interpretation. But since the main line emission region is not located in the base of the wind, where the optical depth is most extreme, the bulk of the Balmer photons will only experience moderate optical depths. They are less likely to be absorbed. Even if the main emitting region was in the dense wind base, photons can still be beamed down paths of low optical depth, lowering their probability of absorption. This could account for why there are no spectra produced reminiscent of TDE-He objects.

Qualitatively, the models do a good job for matching both of the observed spectra in

Figure 4.8. They exhibit the same recombination features, and some with similar line strengths and line profiles, as well as the optical continua which agree quite well. From a more quantitative perspective, there is good agreement between the fiducial model and ASASSN-14li’s continuum and emission line spectrum. The only feature(s) missing entirely from the model are Bowen fluorescence features, which (as noted previously) is produced by a process that is not yet included in PYTHON. The agreement is, of course, far from perfect: for example, the Balmer and the He II emission lines are too weak and the continuum is slightly too blue at UV wavelengths.

The match between model and observation is poor for AT2019qiz. The synthetic spectrum is redder than the data. Increasing the mass accretion rate of the disc (and scaling the mass loss of the wind appropriately) would probably fix this and make the spectrum slightly bluer. But the model produces the similar emission features, although the Balmer lines are significantly weaker than the data, with the higher order Balmer features missing entirely.

Overall, given that the models have not been fine-tuned to precisely match the data, I consider the qualitative agreement with observations extremely promising. More specifically, it confirms that reprocessed disc emission can naturally produce both the continuum and emission lines that are commonly seen in the optical spectra of TDE-H+He objects.

4.4.5 UV spectral lines as geometry and orientation indicators

In Chapter 3, I showed how the BEL vs. BAL dichotomy found in the UV spectra of TDEs (e.g., Cenko et al., 2016; Blagorodnova et al., 2019; Hung et al., 2019, 2020) could be explained via line formation in an accretion disc wind. In this picture, BALs are preferentially produced for sight lines which look “into” the wind cone. For other orientations, BELs are observed. The fraction of BAL vs. BEL TDEs can then provide an estimate of the covering fraction of outflows in TDEs. Just as importantly, UV lines could be used to infer the orientation with respect to the TDE disc plane. The models presented in this work all produce the UV transitions commonly seen in the spectra of TDEs. However, they do not have the same inclination dependence as the synthetic UV spectra in Chapter 3. Specifically, none of the in-wind sight lines give rise to BALs in the models. Instead, BELs are produced for all inclinations.

The absence of BALs in the UV spectra of the models is due to their higher ionization state (relative to the models explored by Chapter 3). This is the result of the lower black hole masses considered, which give rise to harder SEDs. For example, in the fiducial model of Chapter 3, the adopted black hole mass is $M_{\text{BH}} = 3 \times 10^7 M_{\odot}$. By contrast, the fiducial model in this work here assumes a black hole mass of $M_{\text{BH}} = 3 \times 10^6 M_{\odot}$.

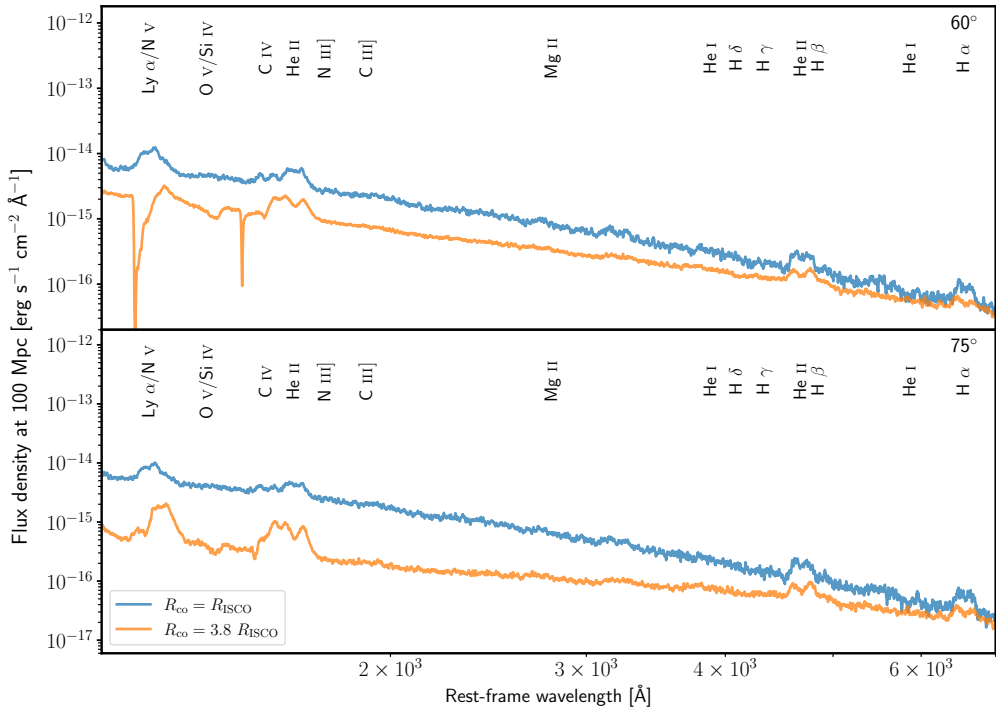


FIGURE 4.9: Synthetic spectra of the fiducial model (blue) and a modified fiducial model with a truncated inner disc radius (orange, $R_{\text{co}} = 3.8 R_{\text{ISCO}}$). The fiducial model in this work (blue) is too highly ionized to produce the UV BAL features reported by Chapter 3. By truncating the inner disc radius of the fiducial model, the disc SED is softened and the ionization state of the wind is lowered. The result is that the BEL vs. BAL behaviour reappears for the truncated disc model (orange). Absorption features, such as in C IV, form for sight lines which look into the wind cone (top panel) and emission features form for sight lines with do not look into the wind cone (bottom panel). *Top panel:* an intermediate sight line looking into the wind cone (60°). *Bottom panel:* a sight line looking below the wind cone (75°).

As discussed in section 4.2, this choice, and the range explored, is based on the data in Figure 4.1.

Given that BALs are observed in the UV spectra of at least some TDEs, it is worth asking whether disc wind models could still produce these features, even at the lower black hole masses considered here. Fundamentally, the answer is clearly yes. For example, the ionization state of a wind model can be lowered by stronger clumping (i.e. a lower volume filling factor and denser clumps), by self-shielding (see, e.g. Murray et al., 1995; Proga et al., 2000; Proga & Kallman, 2004), or by a softer underlying SED.

How significant a change is required in order for the fiducial model to produce BALs? In order to address this question, I ran models with both lower filling factors and modified SEDs. These revealed that a reduction in the filling factor by a factor of 10, to $f_V = 0.01$, is often times not sufficient to produce BALs. By contrast, only a modest change to the disc SED is required before BALs reliably reappear in the UV spectrum.

The modified SED test is illustrated in Figure 4.9. For this test, the inner disc radius was simply truncated to $3.8 R_{\text{ISCO}}$, which decreases the maximum temperature and softens the SED. This models illustrates that these models can recover the BEL vs. BAL behaviour, even if the absorption is significantly narrower here, found in Chapter 3 where absorption is seen for inclinations looking into the wind cone (60°), whereas only emission features are observed for other sight lines which do not look into the wind cone (75° in Figure 4.9).

The choice of a blackbody α -disc SED is clearly a highly idealized description of the spectrum produced by the central engine (see also Section 4.4.6 below). Since BAL formation in these models depends sensitively on the shape of this spectrum, the presence or absence of these features cannot be used as a “pure” orientation indicator. However, the fundamental point made in Chapter 3 remains: BALs can only be observed for specific sight lines, typically those looking into the wind cone.

4.4.6 Limitations

As is the case for any numerical simulation, modelling involves a number of limiting assumptions and simplifications. First, whilst PYTHON now takes into account special relativistic effects, it still neglects general relativistic effects, i.e. whilst PYTHON simulates the full random walk of photons, they still travel along straight lines between interaction points. PYTHON also does not include any concept of an event horizon within the computational domain. In Chapter 3, I partially tested the importance of general relativistic effects by imposing an absorbing spherical boundary at R_{ISCO} . The ionization state and the emergent spectrum were changed only marginally in this test. Repeating the same test for the fiducial model here, the results were the same.

Second, all PYTHON simulations are time-independent. This makes the implicit assumption that the outflow is in a steady state, which, especially at early times in the evolution of TDEs, may not be true. More specifically, the steady state assumption is valid so long as photon travel times through the flow are short relative to the time-scale over which the luminosity, the SED or the outflow itself can evolve significantly.

In some TDEs, i.e. ASASSN-14ae, AT2018zr and AT2019qiz, the optical spectra have been observed to evolve significantly over time-scales as short as 10-20 days at early times. In the modelled outflows here, photons typically take up to 1-3 days to escape from the simulation grid. Although, some photons may stay within the wind cone for almost 231 days. However, since I am not modelling the initial super-Eddington phase, the steady state assumption is likely to be quite reasonable. In line with this, simulations have shown that TDEs are able to reach a quasi-steady state after their initial super-Eddington phase (e.g. [Dai et al., 2018](#)).

Third, reiterating another limitation mentioned previously, I have assumed that the accretion disc is in a steady state, and is geometrically thin and optically thick. Specifically, the accretion disc SED is modelled by assuming a steady state α -disc, with constant \dot{M}_{acc} , that locally emits as a blackbody (Shakura & Sunyaev, 1973). Strictly speaking, the use of the standard α -disc temperature profile – which assumes \dot{M}_{acc} as a function of radius – is not self-consistent, since the discs suffer significant mass loss from the surface. In principle, this can be modelled by adjusting the effective temperature distribution (see, e.g. Knigge, 1999). Such models have, in fact, already been considered for TDEs. Specifically, Miller et al. (2015) outlined such an idea, constructed from work by Laor & Davis (2014) for AGN. In this scheme, Miller et al. (2015) show that mass losses from the disc, via a disc wind, reduces the accretion rate at the inner edge of the disc, decreasing the temperature and regulating the thermal emission. In practice, the net effect is likely to be similar to the inner disc truncation explored in Section 4.4.5.

Another limitation of the disc model is that the inner regions of TDE discs are dominated by radiation pressure and probably vertically extended. The most important effect of the thin-disc approximation in this context is on the angular distribution of the radiation field. Due to foreshortening and limb darkening, geometrically thin and optically thick discs generate highly anisotropic radiation fields. This degree of anisotropy is likely an overestimate for the vertically extended inner discs in TDEs. However, the structure, evolution and even the stability of such radiation dominated discs is the subject of ongoing intense research (e.g. Murray & Chiang, 1996; Jiang et al., 2013). The choice to use a simple disc model is, then, one borne out of practicality. Given that the emission from the disc is reprocessed by the outflow, which isotropizes the radiation field, this should not cause the qualitative results to change significantly.

Fourth and finally, only hydrogen and helium are modelled self-consistently with full, multi-level model atoms. By contrast, bound-bound transitions in metals are treated using a 2-level atom approximation. Whilst this is perfectly reasonable for resonance lines, it is not reasonable for transitions involving excited and/or meta-stable states. With the exception of C III] $\lambda 1909$ (which is treated in an approximate manner via a modified 2-level atom approximation), the simulations do not include realistic treatments for semi-forbidden transitions such as N III] $\lambda 1750$. The simplified treatment of metals also currently prevents modelling the fluorescence process that gives rise to the Bowen blend between 4630 Å and 4660 Å, commonly seen in observations.

4.5 Summary

I have shown that the reprocessing of disc radiation by an accretion disc wind can naturally produce the optical line and continuum spectra seen in TDEs. In order to

achieve this, I ran a grid of Monte Carlo radiative transfer and ionization simulations to produce synthetic UV and optical spectra of wind- and disc-hosting TDEs.

The disc winds I model are rotating, biconical and clumpy, and are illuminated by a geometrically thin and optically thick accretion disc. The model grid covers a realistic range of wind kinematics, black hole masses and accretion states, inspired by observations. Using this grid, I explored how the mass of the black hole, the accretion rate and the wind properties affect the broadband SED and optical line spectra.

All models and synthetic spectra presented in this work are available online or upon request. The main results are as follows:

1. The hydrogen and helium emission lines commonly seen in the optical line spectra of TDEs can be produced by an optically thick accretion disc wind that reprocesses the SED of the underlying disc. Reprocessing in such an outflow can also naturally produce the UV line spectra seen in TDEs.
2. The models produce good matches to the optical spectra of TDEs of the TDE-H+He class, reproducing the correct continuum shapes and emission line properties. However, they do not produce the pure Balmer spectra seen in the TDE-H spectroscopic class.
3. All of the outflow models are optically thick. There is significant opacity in all of the modelled outflows at the He II (54 eV) photo-ionization edge, with typical integrated optical depths of $\tau \sim 10^7$ at high and intermediate inclinations. At low inclinations, the optical depth of this edge is still large, but can be of similar magnitude to the electron scattering optical depth. The models also present significant opacity at the He I (24.6 eV) and, in some models, the hydrogen Lyman edges. The electron scattering optical depth is similar in all of the models, with $\tau \simeq 1 - 55$ depending on inclination.
4. The optical colour temperature of the reprocessed SED is much redder than that of the input accretion disc SED. Changes to the black hole mass, accretion rate and the kinematics of the wind affect the degree of reprocessing and the properties of the line spectra. In general, slower and denser winds result in a greater amount of reprocessing, as well as stronger Balmer and helium recombination features.
5. The main reprocessing mechanism is photo-ionization of He I and He II near the base of the wind. The absorbed luminosity is then re-radiated at longer wavelengths via recombination, or as free-free or line emission. Based on the simulations, He II bound-free interactions are expected to be a critical source of opacity for reprocessing continuum emission in TDEs. Free-free absorption can also play an important role, but affects the spectra to a lesser degree.

6. The optical emission lines are often double peaked, since the kinematics of the line-forming regions are dominated by rotation. Some lines exhibit asymmetric red wings due to bulk scatter reprocessing. Electron scattering also dramatically affects the line profiles, both by increasing the width of the lines and, for low inclinations, by smoothing out the double peaked shape.
7. The models produce synthetic UV spectra with the same set of atomic transitions commonly seen in TDEs. However, I find that the winds are often too highly ionized to produce UV absorption features. Truncating the inner radius of the accretion disc at $\simeq 4 R_{\text{ISCO}}$ softens the SED, lowering the ionization state of the wind and recovers UV broad absorption lines for eight lines that look into the wind cone.

Data availability

The models and their synthetic spectra from this chapter are publicly available online at https://github.com/saultyevil/tde_optical_reprocessing.

Chapter 5

Reprocessing in Super-Eddington Tidal Disruption Events

It's better to burn out than to fade away.

Neil Young

5.1 Introduction

In all of the previous chapters, modelling has been limited to the sub-Eddington accretion regime. But, early in their evolution, some TDEs with $M_{\text{BH}} \lesssim 10^7 M_{\odot}$ are expected to undergo super-Eddington accretion (e.g. Strubbe & Quataert, 2009; Lodato & Rossi, 2011; Metzger & Stone, 2016; Wu et al., 2018). In this regime, the inner region of the accretion disc is expected to be vertically extended because of radiation pressure (Rees, 1988; Ulmer, 1999). The structure, evolution and stability of such radiation dominated super-Eddington accretion discs and their outflows are still an area of intense and active research, with no certain answers. The choice to limit the previous work to sub-Eddington TDEs was, therefore, borne out of practicality: it avoids having to deal with an uncertain regime that PYTHON was not intended to model.

Much of the work so far on super-Eddington accretion in TDEs has relied on various approximations to simplify the problem considerably. Such work usually involves semi-analytic methods, simplified quasi-spherical outflow geometries, quasi-steady accretion, or simplified disc and emission models (Loeb & Ulmer, 1997; Strubbe & Quataert, 2009; Roth et al., 2016; Miller et al., 2015; Metzger & Stone, 2016; Wu et al., 2018). However, recent simulations by both Dai et al. (2018, hereafter D18) and Curd & Narayan (2019) have simulated super-Eddington TDE accretion using 3D general-relativistic radiation

magneto-hydrodynamics (GRRMHD), relaxing a number of approximations mentioned earlier. The results of these *complex* simulations revealed that powerful mass-loaded outflows, in the form of an accretion disc wind and a jet, can quite naturally and self-consistently form during the super-Eddington phase. And, at least to first order, both models, with different initial conditions, result in very similar large-scale disc and outflow structures.

One approximation which could not be relaxed is the radiation transfer. Given the high dimensionality of the problem, it is often computationally too expensive to calculate the full radiative transfer, whilst taking into account all the degrees of freedom. Therefore, both D18 and Curd & Narayan (2019) use the M1 closure relation (Levermore, 1984) to considerably simplify the situation. The equation of radiative transfer can be expressed as a system of coupled (angular averaged) moment equations (see Section 2.1.1). A closure relation is a mathematical technique used to express a higher order moment by its lower order moments, to *close* the system. In the case of the M1 closure, the first order (radiative flux) is closed using the zeroth order (the mean intensity). With such a closure, the problem is effectively recast as a diffusion approximation. Both simulations therefore effectively use a grey opacity when including radiative effects.

Given the reliance on the M1 closure in the GRRMHD, there is no frequency or angular dependence to the radiation transfer. Therefore in order to model the angular and frequency dependence of the radiation field, D18, and Curd & Narayan (2019), use sophisticated RT codes to post-process their models. This post-processing is also not without limitations. Curd & Narayan (2019) choose to neglect bound-bound opacities and use a simplified treatment for bound-free opacity. In D18, the authors include a wider range of opacities, but restrict themselves to a quasi-1D treatment of RT. More specifically, they discretise their outflow into four θ -averaged spherical models to explore the inclination dependence of emission.

Based on the results of their post-processing, D18 propose a unification scenario for X-ray and optically bright TDEs. In this scenario, the existence of both X-ray bright and optically bright (i.e. X-ray weak) TDEs are explained via an inclination effect. It is not precisely a geometric effect, but a result of how the thermal X-ray emission is reprocessed depending on the outflow properties along a given sight line. Polar observers see bare disc emission, which has not been reprocessed, and thus observe an X-ray bright TDE. By contrast, observers at intermediate and equatorial inclinations do not see direct disc emission. Along these sight lines, the X-ray photons are reprocessed, which shifts the luminosity away from X-ray wavelengths, and toward longer optical wavelengths. The net effect of this reprocessing is enhanced optical, but attenuated X-ray emission.

However, the simple spherical RT geometry adopted by D18 can be quite limiting. Spherical models cannot take into account the photon transfer and associated radiative transfer effects associated with the complex three dimensional velocity, density and temperature

structure of the 3D-GRRMHD model. In this chapter, I have therefore extended the post-processing of this model to two dimensions, using the same ϕ - and t -averaged snapshot over the quasi-steady phase of the D18 simulation. Using this model, I test and explore the global reprocessing picture: how does reprocessing affect the emergent light we observe? I also post-process the same four θ -averaged models from D18, to understand to just what extent PYTHON recovers the results of D18. And I use these four quasi-1D models to compare how the predicted spectra differ between the one and two dimensional geometries: just how limiting is the adoption of spherical geometry in RT post-processing?

The chapter is structured as follows. In the next section, I describe how the models are imported into PYTHON, describing the setup of the geometries and radiative transfer. Following on from this, in Section 5.4, I present and discuss the results of the models making up this work. First, in Section 5.4.1, I present the results of the θ -averaged models, and in Section 5.4.2 I present the physical properties and synthetic spectra produced for the 2D model. Turning the focus exclusively onto the 2D outflow, in Section 5.5 I delve into the details of how the outflow reprocesses the emission, resulting in an optically bright spectrum. Some time is spent discussing the differences between the 1D and 2D models in Section 5.5.3, before summarizing the limitations in Section 5.6, future work in Section 5.7 and finally the conclusions in Section 5.8.

5.2 Model setup

D18 use the GRRMHD code HARMRAD (McKinney et al., 2014), using the M1 radiation closure as already mentioned. Solar abundances are assumed for the material in the simulation, and mean-frequency opacities are used for the radiative transfer. HARMRAD also includes thermal Comptonization effects. The initial conditions and simulation parameters are set to model a small TDE accretion disc, with a black hole mass $M_{\text{BH}} = 5 \times 10^6 M_{\odot}$ and spin parameter of $a = 0.8$. As they have no intention of modelling the formation of the disc itself, the basic disc is therefore instantiated in the initial grid conditions. The original disc structure is initially quite small, with a radius of $R_{\text{disc}} = 500 r_g$. The material within initially follows a Keplerian velocity profile, and the disc has a height-to-radius ratio of $H/R \approx 0.3$. The radial density profile follows a power law $\rho \propto r^{1.3}$.

The simulation is run until converged to a steady state. This is said to be when the disc has achieved inflow equilibrium, i.e. where the flow transitions from inflow to outflow, out to $r/r_g = 200$, and additional when there is constant flux of mass, energy and specific angular momentum along the radial direction. During this quasi-steady phase, the average accretion rate is $15 \dot{M}_{Edd}$, which exceeds the maximum fallback rate for the disruption of a solar-like star ($\dot{M}_{\text{fb}} \sim 12 \dot{M}_{Edd}$) disrupted by a $M_{\text{BH}} = 5 \times 10^6 M_{\odot}$

SMBH. A relativistic jet and wide-angled, optically thick wind outflow are launched – driven by the intense radiation pressure from the inner disc. The properties of this outflow vary drastically with inclination. At high inclinations angles (i.e. close to the mid-plane), the wind is very dense and slow. This part of the outflow efficiently absorbs and reprocesses emission from the disc. At higher inclinations, the outflow is more dilute and is moving fast with a radial velocity component of a few $\times 0.1 c$. Absorption of the disc emission is far less efficient in this part of the wind, and is instead reprocessed by repeated scattering. The reprocessing properties of the outflow are discussed in more detail in Section 5.3.

Instead of using a kinematic outflow prescription, I import the output from the D18 simulation to construct the outflow in PYTHON. The radiative transfer through the model is carried out just as before. Multiple generations of photons are flown through the grid, incrementing MC estimators, until a converged electron temperature is found which balances the heating and cooling rates. The only difference is how the density and velocity structures are defined.

In D18, the 3D-GRRMHD model is a ϕ - and t -averaged snapshot of the model over the quasi-steady phase of the simulation. This is discretized onto a 2D *warped* polar coordinate grid. PYTHON is designed with structured grids in mind, therefore the 3D-GRRMHD model *has* to be re-mapped onto a structured grid before it can be imported. Remapping to a new coordinate grid first requires a new set of coordinates to be defined. The new grid is split finely into 256×128 cells, spaced logarithmically in the r direction, from 1.3 to $8478 r_g$, and linearly spaced in the θ direction, covering $0^\circ < \theta < 90^\circ$. The new coordinate grid is higher resolution to avoid a poor representation of the very finely resolved, warped, polar region of the original model¹.

The properties of the 3D-GRRMHD model are interpolated onto this new grid, using the Python library function `scipy.interpolate.griddata` (Virtanen et al., 2020). Both the density and temperature of each cell are defined at the centre, whereas the cell coordinates and velocities are defined at the inner cell vertex. Only one quadrant ($0^\circ < \theta < 90^\circ$) has been re-mapped, as PYTHON is designed to model outflows that are symmetric about both the equatorial plane and the rotation axis. Whilst this does not include the full θ extent of the 3D-GRRMHD model, it should not drastically modify the results. Both quadrants have broadly similar density and velocity structures.

5.2.1 θ -averaged models

To benchmark this method against D18, the same four θ -averaged models are imported into PYTHON, following the method outlined in D18. The re-mapped ϕ - and t -averaged snapshot is split into four bins, shown in Figure 5.1. To transform each 2D wedge into a

¹This is because the coordinate grid is linear in the θ -direction.

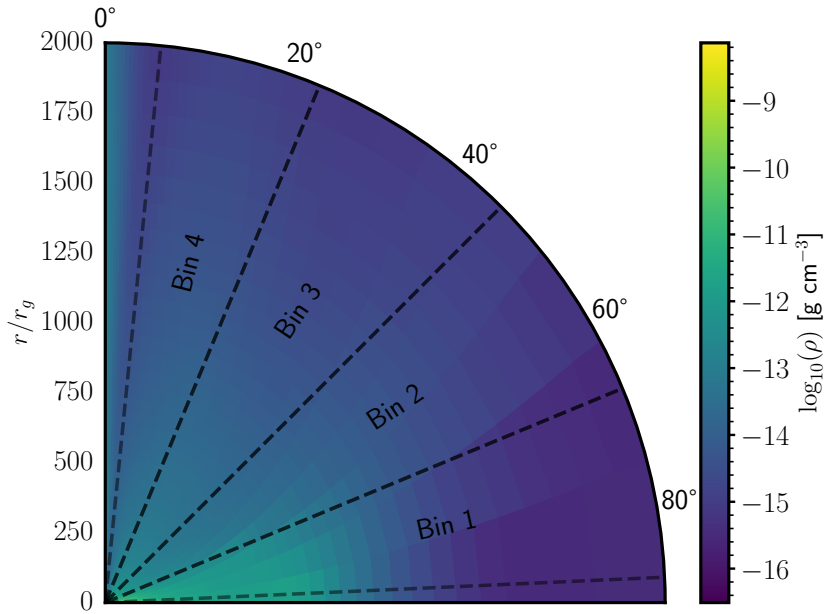


FIGURE 5.1: A colour plot showing the mass density of the model from D18 for the region covering $0^\circ < \theta < 90^\circ$. The regions labelled and bounded by the dashed lines are the four 1D θ -averaged models described by D18 in their section 2.2. As in previous PYTHON models, the disc plane is located at 90° .

1D spherical model, the density and velocity are squashed into a single point by taking a volume weighted average in the θ direction. The aim here is to model the outflow where inflow equilibrium has broadly been reached. This is set to where the radial velocity goes first from inflow to outflow. But the complex velocity structure of the outflow means there are a handful of cells, especially near the mid-plane, which are still inflowing past where equilibrium has broadly been reached. These cells are not included when taking the volume weighted average.

The outer boundaries are set to a fixed value of $r/r_g = 1000$. This is specifically chosen as material beyond this radius for bin 1 includes material from an artificial reservoir used to fuel the accretion process; including this material could artificially impact the reprocessing, artificially softening the SED and attenuating the emerging X-ray luminosity. For purely the sake of consistency, this outer boundary is imposed across all models, although it is not necessary. There is an additional constraint for PYTHON which limits the total inward integrated electron scattering optical depth to $\tau_{\text{es}} \leq 100$. This is imposed due to computational difficulties for PYTHON when modelling highly optically thick spherical outflows. This constraint only affects bin 1, moving the inner boundary from $r/r_g \approx 4$ to $r/r_g \approx 37$. A comparison between the θ -averaged models in this work and those in D18 is shown in Figure 5.2, which shows excellent agreement.

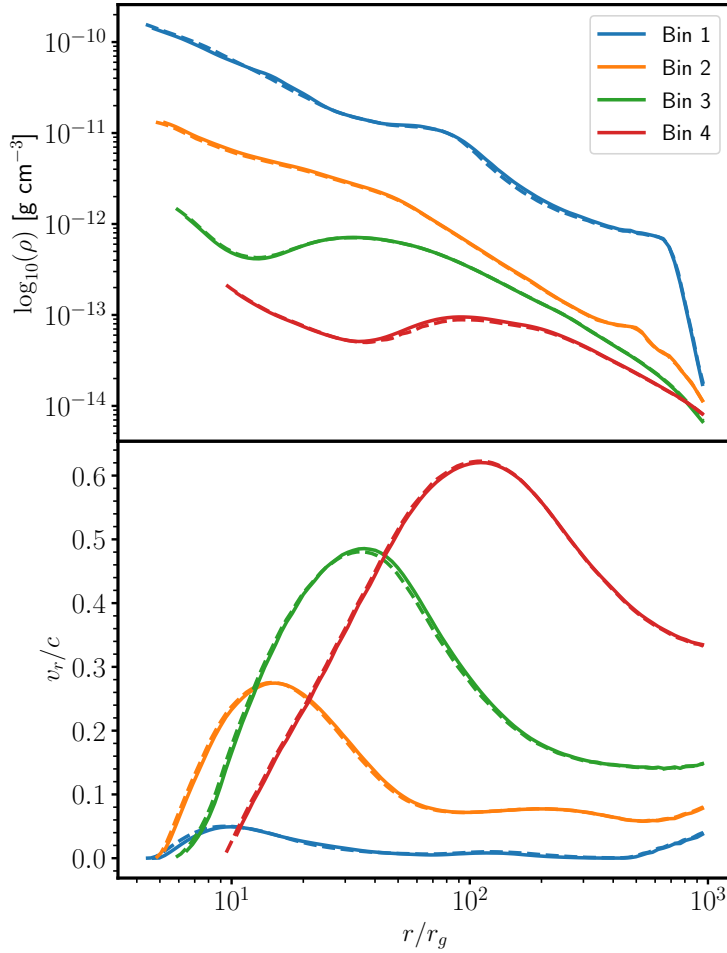


FIGURE 5.2: Density and velocity profiles, as a function of r , for the 1D model in this work (solid) and the 1D models (dashed) by D18. The profiles shown for the remapped model are excellent agreement with the original models. The small discrepancies in some of the profiles are due to differences from remapping.

Bin	θ_1 ($^\circ$)	θ_2 ($^\circ$)	r_{in} (r_g)	L_{in} (L_{Edd})
1	67	87	37	677
2	45	67	5	33
3	22	45	6	33
4	5	22	10	33

TABLE 5.1: The opening θ_1 and closing θ_2 angles for the wedges shown in Figure 5.1, as well as the radius of the central source and the luminosity of the radiation source in units of $L_{\text{Edd}} = 6.28 \times 10^{44}$ ergs s^{-1} .

Photon packets are emitted from an absorbing spherical central source, with a radius given by the inner boundary condition. The frequency distribution of the photons is that of a $T_{\text{BB}} = 10^6$ K blackbody. This temperature is the radiation temperature at the inner boundary in the 3D-GRRMHD model, derived from the M1 radiation treatment. The luminosity of the central source is set using the Stefan-Boltzmann law, and are hyper-Eddington ($L_{\text{Edd}} \gg 1$). But because of the absorbing inner boundary, most of the photons emitted are back-scattered to the inner boundary and are removed from the simulation. Just as in D18, this results in an emitted luminosity of roughly twice the Eddington luminosity ($L_{\text{Edd}} = 6.28 \times 10^{44}$ ergs s $^{-1}$) escaping along the mid-plane model (bin 4)². PYTHON does not include the concept of an event horizon, nor does it account for general relativistic effects. However, the absorbing nature of the spherical source acts as a crude approximation of an event horizon and acts as a sink for photons. The key parameters of the models are summarized in Table 5.1.

5.2.2 ϕ - and t -averaged model

The 2D ϕ - and t -averaged model is a remapped version of the 3D-GRRMHD model, instantiated onto a 2D structured polar coordinate grid as described earlier. Figure 5.3 shows a comparison of six density and radial velocity profiles, as a function of r , of the remapped model compared to the original. The density profiles are in excellent agreement. The velocity profiles, on the other hand, are less perfect. These discrepancies are due to the necessary re-mapping and interpolation steps. None of the differences are large enough to cause concern.

The outer boundary is set to the original boundary of the grid: $r/r_g = 8478$. The inner boundary is set to $r/r_g = 30$, a point where the radial component of the outflow velocity has transitioned from inflow to outflow for most inclinations and follows the optical depth limitation described in the previous section. Photons again are injected from the inner boundary, with a frequency distribution governed by a $T_{\text{BB}} = 2.2 \times 10^5$ K blackbody, which is roughly equal to the radiation temperature at the inner boundary. Following from the Stefan-Boltzmann law, the photon source then has a luminosity $L_{\text{in}} = 7.6 L_{\text{Edd}}$ which is again hyper-Eddington. As in the 1D models, the majority of this is lost to the absorbing inner edge when photons are back-scattered and absorbed by the central source. This model is essentially “as it is” in the quasi-steady phase of the original 3D-GRRMHD simulation, other than the evacuated jet region, which has not been included. This means that a handful of inflowing cells are included that are associated with regions with a complex velocity structure.

An important limitation is that rotation has been ignored, since the ϕ - and t -averaged snapshot provided does not include a v_ϕ component. A Keplerian velocity profile was originally tested, but resulted in super-luminal velocities in parts of the grid where the

²This is the same methodology D18 adopted to ensure enough luminosity escapes.

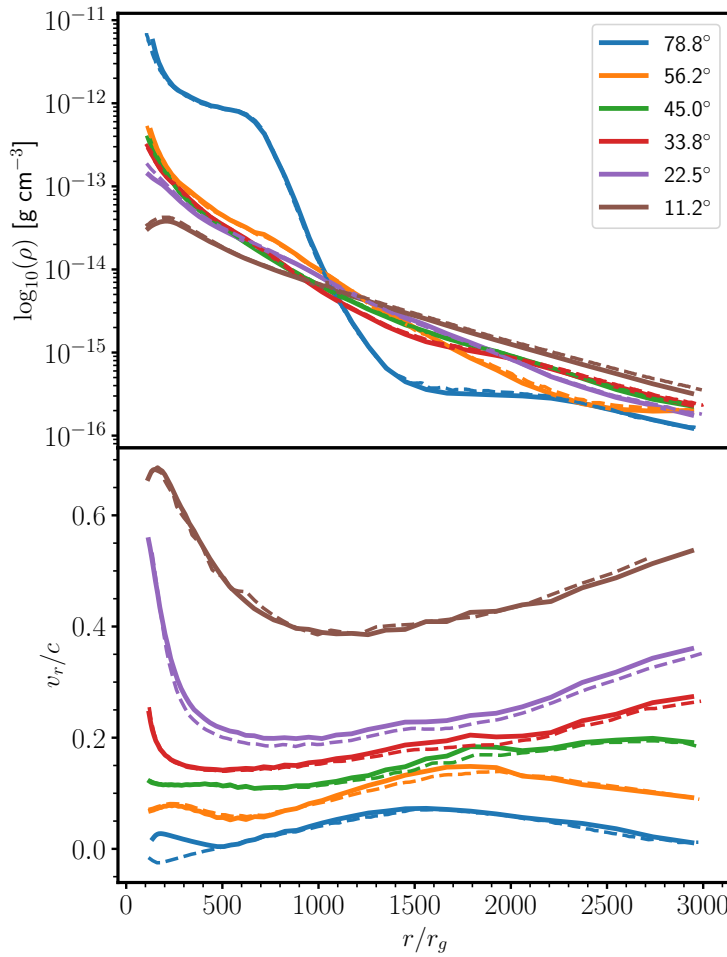


FIGURE 5.3: Density and velocity profiles, as a function of r , for a selection of eight lines for the 2D model in this work (solid) and the 3D-GRRMHD model (dashed) from D18. The profiles shown for the 2D remapped model are generally in good agreement with the original.

disc atmosphere likely follow a sub-Keplerian velocity profile (e.g. Thomsen et al., 2019, who have a very similar model). Since there is no clear path forward to defining a sensible rotational velocity profile, it is instead set to zero. The choice to ignore rotation should not impact the global reprocessing picture being tested. But if this approach is to be used to compare to TDE observations, then rotation should not be neglected for meaningful quantitative comparisons.

5.2.3 Atomic data

The radiative transfer in D18 considered the opacity from only hydrogen, helium and oxygen. In this work, two atomic data sets are used. For comparisons directly against D18, I include only the same three elements. However, for all other purposes – including

particularly the 2D modelling – I include the full complement of elements described in Section 2.3.4. These two distinctive data sets are otherwise identical, only differing in the elements which are included. Hydrogen and helium are treated using the macro atom formalism, whilst oxygen and other metals are modelled using a simple two-level approximation.

5.3 Reprocessing mechanisms

Much of the radiation produced in the D18 models was reprocessed as it travelled through the outflow and outer disc. Two distinct mechanisms for changing the SED of the photons were identified. The first is the so-called bulk scatter reprocessing (Roth & Kasen, 2018), which modifies the SED through successive electron scattering of trapped photons (Titarchuk & Shrader, 2005; Laurent & Titarchuk, 2007; Roth & Kasen, 2018). At each scattering event, photons transfer some of their energy into the outflow due to the electron recoil. These losses reduce the mean energy of the photons, and redshift the overall spectrum to longer wavelengths. This type of reprocessing is important for forming the optical spectrum away from the mid-plane (i.e. bins 2 through 4), where the density of outflow is low and ionization state high. It is far more important in the D18 and the models which I will present later, than in the models from Chapter 3 and Chapter 4. This is in-part due to the biconical geometry of the previous models, meaning photons are far more likely to escape without scattering and being reprocessed by the flow. But also because the optical depths of the super-Eddington outflow are far higher and photons are trapped for longer in the outflow.

Broadly speaking, bulk scatter reprocessing is important throughout the entire outflow, as photons are trapped by the high optical depths. But along the mid-plane (bin 1), the majority of radiation is reprocessed mainly through absorption and re-emission of photons, since the lower ionization state and higher densities make this far more efficient. This type of “atomic” reprocessing is mainly due to absorption of photons associated with the photo-ionization of He II and O VI, and free-free absorption. The absorbed energy is then re-emitted at longer wavelengths via recombination or free-free radiation, along with some line emission (see Roth, 2016; Roth & Kasen, 2018; Dai et al., 2018, but also Chapter 4). Additionally, the thermal state of electrons and the effects of non-coherent (Compton) scattering also modify the spectrum, by up- and down-scattering photons. However, this process plays a relatively minor role in these models.

5.4 Results

In this section, I will first present the predicted spectra for the θ -averaged models and compare them to the spectra generated by D18. I will then go on to describe the physical

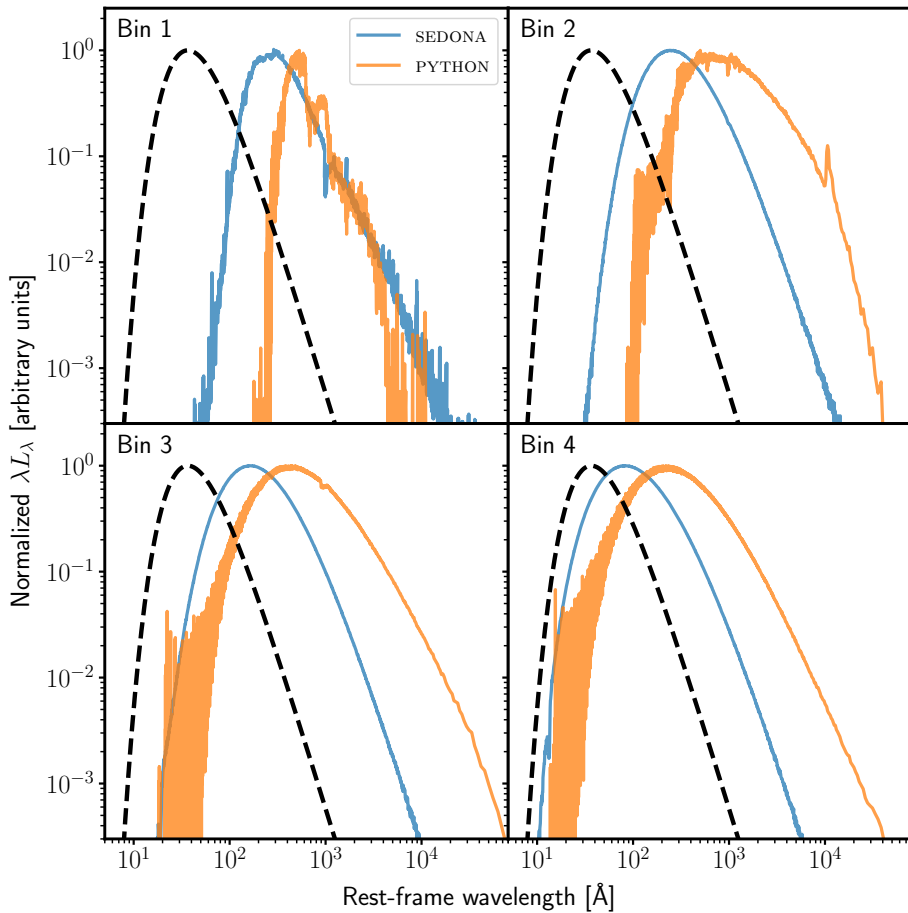


FIGURE 5.4: Synthetic rest-frame spectra generated by PYTHON using a reduced atomic data set for the four 1D θ -averaged models, and the same spectra by D18 using SEDONA. Additionally, shown, as a black dashed line, is the input SED. The name of each model has been labelled in the top left. The spectra have been smoothed slightly and normalized to the peak. All of the PYTHON spectra have been reprocessed more, relative to SEDONA.

properties of the 2D ϕ - and t -averaged model, along with the synthetic spectra predicted as a function of inclination for this model.

5.4.1 A benchmark test case

Shown in Figure 5.4 is a comparison of the peak normalized synthetic spectra (where each wavelength bin has been normalised by the peak luminosity of the spectrum) created by PYTHON and D18, who used the MCRT software SEDONA (Kasen et al., 2006; Roth & Kasen, 2015). The spectra for bins 3 and 4 broadly resemble one another. In both simulations, the spectra take the shape of a stretched blackbody, which have been redshifted to optical wavelengths. The redshifting, as in D18, is caused by bulk scatter reprocessing, which reduces the mean photon energy of the photon population through successive scattering (Titarchuk & Shrader, 2005; Laurent & Titarchuk, 2007; Roth &

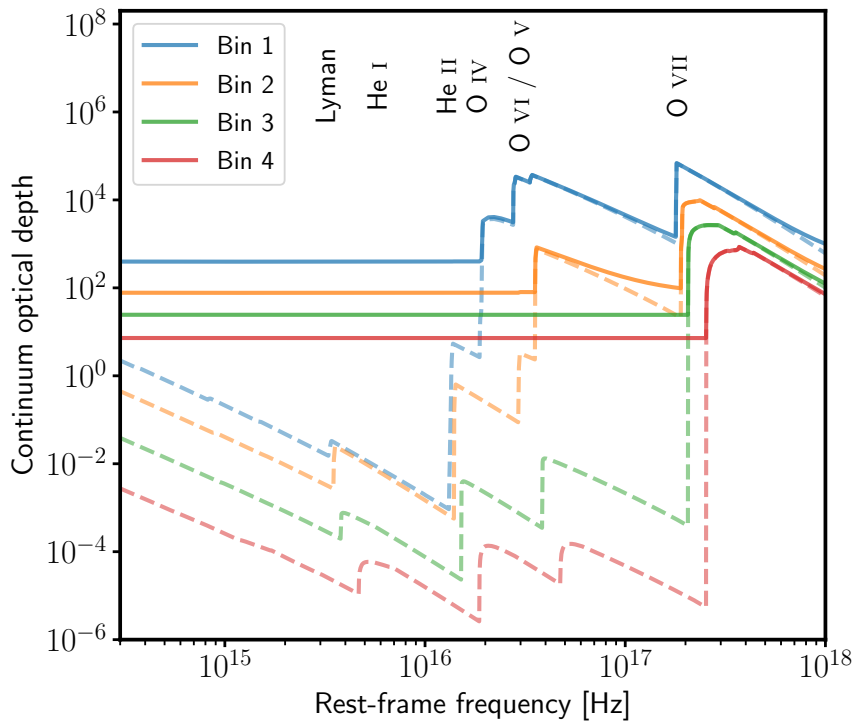


FIGURE 5.5: The continuum optical depth as a function of frequency for the θ -averaged models. Solid coloured lines show the total continuum optical depth, whereas the dashed lines show the optical depth without electron scattering. For bin 3 and 4, electron scattering dominates the opacity throughout. But in bin 1 and 2, opacity due to photo-ionization of oxygen is important at soft X-ray and EUV frequencies.

Kasen, 2018). Since hydrogen and helium are almost completely ionized throughout the PYTHON outflow, and oxygen exists mostly in O VII and above (but is completely ionized for $r/r_g < 100$), there is very little absorption of the radiation. Whilst the spectra take broadly the same form, the predicted spectra from PYTHON peak at and extend to longer wavelengths. This implies that bulk scatter reprocessing is stronger in PYTHON. It is not clear why this is the case since, at least to first order, both programs do essentially the same when calculating the velocity and electron scattering opacity, as well as when transforming between frames. Further testing is required to understand the crux of the difference but, due to time constraints, this has not yet been done. It is important to note, however, that this residual uncertainty associated with the implementation of bulk scatter reprocessing does not significantly affect the results of the previous chapters, since this mechanism plays a negligible role in the models discussed there.

In addition to peaking at a longer wavelength, the PYTHON bin 2 model produces line features which are not produced by D18. There is a significant emission feature due to He I $\lambda 10,833$ and a number of absorption features in the EUV, caused by resonance scattering with O V and O VI. The opacity of these ions can be seen in the continuum optical depth of this model, shown in Figure 5.5.

The differences between the two results are even larger for bin 1. Here, the PYTHON spectrum is narrower, peaks at a longer wavelength and the quasi-Rayleigh-Jeans (RJ) tail is steeper. There are also differences in the lines that are produced. The differences between PYTHON and SEDONA for these bin 1 and 2 are caused by differences in atomic physics, which has manifested as different ionization and thermal states. These models are far more sensitive to differences in atomic physics, because of their larger densities and lower ionization states. Perhaps the most important numerical difference – which is likely to be responsible for at least some of the differences in the predicted spectra – is that D18 do not include Compton heating and cooling in their thermal balance (Roth & Kasen, 2015, and private communication). At least in bin 1, Compton heating and cooling dominates the thermal balance in PYTHON, resulting in a cooler outflow and greater metal opacity. This explains why the SED is narrower, as more of the high frequency radiation has been absorbed by the outflow.

More generally, given the higher densities and lower ionization states in bins 1 and 2, reprocessing via absorption and re-remission should be more important in these models. And it clearly is. At short wavelengths, there are significant edges in the spectra and continuum optical depth, characteristic of photo-ionization. In these bins, the dominant EUV opacity has shifted from electron scattering to photo-ionization associated oxygen and helium. Whilst bulk scatter reprocessing is still important for bin 2, given by the redshift of the spectrum, such reprocessing is much less important for bin 1, where reprocessing via absorption is significantly stronger.

5.4.2 Results in two dimensions

5.4.2.1 Physical properties

A selection of physical properties for the ϕ - and t -averaged model are shown in Figure 5.6, where the full atomic data set has been used; the properties of the simulation using the full and reduced atomic data are quite similar, other than a few differences which will be discussed where appropriate.

The electron temperature (top left) is largest at the launching point of the outflow, where it reaches temperatures close to $\log_{10}[T_e] \gtrsim 5$ K. Thus, as expected, the electron and radiation temperatures are roughly equal here, $T_e \sim T_r$. The wind remains this temperature until at $\log_{10}[r/r_g] \sim 3.3$. Beyond here, the temperature decreases to $\log_{10}[T_e] \sim 4.3$ K by $\log_{10}[r/r_g] \sim 3.3$. The cool shell of material at this radius is caused by line cooling by collisional excitation, which produces a family of EUV emission lines. This feature is not part of the reduced atomic species version of this model, suggesting it is line cooling from metals other than oxygen. Beyond $\log_{10}[r/r_g] \sim 3.5$, the wind heats up to $\log_{10}[T_e] \sim 5$ K and is heated primarily via photo-ionization by high frequency photons. Even though the SED is heavily reprocessed by this point, there is still a

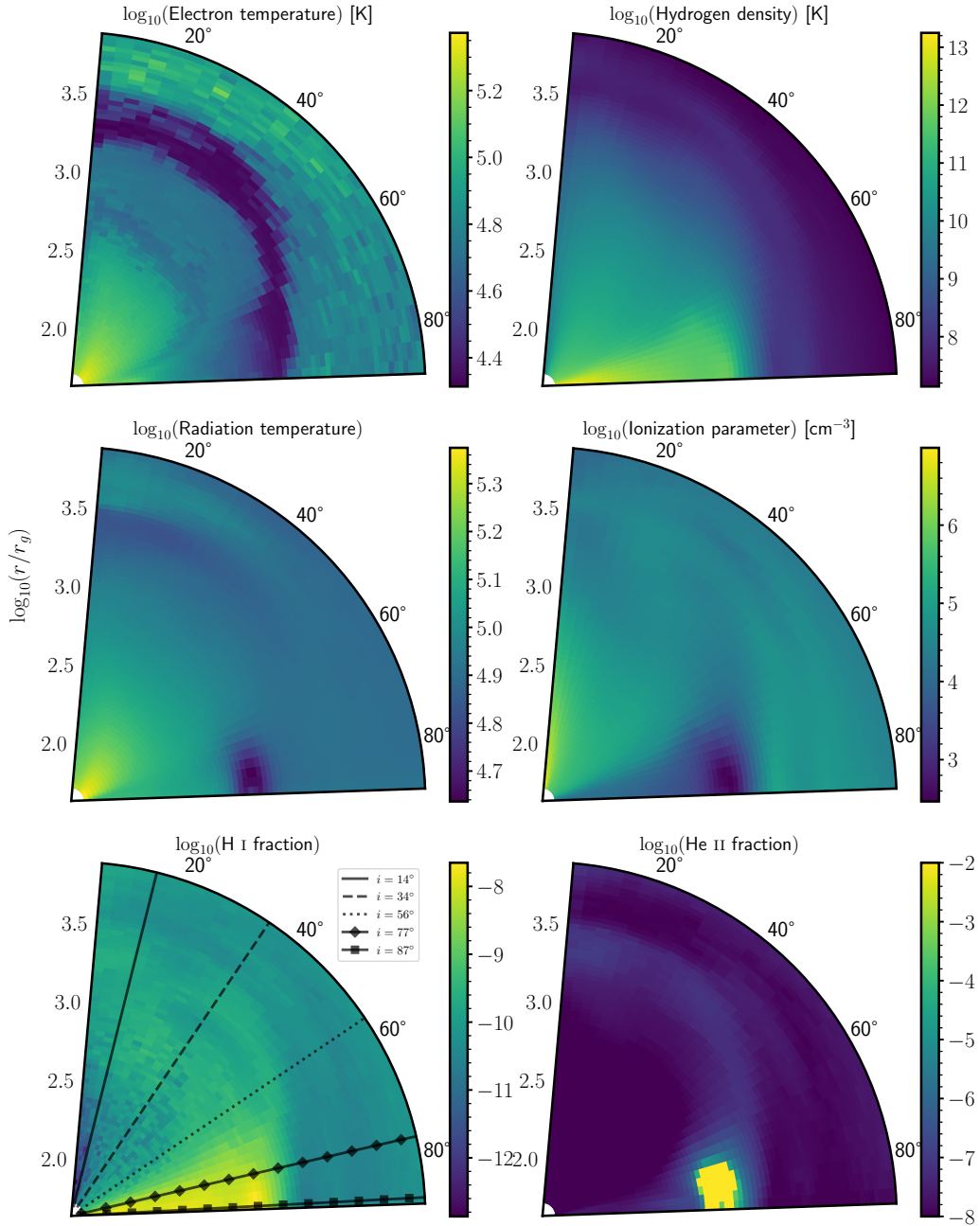


FIGURE 5.6: Various colour plots for a selection of physical parameters for the 2D model using the full atomic species, constrained to $5^\circ < \theta < 88^\circ$. *Top left:* electron temperature. *Top right:* hydrogen density. *Middle left:* radiation temperature. *Middle right:* ionization parameter. *Bottom left:* H I ion fraction. *Bottom right:* He II ion fraction.

significant population of high energy photons that avoided reprocessing by virtue of travelling along low optical depth paths.

The hydrogen density (top right) tracks the matter density. The most dense region of the wind is the accretion disc atmosphere. At the inner boundary along the mid-plane, the density reaches $\log_{10}[n_{\text{H}}] \sim 13 \text{ cm}^{-3}$ and decreases to $\log_{10}[n_{\text{H}}] \sim 12 \text{ cm}^{-3}$ by $\log_{10}[r/r_g] \sim 2.7$ and drops further past $\log_{10}[r/r_g] \sim 2.7$. For intermediate regions, the density is not as large and roughly follows $\log_{10}[n_{\text{H}}] \sim 11 \text{ cm}^{-3}$ at the launch point of the wind, and decreases to $\log_{10}[n_{\text{H}}] \sim 7 \text{ cm}^{-3}$ by the outer boundary. Along polar directions ($i < 10^\circ$), the gas is more dilute and is typically an order of magnitude, or two, less dense. Throughout most of the wind, hydrogen and helium are almost entirely ionized. But the edge of the disc atmosphere, which has been shielded, houses a small enhanced population of both neutral and singly ionized helium ($\log_{10}[n_{\text{He II}}] \sim 10 \text{ cm}^{-3}$) and neutral hydrogen. This part of the flow is illuminated by an SED which has been reprocessed and attenuated, resulting in a lower ionization state.

The level of reprocessing can be traced via the radiation temperature (middle left panel of Figure 5.6), which essentially represents the mean photon frequency of a blackbody radiation field, defined as,

$$T_r = \frac{h\bar{\nu}}{3.832k_B}, \quad (5.1)$$

where $\bar{\nu}$ is the average photon frequency (in a cell), h is Planck's constant and k_B Boltzmann's constant. At the same position where hydrogen and helium are in a lower ionization state, the radiation temperature is lower. This shows that this region is illuminated by a softer SED, since the average photon frequency is lower. To quantify the ionization state, it is possible to, once again, use the ionization parameter, U_{H} (Equation 3.1). The ionization parameter is fairly constant throughout the outflow, with $\log_{10}[U_{\text{H}}] \sim 5.5$. But it is substantially lower in the disc atmosphere at $\log_{10}[r/r_g] \sim 2.5$. Here, it is illuminated by a reprocessed SED, with a reduced number of hydrogen ionizing photons. But since $\log_{10}[U_{\text{H}}] \sim 3$, this means there is still a fairly significant number of ionizing photons. In line with this, the fraction of neutral hydrogen is relatively modest. Along low inclination angles, at the inner boundary, the ionization parameter is large. But by $\log_{10}[r/r_g] \sim 2.7$, the ionization parameter has been moderated slightly by reprocessing.

An interesting feature worth noting is that, at $\log_{10}[r/r_g] \sim 3.2$, the ionization parameter is slightly reduced for practically all inclinations. This means there is a slightly enhanced population of material in a lower ionization state, such as singly ionized helium. A similar situation is also happening in the polar outflow, at $\log_{10}[r/r_g] \sim 3.4$. There is a reduction in radiation temperature here, suggesting the radiation field has been fairly significantly reprocessed. This is likely caused by photo-absorption, possibly associated

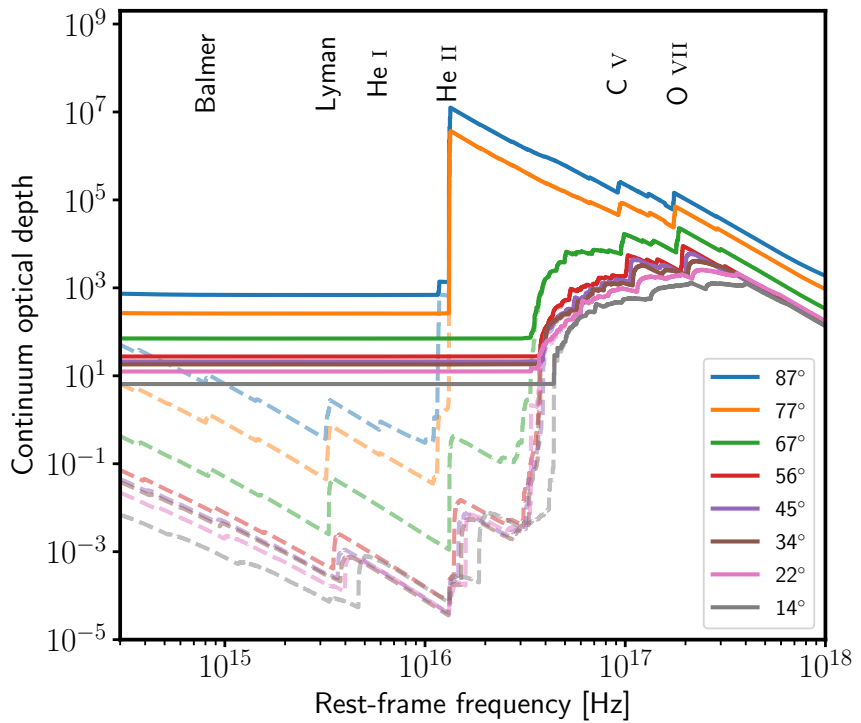


FIGURE 5.7: The continuum optical depth, for the 2D model, as a function of frequency for various sight lines with electron scattering included (solid lines) and without electron scattering (dashed lines). Along the base of the wind, there is significant opacity due to the photo-ionization of He II.

with neutral hydrogen. These features are not in the reduced atomic data model, since the properties at this radius are influenced by line cooling associated with metals other than oxygen.

5.4.2.2 The optical depth

The continuum optical depth for multiple sight lines is shown in Figure 5.7, with (solid) and without (dashed) electron scattering included. For the majority of the frequency range considered, the scattering optical depth dominates over any other source of opacity, such as photo-ionization or free-free absorption. For intermediate angles $\tau_{\text{es}} \sim 50$, but is closer to $\tau_{\text{es}} \lesssim 9$ for polar sight lines and $\tau_{\text{es}} \gtrsim 700$ along the mid-plane. For high inclinations, which look through the disc atmosphere, the dominant opacity is not scattering, but is from the photo-ionization of singly ionized helium, as well as other metals such as ionized oxygen and carbon. This means that along high inclination sight lines, atomic reprocessing (due to photo-ionization) will be extremely efficient. The large opacity for helium corresponds to the enhanced population of He II in the disc atmosphere.

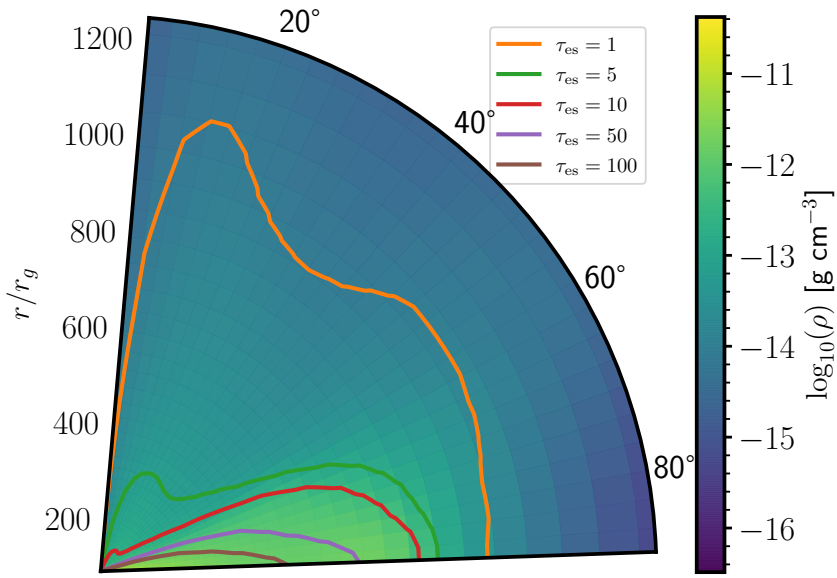


FIGURE 5.8: A colour plot showing the the mass density of the outflow and solid lines showing the outline for multiple electron scattering photospheres for values of τ_{es} labelled in the legend. The outflow is optically thick to electron scattering ($\tau_{\text{es}} > 1$) out to a radius of $1000 r_g$, with the highest electron scattering in the disc atmosphere which is traced almost neatly by the $\tau_{\text{es}} = 10$ photosphere.

Even though the scattering optical depth dominates, by removing this contribution it is revealed that there is also still significant opacity from photo-ionization. Within the disc atmosphere, photo-ionization of the hydrogen Lyman and Balmer edges, as well as He I are still relatively important with $\tau \sim 10$. They are still significantly weaker compared to the He II and higher energy edges though. The majority of the high frequency opacity is located close to the inner boundary of the wind where the matter density is largest. However, the line cooling at $\log_{10}[r/r_g] \sim 3.2$ (cf. top right of Figure 5.6) results in a lower ionization state at this radius, which contributes to some of the high frequency (EUV) metal opacity.

Several electron scattering “photospheres” (strictly speaking, constant optical depth contours) are shown in Figure 5.8, for radially integrated inward optical depths of $\tau_{\text{es}} = 1, 5, 10, 50$ and, 100 . The $\tau_{\text{es}} = 1$ photosphere is located at $r/r_g \sim 1000$, but is considerably closer to the central source for polar angles near the jet region. For larger values of τ_{es} , the photospheres are located nearly entirely within the accretion disc atmosphere, with $\tau_{\text{es}} = 10$ almost neatly tracing out the boundary. Along lower inclination angles ($\theta < 15^\circ$), the surfaces of the photospheres are located further in, suggesting that photons travelling along these sight lines travel freely and are reprocessed less. Polar observers are far more likely to see *bare* disc emission. But, there is nothing to stop reprocessed photons from eventually escaping along these inclinations, either.

5.4.2.3 The synthetic spectra

The (peak normalized) synthetic spectra generated for the 2D model are shown in Figure 5.9 for five inclination angles, using both the full atomic data (orange) and the reduced data (blue). Considering first the differences between the spectra associated with the two atomic data sets, the first and most obvious is that the inclusion of more metals results in numerous EUV emission and absorption lines that are missing from the spectra based on the reduced atomic data set. The extra metal opacity also causes more absorption of high frequency photons, particularly in the intermediate and high inclination spectra. But, in general, the shape and the modification due to reprocessing are essentially the same between the two types of models. This makes the reduced atomic data simulation – which is easier to interpret – quite useful for the purpose of developing physical intuition.

To begin the detailed analysis, it appears that the general shape of the spectra are quite similar to the spectra produced by the 1D θ -averaged models³. The qualitative shape of the spectra take the form of a stretched (multi-colour) blackbody, and all but the lowest inclination spectrum have been significantly redshifted. The overall result of the redshifting, as well as other reprocessing mechanisms, is that the optical emission is enhanced. The low inclination spectra have not undergone any significant amount of atomic reprocessing, which is clear from the fact that the exponential tail of the emergent SED is similar to the initial SED. However, bulk scatter reprocessing has increased the *spread* of photon energies, which stretches the spectrum out. Although photons which have been reprocessed in the mid-plane can escape along low inclinations, which present paths of lower optical depth. Some of the optical emission is therefore due to some of these photons.

The higher inclination spectra, which depend more on the photon transport through the optically thick part of the outflow, display significant absorption of high frequency photons and a larger redshift. The absorption suggests that photo-ionization is significant at the base of the outflow. Because of the large optical depth at the base, photons are trapped. These trapped photons are reprocessed again and again before they can escape the outflow. This results in far more redshifted, absorbed and optically enhanced spectra. It is, in-fact, a combination of atomic reprocessing and bulk scatter reprocessing that ultimately creates the optically bright emergent spectrum. Along these high inclination sight lines, the proportion of X-ray photons contributing to the observed spectrum is small, as most of the radiant energy escapes at EUV, FUV, optical and longer wavebands.

The spectra are also characterized by line emission and absorption. For all the spectra in Figure 5.9, there is a strong recombination emission feature at $\approx 10,000 \text{ \AA}$ by He I $\lambda 10,833$. There are also the previously mentioned EUV lines, which are only present in

³A detailed comparison between the 1D and 2D spectra is included in Section 5.5.3.

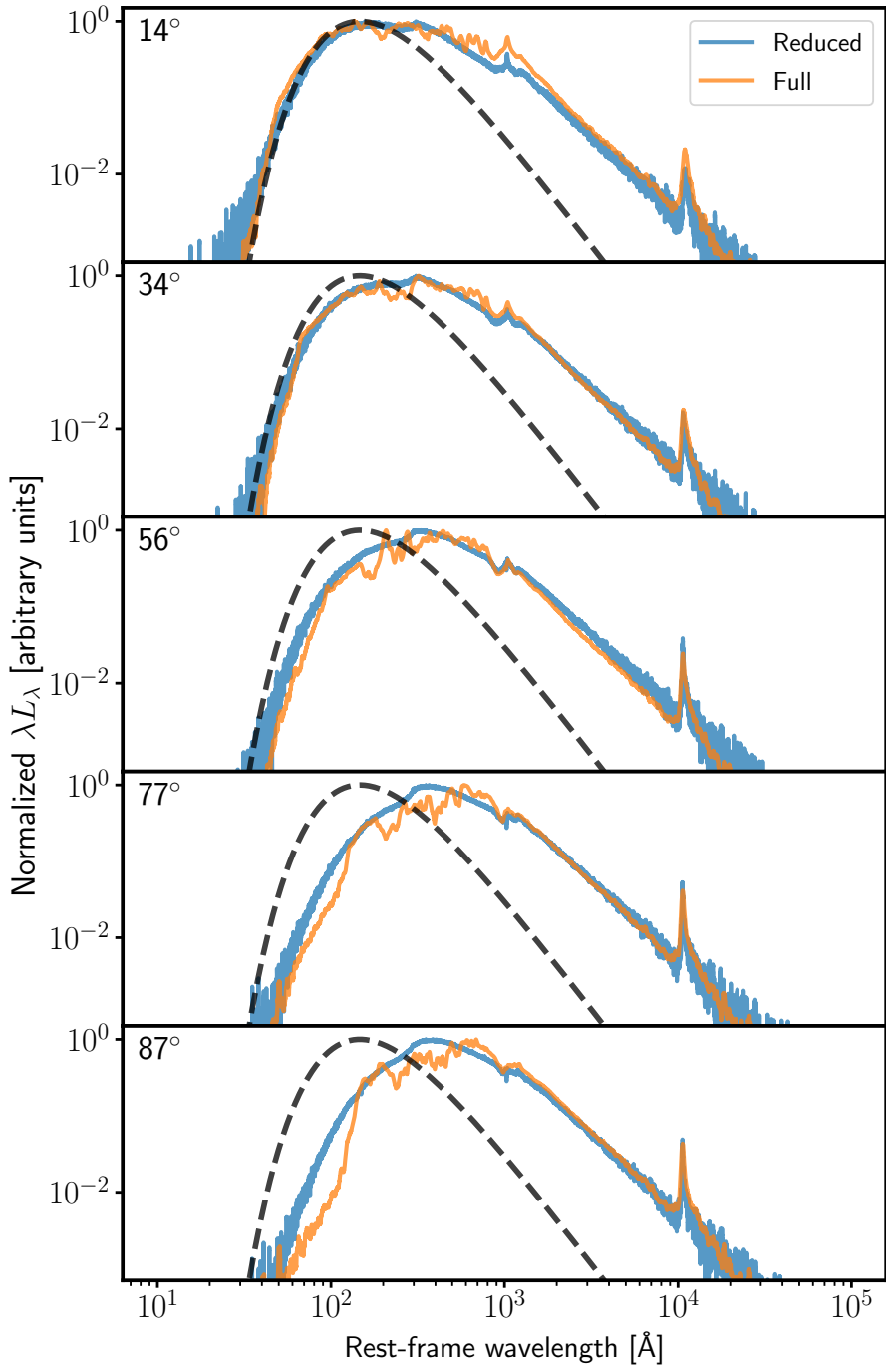


FIGURE 5.9: Rest-frame synthetic spectra for the 2D geometry using both the reduced and full atomic data sets, as labelled in the legend. Each panel shows a different inclination spectrum, which has been labelled in the top left, as well as the input SED shown by a dashed black line. The spectra have been smoothed and normalized to peak. Each spectrum has been reprocessed, forming a distinctive stretched blackbody SED with an enhanced optical continuum.

the spectra produced by simulations that use the full atomic data set. Unfortunately, these lines, and also the EUV continuum, are hard to observe, as EUV photons are easily extinguished by interstellar absorption in the host galaxy and/or the Milky Way. There is also a feature present at $\approx 1000 \text{ \AA}$ that is attributed to Ly α . However, unlike the He I emission, there does appear to be some inclination dependence to this line. At low inclinations, the line is in emission, but it transitions into an absorption feature as the inclination, and the column density between emission and observer, increases.

5.5 Discussion

5.5.1 Bulk scatter vs. atomic reprocessing in the outflow

As already noted by D18 and above, there are two distinct reprocessing mechanisms at work in this outflow. First, there is bulk scatter reprocessing, which redshifts photons at each scattering event. Second, there is the atomic reprocessing, which absorbs high frequency photons (mainly via photo-ionization) and re-emits them at lower frequencies. Both mechanisms tend to redden the SED, and both scale with optical depth. Correspondingly, the spectra for the high inclination, high column density sight lines exhibit the strongest degree of reddening/reprocessing.

However, the *relative* importance of the two mechanisms is a function of inclination. At the poles of the outflow, where it is fast and dilute, bulk scatter reprocessing dominates. Thus the entire spectrum is redshifted to longer wavelengths via electron scattering, without any significant absorption/re-emission. Bulk scatter reprocessing is associated with photons scattering in a diverging outflow. Each time a photon scatters, some of its energy is transferred to the outflow. Thus the net consequence of repeated scattering, for the whole photon population, is to lower the mean photon energy. This shifts the peak (and the rest of the spectrum) to redder wavelengths. Since bulk scatter reprocessing needs photons to scatter multiple times, the polar region of the outflow does not reprocess that much, as the scattering optical depth is relatively low. Therefore, the SED along these sight lines has undergone relatively little reprocessing, so an X-ray bright spectrum should be seen by an observer.

Referring back to Figure 5.7, the scattering optical is $\tau_{\text{es}} \sim 9 - 20$ along the low and intermediate inclinations, but it is closer to $\tau_{\text{es}} \gtrsim 700$ for high inclinations. This means photons almost certainly undergo many scatters before they escape. As the number of scatters scales with optical depth as $N_{\text{sc}} = \tau^2$, even a modest increase in optical depth can cause a substantial increase in the number of scatters. As a result, the redshifting associated with bulk scatter reprocessing is significantly higher for high inclination sight lines that skim along the dense mid-plane. This quadratic scaling with the mean number of scatters also explains why there is a noticeable difference between the spectra predicted

for $i = 14^\circ$ and $i = 34^\circ$ spectra in Figure 5.9, even those both of these sight lines pass through relatively low density regions.

Along the mid-plane, the outflow is higher density and is in a lower ionization state. Therefore absorption of radiation by atomic processes (e.g. photo-ionization) is far more efficient, and radiation is reprocessed through this mechanism. This type of reprocessing absorbs high frequency photons, via, e.g. photo- or free-free absorption, and re-emits them at longer wavelengths through recombination of free electrons or free-free emission. There is clear evidence that such reprocessing is happening by looking at the continuum optical depth of the model in Figure 5.7. There is significant opacity presented by He II, in addition to other metal ions such as C V, O VI and O VIII. These edges are many orders of magnitude larger than the electron scattering optical depths, and absorption by these edges accounts for many features seen in Figure 5.9. Whilst atomic reprocessing is clearly important in shaping the emergent light, given the extreme scattering optical depths along the mid-plane, bulk scatter reprocessing still plays an indispensable role in redshifting the entire spectrum at high inclinations.

One way to visualise how the SED is reprocessed within the two outflow regimes (slow and dense vs fast and dilute) is by looking at how the local SED changes as a function of position in the outflow. This is shown in Figure 5.10 for a characteristic low and high inclination. Focusing first on the top panel, showing the low inclination SEDs, it is seen that there is little photo-ionization, although there are a few edges at small radii associated with helium. There are also some edges which are in emission, notably the Lyman edge at $r/r_g = 1788$. This SED lies somewhere in polar region of the outflow, where the SED has been more reprocessed relative to the local SED in the surrounding region, traced by the low radiation temperature in Figure 5.6. It is also of interest how the high frequency tail of the SED has already been significantly attenuated by $r/r_g = 69$. This must mean that the launching region of the wind, even for polar inclinations, is dense and highly absorbing from the metal opacity. The SEDs become noticeably weaker at each radial sample point, as the radiation field becomes more dilute.

The bottom panel of Figure 5.10 shows the SED at the same radial points, but for a high inclination sight line. These SEDs exhibit many more edges and lines. Clear evidence for the importance of atomic reprocessing. Photons with energies high enough to ionize He II are efficiently absorbed, and very little radiation escapes above this edge. For example, at $r/r_g = 714$, where an enhanced population of He II ions exists (c.f. Figure 5.6), the SED is essentially discontinuous, showing the powerful impact photo-ionization has on the SED. But, at the next radial point, the SED is no longer discontinuous, suggesting photons have been able to scatter around the absorbing material. The SEDs also display a prominent emission feature associated with He II recombination. This provides yet more evidence that absorption via photo-ionization and re-emission via recombination is critical in these regions.

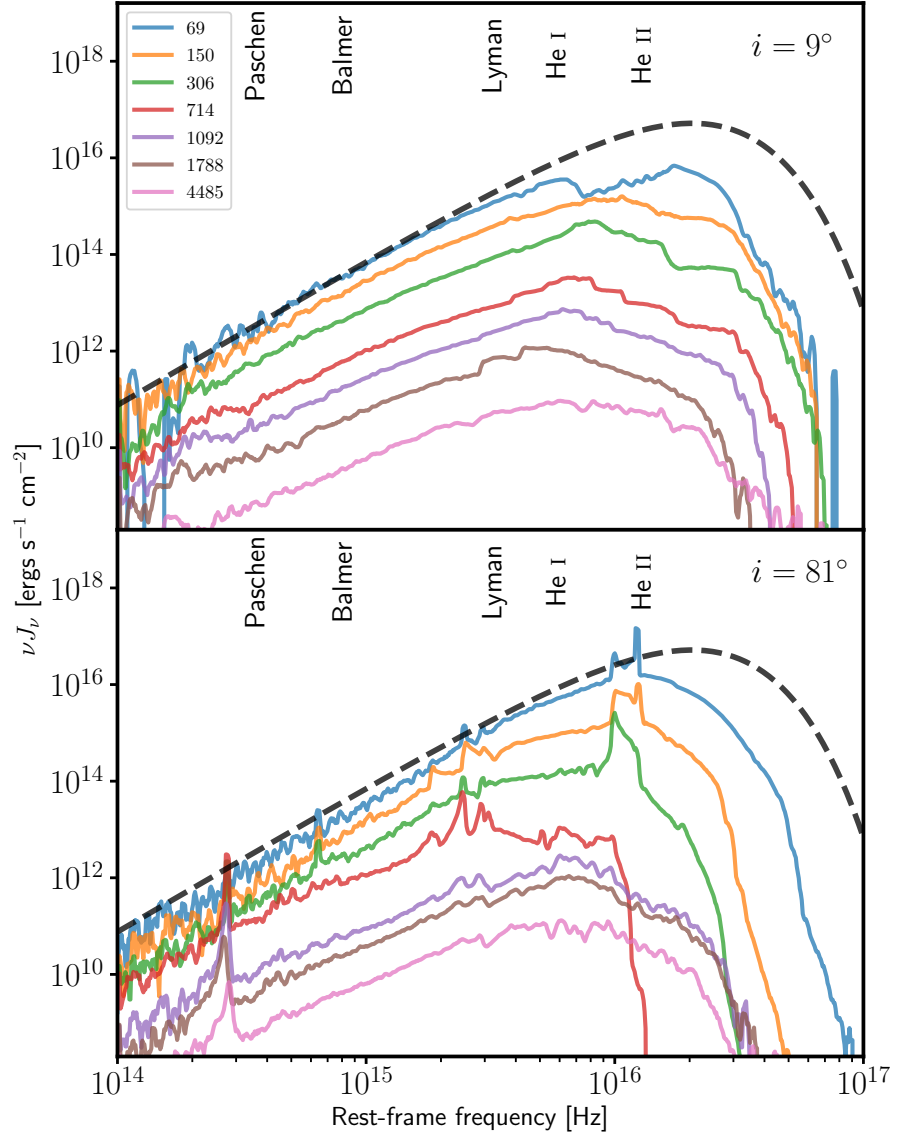


FIGURE 5.10: Rest-frame synthetic spectra generated for various grid cells at different gravitational radii along two sight lines, labelled in the top right of each panel. Each SED represents the local SED of a grid cell at the given radius and inclination. Various photo-absorption edges have been labelled at the top of each panel. Along the low sight line, there is very little absorption of the radiation and the SED has been modified due to bulk scatter reprocessing, reducing the photon energy of the population. But along high inclinations, there is significant absorption of high frequency radiation which is re-emitted at longer wavelengths.

The emerging 2D reprocessing picture is qualitatively similar to the 1D reprocessing picture for the models discussed in Section 5.4.1 and by D18. In the polar (and intermediate inclination) region of the outflow, bulk scatter reprocessing dominates, since the high ionization state of the dilute material makes absorption via atomic processes inefficient. Such reprocessing produces an optically enhanced spectrum by redshifting the entire SED to longer wavelengths. At the mid-plane, the ionization state is lower, and the density is much larger. This results in efficient reprocessing via atomic absorption and re-emission. The atomic species responsible are also similar to the quasi-1D D18 picture. Notably, photons are photo-absorbed by He II, C V and O VII. However, 2D radiative transfer effects do matter. For example, the high-energy ($\nu \gtrsim 10^{16}$ Hz) tail of the $i = 81^\circ$ SEDs at $r/r_g > 1000$ is mainly due to photons that have been scattered into this region from more polar directions.

5.5.2 The optical-to-X-ray ratio as a function of inclination

In the unified model of D18, the optical-to-X-ray ratio increases with inclination. This led to their proposal that X-ray bright TDEs correspond to systems observed at low inclinations, where the SED has been reprocessed the least. Whereas optically bright TDEs (with weak X-ray components) correspond to systems observed at high inclinations. These conclusions, and the unified model, were based on the 1D θ -averaged models from Section 5.4.1. Here, I will present the same analysis for the 2D ϕ - and t - averaged model.

In Figure 5.11, four sight lines have been plotted in luminosity units for the 2D model using the full atomic data. The wavelength range encapsulating the X-ray and optical bands are also shown in Figure 5.11. To quantify the dependence of X-ray to optical ratio on inclination, the X-ray band has been defined as 0.2 keV and above⁴ and the optical band as the interval between 1500 - 7000 Å. A quick visual inspection of Figure 5.11 shows that the optical-to-X-ray ratio increases with inclination. The input SED has been bulk scatter reprocessed to peak at longer wavelengths and the optical emission has additionally been enhanced by atomic reprocessing. The exact ratios of the integrated optical to X-ray flux are shown in Figure 5.12.

The findings here are consistent with the D18 unified model. For observers along the mid-plane, the spectra appear optically bright, with almost no X-ray emission. This is because high energy (X-ray) photons are efficiently absorbed and re-emitted at optical wavelengths. At low inclinations, since the ionization state is so high, and the density so low, photons are reprocessed very little – there is still some reprocessing at the base of the outflow – meaning the X-ray luminosity is much higher.

⁴In D18, the X-ray band is defined as 0.3 keV and above.

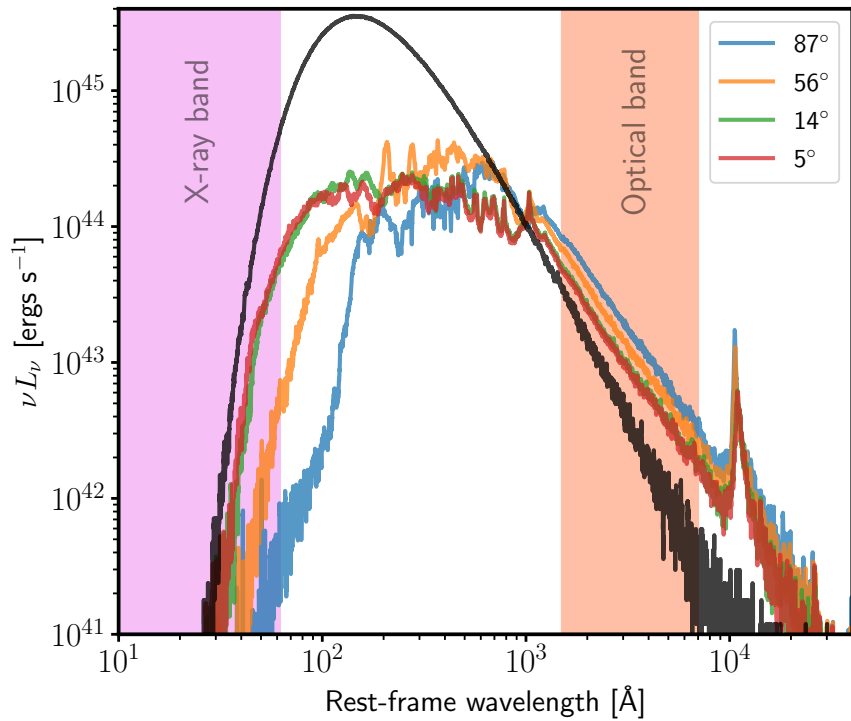


FIGURE 5.11: Rest frame synthetic spectra for four sight lines (labelled in the legend) for the ϕ - and t -averaged 2D model. The input SED is shown in black. Shown by the shaded purple and coral areas are the X-ray and optical wavebands. The optical-to-X-ray ratio increases with inclination angle. At high inclinations, observers see a bright optical spectrum with little to no accompanying X-ray emission. This result is consistent with the unified model proposed by D18.

In this model, however, there are no (low) inclinations where the X-ray luminosity is much greater than the optical luminosity, as in the bin 4 model by D18. But on the other hand, the range in optical-to-X-ray ratios in my simulation is consistent with observations of real TDEs, which tend to have optical-to-X-ray ratio ratios of $\gtrsim 1$ (Auchettl et al., 2017; Wevers et al., 2019). This is not necessarily because the 2D model is reprocessing far more X-ray photons, but comes as a result that the input SED is a lower temperature blackbody because of the different boundary condition used. There are therefore already fewer (non-reprocessed) X-ray photons available in the 2D model compared to the 10^6 K blackbody used by D18. The result of this means there is no sight line which produces significantly more X-ray emission than optical. In D18, the polar bin 4 model produces an optical-to-X-ray ratio of 0.036. But, referring Figure 5.12, the lowest inclination spectrum produces a ratio closer to unity. Even so, this is still consistent with the D18 unification scenario, as the number of non-reprocessed (X-ray/EUV) photons which contribute to the emergent spectrum is greater at low inclinations.

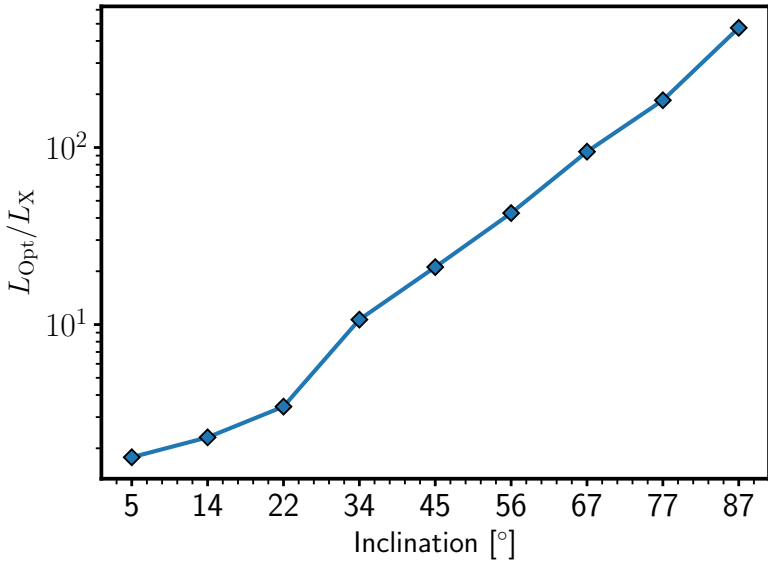


FIGURE 5.12: The integrated optical-to-X-ray luminosity ratios as a function of inclination angle. The X-ray band has been defined to include photons with energies 0.2 keV and above, and the optical waveband is defined between 1500 - 7000 Å. The optical luminosity of the spectra increases with inclination, whilst the X-ray luminosity decreases. Observers who look at high inclinations will see an optically bright TDE.

5.5.3 How important is treating radiative transfer in 2D?

The intention of this work was to extend the previous one-dimensional modelling (or post-processing) into two dimensions. But I also made the brash claim that the 1D approximations considered so far are quite limiting. So, just how limiting is the 1D treatment? In Section 5.4.1 and Section 5.4.2, the results of the 1D and 2D models were presented separately. In this section, I will discuss the differences between these two geometries. For a more meaningful comparison, the inner boundary condition for the 1D models have been changed to match the boundary condition of the 2D models, e.g. the inner boundary is set at $r/r_g = 30$ and the frequency distribution is set by a $T_{\text{bb}} = 2 \times 10^5$ K blackbody. The predicted spectra, therefore, are different to those presented in Section 5.4.1.

Figure 5.13 shows the peaked normalized spectra for the four θ -averaged models described in Section 5.2.1. To compare the spectra to the 2D (reduced atomic data) model, I have included the respective mid-point inclination for each bin, as indicated in the top left of each panel. To start with a broad, top-level comparison, the *shapes* of the synthetic spectra produced by the 1D and 2D models are quite similar. Both models essentially produce a reprocessed – shifted/stretched – blackbody SED. This makes sense. As I have already discussed in the previous section, the global reprocessing picture is essentially the same in the 1D and 2D models. But this is really the only similarity.

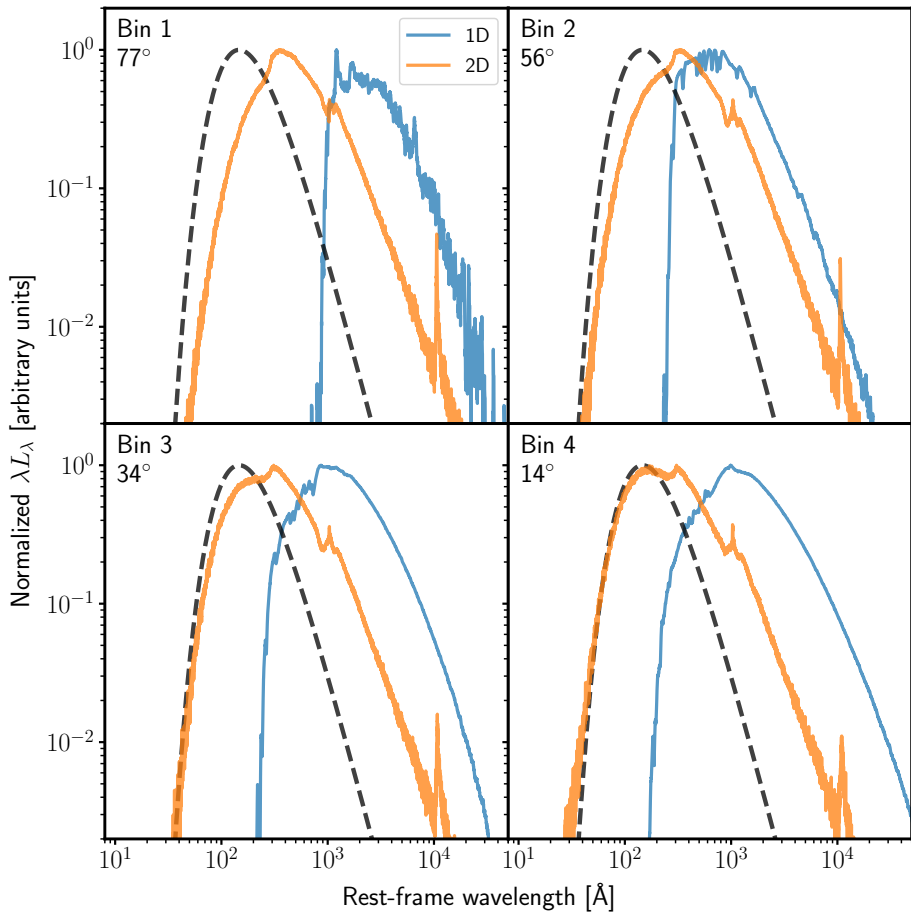


FIGURE 5.13: Peak normalized rest-frame synthetic spectra for the 1D and 2D models, including hydrogen, helium and oxygen. The 2D models shown are the respective mid-point inclination angles for the opening angles of each 1D bin. Shown by the black dashed line is the input SED used for the models. The emergent spectra in both geometries are reprocessed blackbodies, which have been stretched and redshifted to longer wavelength. But in 1D, the amount of shifting is far greater (due to more efficient photon trapping) and a number of absorption and line features differ between the two geometries. At the core of it, most of these differences are due to multi-d photon transport effects.

For bins 4 and 3, the most obvious difference between the two geometries is how much the emergent SED has been shifted relative to the input. In both models, the 1D model has been shifted to longer wavelengths whereas in 2D, the spectra peak close to the peak of the input SED. This comes down to the fact that photon trapping is not as efficient in 2D, as photons are able to scatter around optically thick regions. Whereas in 1D, photons must push through the full optical depth because of the spherical symmetry of the models. This increases the number of electron scattering events, leading to stronger bulk scatter reprocessing causing the 1D models to peak at longer wavelengths. This is not to say the 2D models are not affected strongly by bulk scatter reprocessing. The emergent spectra at high inclinations are still significantly redshifted, and all spectra are *stretched* due bulk scatter reprocessing creating a spread of photon energies.

Another difference is the absence (presence) of atomic features in 1D (2D). In 1D, the ionization state of the winds are higher so that the spectra are essentially featureless; other than some absorption features in the EUV in both geometries. By contrast, there are line features in the 2D spectrum, e.g. associated with Ly α and He I recombination. This is because in 2D, photons from a lower ionization region of the flow (i.e. the mid-plane) are able to escape along low inclinations. This point is made clearer by looking again at Figure 5.10. The bottom panel shows that the strong He I feature is generated in the mid-plane, but is not present in the low inclination local SEDs (top panel). Therefore this line *must* be forming in the base of the outflow, and these photons are able to escape along low inclinations (of low optical depth) to appear in the low inclination spectra.

In the case of bin 2, the emergent spectra are quite different in 1- and 2D. One major difference is the absence of some line features in 1D, notably, again, Ly α and He I, for the reasons discussed earlier. The 2D model is missing the EUV absorption lines which are present in the 1D spectrum. There is also a significant edge in the 1D spectrum, caused by absorption of the high frequency photons by photo-ionization of helium and oxygen, which is not there in 2D. This is likely as before, where the 1D geometry means photons have to push through the full optical depth, increasing their chance of being absorbed and reprocessed. Bin 1 also displays a big difference between the two geometries. Again, this is expected: in 1D, photons are trapped as they attempt to push through the highly optically thick atmosphere. The SED in 2D peaks at a shorter wavelength, and is broader than the 1D spectrum since there is no edge due to decreased absorption of high energy photons, since they can travel along paths of low optical depth and remain relatively unperturbed.

Across all of the 2D sight lines presented, the spectra have not been redshifted or re-processed as much as the 1D models. Furthermore, there are differences in the lines which are present in the spectra. In 2D, lines can form in the dense base of the outflow, and escape along more polar directions because of lower optical depths. However, the conditions along the 2D sight lines are not too dissimilar to the conditions in the quasi-1D model. If the appearance of the spectra depended *only* on the physical conditions along a given sight line, then the 1D and 2D spectra should be more similar. But this is clearly not the case. So, does this comparison suggest the need for two dimensional radiative transfer models? In general, the answer is: *yes, I believe it does*. That said, the 1D models do predict qualitatively similar SED shapes and trends. Thus the unified picture developed by D18 from their 1D post-processing models is valid. Clearly, however, 1D models will not result in quantitatively correct results: the differences between 1D and 2D spectra for the same sight lines in Figure 5.9 are large enough to matter at all inclinations.

5.6 Limitations

Even though I have been able to relax a number of approximations and assumptions made in previous attempts to post-process 3D-GRRMHD simulations, several limitations remain. First, it is assumed that the outflow is in radiative equilibrium, that it is in a steady state and that it is time independent. In a handful of TDEs, such as AT2018zr (Hung et al., 2019) and AT2019qiz (Nicholl et al., 2020; Hung et al., 2020), the optical and UV spectra have been observed to change over timescales as short as 10-20 days, early in their life. The ϕ - and t -averaged snapshot essentially represents the $\Delta t \approx 5$ days epoch, when inflow equilibrium of the disc and a quasi-steady state has been reached. By post-processing a time-averaged snapshot, the evolution of the outflow – including its effect on the emergent light – is completely ignored. An obvious next step for future work would be to post-process multiple snapshots. Additionally, the models here are still limited to 2D (without rotation), due to the ϕ -averaged nature of the model. While this is an advancement over the earlier 1D treatments, it is still not the complete picture.

It is also probably worthwhile to use a radiation hydrodynamic model with a frequency dependent treatment (using MCRT) for the radiation field. With the current 3D-GRRMHD approaches using the M1 radiation closure relation, radiative processes such as any additional outflow driving by the photon field via bulk scatter reprocessing are not taken into account. PYTHON implicitly assumes that this type of driving is already taken account in the velocity structure, due to the kinematic approach taken. Therefore detailed radiation hydrodynamics models will be required to appreciate the full impact of such processes. This could be done using PYTHON, as illustrated by the radiation hydrodynamic simulations of XRBs carried out by Higginbottom et al. (2017, 2018, 2019).

The main limitation of the models, particular for the 2D model, is how the radiation source has been treated. In both 1D and 2D models, the central radiation source is a single temperature spherical blackbody. However, if the emission from TDEs comes from an accretion disc, then a single colour blackbody is a poor approximation for the shape of the SED. Moreover, the spherical source employs an isotropic angular distribution for the radiation emitted. It is more likely that the radiation will be anisotropic in TDEs. Whilst the radiation source used here is a reasonable first approximation, it is not yet clear whether a more realistic model of the continuum is needed to obtain quantitatively reliable results. However, the addition of such a model imposes additional conceptual and computational complexities. For example, it is not so simple to automatically define the surface of the accretion disc, or to know the angular distribution of the photons. Additionally, it is unclear how to realistically model the emission expected from radiation dominated, and vertically extended, accretion discs. Indeed, the structure and properties of such discs are still an area of intense and active research (e.g. Hirose et al., 2009; Jiang et al., 2013; Shen & Matzner, 2014). However, as a potential first step, a simple parameterization given by thin- or slim-disc models could be used.

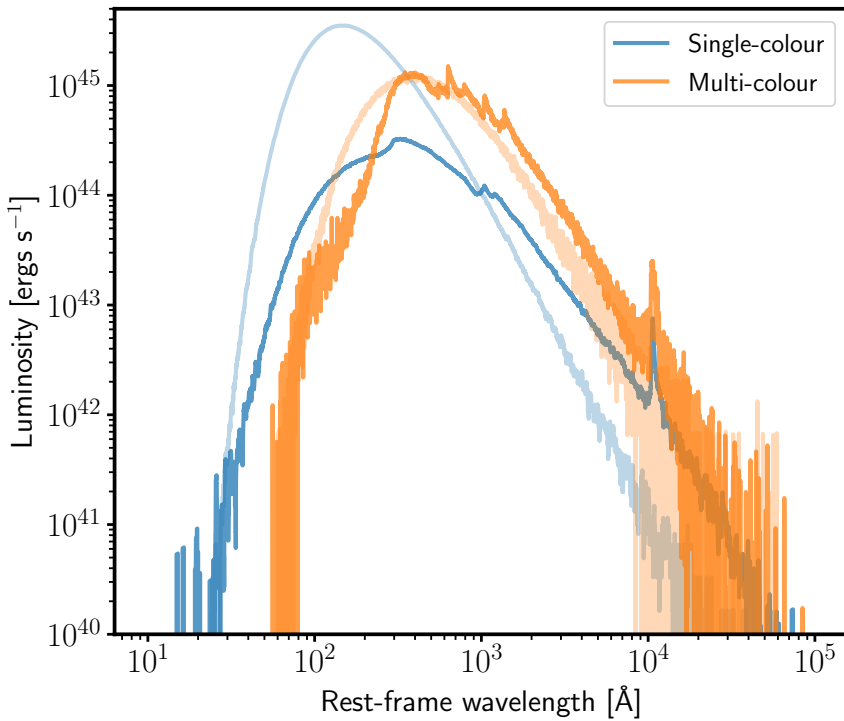


FIGURE 5.14: Angle integrated synthetic spectra generated for the 2D model using the reduced atomic species data. In blue is the spectra produced where the input SED is a single colour blackbody emitted from the origin of the model. In orange is the same outflow, but using a multi-colour disc SED following from a simple slim-disc prescription (e.g. Strubbe & Quataert, 2009). The faded curves of the same colour are the input SEDs for the respective simulation.

Another limitation, which would probably only cause a subtle difference to the ionization state, is the neglect of 3D-GRRMHD effects. In PYTHON, there is no concept of an event horizon (although this is somewhat approximated by the use of an absorbing inner boundary in the simulations). Moreover, photons travel in straight lines between their interaction points. Close to the SMBH, the curved paths of photons could change the MC estimators from which the ionization state is determined. However, the majority of reprocessing happens at $r/r_g \approx 500$, where GR effects are less likely to matter.

5.7 Future work

Due to (mostly) time constraints, a number of tests, investigations and further model refinements could not be done for the work presented here. Therefore, there is plenty of scope for further work. First, it is not clear why the spectra are redshifted to longer wavelengths by bulk scatter reprocessing in PYTHON compared to SEDONA . In principle, both SEDONA and PYTHON are treating the relevant physics in similar ways. But, clearly, they are producing different degrees of bulk scatter reprocessing, and it is not

immediately obvious why. Additional tests of SEDONA vs. PYTHON for simpler tests cases should be done, so as to understand the differences in bulk scatter reprocessing. There may also be scope to use analytic models as “ground truth” for testing both programs (e.g. Titarchuk & Shrader, 2005; Laurent & Titarchuk, 2007). Some of this work is already underway.

In addition, further tests should be performed to test the sensitivity of the results to the inner boundary conditions, specifically the radius, temperature and luminosity of the central blackbody. D18 found that their models are largely insensitive to the input SED, at least in terms of their overall shape (Roth, private communication), so as long as the outflow remains in a relatively high ionization state. Extensive testing has not yet been carried out for PYTHON to understand the SED dependence on the models. The different SEDs used for the same quasi-1D models in Section 5.4.1 and Section 5.5.3 result in different emergent SEDs, showing that this is important to explore further.

Finally, one other obvious avenue for future work, briefly discussed already, would be to improve the continuum model. As a starting point, in Figure 5.14, the synthetic spectrum for the 2D model is presented using as prototype slim-disc SED, compared against the same model using a single colour blackbody. Ignoring the fact that SEDs are quite different, notably in terms of the luminosity and peak frequencies, on first inspection, it is clear to see that there are a number of differences in terms of line features, reprocessing and escaping luminosity from changing the SED. But the angular distribution of the (ansotropic) disc radiation is likely much closer to the physical reality of an accreting TDE. The differences in Figure 5.14 show that a more realistic continuum model warrants further exploration for post-processing this, and future models.

5.8 Summary

I have conducted MCRT simulations to model the effect of reprocessing on the emergent spectrum of an outflow from a TDE during the super-Eddington phase. The model outflow is the output from a 3D-GRRMHD simulation by D18, which was remapped onto a structured grid and imported into PYTHON. By using the 1D models first discussed in D18, I showed how PYTHON qualitatively produces similar reprocessed SEDs as D18, with the caveat that bulk scatter reprocessing is stronger in PYTHON than in the original models, for reasons that are not currently understood. The main focus of this work, however, was post-processing a 2D t - and ϕ -averaged snapshot of the 3D-GRRMHD model to examine the emergent emission and reprocessing properties of the outflow. The main results of these simulations are as follows:

1. The synthetic spectra generated by SEDONA and PYTHON in 1D are broadly similar, producing a *stretched* blackbody which has been redshifted relative to the original

SED. However, reprocessing via bulk scatter reprocessing is far greater in PYTHON. Work is underway to understand this difference.

2. The spectra produced by the 1D and 2D models are qualitatively quite similar, producing the same continuum shape and general reprocessing trend. However, the spectra reveals that the degree of reprocessing is far stronger in 1D, where photons have to push through the full optical depth of the model. In 2D, photon trapping and reprocessing is less efficient as photons are able to travel along paths of low optical depth experiencing less reprocessing interactions. In addition, photons which form in the base of the 2D outflow can contribute to the spectra generated for polar observers. This suggests that future modelling needs to include the effects of the multi-dimensional ionization structure and photon transport.
3. The peak of the emergent SEDs, and the majority of the emission, emerges at EUV wavelengths. The spectral features in this region are acutely sensitive to the number of metals included in the model and can pose a significant opacity for high frequency photons. In addition, these EUV emission lines also dominate the cooling at $r/r_g \approx 1500$.
4. The dominant opacity at most wavelengths is electron scattering, with $\tau_{es} \sim 10$ for polar inclinations and $\tau_{es} \gtrsim 700$ for high inclinations close to the mid-plane. However, at short wavelengths, photo-ionization of metals dominates the opacity, and at the mid-plane there is significant opacity due to photo-ionization of ionized helium, carbon and oxygen ions.
5. The majority of reprocessing responsible for the optical continuum occurs at the edge the disc atmosphere. Here, photons are absorbed due to the photo-ionization of He II, C V and O VII and are then re-emitted via recombination. However, in the regions well above the mid-plane, reprocessing via repeated scattering (bulk scatter reprocessing) dominates and shifts the SED towards longer, optical wavelengths. This type of reprocessing also creates a greater spread in photon energies, which produces the distinctive stretched blackbody shape.
6. The optical-to-X-ray emission ratio for all the models increases as a function of inclination angle, consistent with the unification scenario proposed by D18.

Data availability

The models and their synthetic spectra from this chapter are publicly available online at https://github.com/saultyevil/tde_super_eddington.

Chapter 6

Conclusions and Future Work

Only in death does duty end.

Astra Militarum

6.1 Conclusions

The earliest models for TDEs proposed that the light we observe should be dominated by thermal X-ray emission from the inner edge of a hot and compact accretion disc. For a long time, when there was only a meagre few TDEs in the population of studied events, this model fit the observations perfectly well. But, within the past decade or so, an increasing number of TDEs whose light is dominated by optical and UV emission have been discovered. Clearly, then, we are still ignorant with regards to the emission and radiative transfer processes that produce the light we see from these events.

The aims of this thesis were to shed light on and develop our understanding of the UV and optical emission of TDEs, and to test the potentially important impact accretion disc winds could have on shaping the light we observe. This is quite a natural scenario to explore. Given the extreme luminosities associated with ripping a star apart and gorging on its remains, powerful radiation-driven outflows will rather naturally form. To explore this scenario, I conducted state-of-the-art Monte Carlo radiative transfer and ionization simulations, modelling the random walk of photons from emission to escape to predict the emergent spectra.

The first problem tackled by this thesis was to investigate the dichotomy in the UV spectra of TDEs. At the same evolutionary phase, some TDEs display blueshifted BALs, whilst others instead show BELs. A similar phenomenology exists in CVs and QSOs, which can be explained via an orientation effect associated with line formation in an accretion disc wind. Given the striking similarity between the UV spectra of TDEs and

QSOs, I proposed and tested in Chapter 3 if the BAL vs. BEL dichotomy in TDEs could also be explained via a similar accretion disc wind model. To test this, I ran a grid of simulations exploring a range of wind geometries and kinematics, to generate synthetic spectra for sight lines which look into and out of the wind cone. The simulations show that line formation in a TDE disc wind can naturally produce both BALs and BELs, depending on the orientation of the observer. Observers whose line of sight falls into the wind cone preferentially observe BALs, whilst other observers are more likely to see BELs. The fiducial model of this work consisted of a clumped, wide-angled wind, which subtended more than 50% of the sky as seen from the central engine. This geometry is consistent with the high covering factor implied by the detection of BALs in most of the UV spectra, suggesting that the relative number of BAL TDEs could be used to estimate the covering fraction of TDE outflows. Additionally, I further tested how the disruption of a CNO-processed star changes the characteristics of the UV spectra, finding that such abundances result in weaker carbon and stronger nitrogen lines, consistent with the spectra of some TDEs.

These initial simulations, showing the viability of line formation in an outflow, were extremely promising. Using the fiducial model as a jumping-off point, I conducted a tighter and more focused parameter search in Chapter 4, exploring if and how reprocessing by an accretion disc wind could produce the bright optical emission seen in a sub-set of TDEs. This grid of simulations produced encouraging matches to observational data, and showed that the hydrogen and helium emission lines, commonly seen in the optical line spectra of TDEs, can be naturally produced in a optically thick disc wind which reprocesses the underlying accretion disc SED. These features are relatively insensitive to moderate changes to the kinematics of the outflow. But, if the base of the wind is not dense enough to shield or reprocess the accretion disc continuum, then the characteristic emission features are significantly weaker. In contrast, the bright optical continuum is insensitive to such changes in the outflow structure, forming for a wide range of outflow parameters.

By examining the models further, I found that the dominant reprocessing mechanism is photo-ionization of He II (in some outflows He I and H I are also important), which absorbs X-ray (and EUV) photons, re-emitting them at longer wavelengths via recombination. Furthermore, the emission lines are modified by repeated scattering in a diverging outflow (the so-called bulk scatter reprocessing), which creates distinctive red-skewed wings, commonly seen in many TDEs. But these winds were often too highly ionized to produce UV absorption features. By truncating the inner disc radius, softening the SED, the same BAL vs. BEL dichotomy of the previous chapter is recovered whilst still preserving the optical features. This suggests that BAL formation is acutely sensitive to the shape of the SED.

Given the encouraging results in Chapter 4 (and after many necessary improvements to PYTHON), in Chapter 5, I turned my attention toward examining the reprocessing

in an outflow from a GRRMHD simulation by [Dai et al. \(2018\)](#), who modelled the super-Eddington accretion phase expected in some TDEs. I post-processed their model, producing synthetic spectra as a function of inclination angle, expanding on previous quasi-one dimensional radiative transfer modelling by [Dai et al. \(2018\)](#) into two dimensions. However, at first I restricted my work to one dimension, to benchmark the results produced by the software used throughout this thesis against the 1D results presented in [Dai et al. \(2018\)](#). The comparison between results is promising, as both my and the simulations by [Dai et al. \(2018\)](#) produce qualitatively similar emergent spectra, in that they both take the form of a reprocessed and stretched blackbody. The peaks of the SED are redshifted, relative to the input SED (due to reprocessing via scattering), albeit to longer wavelengths in PYTHON simulations than in the original models. The reason for this discrepancy is not yet known.

The synthetic spectra produced for the two dimensional model are not too dissimilar to the one dimensional models. They produce reprocessed stretched blackbodies, radiating mainly in the EUV. However, in this geometry, bulk scatter reprocessing is weaker, as photons are not as trapped: the two dimensional geometry of the outflow allows photons to be beamed along directions of low optical depth. The same photo-ionization reprocessing as in the previous chapter is, again, the main mechanism for producing the bright optical continuum. However, this continuum is only observed for high inclination angles, which look along the mid-plane through the dense accretion disc atmosphere. Most of the reprocessing is done by singly ionized helium and multiply ionized oxygen, but carbon also plays a role. Perhaps most importantly, I found that the optical-to-X-ray ratio increased with inclination angle, with X-ray emission being strongest at polar angles. This is consistent with the results from the post-processing by [Dai et al. \(2018\)](#), and is therefore also consistent with the optical and X-ray bright unified model of TDEs proposed by [Dai et al. \(2018\)](#). But whilst the one and two dimensional models share the same global reprocessing picture, the quasi-1D models fail to capture the line features present in two dimensions. The detailed spectra are significantly different in shape, features and the amount of redshifting. In the end, this comes down to complex multi-dimensional photon transport effects. Fundamentally, as already noted above, spherical models trap photons far more efficiently than two-dimensional wind models. So whilst the same “global” picture can be investigated with simple quasi-1D models, at least two (or more) dimensions will be required in the future for meaningful quantitative comparisons to real data.

To summarize this thesis: mass loss, in the form of an accretion disc wind, is important in modifying and shaping the light which we observe from these events. I first showed how the dichotomy in the UV spectroscopic observations can be explained via an orientation effect associated with line formation in an accretion disc wind. And I have also shown how disc winds are viable reprocessing envelopes, which absorb thermal X-ray radiation, and re-emits it at longer, optical wavelengths forming the enhanced optical continuum

and spectral features in a sub-set of TDEs. This thesis has clear consequences for the field. Not only does it provide a substantial contribution to our understanding of the optical and UV emission in TDEs, it additionally has shown how reprocessing is an extremely promising candidate for unifying optically bright events with the TDE accretion disc picture.

6.2 Future work

6.2.1 Accelerating photon transport in optically thick regions

The outflows expected to form in TDEs are expected to be optically thick, especially during early times, given the super-Eddington accretion rates in this regime. I have shown in this thesis that detailed radiative transfer calculations are required to fully appreciate and understand the emission in TDEs. Fortunately, given the complex geometries and radiative transfer and atomic processes, the MCRT method is perfectly suited for modelling this emission. But, MCRT has one failing. It is extremely computationally inefficient when simulating photon transport through optically thick media. The number of times a photon is expected to scatter scales with the square of the optical depth (Equation 2.16). As each individual interaction is simulated, even if it takes only a few hundred nanoseconds to compute, it is not long before the cumulative time taken to simulate hundreds of interactions for potentially hundreds of millions of photons becomes computationally infeasible.

Photons additionally have a hard time penetrating through optically thick media, as they could be absorbed, become trapped or be back-scattered. For a finite and computationally tractable number of photons, it is likely that only a small fraction of them will make it through. This results in poor model convergence and can affect the MC estimators and modify the results. Furthermore, even the photons that do penetrate can be heavily attenuated and thus carry low statistical weight, causing estimators to grossly under- or over-estimate their true value (see, e.g. [Camps & Baes, 2018](#)).

Over the years, a toolbox of clever and sophisticated algorithms have become available that can be used to modify the Monte Carlo transport process, increasing its computational efficiency. These include diffusion approximations, such as, for instance, the modified random walk ([Fleck & Canfield, 1984](#); [Min et al., 2009](#); [Robitaille, 2010](#); [Keady & Cleveland, 2017](#)), which turns multiple photon *micro-steps* into one diffuse *macro-step*. There are also a set of variance reduction methods which can be used to improve the Monte Carlo statistics and reduce the number of photons that need to be tracked (e.g. Russian Roulette, packet splitting and patch stretching; [Khisamutdinov, 1989](#); [Melnik-Melnikov et al., 1997](#); [Dupree & Fraley, 2002](#); [Harries, 2015](#); [Baes et al., 2016](#)).

Work has already been undertaken, multiple times, to improve photon transport in PYTHON. However, it has not been a simple problem to solve, and no method to improve photon transported has been implemented. But a description of four promising methods, which were tested and experimented with, have been included in Appendix A for completeness sake. Even so, the robustness of many of the numerical routines has been improved, which prevents simulations from failing due to photons (with bogus physical properties) becoming trapped in the simulation, or numerical issues/noise. But this has not fixed the long run time of simulations; in fact, it may have made it worse. There are many numerical and computational difficulties to overcome, but improving optically thick photon transport is likely the natural next step for the evolution of PYTHON.

6.2.2 Emission from different disc geometries

I have mentioned tirelessly through this thesis that the exact emission geometry and the underlying physics for TDE accretion discs is not fully understood. Therefore, I made the brash, but reasonable assumption that the emission is thermal radiation from a geometrically thin and optically thick α -disc (Shakura & Sunyaev, 1973). As a first step, and during the late time life of TDEs, this is not a bad approximation at all. But given the extreme luminosities expected during the early evolution, the inner edge of an accretion disc is almost certainly vertically extended due to the extreme radiation pressure (Rees, 1988; Ulmer, 1999).

The temperature profile, and therefore the thermal emission, is almost certainly going to be different in the super-Eddington disc case, compared to the α -disc, as shown in, e.g., Section 1.2.2 and by Strubbe & Quataert (2009). But the most important aspect of the thin disc approximation is most likely the angular distribution it imposes on the photon emission. Due to fore-shortening and limb-darkening, geometrically thin and optically thick discs generate a highly anisotropic radiation field. This level of anisotropy is likely an overestimate for vertically extended inner discs. Therefore a more physically realistic description of the accretion discs in (especially super-Eddington) TDEs should be used, to enable meaningful quantitative modelling of observational data.

6.2.3 Radiation hydrodynamic simulations of TDEs

The dynamic effects of radiation are often important in astrophysical contexts, and therefore numerical models often address the effects of radiation. There are a number of ways to model the radiative transfer, but given the high dimensionality of the problem, it is often prohibitively expensive and difficult to do so. Therefore various approximations which ignore certain dependencies (i.e. frequency) are often used in place of a full treatment (such as the M1 relation; Levermore, 1984). So far, the radiation hydrodynamics (RHD) for TDE modelling has mostly restricted itself to the domain of diffusion

approximations (Bonnerot et al., 2017; Dai et al., 2018; Curd & Narayan, 2019; Lu & Bonnerot, 2019; Bonnerot et al., 2021; Lodato et al., 2020), which completely ignores the frequency dependence of the radiation field.

I have shown throughout this thesis that detailed radiative transfer models are required to understand the emission in TDEs. MCRT has several advantages when it comes to modelling this. It is straightforward to include complex physical processes, parallelizes very well and can naturally incorporate many of the dependencies of the radiation field. There are some disadvantages though, most notably the computational expense in comparison to other methods. However, as the dimensionality of the simulations increases, the advantages of MCRT shine bright even if it is more expensive.

A lot of work has already been done which put in place the necessary infrastructure to use PYTHON in conjunction with popular hydrodynamics codes to conduct RHD simulations (Higginbottom et al., 2017, 2018, 2019). Therefore, one future avenue of research would be to conduct RHD simulations, to study the evolution of the spectroscopic properties of TDEs. However, one could also use such RHD models to further our knowledge on the formation of TDE accretion discs, and the launching of an outflow. Both of which are affected by the dynamics of the radiation field. Furthermore, as I have already mentioned in Chapter 5, dynamical models could be required to fully appreciate the effect of bulk scatter reprocessing.

6.2.4 Extending modelling into three dimensions

The geometries of outflows are often far more complicated than a neat rotationally (and axially) symmetric model. To fully capture and model the complex emission mechanisms, radiative transfer and the reprocessing in TDEs, full 3D simulations will be required in the future to make quantitative comparisons against observations. This was shown in Chapter 5, which compared the results from one and two dimensional models. But for all of its life, PYTHON has been limited to a maximum of 2.5 measly dimensions. The .5 of a dimension refers to the fact that, whilst the model grid exists in 2D, it has been assumed to be rotationally symmetric. This means that photon transport can still take place in 3D and, for example, the affects of 3D radiative transfer and rotation can be crudely taken into account.

Extending MCRT into 3D is conceptually simple. Not much has to be done, other than to program a 3D coordinate grid and set of models. The photon transport will take place exactly as it did in 2.5D. Whilst conceptually simple, it is technically not computationally feasible for PYTHON. This is partly due to the increased computational workload associated with transporting more photons through more grid cells. But the main limiting factor is the memory required to store the 3D coordinate grid. PYTHON currently uses a distributed memory parallel processing paradigm, which results in duplicated data

across the distributed jobs. It is relatively easy to create an impressively large memory footprint with this architecture, even for a simple simulation.

Therefore, before the extension into 3D can even begin, the memory footprint has to be reduced. This, unfortunately, will require a complete overhaul of the program to use, instead, a hybrid shared- and distributed-memory parallelization scheme. Whilst difficult, and potentially error prone – due to the organic nature in which the software grew – this will massively reduce the memory footprint without removing any of the functionality.

Appendix A

Optically Thick Monte Carlo Radiative Transfer

What does not kill me.. is not trying hard enough.

Primarch Roboute Guilliman of the Ultramarines

Broadly speaking for astrophysical applications, there exists two classes of algorithms which enable faster, but more approximate, treatment for photon transport through an optically thick medium. These are diffusion methods, and variance reduction techniques. In this appendix, I will outline four methods for improving photon transport in optically thick MCRT simulations.

In optically thick regions of an atmosphere, the photon mean free path is actually much smaller than the length scales over which the density and the temperature changes. Photons becomes trapped, and approach thermal equilibrium with the surrounding medium. Here, the transport of energy becomes a diffusion process which results in a significant simplification of the radiative transfer. This allows us to use a diffusion approximation (DA) to approximate the transport of energy, instead of using the brute force techniques of MCRT.

Variance reduction (VR) algorithms, on the other hand, are a broad class of algorithms which aim to improve the statistical efficiency of MCRT, without modifying the transpot process. One of the most common forms of VR, which is already is use in PYTHON, is stratified sampling. The purpose of VR is to remove “redundant” and “uninteresting” photons from the simulation, which contribute little to the final result, whose existence can dramatically lower the statistical and computational efficiency.

A.1 Modified random walk

The Modified Random Walk (MRW) is a DA algorithm which converts multiple *microsteps* into one *macrostep*. The first iteration of the MRW algorithm was proposed by Fleck & Canfield (1984), and was used to improve efficiency of implicit Monte Carlo (IMC) simulations (Fleck & Cummings, 1971). Further descriptions and improvements to the method have been done by Min et al. (2009), Robitaille (2010) and Keady & Cleveland (2017).

A.1.1 Diffusion along a random path

The underlying idea in MRW is that in regions of high optical depth, photons will travel a long path undergoing multiple scatters which can be approximated as a diffusion process. Instead of tracking all individual interactions, conventional MC transport is disabled and photon transport is replaced by a diffusive process.

To do this, the MRW algorithm makes use of the time-dependent grey radiative diffusion equation,

$$\nabla \cdot (D \nabla E) = \frac{1}{c} \frac{\partial E}{\partial t}, \quad (\text{A.1})$$

where E is the local energy density, c is the speed of light and D is the diffusion constant. In the case of an infinite homogeneous medium, Equation A.1 has the solution,

$$\psi(\mathbf{r}, t) = \frac{1}{(4\pi Dct)^{3/2}} \exp\left(-\frac{r^2}{4Dct}\right), \quad (\text{A.2})$$

where $\psi(\mathbf{r}, t)$ is the fraction of energy that has diffused to a position \mathbf{r} in a time t . Fleck & Canfield (1984) show that for a random walk, in the limit of a large number of steps, the PDF of a photon's coordinates is a solution of Equation A.1 and is of a similar form to Equation A.2. Thus, Fleck & Canfield (1984) suggest that a photon's meandering random walk can be replaced by a diffusive path, turning the random walk's *microsteps* into one diffusive *macrostep*. For simplicity, the random walk and diffusive path of a photon is assumed to be contained within a grey sphere¹ of radius R_0 centred at the initial position of the photon, hereafter known as the MRW sphere.

To solve Equation A.1 in the context of a MRW, an absorbing boundary condition is set at the edge of the MRW sphere such that $\psi(R_0, t) = 0$. This restricts photons from transporting past the surface of the sphere in a time interval t , and photons reach the

¹i.e. opacity has no frequency dependence.

surface of the MRW sphere in that time interval t . Applying this boundary condition to Equation A.2 results in the modified solution,

$$\psi(\mathbf{r}, t) = \frac{1}{R_0^2} \sum_{n=1}^{\infty} \frac{n}{r} \exp\left\{-\left(\frac{n\pi}{R_0}\right)^2 Dct\right\} \sin\left(\frac{n\pi r}{R_0}\right). \quad (\text{A.3})$$

The probability that a photon reaches the surface of the MRW sphere in a time interval t is given by integrating Equation A.3 from 0 to R_0 ,

$$P_R(t) = 4\pi \int_0^{R_0} r^2 \psi(\mathbf{r}, t) dr, \quad (\text{A.4})$$

$$= 2 \sum_{n=1}^{\infty} (-1)^{n+1} y^{n^2}, \quad (\text{A.5})$$

where,

$$y = \exp\left\{-\left(\frac{\pi}{R_0}\right)^2 Dct\right\}. \quad (\text{A.6})$$

However, as this solution is only valid for a large number of steps, reasonable criteria has to be satisfied before a photon can be transported using MRW. Firstly, the distance to a photon's next interaction must be within the MRW sphere of radius R_0 , where R_0 is *always* the minimum distance to the current cell boundary. Secondly, the radius R_0 must be larger than the mean free path in the cell. Thirdly, a photon must have already scattered at least a few tens of times. This ensures that the distance to a photon's next interaction is within the MRW sphere. This translates into the following criteria,

$$R_0 > \lambda_R, \quad (\text{A.7})$$

$$l < R_0, \quad (\text{A.8})$$

where l is the distance to the next interaction and λ_R is the Rosseland mean free path. [Min et al. \(2009\)](#) also suggests that a photon must be within the interior of the cell, as at the edges of a cell the photon is unlikely to undergo a sufficient amount of interactions for diffusion to be a valid approximation of the photon's path. To control this, [Min et al. \(2009\)](#) suggests comparing the photon's position to the parameter d_{min} ,

$$d_{min} > \frac{\gamma}{\rho} \lambda, \quad (\text{A.9})$$

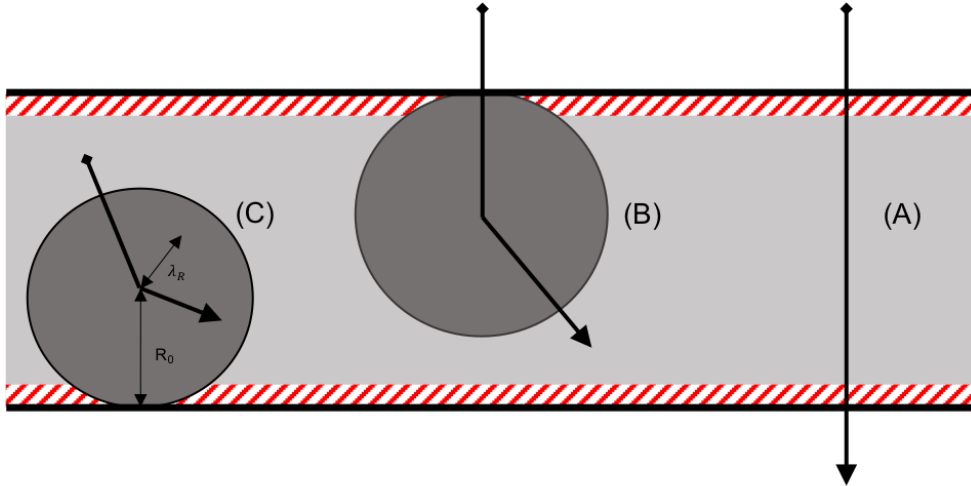


FIGURE A.1: A schematic of three photons which can be considered for MRW transport. Photon (A) is not transported via MRW as it travels straight through the cell without interacting. Photon (B) interacts within the cell, but as the distance to the next interaction is larger than R_0 , it is not transported via MRW. Photon (C) will be transported via MRW as it interacts in the cell and the next interaction event is within the MRW sphere with radius R_0 . The hatched regions at the edge indicate regions where MRW will not be invoked due to being close to the edge of the cell.

where d_{\min} is the distance to the closest cell edge, ρ is the density of the cell, λ is the mean free path of the cell, typically the Rosseland mean free path, and γ is a controllable parameter. Values of γ close to unity result in fast computation, but larger errors, whereas larger values of γ result in smaller errors at the expense of slower computation. If a photon satisfies all four criteria, it will scatter at least once inside the MRW sphere and can be transported via a MRW. Figure A.1 shows a summary of these criteria.

A.1.2 The modified random walk algorithm

Equation A.3 and Equation A.5 are the key components which form the MRW algorithm. Once the four criteria have been satisfied for a photon, the photon is moved onto a random location upon the surface of the MRW sphere. By solving Equation A.5, the amount of time it took the photon to travel the diffusive path can be calculated. This is done by generating a uniform random deviate $P_0 \in [0, 1]$ and setting,

$$P_0 = P_R(t) = 2 \sum_{n=1}^{\infty} (-1)^{n+1} y^{n^2}. \quad (\text{A.10})$$

By solving for y in Equation A.10 and re-arranging Equation A.6, the time required to travel the diffusive path t is given by,

$$ct = -\frac{\ln(y)}{D} \left(\frac{R_0}{\pi} \right)^2. \quad (\text{A.11})$$

The diffusion constant D can be approximated by using the average distance and time between interactions,

$$D = \frac{\langle R^2 \rangle}{6T_c} = \frac{c}{3\sigma(1-\epsilon)}, \quad (\text{A.12})$$

where R is a random variate representing the average distance between interactions, T_c is the average time between interactions, ϵ is the thermalisation fraction and σ is the interaction cross section. However, the diffusion constant can also be calculated through use of the Rosseland mean free path λ_R ,

$$D = \frac{1}{3}\lambda_R = \frac{1}{3\rho\bar{\kappa}_R}, \quad (\text{A.13})$$

where $\bar{\kappa}_R$ is the Rosseland mean opacity.

By calculating the time to complete the diffusive step, the amount of energy the photon deposits into the cell is calculable,

$$E = E_p c t \rho \bar{\kappa}, \quad (\text{A.14})$$

where E_p is the energy of the photon and $\bar{\kappa}$ is the absorption coefficient. At the end of MRW transport, the weight of the photon is modified to account for absorption and a new frequency for the photon is sampled, typically from the Planck function $B_\nu(T)$ due to the assumption of LTE in the MRW sphere . Fleck & Canfield (1984) suggest that the photon weight should be reduced by the average weight reduction expected over all microsteps due to absorption. Thus, they propose that the new photon weight should be,

$$W_{\text{new}} = W_{\text{old}} e^{-ct\sigma_{\text{eff}}},$$

where σ_{eff} is the effective absorption coefficient of the cell.

A.1.3 Partially grey random walk

The MRW is a grey solution, meaning it is inadequate for simulations where the opacity is strongly frequency dependent. To better handle frequency dependence, Keady & Cleveland (2017) propose a modification of the MRW algorithm with their Partially Grey Random Walk algorithm (PGRW). In this modification, a cut off frequency is defined in each cell which permits photons of certain frequencies from being ineligible for MRW transport. Frequency dependence is said to be improved as the optical depth for frequency bands within a cell are collapsed into a grey equivalent for each frequency

band. Hence, as the number of frequency bands are increased, the treatment of frequency dependence improves.

In addition to improving the treatment of frequency dependent opacities, PGRW is also shown to offer more efficient computation than vanilla MRW by [Keady & Cleveland \(2017\)](#) in their benchmarks tests. They argue that this is due to more photons being eligible for MRW transport. However, the PGRW method only really excels when opacities are monotonic functions of frequency. With more complex and realistic frequency dependence, PGRW is often no better than standard MRW.

A.2 Packet splitting and Russian Roulette

Packet splitting (PS) and its inverse procedure Russian Roulette (RR) are techniques which can be used to control the sample size and significance of photons in MCRT simulations. PS and RR methods were originally introduced by [Kahn \(1956\)](#), and found considerable success in early simulations of neutron transport (see [Hammersley & Handcomb, 1964](#); [Cashwell et al., 1959](#)). PS and RR techniques excel in most MC simulations, but notably so in Rare Event Monte Carlo ([L'Ecuyer et al., 2007](#)).

A.2.1 Packet splitting

Photons which are emitted in optically thick regions will, in general, spend most of their time in that region undergoing tens to hundreds of scattering events and will, comparatively, spend very little time in optically thin regions. Estimators who are based on interactions, then, are likely to be noisier in optically thin regions. PS is an unbiased technique which can be used to combat this by increasing the sample size of photons in optically thin regions, and allows the use of a small number of photons in an optically thick region.

The underlying principle behind PS is to generate N_{high} high weight photons and at some point, split each high weight photon into N_{low} lower weight photons. This will result in $N = N_{\text{low}} \cdot N_{\text{high}}$ photons leaving the simulation domain. When a high weight photon is split, each lower weight photon takes an equal fraction of the high weight photon's weight,

$$W_{\text{low},i} = \frac{W_{\text{high}}}{N_{\text{low}}}, \quad (\text{A.15})$$

where $W_{\text{low},i}$ is the weight of the i -th low weight photon and W_{high} is the weight of the high weight photon. PS is an unbiased method as it preserves the original weight of the high weight photon after being split,

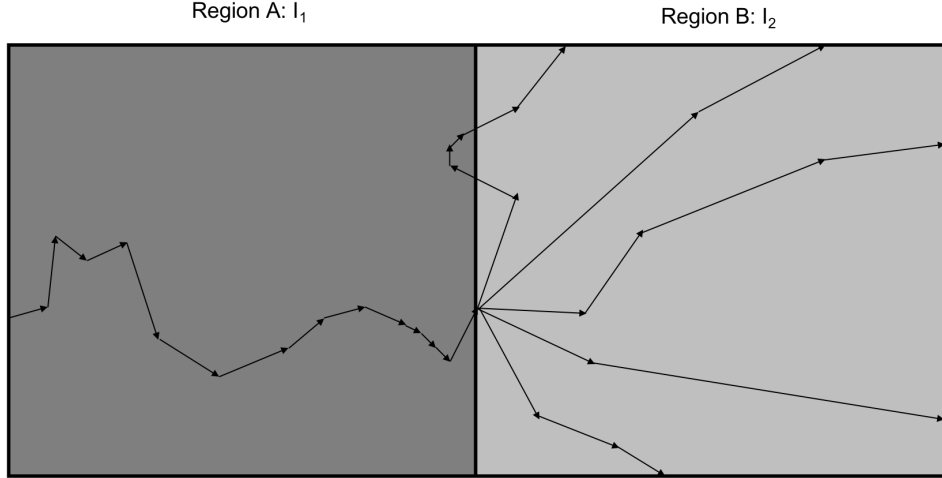


FIGURE A.2: Packet splitting with $N_{\text{high}} = 1$ and $N_{\text{low}} = 5$. A high luminosity photon enters an optically thick region and interacts until it reaches the boundary between an optically thick and thin region. At the boundary, the high luminosity photon is split into N_{low} photons which interact with the optically thin region until they exit.

$$E\left(\sum_{i=1}^{N_{\text{low}}} W_{\text{low},i}\right) = E(W_{\text{low},1} + W_{\text{low},2} + W_{\text{low},3} + \dots), \quad (\text{A.16})$$

$$= N_{\text{low}} \frac{W_{\text{high}}}{N_{\text{low}}}, \quad (\text{A.17})$$

$$= W_{\text{high}}. \quad (\text{A.18})$$

To aid high optical depth transport in MCRT simulations, a high weight photon would be emitted in an optically thick region and would split upon reaching an optically thin region, as shown in Figure A.2.

The boundary between the optically thick and optically thin region has to be defined such that high weight photons will not propagate into an optically thin region, as they will increase the noise in the estimators². The low weight photons must also undergo a small, but most importantly, *non-zero* amount of interactions in the optically thin region before leaving the simulation domain.

The overall goal of PS in this context is to reduce the total number of scattering events tracked. This is achieved by tailoring the number of high weight photons emitted, to reduce the number of scattering events within the optically thick region. For example, photons may scatter 20,000 times in an optically thick region, thus if $N_{\text{high}} = 10^5$ and $N_{\text{low}} = 10^2$, there will be 10^7 photons scattering in the optically thin region, but, there will be, on average, a factor of 100 times less scattering events in the optically thick region, compared to a simulation using a fixed number of photons of $N = 10^7$.

²This is due to the large photon weights increasing the variance in the estimators.

A.2.2 Russian Roulette

Whilst PS can be used to increase a photon sample size, the inverse is true for RR. As with the real life game of chance, the survival of a photon depends entirely on chance. In order to play a game of RR with a photon, a kill probability P_{kill} is defined which, over the full simulation, controls the number of photons which are removed from the sample; i.e. $P_{\text{kill}} = 1/6$ will remove approximately 17% of photons.

When a photon is unfortunate enough to play a game of RR, a uniform random deviate is sampled such that $\xi \in [0, 1]$. If $\xi \leq P_{\text{kill}}$, then the photon is removed from the sample and its weight is set to zero. Otherwise the photon survives and its weight is increased by a factor,

$$W_{\text{new}} = \frac{W_{\text{old}}}{1 - P_{\text{kill}}} \quad (\text{A.19})$$

where W_{new} is the new weight of the photon and W_{old} is the old weight of the photon. RR is also another unbiased method as it retains the original value of weight in the simulation,

$$\begin{aligned} E(W_{\text{new}}) &= P_{\text{kill}}W_{\text{kill}} + (1 - P_{\text{kill}})\frac{W_{\text{old}}}{1 - P_{\text{kill}}} \\ &= W_{\text{old}}, \end{aligned}$$

where $W_{\text{kill}} = 0$.

There are multiple ways to implement RR to alleviate problems with high optical depths, with arguably no *incorrect* (just less efficient) implementations. One way to implement RR is to play RR with photons which have been transported into certain regions of the simulation. Doing this will result in a reduced number of photons interacting in this region, for example this could be used to reduce the number of photons which enter and interact in an optically thick region. It is also possible to play RR with a photon after each event once it has reached a critical number of interactions. This has the effect of reducing the number of trapped photons. Finally, photons could also play RR once their weight has fallen below a critical value, i.e. $W_{\text{min}} = 10^{-3}W_0$ where W_0 is the photon's original value. This removes photons which will contribute little to the final result and have become pointless to continue to simulate.

A.2.3 Coupled packet splitting and Russian Roulette

PS and RR are seldom used on their own, as coupling PS and RR together allows for greater flexibility in controlling the sample size and constraining photon weights. Coupled PS and RR (CPR) operates on the basis that the simulation domain has been split into varying regions of *importance*. The importance of a region is used to define the *significance* of that region to the overall simulation. How the importance is defined is crucial to the performance of CPR and varies depending on the simulation and quantities of interest; this makes it difficult for a “catch all” set of parameter values.

In CPR, photons propagate through the simulation domain and each time a photon moves from one cell into another, the importance of those two cells are compared. If the cell the photon is travelling into has a *lower importance*, then the photon plays RR and is either killed or increases in significance. Conversely, if a photon moves into a cell with a *larger importance*, then the photon is split into multiple lower weight photons via PS. Finally, if the importance of the two cells is the same, then the photon neither splits nor plays RR and propagates freely between the cells.

This leaves the problem of how to split a simulation domain into regions of importance. Most commonly, the best way to do this is not known *a priori*. But will require an intelligent algorithm which assigns importance values due to the current conditions in each cell. One possible quantity is the Rosseland mean free path within a cell. By defining cells with large mean free paths (small optical depth) as being more important, photons propagating into these regions will split. Then in regions with a small mean free path, i.e. where optical depth is large, the importance will be low and thus there will be a reduced amount of photons propagating through these regions. This helps to mediate the number of interactions occurring in the simulation, whilst maintaining an unbiased sample.

To further constrain photon weights within a CPR scheme and lower statistical noise, Dupree & Fraley (2002) suggest assigning a lower and upper limit for photon weights within each importance region. When a photon weight is smaller than the lower limit, it will play a game of RR to either increase the weight of the photon or to remove the insignificant photon. When a photon has a weight larger than the upper limit, it will split via PS to create multiple lower weight photon packets. The effect of doing this is to constrain photon weights between these two limits, lowering the variance of the photon weights in the simulation.

A.3 Path stretching

Path Stretching (PaS) is form of biased sampling³. In PaS, instead of sampling a random optical depth from the regular exponential distribution,

$$p(\tau) = e^{-\tau},$$

a biased, stretched distribution is used instead,

$$q(\tau) = \alpha e^{-\alpha\tau}, \quad (\text{A.20})$$

where α is a stretching parameter with a value between 0 and 1. A random optical depth is sampled from this distribution using,

$$\tau = -\frac{\ln(1-\xi)}{\alpha}, \quad (\text{A.21})$$

where ξ is a uniform random deviate such that $\xi \in [0,1]$. By choosing a suitable value of α , the size of the steps between photon interactions is increased, allowing photons to penetrate deeper into an optically thick region with less steps. Values of $\alpha \sim 1$ result in a small amount of stretching, whereas values of $\alpha \sim 0$ result in a significant amount of stretching. Typically, the value of α is a fixed value. However, this can lead to excessive amounts of noise and instead Baes et al. (2016) suggest that α should be calculated on the fly for each photon, such that a optimal value of α is always being used. Baes et al. (2016) suggest using,

$$\alpha = \frac{1}{1 + \tau_{\text{path}}}, \quad (\text{A.22})$$

where τ_{path} is the maximum optical depth between the photon's current position and the cell boundary.

When an optical depth has been sampled from this biased distribution, the weight of the photon must be adjusted accordingly by,

$$W_{\text{new}} = W_{\text{old}} \frac{p(\tau)}{q(\tau)} = W_{\text{old}} \frac{e^{\tau(\alpha-1)}}{\alpha}, \quad (\text{A.23})$$

where τ is the sampled optical depth. The maximum weight change occurs when $\tau = 0$ which corresponds to a maximum weight change of,

³Which itself is a type of importance sampling.

$$W = \frac{1}{\alpha}. \quad (\text{A.24})$$

This can create photons with large weights relative to the rest of the photon sample, subsequently increasing the noise within the simulation due to high weight photons dominating any MC estimators. To combat this, Baes et al. (2016) suggest using a sampling scheme known as *composite biasing*, which samples from a linear combination of the original and biased distributions. In the context of sampling a stretched path, this composite distribution takes the form,

$$q_*(\tau) = (1 - \chi)e^{-\tau} + \chi\alpha e^{-\alpha\tau}, \quad (\text{A.25})$$

where χ is the biasing factor with a value between 0 and 1. A value of $\chi = 0$ corresponds to no biasing and $\chi = 1$ corresponds to complete biasing. By sampling from Equation A.25, the maximum weight change is now,

$$W_* = \frac{1}{1 - \chi}. \quad (\text{A.26})$$

This limits the maximum weight change to be less, in general, than sampling straight from the biased distribution $q(\tau)$. However, the disadvantage of this is now that sampling from Equation A.25 is more complicated than sampling from Equation A.20, requiring a more sophisticated approach to sample. It is possible, however, that a photon's weight can become vanishingly small if a biasing technique like this is used repeatedly on it. Since these photons will not contribute significantly to the simulation, but cost the same to continue to simulate, it is often best to terminate these low weight photons using RR as discussed in the previous section.

References

- Abbott D. C., Lucy L. B., 1985, *The Astrophysical Journal*, 288, 679
- Alexander K. D., Berger E., Guillochon J., Zauderer B. A., Williams P. K. G., 2016, *The Astrophysical Journal*, 819, L25
- Alexander K. D., van Velzen S., Horesh A., Zauderer B. A., 2020, *Space Science Reviews*, 216, 81
- Allen J. T., Hewett P. C., Maddox N., Richards G. T., Belokurov V., 2011, *Monthly Notices of the Royal Astronomical Society*, 410, 860
- Arcavi I., et al., 2014, *The Astrophysical Journal*, 793, 38
- Auchettl K., Guillochon J., Ramirez-Ruiz E., 2017, *The Astrophysical Journal*, 838, 149
- Auer L. H., van Blerkom D., 1972, *The Astrophysical Journal*, 178, 175
- Baes M., Gordon K. D., Lunttila T., Bianchi S., Camps P., Juvela M., Kuiper R., 2016, *Astronomy & Astrophysics*, 590, A55
- Balbus S. A., Hawley J. F., 1991, *The Astrophysical Journal*, 376, 214
- Balbus S. A., Mummery A., 2018, *Monthly Notices of the Royal Astronomical Society*, 481, 3348
- Batra N. D., Baldwin J. A., 2014, *Monthly Notices of the Royal Astronomical Society*, 439, 771
- Begelman M. C., McKee C. F., Shields G. A., 1983, *The Astrophysical Journal*, 271, 70
- Bellm E. C., et al., 2018, *Publications of the Astronomical Society of the Pacific*, 131, 018002
- Blagorodnova N., et al., 2017, *The Astrophysical Journal*, 844, 46
- Blagorodnova N., et al., 2019, *The Astrophysical Journal*, 873, 92
- Blandford R. D., 1999. Isaac Newton Institute for Mathematical Sciences Cambridge, p. 265, <https://ui.adsabs.harvard.edu/abs/1999ASPC..160..265B>

- Blandford R. D., Payne D. G., 1982, *Monthly Notices of the Royal Astronomical Society*, 199, 883
- Bloom J. S., et al., 2011, *Science*, 333, 203
- Bonnerot C., Lu W., 2020, *Monthly Notices of the Royal Astronomical Society*, 495, 1374
- Bonnerot C., Stone N. C., 2021, *Space Science Reviews*, 217, 16
- Bonnerot C., Rossi E. M., Lodato G., Price D. J., 2016, *Monthly Notices of the Royal Astronomical Society*, 455, 2253
- Bonnerot C., Rossi E. M., Lodato G., 2017, *Monthly Notices of the Royal Astronomical Society*, 464, 2816
- Bonnerot C., Lu W., Hopkins P. F., 2021, *Monthly Notices of the Royal Astronomical Society*, p. stab398
- Bowen I. S., 1934, *Publications of the Astronomical Society of the Pacific*, 46, 146
- Bowen I. S., 1935, *The Astrophysical Journal*, 81, 1
- Bowers R. L., Deeming T., 1984, *Astrophysics. Volume 1 - Stars*, 1 edn. Jones and Bartlett Publishers
- Brotherton M. S., Tran H. D., Becker R. H., Gregg M. D., Laurent-Muehleisen S. A., White R. L., 2001, *The Astrophysical Journal*, 546, 775
- Brown G. C., Levan A. J., Stanway E. R., Tanvir N. R., Cenko S. B., Berger E., Chornock R., Cucchiaria A., 2015, *Monthly Notices of the Royal Astronomical Society*, 452, 4297
- Brown J. S., Holoién T. W.-S., Auchettl K., Stanek K. Z., Kochanek C. S., Shappee B. J., Prieto J. L., Grupe D., 2017a, *Monthly Notices of the Royal Astronomical Society*, 466, 4904
- Brown J. S., et al., 2017b, *Monthly Notices of the Royal Astronomical Society*, 473, 1130
- Camps P., Baes M., 2018, *The Astrophysical Journal*, 861, 80
- Cannizzo J. K., Lee H. M., Goodman J., 1990, *The Astrophysical Journal*, 351, 38
- Cardelli J. A., Clayton G. C., Mathis J. S., 1989, *The Astrophysical Journal*, 345, 245
- Carroll B. W., Ostlie D. A., 1996, *An Introduction to Modern Astrophysics*, 1 edn. Addison-Wesley Publishing Company Inc.
- Cashwell E. D., Everett C. J., Rechard O. W., 1959, *A Practical Manual on the Monte Carlo Method For Random Walk Problems*, 1 edn. Pergamon Press, London, <https://onlinelibrary.wiley.com/doi/abs/10.1002/zamm.19600400727>

- Castor J. I., 1972, *The Astrophysical Journal*, 178, 779
- Castor J. I., Abbott D. C., Klein R. I., 1975, *The Astrophysical Journal*, 195, 157
- Cen R., 2019, arXiv:1912.04372 [astro-ph]
- Cenko S. B., et al., 2012, *The Astrophysical Journal*, 753, 77
- Cenko S. B., et al., 2016, *The Astrophysical Journal*, 818, L32
- Cordova F. A., Mason K. O., 1982, *The Astrophysical Journal*, 260, 716
- Coughlin E. R., Nixon C. J., 2019, arXiv:1907.03034 [astro-ph]
- Coughlin E. R., Nixon C., Begelman M. C., Armitage P. J., 2016, *Monthly Notices of the Royal Astronomical Society*, 459, 3089
- Coughlin E. R., Armitage P. J., Lodato G., Nixon C. J., 2019, *Space Science Reviews*, 215, 45
- Cunningham C. T., 1975, *The Astrophysical Journal*, 202, 788
- Curd B., Narayan R., 2019, *Monthly Notices of the Royal Astronomical Society*, 483, 565
- Czerny B., Nikołajuk M., Różańska A., Dumont A.-M., Loska Z., Zycki P. T., 2003, *Astronomy and Astrophysics*, 412, 317
- Dai X., Shankar F., Sivakoff G. R., 2008, *The Astrophysical Journal*, 672, 108
- Dai L., McKinney J. C., Miller M. C., 2015, *The Astrophysical Journal*, 812, L39
- Dai L., McKinney J. C., Roth N., Ramirez-Ruiz E., Miller M. C., 2018, *The Astrophysical Journal*, 859, L20
- Dannen R., Proga D., Waters T., Dyda S., 2019, arXiv:2001.00133 [astro-ph]
- Davis S. W., El-Abd S., 2019, *The Astrophysical Journal*, 874, 23
- Dere K. P., Landi E., Mason H. E., Monsignori Fossi B. C., Young P. R., 1997, *Astronomy and Astrophysics Supplement Series*, 125, 149
- Donley J. L., Brandt W. N., Eracleous M., Boller T., 2002, *The Astronomical Journal*, 124, 1308
- Drew J., Verbunt F., 1985, *Monthly Notices of the Royal Astronomical Society*, 213, 191
- Duderstadt J. J., Martin W. R., 1979, *Transport Theory*, 1 edn. Wiley-Interscience
- Dupree S. A., Fraley S. K., 2002, *A Monte Carlo Primer: A Practical Approach to Radiation Transport*, 1st edn. Springer US, doi:10.1007/978-1-4419-8491-3

- Ellinger C. I., Young P. A., Desch S. J., Fryer C. L., Rockefeller G., 2012, in American Astronomical Society, AAS Meeting #219, id.203.02. p. 203.02, <https://ui.adsabs.harvard.edu/abs/2012AAS...21920302E>
- Elvis M., 2000, *The Astrophysical Journal*, 545, 63
- Emmering R. T., Blandford R. D., Shlosman I., 1992, *The Astrophysical Journal*, 385, 460
- Eracleous M., Lewis K. T., Flohic H. M. L. G., 2009, *New Astronomy Reviews*, 53, 133
- Feldmeier A., Shlosman I., 1999, *The Astrophysical Journal*, 526, 344
- Fleck J. A., Canfield E. H., 1984, *Journal of Computational Physics*, 54, 508
- Fleck J. A., Cummings J. D., 1971, *Journal of Computational Physics*, 342, 313
- Foote H. R., Generozov A., Madigan A.-M., 2019, arXiv:1911.01426 [astro-ph]
- Frank J., 1978, *Monthly Notices of the Royal Astronomical Society*, 184, 87
- Frank J., Rees M. J., 1976, *Monthly Notices of the Royal Astronomical Society*, 176, 633
- Frank J., King A., Raine D., 2002, *Accretion Power in Astrophysics*, 3 edn. Cambridge University Press
- French K. D., Arcavi I., Zabludoff A., 2016, *The Astrophysical Journal*, 818, L21
- Friend D. B., Abbott D. C., 1986, *The Astrophysical Journal*, 311, 701
- Froning C. S., 2005. eprint: arXiv:astro-ph/0410200, p. 81, <http://adsabs.harvard.edu/abs/2005ASPC..330...81F>
- Gafton E., Rosswog S., 2019, *Monthly Notices of the Royal Astronomical Society*, 487, 4790
- Galassi M., 2006, *GNU Scientific Library Reference Manual*, 2 edn. 1 Vol. 1, Network Theory Ltd, <https://www.gnu.org/software/gsl/doc/html/index.html>
- Gallegos-Garcia M., Law-Smith J., Ramirez-Ruiz E., 2018, *The Astrophysical Journal*, 857, 109
- Gayley K. G., 1995, *The Astrophysical Journal*, 454, 410
- Gezari S., 2021, *Annual Review of Astronomy and Astrophysics*, 59, null
- Gezari S., et al., 2012, *Nature*, 485, 217
- Gezari S., Cenko S. B., Arcavi I., 2017, *The Astrophysical Journal*, 851, L47
- Gibson R. R., et al., 2009, *The Astrophysical Journal*, 692, 758

- Gierliński M., Maciołek-Niedźwiecki A., Ebisawa K., 2001, *Monthly Notices of the Royal Astronomical Society*, 325, 1253
- Gofford J., Reeves J. N., McLaughlin D. E., Braito V., Turner T. J., Tombesi F., Cappi M., 2015, *Monthly Notices of the Royal Astronomical Society*, 451, 4169
- Golightly E. C. A., Nixon C. J., Coughlin E. R., 2019, *The Astrophysical Journal*, 882, L26
- Greenstein J. L., Oke J. B., 1982, *The Astrophysical Journal*, 258, 209
- Guillochon J., Ramirez-Ruiz E., 2013, *The Astrophysical Journal*, 767, 25
- Guillochon J., Manukian H., Ramirez-Ruiz E., 2014, *The Astrophysical Journal*, 783, 23
- Guillochon J., Nicholl M., Villar V. A., Mockler B., Narayan G., Mandel K. S., Berger E., Williams P. K. G., 2018, *The Astrophysical Journal Supplement Series*, 236, 6
- Hamann W.-R., Koesterke L., 1998, *Astronomy and Astrophysics*, 335, 1003
- Hamann F., Chartas G., McGraw S., Rodriguez Hidalgo P., Shields J., Capellupo D., Charlton J., Eracleous M., 2013, *Monthly Notices of the Royal Astronomical Society*, 435, 133
- Hammersley J., Handscomb D. C., 1964, *Monte Carlo Methods*, 1 edn. Spottiswood, Ballantyne and Co Ltd.
- Harries T. J., 2015, *Monthly Notices of the Royal Astronomical Society*, 448, 3156
- Hartley L. E., Drew J. E., Long K. S., Knigge C., Proga D., 2002, *Monthly Notices of the Royal Astronomical Society*, 332, 127
- Hastings W. K., 1970, *Biometrika*, 57, 97
- Hayasaki K., Stone N., Loeb A., 2016, *Monthly Notices of the Royal Astronomical Society*, 461, 3760
- Higginbottom N., Knigge C., Long K. S., Sim S. A., Matthews J. H., 2013, *Monthly Notices of the Royal Astronomical Society*, 436, 1390
- Higginbottom N., Proga D., Knigge C., Long K. S., Matthews J. H., Sim S. A., 2014, *Astrophysical Journal*, 789
- Higginbottom N., Proga D., Knigge C., Long K. S., 2017, *The Astrophysical Journal*, 836, 42
- Higginbottom N., Knigge C., Long K. S., Matthews J. H., Sim S. A., Hewitt H. A., 2018, *Monthly Notices of the Royal Astronomical Society*, 479, 3651

- Higginbottom N., Knigge C., Long K. S., Matthews J. H., Parkinson E. J., 2019, *Monthly Notices of the Royal Astronomical Society*, 484, 4635
- Hillier D. J., Miller D. L., 1999, *The Astrophysical Journal*, 519, 354
- Hills J. G., 1975, *Nature*, 254, 295
- Hills J. G., 1978, *Monthly Notices of the Royal Astronomical Society*, 182, 517
- Hirose S., Krolik J. H., Blaes O., 2009, *The Astrophysical Journal*, 691, 16
- Holoien T. W.-S., et al., 2014, *Monthly Notices of the Royal Astronomical Society*, 445, 3263
- Holoien T. W., et al., 2016, *Monthly Notices of the Royal Astronomical Society*, 455, 2918
- Holoien T. W. S., et al., 2019, *The Astrophysical Journal*, 880, 120
- Horesh A., Cenko S. B., Arcavi I., 2021, *Nature Astronomy*, 5, 491
- Hummer D. G., Rybicki G. B., 1985, *The Astrophysical Journal*, 293, 258
- Hung T., et al., 2018, *The Astrophysical Journal Supplement Series*, 238, 15
- Hung T., et al., 2019, *The Astrophysical Journal*, 879, 119
- Hung T., et al., 2020, arXiv:2011.01593 [astro-ph]
- Hunter J. D., 2007, *Computing in Science Engineering*, 9, 90
- Jiang Y.-F., Stone J. M., Davis S. W., 2013, *The Astrophysical Journal*, 778, 65
- Jiang N., Wang T., Hu X., Sun L., Dou L., Xiao L., 2021, arXiv:2102.08044 [astro-ph]
- Kahn H., 1956, *Symposium on Monte Carlo Methods*, pp 146–190
- Kara E., Dai L., Reynolds C. S., Kallman T., 2018, *Monthly Notices of the Royal Astronomical Society*, 474, 3593
- Kasen D., Thomas R. C., Nugent P., 2006, *The Astrophysical Journal*, 651, 366
- Keady K. P., Cleveland M. A., 2017, *Journal of Computational Physics*, 328, 160
- Kepler J., 1619, *Ioannis Keppleri Harmonices mundi libri V. sumptibus Godofredi Tampachii ...*, excudebat Ioannes Plancus, doi:10.5479/sil.135810.39088002800316, <https://doi.org/10.5479/sil.135810.39088002800316>
- Kesden M., 2012, *Physical Review D*, 85, 024037
- Khisamutdinov A. I., 1989, *USSR Computational Mathematics and Mathematical Physics*, 29, 198

- King A., Pounds K., 2015, *Annual Review of Astronomy and Astrophysics*, 53, 115
- Kirchhoff G., 1860, *Annalen der Physik*, 185, 275
- Klein O., Nishina Y., 1929, *Zeitschrift für Physik*, 52, 853
- Knigge C., 1999, *Monthly Notices of the Royal Astronomical Society*, 309, 409
- Knigge C., Woods J. A., Drew J. E., 1995, *Monthly Notices of the Royal Astronomical Society*, 273, 225
- Knigge C., Scaringi S., Goad M. R., Cottis C. E., 2008, *Monthly Notices of the Royal Astronomical Society*, 386, 1426
- Kochanek C. S., 1994, *The Astrophysical Journal*, 422, 508
- Kochanek C. S., 2016, *Monthly Notices of the Royal Astronomical Society*, 458, 127
- Konigl A., Kartje J. F., 1994, *The Astrophysical Journal*, 434, 446
- Krolik J. H., Kriss G. A., 2001, *The Astrophysical Journal*, 561, 684
- Krolik J. H., Raymond J. C., 1985, *The Astrophysical Journal*, 298, 660
- Krolik J., Piran T., Svirski G., Cheng R. M., 2016, *The Astrophysical Journal*, 827, 1
- Kudoh T., Shibata K., 1997, *The Astrophysical Journal*, 474, 362
- L'Ecuyer P., Demers V., Tuffin B., 2007, *ACM Transactions on Modeling and Computer Simulation*, 17
- LaMassa S. M., et al., 2015, *The Astrophysical Journal*, 800, 144
- Landi E., Zanna G. D., Young P. R., Dere K. P., Mason H. E., 2011, *The Astrophysical Journal*, 744, 99
- Laor A., Davis S. W., 2014, *Monthly Notices of the Royal Astronomical Society*, 438, 3024
- Laurent P., Titarchuk L., 2007, *The Astrophysical Journal*, 656, 1056
- Law-Smith J. A. P., Coulter D. A., Guillochon J., Mockler B., Ramirez-Ruiz E., 2020, *The Astrophysical Journal*, 905, 141
- Law N. M., et al., 2009, *Publications of the Astronomical Society of the Pacific*, 121, 1395
- Levermore C. D., 1984, *Journal of Quantitative Spectroscopy and Radiative Transfer*, 31, 149
- Lezhnin K., Vasiliev E., 2019, *Mon. Not. R. Astron. Soc.*, 000, 0

- Liu T., et al., 2018, *Monthly Notices of the Royal Astronomical Society*, 479, 5022
- Liu F., Cao C., Abramowicz M. A., Wielgus M., Cao R., Zhou Z., 2021, *The Astrophysical Journal*, 908, 179
- Lodato G., Rossi E. M., 2011, *Monthly Notices of the Royal Astronomical Society*, 410, 359
- Lodato G., King A. R., Pringle J. E., 2009, *Monthly Notices of the Royal Astronomical Society*, 392, 332
- Lodato G., Cheng R. M., Bonnerot C., Dai J. L., 2020, *Space Science Reviews*, 216, 63
- Loeb A., Ulmer A., 1997, *The Astrophysical Journal*, 489, 573
- Long K. S., Knigge C., 2002, *The Astronomical Journal*, 579, 725
- Lu W., Bonnerot C., 2019, arXiv:1904.12018 [astro-ph]
- Lucy L. B., 1999, *Astronomy and Astrophysics*, 344, 282
- Lucy L. B., 2002, *Astronomy & Astrophysics*, 384, 725
- Lucy L. B., 2003, *Astronomy & Astrophysics*, 403, 261
- MPI Forum T., 1994, MPI: A Message Passing Interface Standard, 1 edn. University of Tennessee
- MacLeod M., Guillochon J., Ramirez-Ruiz E., 2012, *The Astrophysical Journal*, 757, 134
- Madej J., 1974, *Acta Astronomica*, 24, 327
- Magorrian J., Tremaine S., 1999, *Monthly Notices of the Royal Astronomical Society*, 309, 447
- Mainetti D., Lupi A., Campana S., Colpi M., Coughlin E. R., Guillochon J., Ramirez-Ruiz E., 2017, *Astronomy & Astrophysics*, 600, A124
- Matsumoto T., Piran T., 2021a, *Monthly Notices of the Royal Astronomical Society*
- Matsumoto T., Piran T., 2021b, *Monthly Notices of the Royal Astronomical Society*, 502, 3385
- Matthews J., 2016, PhD thesis, University of Southampton: Faculty of Physical Sciences and Engineering
- Matthews J. H., Knigge C., Long K. S., Sim S. A., Higginbottom N., 2015, *Monthly Notices of the Royal Astronomical Society*, 450, 3331

- Matthews J. H., Knigge C., Long K. S., Sim S. A., Higginbottom N., Mangham S. W., 2016, *Monthly Notices of the Royal Astronomical Society*, 458, 293
- Matthews J. H., Knigge C., Long K. S., 2017, *Monthly Notices of the Royal Astronomical Society*, 467, 2571
- Mazzali P. A., Lucy L. B., 1993, *Astronomy and Astrophysics*, 279, 447
- McCourt M., Oh S. P., O'Leary R., Madigan A.-M., 2018, *Monthly Notices of the Royal Astronomical Society*, 473, 5407
- McKinney J. C., Tchekhovskoy A., Sadowski A., Narayan R., 2014, *Monthly Notices of the Royal Astronomical Society*, 441, 3177
- Melnik-Melnikov P. G., Dekhtyaruk E. S., Labu M., 1997, *Strength of Materials*, 29, 308
- Metropolis N., Rosenbluth A. W., Rosenbluth M. N., Teller A. H., Teller E., 1953, *The Journal of Chemical Physics*, 21, 1087
- Metzger B. D., Stone N. C., 2016, *Monthly Notices of the Royal Astronomical Society*, 461, 948
- Mihalas D., 1978, *Stellar Atmospheres*, 2 edn. W.~H.~Freeman and Co.
- Mihalas D. M., 1982, *Stellar atmospheres..* D. M. Mihalas. Translated from the English edition. Mir
- Mihalas D., Mihalas B. W., 1984, New York, Oxford University Press, 1984, 731 p.
- Miller J. M., et al., 2015, *Nature*, 526, 542
- Min M., Dullemond C. P., Dominik C., de Koter A., Hovenier J. W., 2009, *Astronomy & Astrophysics*, 497, 155
- Mizumoto M., Done C., Tomaru R., Edwards I., 2019, arXiv:1907.01447 [astro-ph]
- Mockler B., Guillochon J., Ramirez-Ruiz E., 2019, *The Astrophysical Journal*, 872, 151
- Mummery A., Balbus S. A., 2020, arXiv:1912.06577 [astro-ph]
- Murray N., Chiang J., 1996, *Nature*, 382, 789
- Murray N., Chiang J., 1997, *The Astrophysical Journal*, 474, 91
- Murray N., Chiang J., Grossman S. A., Voit G. M., 1995, *The Astrophysical Journal*, 451, 498
- Nicholl M., et al., 2020, *Monthly Notices of the Royal Astronomical Society*, 499, 482
- Nicholl M., Lanning D., Ramsden P., Mockler B., Lawrence A., Short P., Ridley E. J., 2022, arXiv:2201.02649 [astro-ph]

- Nickolls J., Buck I., Garland M., Skadron K., 2008, Association of Computing Machinery, 6
- Nixon C., Coughlin E., Miles P., 2021, arXiv:2108.04242 [astro-ph]
- Novikov I. D., Thorne K. S., 1973, Astrophysics of black holes.. <https://ui.adsabs.harvard.edu/abs/1973blho.conf..343N>
- Oskinova L. M., Hamann W.-R., Feldmeier A., 2008, arXiv:0806.2348 [astro-ph]
- Owocki S. P., Holzer T. E., Hundhausen A. J., 1983, *The Astrophysical Journal*, 275, 354
- Owocki S. P., Castor J. I., Rybicki G. B., 1988, *The Astrophysical Journal*, 335, 914
- Parkinson E. J., Knigge C., Long K. S., Matthews J. H., Higginbottom N., Sim S. A., Hewitt H. A., 2020, *Monthly Notices of the Royal Astronomical Society*, 494, 4914
- Parkinson E. J., Knigge C., Matthews J. H., Long K. S., Higginbottom N., Sim S. A., Mangham S. W., 2022, *Monthly Notices of the Royal Astronomical Society*, 510, 5426
- Pasham D. R., Velzen S. v., 2018, *The Astrophysical Journal*, 856, 1
- Patterson J., Thorstensen J., Fried R., Skillman D., Cook L., Jensen L., 2001, *Publications of the Astronomical Society of the Pacific*, 113, 72
- Pelletier G., Pudritz R. E., 1992, *The Astrophysical Journal*, 394, 117
- Pereyra N. A., Kallman T. R., Blondin J. M., 1998, *AIP Conference Proceedings*, 431, 471
- Piran T., Svirski G., Krolik J., Cheng R. M., Shiokawa H., 2015, *The Astrophysical Journal*, 806, 164
- Piro A. L., Lu W., 2020, *The Astrophysical Journal*, 894, 2
- Ponti G., Fender R. P., Begelman M. C., Dunn R. J. H., Nielsen J., Coriat M., 2012, *Monthly Notices of the Royal Astronomical Society: Letters*, 422, L11
- Poutanen J., Lipunova G., Fabrika S., Butkevich A. G., Abolmasov P., 2007, *Monthly Notices of the Royal Astronomical Society*, 377, 1187
- Pringle J. E., 1981, *Annual Review of Astronomy and Astrophysics*, 19, 137
- Proga D., 2003, *The Astrophysical Journal*, 585, 406
- Proga D., 2007, in *The Central Engine of Active Galactic Nuclei*. Jiaotong University, Xi'an, China, p. 267, <https://ui.adsabs.harvard.edu/abs/2007ASPC..373..267P>
- Proga D., Kallman T. R., 2004, *The Astrophysical Journal*, 616, 688

- Proga D., Stone J. M., Drew J. E., 1998, *Monthly Notices of the Royal Astronomical Society*, 295, 595
- Proga D., Stone J. M., Kallman T. R., 2000, *The Astrophysical Journal*, 543, 686
- Pszota G., Cui W., 2007, *The Astrophysical Journal*, 663, 1201
- Rees M. J., 1984, *Annual Review of Astronomy and Astrophysics*, 22, 471
- Rees M., 1988, *Nature*, 333, 523
- Reichard T. A., et al., 2003, *The Astronomical Journal*, 126, 2594
- Robitaille T. P., 2010, *Astronomy & Astrophysics*, 576, C1
- Roming P. W. A., et al., 2005, *Space Science Reviews*, 120, 95
- Roth N. J., 2016, PhD thesis, UC Berkeley, <https://escholarship.org/uc/item/7sd297p2>
- Roth N., Kasen D., 2015, arXiv:1404.4652 [astro-ph 10.1088/0067-0049/217/1/9]
- Roth N., Kasen D., 2018, *The Astrophysical Journal*, 855, 54
- Roth N., Kasen D., Guillochon J., Ramirez-Ruiz E., 2016, *The Astrophysical Journal*, 827, 3
- Roth N., Rossi E. M., Krolik J., Piran T., Mockler B., Kasen D., 2020, *Space Science Reviews*, 216, 114
- Rybicki G. B., Hummer D. G., 1978, *The Astrophysical Journal*, 219, 654
- Rybicki G. B., Lightman A. P., 1985, Radiative Processes in Astrophysics, new ed edition edn. Wiley VCH, Weinheim
- Ryu T., Krolik J., Piran T., 2020, *The Astrophysical Journal*, 904, 73
- Saxton R., Komossa S., Auchettl K., Jonker P. G., 2020, *Space Science Reviews*, 216, 85
- Shakura N. I., Sunyaev R. A., 1973, *Astronomy & Astrophysics*, 24, 337
- Shappee B. J., et al., 2014, *The Astrophysical Journal*, 788, 48
- Shen R. F., Matzner C. D., 2014, *Astrophysical Journal*, 784
- Shimura T., Takahara F., 1995, *The Astrophysical Journal*, 445, 780
- Shiokawa H., Krolik J. H., Cheng R. M., Piran T., Noble S. C., 2015, *The Astrophysical Journal*, 804, 85
- Shlosman I., Vitello P., 1993, *The Astrophysical Journal*, 409, 372

- Shlosman I., Vitello P. A., Shaviv G., 1985, *The Astrophysical Journal*, 294, 96
- Short P., et al., 2020, *Monthly Notices of the Royal Astronomical Society*, 498, 4119
- Sobolev V. V., 1957, *Soviet Astronomy*, 1, 678
- Spaulding A., Chang P., 2021, *Monthly Notices of the Royal Astronomical Society*, 501, 1748
- Steele I., Oschmann J., 2004. SPIE, Bellingham
- Steffen A. T., Strateva I., Brandt W. N., Alexander D. M., Koekemoer A. M., Lehmer B. D., Schneider D. P., Vignali C., 2006, *The Astronomical Journal*, 131, 2826
- Stone N. C., Metzger B. D., 2016, *Monthly Notices of the Royal Astronomical Society*, 455, 859
- Stone N. C., Velzen S. v., 2016, *The Astrophysical Journal*, 825, L14
- Stone N. C., Kesden M., Cheng R. M., van Velzen S., 2019, *General Relativity and Gravitation*, 51, 30
- Stoughton C., et al., 2002, *The Astronomical Journal*, 123, 485
- Strubbe L. E., Quataert E., 2009, *Monthly Notices of the Royal Astronomical Society*, 400, 2070
- Thomsen L. L., Dai J. L., Ramirez-Ruiz E., Kara E., Reynolds C., 2019, arXiv:1907.11462 [astro-ph]
- Titarchuk L., Shrader C., 2005, *The Astrophysical Journal*, 623, 362
- Ulmer A., 1999, *The Astrophysical Journal*, 514, 180
- Verner D. A., Barthel P. D., Tytler D., 1995, *Astrophysical Applications of Powerful New Databases*, 78, 145
- Vetterling W. T., Teukolsky S. A., Flannery B. P., Press W. H., 1993, *Numerical Recipes in FORTRAN: The Art of Scientific Computing*, 2 edn. 1 Vol. 1, Cambridge University Press, Oxford
- Virtanen P., et al., 2020, *Nature Methods*, 17, 261
- Voges W., 1993, *Advances in Space Research*, 13, 391
- Wang C.-Y., Chevalier R. A., 2001, *The Astrophysical Journal*, 549, 1119
- Wang Y.-H., Perna R., Armitage P. J., 2021, *Monthly Notices of the Royal Astronomical Society*, 503, 6005
- Waters T., Proga D., 2019, *The Astrophysical Journal*, 876, L3

- Wevers T., van Velzen S., Jonker P. G., Stone N. C., Hung T., Onori F., Gezari S., Blagorodnova N., 2017, *Monthly Notices of the Royal Astronomical Society*, 471, 1694
- Wevers T., et al., 2019, *Monthly Notices of the Royal Astronomical Society*, 488, 4816
- Weymann R. J., Morris S. L., Foltz C. B., Hewett P. C., 1991, *The Astrophysical Journal*, 373, 23
- White N. E., Stella L., Parmar A. N., 1988, *The Astrophysical Journal*, 324, 363
- Woods J. A., 1991, PhD thesis, University of Oxford: Faculty of Physical Sciences
- Wu S., Coughlin E. R., Nixon C., 2018, *Monthly Notices of the Royal Astronomical Society*, 478, 3016
- Yang C., Wang T., Ferland G. J., Dou L., Zhou H., Jiang N., Sheng Z., 2017, *The Astrophysical Journal*, 846, 150
- Young P. J., Shields G. A., Wheeler J. C., 1977, *The Astrophysical Journal*, 212, 367
- Zhou Z. Q., Liu F. K., Komossa S., Cao R., Ho L. C., Chen X., Li S., 2020, arXiv:2002.02267 [astro-ph, physics:gr-qc]
- Zhuravlev V. V., 2015, *Physics-Uspekhi*, 58, 527
- de Kool M., Begelman M. C., 1995, *The Astrophysical Journal*, 455, 448
- van Velzen S., Stone N. C., Metzger B. D., Gezari S., Brown T. M., Fruchter A. S., 2019, *The Astrophysical Journal*, 878, 82
- van Velzen S., et al., 2020a, arXiv:2001.01409 [astro-ph]
- van Velzen S., Holoien T. W.-S., Onori F., Hung T., Arcavi I., 2020b, *Space Science Reviews*, 216, 124